Strongly Interacting Fermi Gases: Non-Equilibrium Dynamics and Dimensional Crossover

by

Ariel T. Sommer

Submitted to the Department of Physics
in partial fulfillment of the requirements for the degree of

Doctor of Philosophy

at the

MASSACHUSETTS INSTITUTE OF TECHNOLOGY

February 2013

Author .....
Department of Physics
January 30, 2013

Certified by .....
Martin W. Zwierlein
Silverman Family Career Development Associate Professor of Physics
Thesis Supervisor

Accepted by .....
John Belcher
Professor of Physics, Associate Department Head for Education

Strongly Interacting Fermi Gases: Non-Equilibrium Dynamics and Dimensional Crossover

by

Ariel T. Sommer

Submitted to the Department of Physics
on January 30, 2013, in partial fulfillment of the
requirements for the degree of
Doctor of Philosophy

Abstract

Experiments using ultracold atomic gases address fundamental problems in many-body physics. This thesis describes experiments on strongly-interacting gases of fermionic atoms, with a focus on non-equilibrium physics and dimensionality.

One of the fundamental dissipative processes in two-component gases is the transport of spin due to relative motion between the two spin components. We generate spin transport in strongly-interacting Fermi gases using a spin dipole excitation and measure the transport coefficients describing spin drag and spin diffusion. For resonant interactions, we observe strong suppression of spin transport, with the spin transport coefficients reaching quantum-mechanical limits.

Dimensionality plays an important role in the formation of bound states between pairs of particles. We tune the dimensionality of a Fermi gas from three to two dimensions (2D) using an optical lattice potential and observe the evolution of the pair binding energy using radio-frequency spectroscopy. The binding energy increases as the lattice depth increases, approaching the 2D limit. Gases with resonant interactions, which have no two-body bound state in three dimensions, show a large binding energy determined by the confinement energy of the lattice wells.

The themes of non-equilibrium dynamics and dimensionality come together in the study of soliton excitations in superfluid Fermi gases. We create a planar defect in the superfluid order parameter of an elongated Fermi gas using detuned laser light. This defect moves through the gas as a solitary wave, or soliton, without dispersing. We measure the oscillation period of the soliton and find it to exceed the predictions of mean-field theory by an order of magnitude.

Thesis Supervisor: Martin W. Zwierlein
Title: Silverman Family Career Development Associate Professor of Physics

To My Family,

Mark and Phyllis,

Everett, Adrian, and David

Acknowledgments

I would like to thank the many people who made this work possible, and who contributed to the quality of my time at MIT.

First of all, my research advisor, Martin Zwierlein, deserves many thanks for his guidance over the years. I am fortunate to have had an advisor who cares greatly about the work we do, and who takes the time to share his knowledge with his students. Our discussions and brainstorming lead to many fruitful ideas, and I certainly enjoyed thinking about physics with him. Martin has been a colleague as well as an advisor, often joining his students in the lab and sharing with us the challenges and the exciting moments of experimental physics.

I learned new lessons in physics from everyone with whom I worked. Together with Martin, André Schirotzek taught me the how to set up and run atomic physics experiments. We set up many complicated experimental sequences, puzzled over interesting results, and repaired countless water leaks. Under his mentorship I learned the necessary experimental skills to keep the lab running after he graduated. Mark Ku joined the group about two years after I did, and I have had the pleasure of working with him on many projects. Mark set a high standard both in the quality of his data analysis and in his exceptional thoughtfulness as a coworker.

In the following years, our lab gained many excellent members, with Lawrence Cheuk, Wenjie Ji, and postdocs Waseem Bakr and Tarik Yesfsah and joining the team. Lawrence arrived with a solid skill set in atomic physics experiments, and was immediately able to help in the lab. Together we added an optical lattice to our machine, and shared the moment of discovery when we saw the spectrum of molecules in two dimensions. His abilities at solving both experimental and theoretical problems continue to impress me. Waseem joined us as a postdoc during our experiments on spectroscopy in a 1D lattice, and we immediately benefited from his knowledge of optical lattices. From Waseem I often learned that what seems possible in principle can also be possible in practice. We were fortunate to be joined by a second postdoc, Tarik Yefsah. I am grateful for Tarik's appreciation of doing things properly. He

introduced several improvements to the lab, and contributed greatly to our spin-orbit coupling and soliton projects. The newest member of our lab, Wenjie Ji, continues the trend of new students immediately impressing me with their abilities. I thank her for the contributions she has already made, and hope that she will continue to do well and enjoy her time here. I thank my labmates for their dedicated teamwork, and wish them the best of luck.

Many other students from the Zwierlein group played important roles in my time here. Cheng-Hsun Wu greeted me the first time I visited as a prospective graduate student. I congratulate him on finishing his PhD at this time as well. I thank Cheng and the current and former members of Fermi 1, Jee Woo Park, Ibon Santiago, Jennifer Schloss, Peyman Ahmadi, and Sebastian Will, for their willingness to help my lab on many occasions, and for inspiring everyone with their hard work and accomplishments. I wish luck to the members of Fermi 2, Melih Okan, Matthew Nicols, and Vinay Ramasesh, on their new experiment, and thank them for lending to BEC 1 many pieces of optics. I would also like to thank several undergraduate researchers and visiting students, Christoph Clausen, Caroline Figgatt, Sara Campbell, Thomas Gersdorf, Jacob Sharpe, Jordan Goldstein, Pangus Ho, and Kevin Fischer.

MIT is fortunate to have several research groups in atomic physics, and I got to know many of the students and postdocs in the Ketterle, Vuletic, and Chuang groups. The members of BEC 3 and BEC 5 made great neighbors. Many thanks to Tout Wang, Timur Rvachov, Myoung-Sun Heo, Chenchen Luo, Yeryoung Lee, Caleb Christensen, Gyu-Boong Jo, Jae-Hoon Choi, and Dylan Cotta for sharing the space and often working with us to keep our labs running in harmony. The members of BEC 5, Ivana Dimitrova, Paul Niklas Jepsen, Jesse Amato-Grill, and Michael Messer brought a nice sense of community to the cold atoms labs, and are building a beautiful new experiment with which I wish them luck. Additional thanks go to the students and postdocs of the Ketterle group's BEC 2 and BEC 4 labs, especially Edward Su, Hiro Miyake, Aviv Keshet, David Weld, Colin Kennedy, Wujie Huang, and Georgios Siviloglou. I thank Edward and Hiro for their friendship throughout my time here. Aviv I also thank for creating the word generator software and for helping us to use

it correctly, for helping me integrate my camera software with it, and for sharing his sense of humor. The members of the Vuletic and Chuang groups also shared their knowledge and resources with us, and I particularly thank Marko Cetina, Ian Leroux, Thibault Peyronel, Kristi Beck, Shannon Wang, Peter Herskind, Arolyn Conwill, Amira Eltony, and Molu Shi.

Many researchers from outside MIT played a role in my thesis work. Most notably, Giacomo Roati visited us from Florence and worked with us in the lab for several months, contributing significantly to the spin transport experiments. Later, Zoran Hadzibabic visited from Cambridge, UK, and contributed to the study of spin-orbit coupling. Wilhelm Zwerger visited MIT several times, and I thank him for giving seminars on cold-atom physics, and for many discussions. I also thank the theoretical physicists who exchanging ideas with us and worked on questions related to our experiments, including Felix Werner, Kris Van Houcke, Georg Bruun, Christopher Pethick, Olga Goulko, Tilman Enss, Hyungwon Kim, David Huse, and Giuliano Orso.

I would also like to thank my academic advisors Joseph Formaggio and Vladan Vuletic, and MIT staff including Albert McGurl, Joanna Keseberg, and Maxine Samuels.

Many friends at MIT outside of the physics world added to my time here. Special thanks to Jessica Noss, the members of Graduate Hillel and Techiya, Matthew Schram, and Jason Boggess. Finally, I would like to thank my parents Mark and Phyllis and my brothers Everett, Adrian, and David, for their support and encouragement.

Contents

1 Introduction **17**

1.1 Quantum Simulation with Ultracold Gases 17

1.2 History of Ultracold Fermi Gas Experiments 18

1.3 Overview of This Thesis 20

2 Ultracold Fermi Gases **25**

2.1 Quantum Statistics and Quantum Fields 25

2.1.1 Quantum Statistics 25

2.1.2 Second Quantization 26

2.2 Interactions and Feshbach Resonance 27

2.2.1 General Description of Short-Range Interactions 27

2.2.2 Low Energies: s-Wave Scattering 29

2.2.3 Feshbach Resonances 31

2.2.4 Hamiltonian of an Interacting Fermi Gas 33

2.3 The Density of a Gas at Equilibrium 34

2.3.1 The Density of Ideal Gases 35

2.3.2 Interacting Fermi Gases 37

2.4 Dynamics 39

2.4.1 Kohn's Theorem 39

2.4.2 Boltzmann Transport Theory 40

2.5 Spin Transport Coefficients 42

2.5.1 Spin Drag 43

2.5.2 Spin Conductivity 44

2.5.3 Spin Diffusion 46
2.5.4 Qualitative Behavior of the Spin Transport Coefficients 48
2.5.5 Classical Calculation of Spin Transport Coefficients 49
2.5.6 Kubo Formula for Spin Conduction 52

3 Experimental Techniques for Studying Quantum Gases 55
3.1 The BEC1 Apparatus 55
3.2 Imaging Atomic Clouds 58
3.2.1 Absorption Imaging 58
3.2.2 Phase-Contrast Imaging 60
3.2.3 Obtaining the 3D Density 61
3.3 Measurement of the Trapping Potential 62

4 Spin Transport in Strongly Interacting Fermi Gases 65
4.1 Experimental Realization of Spin Transport 66
4.2 Fermi Gas Collisions 70
4.3 Measuring Spin Transport in a Trapped Fermi Gas 72
4.3.1 Definition of Spin Transport Coefficients for Trapped Gases . 73
4.3.2 Spin Transport Measurements 74
4.4 Spin Transport in Polarized Fermi Gases 79
4.4.1 Highly-Polarized Fermi Gases 79
4.4.2 Spin-Imbalanced Superfluids 84

5 Evolution of Pairing From Three to Two Dimensions 87
5.1 Dimensional Crossover in a 1D Lattice 88
5.1.1 Single-Particle Physics in a 1D Lattice 88
5.1.2 Bound States and Scattering in Two Dimensions 90
5.1.3 Two-Body Physics in a 1D Lattice 91
5.1.4 Mean-Field Theory in Two Dimensions 91
5.2 Measurement of Binding Energies in a 1D Lattice 93
5.2.1 Experimental Procedure 93

5.2.2 RF Spectra in a 1D Lattice 96
5.2.3 Observed Binding Energies 97
5.3 Conclusions on Fermion Pairing in the 3D-to-2D Crossover 102

6 Solitons in Superfluid Fermi Gases 103
6.1 Solitons in Superfluids 103
6.1.1 Soliton Solution of the Gross-Pitaevskii Equation 103
6.1.2 Solitons in fermionic superfluids 106
6.2 Creating Solitons by Phase Imprinting 106
6.3 Detection of Solitons 110
6.4 Measurement of the Soliton Oscillation Period 110

7 Conclusion 115

A Universal Spin Transport in a Strongly Interacting Fermi Gas 117

B Spin Transport in Polaronic and Superfluid Fermi Gases 129

C Revealing the Superfluid Lambda Transition in the Universal Thermodynamics of a Unitary Fermi Gas 145

D Evolution of Fermion Pairing from Three to Two Dimensions 151

E Spin-Injection Spectroscopy of a Spin-Orbit Coupled Fermi Gas 157

List of Figures

2-1 Feshbach resonances and hyperfine structure of ^{6}Li 32

3-1 Schematic of the vacuum system 56
3-2 Hyperfine structure of ^{23}Na and ^{6}Li 57
3-3 Measuring the trapping potential using the atoms 63

4-1 Spin separation by magnetic field gradients 67
4-2 Experimental sequence for spin transport experiments 68
4-3 Collision of two spin-polarized clouds of fermions on resonance 69
4-4 Collisions with varying interaction strength 70
4-5 Frequency and damping times of spin excitations 71
4-6 Spin transport coefficients as a function of interaction strength. . . . 75
4-7 Spin transport coefficients vs. temperature at unitary 77
4-8 Spin transport in highly-polarized Fermi gases 81
4-9 Spin transport in a superfliud Fermi gas 85

5-1 Lattice depth calibration 95
5-2 RF spectrum of strongy-interacting fermions in a 1D lattice 97
5-3 Evolution of fermion pairing from 3D to 2D 98
5-4 Lineshape for bound-to-free spectra in 2D 99
5-5 Binding energy as a function of lattice depth 100
5-6 Binding energy in 2D 102

6-1 Soliton solution to the Gross-Pitaevskii equation 104
6-2 Optical setup for phase imprinting 107

6-3 Detection of solitons in a superfluid Fermi gas 109
6-4 Periodic oscillation of a dark soliton 111
6-5 Measurement of dark soliton oscillation period 111
6-6 Dark soliton oscillation period as a function of interaction strength . 112

List of Tables

Chapter 1

Introduction

1.1 Quantum Simulation with Ultracold Gases

Ultracold atomic gases provide pristine realizations of many-body systems. Researchers studying ultracold atom systems usually know precisely the microscopic model of the atomic gas, but know only approximate solutions to that model. Experiments on the system provide information about the exact solution. Comparing the results of experiments to different approximate solutions allows researchers to identify successful methods of approximation.

Conservation laws, symmetries, and dimensional analysis constrain the possible solutions to many-body problems. These constraints allow us to write the solutions to problems in terms of quantities that we can define, but the numerical values of which we do not know. For example, from Galilean symmetry we know that the friction between two clouds of distinguishable atoms varies, to leading order, proportionally with the relative velocity of the clouds. From the violation of time-reversal symmetry inherent in this relation, we know that this force increases the entropy of the system. Finally, dimensional analysis allows us to write the proportionality coefficient in terms of a dimensionless function of one or more dimensionless quantities composed of observable parameters. We can then measure this function experimentally and compare it to the predictions of calculations based on different approximations. This approach applies in any cold atom experiment–we know the ingredients of the problem, and we

assemble them to define measurable quantities.

Experiments using fermionic atoms address fundamental problems that arise in the study of superconductors, magnets, liquid helium-3, nuclei, neutron stars, and the quark-gluon plasma of the early universe. The theoretical methods tested against ultracold atom experiments often apply to some of these systems as well, allowing a transfer of knowledge.

1.2 History of Ultracold Fermi Gas Experiments

The development of laser cooling and magnetic trapping of neutral atoms in the 1980s and 1990s launched a new direction of research in atomic and condensed matter physics–the study of ultracold atomic gases. Bose-Einstein condensation of ^{87}Rb at JILA [4], ^{23}Na at MIT [34], and ^{7}Li at Rice [14] in 1995 made available quantum degenerate gases of bosons. Early studies included establishing the coherence of the macroscopic wavefunction of a Bose-Einstein condensate (BEC) through interference of two BECs [5] and the observation of vortices [101, 99, 122]. Studies also measured collective excitations [102] including out-of-phase motion of a BEC and thermal cloud [148].

Studies of ultracold fermionic gases began a few years later, with the observation of a degenerate Fermi gas of ^{40}K in 1999 at JILA [37]. In the next four years, experiments on degenerate Fermi gases began in six more groups, with M. Ingusico's group in Florence also using ^{40}K [128] and R. Hulet's group at Rice [156], C. Salomon's group at the ENS [134], J. Thomas's group at Duke [62], W. Ketterle's group at MIT [67], and R. Grimm's group at Innsbruck [74] using ^{6}Li. Observation of superfluidity served as the primary goal. Feshbach resonances [41, 108, 126, 32] provided a tool for enhancing interactions to raise the superfluid transition temperature T_c, as well as to tune the character of interactions. Observations of BEC in dimers of fermionic atoms [174, 63, 13] and in Fermi gases across the Feshbach resonance after a rapid ramp to the molecular limit in [125, 175] provided evidence that experiments had created superfluid Fermi gases. Direct proof came in 2005 with the observation of

vortex lattices in rotating Fermi gases at MIT [170].

With superfluid Fermi gases available, groups around the world began studying their thermodynamics [80, 151, 98] and collective oscillations [10, 79, 2, 164]. Tunable interactions allowed measurements to be made throughout the crossover from Bose-Einstein condensation of molecules to Bardeen-Cooper-Schrieffer superfluidity of long-range Cooper pairs (the BEC-BCS crossover), originally studied theoretically by Popov [118], Keldysh and Kozlov [76] and Eagles [49] in the 1960s and generalized by Leggett [92] and Noziéres and Schmitt-Rink [107] in the early 1980s. The center of this crossover, where interactions are resonant and reach the unitary limit of quantum mechanics, received particular attention. At unitarity, the energy scale associated with interactions drops out and the Fermi energy and temperature become the only energy scales. Because of strong interactions, the point at unitarity also represents the greatest challenge theoretically.

At MIT and at Rice University, experiments on ultracold Fermi gases began to focus on spin-imbalanced superfluids. The first goals addressed the long-standing question of the stability of superfluidity in a system where the spin states have unequal Fermi energies [29, 57, 90]. Studies of density profiles of spin-imbalanced clouds showed phase separation between an unpolarized superfluid core and a polarized normal phase [141, 113]. Experiments at MIT demonstrated superfluidity with imbalanced spin populations through the observation of vortices in spin-imbalanced clouds, and measured the critical population imbalance for superfluidity across the BEC-BCS crossover [172, 173]. The critical number imbalance measured at MIT [172, 173] and at Rice [113, 112] differed significantly. Explanations pointed out that the high aspect ratio of the atomic gases at Rice could lead to additional effects beyond the description of an equilibrium gas in the local density approximation [35, 84] although a clear resolution would come later. Further studies at MIT mapped out the phase diagram of the unitary Fermi gas with spin imbalance [143, 142].

Experiments on superfluidity in spin-imbalanced gases at MIT took place in the BEC1 lab under W. Ketterle. Work in BEC1 then began to use radio-frequency (RF) spectroscopy to probe the microscopic physics of fermionic superfluids [135].

Tomographic reconstruction of 3D densities [140] and the realization of superfluidity in a new combination of hyperfine states to reduce final state effects [137] established RF spectroscopy as a quantitative tool for studying strongly-interacting Fermi gases. By using the quasiparticles in a Fermi gas with small spin imbalance to calibrate energy shifts, the group applied the newly developed spectroscopy techniques to measure the superfluid gap and other parameters of the excitation spectrum [131].

1.3 Overview of This Thesis

When I arrived at MIT in 2007, I spent most of my first year helping to build a new experiment for creating mixtures of atomic species, which has since been used to study Feshbach resonances between ^{6}Li, ^{23}Na, and multiple isotopes of K [166, 111, 165]. I also began learning about the BEC1 apparatus during the RF spectroscopy experiments [131]. In 2008, Martin Zwierlein's group took over operation of the BEC1 lab, and I began working there full time.

The first experiment in BEC1 under the Zwierlein group extended the RF spectroscopy measurements on spin-imbalanced gases [131] to focus on the regime of large spin-imbalance. Beyond the critical imbalance for superfluidity, the system remains normal down to zero temperature. The atoms of the minority spin state interact with the majority atoms to form a fermionic polaron quasiparticle–a quantized excitation of the spin polarization [120, 26]. We applied RF spectroscopy to measure the binding energy of the Fermi polaron and to identify the transition from a polaron to a molecule with varying scattering length [132].

To measure the effective mass of the Fermi polaron, we began to test methods of exciting out-of-phase oscillations of the two spin components in spin-imbalanced Fermi gases. During this time, a group at the ENS reported measurements of the polaron effective mass using an out-of-phase compressional excitation [105]. We decided to use our newly developed tools to go in a different direction, and to study spin transport in Fermi gases.

While observations of out-of-phase oscillations required eliminating damping by

working with imbalanced gases at effectively zero temperature, I felt that the damping itself would provide new insight into these systems. Rather than eliminate it, we set out to measure it. Damping of relative motion between spin states occurs due to spin drag, or the exchange of momentum between the two states. The spin drag coefficient expresses the rate of this momentum transfer. We studied the spin transport properties of strongly-interacting Fermi gases with equal populations in the two spin states over a range of temperatures and interaction strengths [145] (Chapter 4). We found that spin drag and spin diffusion at unitarity followed expected scaling laws at high temperatures, and we measured their evolution into the yet-unexplored realm of low temperatures. At low temperatures we found that the spin diffusivity reaches a lower limit set by $\hbar/m$, where $\hbar$ is the reduced Planck constant and m is the mass of the atoms. The spin transport quantities we measured confirmed an explanation put forward regarding the discrepancy between the critical number imbalance measured at MIT and at Rice, that the system studied at Rice had not reached equilibrium due to the long timescales required for spin transport in weakly-confined clouds [110, 94]. Returning to the subject of polarons, we measured spin transport in highly-imbalanced Fermi gases at unitarity over a wide range of temperatures, and observed the transition from classical scaling, to saturation by quantum degeneracy, to the onset of Pauli blocking at the lowest temperatures [146].

Simultaneously with the experiments on spin transport, we carried out measurements of the equation of state of the unitary Fermi gas. In a trapped atomic gas at equilibrium, the temperature is uniform while the trapping potential varies across the cloud. A measurement of the atomic density distribution then gives a measurement of the density as a function of the local chemical potential (in the local density approximation) at fixed temperature. At unitarity, due to the elimination of the scattering length as a parameter, the equation of state in dimensionless form becomes a function of one dimensionless variable, and each density profile measures the equation of state over some interval in the dimensionless variable. We obtained high-quality measurements of atomic density distributions in a well-calibrated trapping potential and from these obtained the equation of state of the unitary Fermi gas [85, 158]. From

the equation of state, we obtained several thermodynamic functions, and observed a sharp increase in the specific heat at the superfluid transition, giving a transition temperature of 0.167(13) T_F, where T_F is the Fermi temperature [85].

Following the studies of spin transport and thermodynamics, we decided to begin investigating the properties of Fermi gases in two dimensions. In two-dimensional (2D) Bose gases, a Berezinskii-Kosterlitz-Thouless-type superfluid transition had been seen in 2006 [68]. By 2011, groups were beginning to study fermions in 2D [100, 56, 45]. We carried out RF spectroscopy measurements on fermions in a one-dimensional (1D) optical lattice to study fermion pairing in the crossover from 3D to 2D (Chapter 5). Confinement of atoms in one direction by a deep optical lattice restricts motion to a 2D plane, where two-body bound states exist for arbitrarily weak attractive interactions. In a weak lattice, the system remains 3D but anisotropic, and binding requires a minimum interaction strength, or the presence of a Fermi sea. We observed the enhancement of the binding energy with increasing lattice depth toward the 2D limit, and compared our measurements with mean-field theory predictions in 2D. In addition to providing the binding energy, the lineshape of the RF spectra showed the anomalous nature of interactions in 2D.

Recent experiments on spin-orbit coupling in bosonic gases [95] got us thinking about spin-orbit coupling in Fermi gases. We set up Raman laser beams to generate spin-orbit coupling of two hyperfine states, similar to the method used in Bose gases. Spin-orbit coupling results in a modified energy-momentum dispersion, containing two bands with spin texture. Using momentum-resolved radio-frequency (RF) spectroscopy, we measured the energy-momentum dispersion and the spin composition of these two bands by injecting atoms into the spin-orbit coupled states [25]. Adding an additional coupling between the spin-orbit coupled states using an RF drive, we also created an off-diagonal, or spin-orbit coupled, optical lattice. Intricate momentum-resolved RF spectra of atoms injected into the spin-orbit coupled optical lattice allowed us to determine the energy bands and the spin composition of the eigenstates. Spin-orbit coupling is an important ingredient in many topological materials [121]. Future work in this direction offers the prospect of creating topological

states in atomic gases.

Finally, combining interests in dynamics and two dimensions, my colleagues and I studied dark soliton excitations in superfluid Fermi gases (Chapter 6). Soliton excitations propagate without dispersing, and result from non-linearities in fluids. In a dark soliton, the density of the fluid decreases near the excitation, while in a bright soliton the density increases. In a superfluid, dark solitons occur when the phase of the superfluid order parameter jumps by a significant amount over a short distance. Dark solitons in atomic superfluids have previously been observed in Bose gases [19, 38, 11]. Theoretical studies predicted the existence of dark solitons in Fermi superfluids, and calculated many of their properties, using a mean-field approximation [6, 138]. We created dark solitons in superfluid Fermi gases using the phase imprinting technique [19] and measured their oscillation period in a trapped gas. Surprisingly, we found that the oscillation period greatly exceeds the predicted value, reaching about a factor of 10 larger than the prediction at unitarity. Our group is currently investigating the explanation of this result, and we suspect it relates to the role of quantum fluctuations localized at the soliton [47, 91].

The experiments in this thesis have in common a similar spirit–to explore new features of strongly-interacting Fermi gases. Although spin currents constitute one of the fundamental dissipative processes in a Fermi gas, no previous experiments had isolated them and demonstrated their properties in the strongly-interacting regime. Nevertheless, in addition to their conceptual importance, spin transport properties play a practical role in understanding experiments on spin-imbalanced Fermi gases. The crossover from 3D to 2D and dark solitons also represent new features of strongly-interacting Fermi gases. Yet, although we have gone out of our way to observe them, they may turn up on their own in settings where we did not previously know to look for them.

Chapter 2

Ultracold Fermi Gases

2.1 Quantum Statistics and Quantum Fields

2.1.1 Quantum Statistics

In quantum mechanics, particles belong to one of two classes: fermions and bosons. Fermions obey the Pauli exclusion principle, stating that identical fermions cannot occupy the same quantum state, while identical bosons can occupy the same quantum state. These two classes of particles differ in their symmetry under an exchange of identical particles. A system of two identical particles with wavefunction $\Phi(\mathbf{r}_1, \mathbf{r}_2)$ has

$$\Phi(\mathbf{r}_1, \mathbf{r}_2) = \sigma\Phi(\mathbf{r}_2, \mathbf{r}_1), \tag{2.1}$$

with $\sigma = -1$ for fermions (Fermi statistics) and $\sigma = 1$ for bosons (Bose statistics). A collection consisting of an odd number of fermions obeys Fermi statistics, while a collection consisting of an even number of fermions obeys Bose statistics. The constituents of atoms–the electron, neutron, and proton–belong to the fermions. Therefore, atoms with an odd number of constituents obey Fermi statistics, while atoms with an even number of constituents obey Bose statistcs. For the experiments reported in this thesis, we use the fermionic isotope ^{6}Li, which has nine constituent particles.

2.1.2 Second Quantization

Second quantization provides a convenient notation for describing many-body systems [1]. In this notation, we write many-particle operators in terms of local field operators. The field operator $\psi_\alpha(\mathbf{r})$ annihilates a particle at position $\mathbf{r}$ in spin state α, while the hermitian conjugate $\psi_\alpha^\dagger(\mathbf{r})$ creates a particle at $\mathbf{r}$ with spin state α.

In second quantization, the commutation rules of the field operator enforce quantum statistics:

$$\psi_\alpha(\mathbf{r})\psi_\beta(\mathbf{r}') - \sigma\psi_\beta(\mathbf{r}')\psi_\alpha(\mathbf{r}) = \delta_{\alpha\beta}\,\delta(\mathbf{r},\mathbf{r}'), \tag{2.2}$$

where $\sigma = -1$ for fermions and 1 for bosons, as before.[1] In terms of the commutator $[\,,]$ and anti-commutator $\{\,,\}$, bosons obey $[\psi_\alpha(\mathbf{r}), \psi_\beta(\mathbf{r}')] = \delta_{\alpha\beta}\,\delta(\mathbf{r},\mathbf{r}')$ and fermions follow $\{\psi_\alpha(\mathbf{r}), \psi_\beta(\mathbf{r}')\} = \delta_{\alpha\beta}\,\delta(\mathbf{r},\mathbf{r}')$.

The state vector of a system with a many-body wavefunction $\Phi(\mathbf{r}_1, \mathbf{r}_2, \ldots)$ has expressions in both ordinary and second quantization (consider the spinless case for simplicity):

$$|\Phi\rangle = \int \Phi(\mathbf{r}_1, \mathbf{r}_2, \ldots)\,|\mathbf{r}_1, \mathbf{r}_2, \ldots\rangle = \int \Phi(\mathbf{r}_1, \mathbf{r}_2, \ldots)\psi^\dagger(\mathbf{r}_1)\psi^\dagger(\mathbf{r}_2)\ldots.\,|0\rangle\,, \tag{2.3}$$

where integration runs over the position variables.

For a single-particle operator,

$$\hat{F} = \sum_i f(\hat{\mathbf{r}}_i) = \int \psi^\dagger(\mathbf{r}) f(\mathbf{r}) \psi(\mathbf{r})\, d\mathbf{r}, \tag{2.4}$$

while for a two-particle operator,

$$\hat{V} = \sum_{i<j} V(\hat{\mathbf{r}}_i, \hat{\mathbf{r}}_j) = \frac{1}{2}\int \psi^\dagger(\mathbf{r}_1)\psi^\dagger(\mathbf{r}_2) V(\mathbf{r}_1, \mathbf{r}_2)\psi(\mathbf{r}_2)\psi(\mathbf{r}_1). \tag{2.5}$$

[1]The assumption of identical particles implies equation (2.1), while the single-valuedness of Φ requires $\sigma = \pm 1$. However, quasiparticles called anyons in some two-dimensional systems have $\sigma \neq \pm 1$ in (2.2).

2.2 Interactions and Feshbach Resonance

In the experiments reported in this thesis, particles interact through short range, s-wave interactions. The interaction originates in the Van der Waals interaction, and gains additional strength and tunability due to a Feshbach resonance. This section reviews the import aspects of scattering, and the Feshbach resonance mechanism.

2.2.1 General Description of Short-Range Interactions

When we study systems of many particles interacting through a pair-wise potential $V(\mathbf{r})$, we will describe the properties of the systems as functions of some aspect of the interactions. The potential function itself does not provide a suitable summary of the interaction in such contexts because many qualitatively different potential functions can ultimately give rise to the same behavior. Instead, we will describe the interaction in terms of the effect it has on the particles. In the case of low-energy scattering that applies to our experiments, we will see that the potential does only one thing to a pair of interacting particles, and that we can describe the interaction with a single number.

Before specializing to the case of low-energy scattering, we look at the general problem of describing the elastic scattering of two particles. The interaction does not affect the center of mass motion, so we write the Schrödinger equation for the relative part of the wavefunction,

$$\left[-\frac{\hbar^2}{2m_r}\nabla^2 + V(\mathbf{r})\right]\Psi(\mathbf{r}) = E\Psi(\mathbf{r}), \tag{2.6}$$

where $m_r = m/2$ is the reduced mass. In general, when two particles collide elastically, their relative momentum $\mathbf{k}$ undergoes a rotation relative to its original direction. We can find the probability of scattering into a given direction by looking at solutions to (2.6) having the following form outside the range r_0 of the potential (in the case of

three spatial dimensions):

$$\Psi_{\mathbf{k}}(\mathbf{r}) = e^{i\mathbf{k}\cdot\mathbf{r}} + f(\theta,\phi)\frac{e^{ikr}}{r}, \qquad r \gg r_0, \tag{2.7}$$

where the scattering amplitude $f(\theta,\phi)$ is some yet-undetermined function, and the energy is $E_{\mathbf{k}} = \frac{\hbar^2 k^2}{2m_r}$. We refer to solutions of this kind as scattering states.

The scattering amplitude $f(\theta,\phi)$ fully characterizes the elastic scattering of two particles. In particular, the scattering amplitude determines the differential cross-section. The relation between these quantities comes from the scattering state. The first term in (2.7) describes an incident probability flux of $\mathbf{J}_{\text{in}} = \hbar\mathbf{k}/m_r$, while the second term describes an outgoing (scattered) probability flux of $J_{\text{out},r} = \hbar k|f|^2/(m_r r^2)$ in the radial direction. We equate the incident flux through a small area $d\sigma$ normal to the incident wave to the outgoing flux through a small solid angle $d\Omega$ in the outgoing wave, $\mathbf{J}_{\text{in}} \cdot d\sigma = J_{\text{out},r} r^2 d\Omega$. The amount of area represented by a given solid angle defines the differential scattering cross-section,

$$\frac{d\sigma}{d\Omega} = |f|^2. \tag{2.8}$$

To find the scattering amplitude, we expand it in spherical harmonics (the partial-wave expansion). We will assume a rotationally symmetric potential $V(\mathbf{r}) = V(r)$, in which case $f = f(\theta)$ due to conservation of angular momentum. Expanding,

$$f(\theta) = \sum_{l=0}^{\infty} f_l P_l(\cos\theta), \tag{2.9}$$

where the P_l are the Legendre polynomials and the f_l are partial scattering amplitudes, which depend on k. Likewise, we expand the scattering state (2.7) in angular momentum eigenstates, and take the large kr limit,

$$\Psi_{\mathbf{k}}(\mathbf{r}) \to \frac{1}{kr}\sum_{l=0}^{\infty} c_l P_l(\cos\theta)\sin(kr - \frac{l\pi}{2} + \delta_l), \tag{2.10}$$

where c_l are expansion coefficients, and the δ_l are partial-wave phase shifts. The $\frac{l\pi}{2}$

term in the argument of the sine ensures that, for $\delta_l = 0$, the l-th term solves the radial wave equation in the absence of interactions. The phase shifts therefore express the effect of the interactions on the angular momentum eigenstates. One finds the phase shifts by solving for the angular momentum eigenstates and looking at their large kr limit. From the phase shifts, we can find the partial scattering amplitudes using the relation

$$f_l = \frac{2l+1}{k(\cot\delta_l - i)}, \tag{2.11}$$

which comes from equating the scattering state (2.7) to the sum over angular momentum states (2.10).

Scattering of Identical Particles

We have implicitly assumed distinguishable particles–for example, atoms of different species or in different internal states. For identical particles, the scattering states must have the correct behavior under particle exchange, $\Psi(\mathbf{r}) = \sigma\Psi(-\mathbf{r})$, so we replace the plane wave in (2.7) with $e^{i\mathbf{k}\cdot\mathbf{r}} + \sigma e^{-i\mathbf{k}\cdot\mathbf{r}}$ and require $f(\theta) = \sigma f(\pi - \theta)$. The latter implies $f_l = 0$ when $(-1)^l\sigma = -1$. Consequently, identical bosons do not scatter with odd l, while identical fermions do not scatter with even l. In particular, identical fermions do not undergo s-wave scattering. Since we work at low temperatures, this means that identical fermions do not interact in our experiments.

2.2.2 Low Energies: s-Wave Scattering

At low energies, we usually need to consider only the $l = 0$, or s-wave, contribution to the scattering amplitude. To see this, we first observe that the phase shifts typically become small as $k \to 0$. Heuristically, displacing the radial wavefunction by some amount Δr corresponds to a shift of phase by $k\Delta r$, which goes to zero as $k \to 0$. An exception occurs when $\Delta r = \pi/(2k)$, which gives a phase shift of $\pi/2$ for all k, and corresponds to a scattering resonance. In the absence of a resonance, $\delta_l \sim k^{2l+1}$ for small k in a finite-range potential [114, 87], and $f_l \sim k^{2l}$. Therefore, only the $l = 0$ scattering amplitude remains finite in the limit of low energy.

An important parametrization of the scattering amplitude follows from the asymptotic scaling of the s-wave phase shift as $\delta_0 \sim k$. We introduce the s-wave scattering length $a_0 = -\lim_{k\to 0} \delta_0(k)/k$. Then $k\cot\delta_0 \to -1/a_0$. Using this in the formula (2.11) for the partial scattering amplitude, we get

$$f_0 = \frac{1}{-1/a_0 - ik}, \tag{2.12}$$

and

$$\frac{d\sigma}{d\Omega} = \frac{a_0^2}{1 + k^2 a_0^2} \tag{2.13}$$

Note that at an s-wave scattering resonance, where $\delta_0 = \pi/2$, we have $k\cot\delta_0 = 0$, which corresponds to the limit $1/a_0 = 0$; the formulas (2.12) and (2.13) therefore remain applicable at an s-wave resonance. Equation (2.12) shows that a single quantity, the s-wave scattering length, summarizes the effect of short-range interactions at low energy. A related quantity is the overall scattering length $a = -\lim_{k\to 0} f$. It equals the s-wave scattering length, unless one of the higher angular momentum phase shifts equals $\pi/2$, in which case the scattering length diverges. In later sections we will assume none of the higher angular momenta are resonant, and simply refer to the scattering length a due to s-wave interactions.

Looking explicitly at the low-energy s-wave eigenstates provides an intuitive understand of the meaning of the s-wave scattering length, as well as a justification for the asymptotic $\delta_0 \sim k$ scaling. Consider the function $u(r) = r\,R_{k0}(r)$, where $R_{k0}(r)$ solves the radial wave equation with $l = 0$. The function $u(r)$ then satisfies a 1D Schrödinger equation,

$$-u'' + \frac{2m_r V}{\hbar^2} u = k^2 u, \tag{2.14}$$

with boundary condition u(0)=0. Inside the potential, where $r < r_0$, $u(r) \approx u_i(r)$, where $u_i(r)$ is the $k = 0$ solution inside the potential. Matching the solutions gives $u'(r_0)/u(r_0) = u_i'(r_0)/u_i(r_0) \equiv -1/\alpha$, where α is some constant, independent of k. Since $V(r > r_0) = 0$, $u(r > r_0) = \sin(kr + \delta_0)$ for some phase δ_0, which we immediately identify as the s-wave phase shift. The matching condition then gives

$-1/\alpha = k\cot\delta_0 \to k/\delta_0$, assuming $kr_0 \ll \delta_0 \ll 1$. Therefore, $\delta_0 \to -\alpha k$, and α equals the s-wave scattering length a_0. From $u(r > r_0) = \sin(k(r - a_0))$, we see that a_0 is the projected zero-crossing of the $r > r_0$ part of the wavefunction.

We can perform calculations with any potential that gives the right scattering length. Moreover, we can altogether abandon the use of a potential function, and replace it with a boundary condition on the wavefunction. As we see from the previous paragraph, the function $u(r)$ for $r > r_0$ follows the radial wave equation with $V = 0$ and boundary condition $u'(r_0)/u(r_0) = -1/a_0$. For $kr_0 \ll 1$, we can, to a good approximation, move this boundary condition to $r = 0$. In other words, we can replace the potential in the Scrödinger equation (2.6) with the Bethe-Peierl's boundary condition,

$$\lim_{r\to 0} \frac{\partial_r(r\Psi)}{r\Psi} = -\frac{1}{a_0}. \tag{2.15}$$

With the Bethe-Peierl's boundary condition, the Schrödinger equation for $a_0 > 0$ has a single negative-energy solution, with $E = -\hbar^2/(ma_0^2)$. This is the universal low-energy bound-state, with wavefunction $\Psi = e^{-r/a_0}/r$.

2.2.3 Feshbach Resonances

Feshbach resonances [27] allow us to tune the scattering length. In ^{6}Li, each pair of the lowest three hyperfine sublevels of the electronic ground state has a broad s-wave Feshbach resonance [9, 169] (Fig 2-1.a). We use these resonances to control the interaction strength in our experiments.

Feshbach resonances arise due to coupling between scattering channels. Each pair of internal states of two colliding atoms defines a scattering channel. Interactions with an applied magnetic field through the electron and nuclear magnetic moments cause each channel to have a different energy for large interatomic separation. In an open channel the energy associated with coupling to the magnetic field is less than the total energy, and the mechanical energy is positive. In a closed channel, the mechanical energy is negative. Initial and final states of a collision therefore must reside in open channels. However, if the interaction couples the incident open channel to a closed

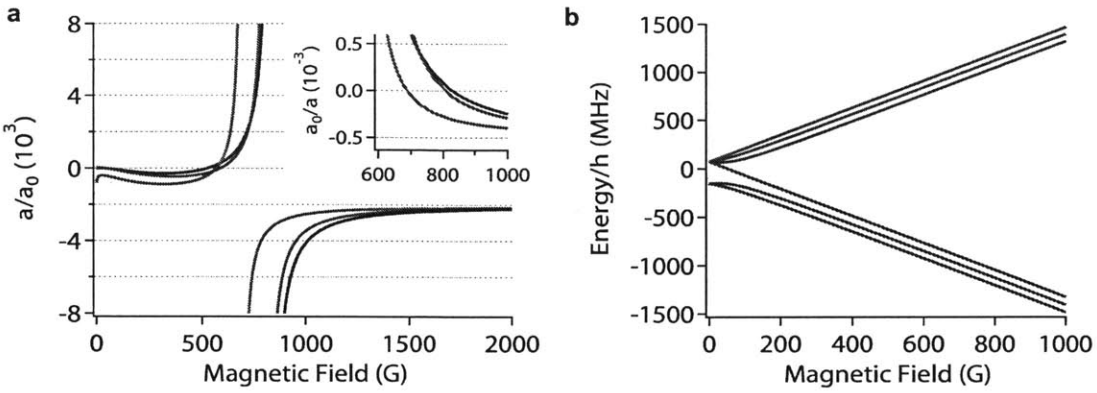

Figure 2-1: Feshbach resonances and hyperfine structure of ^{6}Li. **a**, Scattering length of ^{6}Li as a function of magnetic field, normalized by the Bohr radius. Inset: inverse scattering length versus magnetic field. The zero crossings show the resonance positions (data from Ref. [169]). **b**, Sublevels of the ^{6}Li electronic ground state as a function of magnetic field.

channel, atoms can virtually populate the closed channel during the collision. When a bound state in the closed channel is at or near the same energy as the colliding atoms, scattering is resonant.

For alkali atoms, the interatomic potential depends on the total electronic spin S of the two colliding atoms. For triplet (S=1) scattering, the potential is $V_T(r)$, while for singlet (S=0) scattering the potential is $V_S(r)$. The total potential is then

$$V(r) = V_T(r)\hat{P}_T + V_S(r)\hat{P}_S, \tag{2.16}$$

where $\hat{P}_T$ projects onto the triplet sub-space, and $\hat{P}_S$ projects onto the singlet subspace. In the high-field regime, the hyperfine states of alkali atoms are almost eigenstates of the electron spin projection m_s along the magnetic field axis, with a small admixture of the opposite spin projection due to the hyperfine coupling between the nuclear and electron spins. The scattering states are then predominantly triplet, but with a small singlet component. This singlet term allows the interaction (2.16) to couple the incident channel to other channels, since the eigenstates of the hyperfine interaction are different from the eigenstates of the interatomic interaction.

Pairs of the lowest three hyperfine states in ^{6}Li support Feshbach resonances due to

the presence of the three upper hyperfine states [72]. Figure 2-1.b shows the hyperfine levels of ^{6}Li in a magnetic field. The lower three hyperfine states are predominantly $m_s = -\frac{1}{2}$, while the upper states are predominantly $m_s = +\frac{1}{2}$). Singlet states therefore require an equal contribution from both the upper and lower manifold, causing the energy of the singlet states to lie above the energy of the lowest triplet states. Consequently, bound states in the singlet potential can couple resonantly to scattering states in the triplet potential.

The energy detuning between a scattering state in the triplet potential and a bound state in the singlet potential depends on the magnetic field due to the different magnetic moments in the singlet and triplet configurations. This allows us to tune across the scattering resonance by adjusting the magnetic field. The scattering lengths near the resonance are well-modeled by the expression [9]

$$a = a_b \left(1 + \frac{\Delta}{B - B_0}\right) \left[1 + \alpha(B - B_0)\right], \tag{2.17}$$

where B_0 determines the resonance position, Δ is the width, a_b is a background scattering length, and α is a correction parameter. The Feshbach resonance parameters for each of the state combinations in ^{6}Li are measured in Refs. [9, 169]. For most of the experiments in this thesis we use the earlier values [9], $B_0 = 834$ G (1-2), 811 G (2-3) and 690 G (1-3). However, for the soliton measurements we use the more recent values [169], $B_0 = 832$ G (1-2), 810 G (2-3) and 690 G (1-3).

2.2.4 Hamiltonian of an Interacting Fermi Gas

We will be interested in trapped gases of fermionic atoms at low temperatures, with short-range s-wave interactions. The Hamiltonian for a system of N fermions with positions $\mathbf{r}_i$ and spin quantum numbers α_i is

$$H = \sum_{i=1}^{N} \left[\frac{\mathbf{p}_i^2}{2m} + U(\mathbf{r}_i)\right] + \sum_{i<j} V(r_{ij})(1 - \delta_{\alpha_i \alpha_j}), \tag{2.18}$$

where $U(\mathbf{r})$ is a single-body external potential, $V(r)$ is the pairwise interaction potential, and $r_{ij} = |\mathbf{r}_i - \mathbf{r}_j|$. In second-quantized notation,

$$H = H_0 + H_1, \tag{2.19}$$

$$H_0 = \sum_\alpha \int \psi_\alpha^\dagger(\mathbf{r}) \left[-\frac{\hbar^2}{2m}\nabla^2 + U(\mathbf{r}) \right] \psi_\alpha(\mathbf{r})\, d\mathbf{r} \tag{2.20}$$

$$H_1 = \frac{1}{2} \int \psi_\uparrow^\dagger(\mathbf{r}_1)\psi_\downarrow^\dagger(\mathbf{r}_2)V(r_{12})\psi_\downarrow(\mathbf{r}_2)\psi_\uparrow(\mathbf{r}_1) d\mathbf{r}_1 d\mathbf{r}_2 \tag{2.21}$$

2.3 The Density of a Gas at Equilibrium

Consider a gas in a box, with no external forces acting in the interior of the box. One can measure the density of this gas directly, or predict it from any pair of thermodynamic quantities. For example, the temperature T and chemical potential μ give the density n through a function $n(\mu, T)$,

$$n = n(\mu, T). \tag{2.22}$$

One can use the equation of state $n(\mu, T)$ of the homogeneous gas to predict the density distribution in a potential that varies slowly in space. For sufficiently small potential gradients, the system looks locally homogeneous, so the density follows

$$n(\mathbf{r}) = n(\mu - U(\mathbf{r}), T), \tag{2.23}$$

where $U(\mathbf{r})$ is the trapping potential at the point $\mathbf{r}$. We refer to equation (2.23) as the local density approximation.

In experiments on trapped atomic gases, one usually measures the function $n(\mathbf{r})$. Fitting to the function $n(\mu, T)$ then allows one to determine the temperature and chemical potential of the gas. Conversely, if one knows μ and T, one can use the measured density distribution $n(\mathbf{r})$ to infer the equation of state $n(\mu, T)$.

2.3.1 The Density of Ideal Gases

In the case of non-interacting gases, $n(\mu, T)$ follows from basic statistical mechanics. Consider a gas of identical particles of mass m. In the grand canonical ensemble, the probability of having N_i particles in a state i follows $P_i(N_i) = e^{-\beta(\epsilon_i - \mu)N_i}/Z_i$, with ϵ_i the energy of the state, $\beta = (k_B T)^{-1}$, k_B the Boltzmann constant, and $Z_i(\mu, T)$ the partition function. The partition function follows

$$Z_i(\mu, T) = \sum_{N_i} e^{-\beta(\epsilon_i - \mu)N_i} = (1 - \sigma e^{-\beta(\epsilon_i - \mu)})^{-\sigma}, \tag{2.24}$$

where the sum runs from 0 to 1 for fermions and 0 to ∞ for bosons. The expected occupation $\langle N_i \rangle = \sum_{N_i} N_i P_i(N_i)$ equals $\beta^{-1}\partial_\mu \ln Z_i$, giving

$$\langle N_i \rangle = \frac{1}{e^{\beta(\epsilon_i - \mu)} - \sigma}, \tag{2.25}$$

where $\sigma = -1$ for fermions and 1 for bosons.

The density follows by summing the number of particles in all states and dividing by the volume of the system. For a gas in a box in d dimensions, the energies are $\epsilon_{\mathbf{k}} = \hbar^2 \mathbf{k}^2/(2m)$, where $\mathbf{k}$ has components $k_\alpha = 2\pi n_\alpha / L$, with L the length of the box along each axis, and n_α any integer. Now summing over all $\mathbf{k}$ gives the density, $L^{-d}\sum_{\mathbf{k}} \langle N_{\mathbf{k}} \rangle$. Since we usually study systems that occupy a large number of states, we can approximate the sum with an integral. However, the integral does not correctly include the population in the $\mathbf{k} = 0$ state, so we add it by hand,

$$n(\mu, T) = \int \frac{d^d \mathbf{k}}{(2\pi)^d} \frac{1}{e^{\beta(\epsilon_{\mathbf{k}} - \mu)} - \sigma} + \langle N_0 \rangle / L^d \tag{2.26}$$

$$= \frac{\sigma}{\lambda^d} \mathrm{Li}_{\frac{d}{2}} \left(\sigma e^{\beta\mu}\right) + \langle N_0 \rangle / L^d, \tag{2.27}$$

where Li_s is the polylogarithm function and $\lambda = h/\sqrt{2\pi m k_B T}$ is the thermal de-Broglie wavelength. The $\mathbf{k} = \mathbf{0}$ term only makes a significant contribution in the case of a Bose gas below the Bose-Einstein condensation (BEC) temperature, discussed in a later section. The formula for $n(\mu, T)$ in terms of the polylogarithm allows one

to predict the density of an ideal gas. Additionally, it allows one to determine the temperature of non-interacting and weakly interacting gases from a measurement of the density.

Ideal Gases at High Temperature

We define the high-temperature, or classical, limit by the condition $n\lambda^d \ll 1$. From the fact that $\mathrm{Li}_s(z) \to z$ as $|z| \to 0$, it follows that the classical limit corresponds to $\beta\mu \to -\infty$. In this limit,

$$n(\mu, T) = \frac{1}{\lambda^d} e^{\beta\mu}, \qquad \beta\mu \to -\infty. \tag{2.28}$$

Note that the quantum statistics of the particles no longer affect the equation of state. However, by using μ, we still assume identical particles. The classical limit turns out to help even in strongly-interacting gases when the temperature is sufficiently high and the density sufficiently low.

Ideal Fermi Gases at Zero Temperature

At zero temperature, the density of an ideal Fermi gas approaches a finite value determined by the chemical potential. The average occupation (2.25) becomes 1 for states with energy $\epsilon_i < \mu$ and 0 for states with energy $\epsilon_i > \mu$. The chemical potential therefore equals the Fermi energy E_F, defined as the maximum single-particle energy in a ground-state system of non-interacting fermions. From the formula (2.27) for the density, using an asymptotic limit of the polylog, or by counting the number of occupied states, one finds the density of a zero-temperature ideal Fermi gas,

$$n(\mu, T = 0) = \frac{{k_F}^d}{(4\pi)^{d/2}\,\Gamma(\frac{d}{2}+1)} \tag{2.29}$$

$$= \begin{cases} \frac{k_F}{\pi} & \text{if } d = 1, \\ \frac{{k_F}^2}{4\pi} & \text{if } d = 2, \\ \frac{{k_F}^3}{6\pi^2} & \text{if } d = 3, \end{cases} \tag{2.30}$$

where $k_F = \sqrt{2mE_F/\hbar^2}$, and $\mu = E_F$.

Ideal Bose Gases at (and near) Zero Temperature

From the average occupation (2.25), we learn that $\mu < 0$ for an ideal Bose gas, since each state has a non-negative, non-infinite, number of particles. However, as $\beta\mu \to 0^-$, the ground state occupation becomes infinite. On the other hand, as $\beta\epsilon_1 \to \infty$, the population of the first excited state goes to zero. Therefore, in the limit $|\mu| \ll T \ll \epsilon_1$, where ϵ_1 is the energy of the first excited state, population accumulates entirely in the ground state, and the system becomes fully Bose-Einstein condensed. The density distribution of a non-interacting Bose-Einstein condensate does not follow the local density approximation formula (2.23), but follows the wavefunction of the single-particle ground state in the trapping potential.

2.3.2 Interacting Fermi Gases

The equation of state of a gas with s-wave interactions contains the s-wave scattering length a as a parameter, $n = n(\mu, T; a)$. In the high-temperature regime, one can obtain the equation of state for the pressure P from the virial expansion,

$$P(\mu, T; a)\beta\lambda^d = 2\sum_{j=1}^{\infty} b_j(\mu, T; a)e^{j\beta\mu}. \tag{2.31}$$

The virial coefficients b_j, with $b_1 = 1$, are determined by solving the n-body problem for $n = 1$ up to j. For the three-dimensional case, Ref. [96] gives the second and third virial coefficients using solutions for two [21] and three [162] interacting fermions in a harmonic trap (see also [71] for an earlier determination of b_2). At lower temperatures, the equation of state is calculated in Ref. [69] using a self-consistent ladder approximation and in Ref. [73] using an extension of the theory by Noziéres and Schmitt-Rink [107]. The equation of state at zero temperature for arbitrary scattering length has been determined using a fixed-node diffusion Monte Carlo calculation in Ref. [8].

Thermodynamics of the Unitary Fermi Gas

Many calculations and experiments address the special case of the unitary Fermi gas. At unitarity, the scattering length diverges, and the equation of state of a homogeneous gas can be written as a universal function of one dimensionless parameter, for example,

$$n\lambda^3 = f(\beta\mu). \tag{2.32}$$

The virial coefficients for a homogeneous gas at unitarity become $b_2 = \frac{3\sqrt{2}}{8}$ and $b_3 \approx -0.290\,952\,95$, independent of T and μ [96]. Using $n = \partial P/\partial\mu$ and Eqn. (2.31) gives,

$$n(\mu, T; a = \pm\infty)\lambda^3 = 2\sum_{j=1}^{\infty} j b_j e^{j\beta\mu}. \tag{2.33}$$

The virial expansion in the form (2.33) allows one to determine T and μ by fitting to the low-density region of a trapped unitary gas.

At zero temperature, the equation of state of the unitary Fermi gas becomes

$$\mu = \xi E_F, \tag{2.34}$$

where ξ is the Bertsch parameter [58, 12, 55, 69, 7].

Our group has measured the equation of state of the unitary Fermi gas precisely [85, 158], and found it to agree well with bold-line diagrammatic Monte Carlo calculations in the normal state [158]. We obtained the equation of state using two different analysis methods. The original method [158] fits the low-density region of the atomic gas to a known high-temperature (low $\beta\mu$) equation of state, and uses the points at higher density to extend the equation of state to larger values of $\beta\mu$. The virial expansion (2.33) provides a starting point. The second method [85] uses the compressibility κ and pressure P, obtained directly from the density profiles, to measure the equation of state in the form $\kappa(n, P)$. The latter method avoids the need for a fitting function. Our measurements give $\xi = 0.376(4)$, and a superfluid transition temperature of $T_c = 0.167(13)T_F$ [85].

2.4 Dynamics

2.4.1 Kohn's Theorem

An atomic cloud moving in an arbitrary potential can, in general, stretch, compress, or otherwise distort its shape and dissipate energy as the center of mass moves to different regions of the potential. The center-of-mass motion of the cloud then couples to the relative degrees of freedom. However, in some special cases, the center of mass and relative degrees of freedom decouple. In particular, this occurs in a constant potential and in a harmonic potential. The case of a constant potential follows from Galilean invariance. The harmonic case, shown below, is a generalization of Kohn's theorem [81], the harmonic potential theorem [42].

Consider an atomic cloud in a trapping potential that is harmonic along the z direction,

$$U(x,y,z) = \frac{1}{2}m\omega_z^2 z^2 + U_t(x,y), \tag{2.35}$$

where U_t is the transverse trapping potential. Assume the center of mass only moves in the z direction. The z coordinate of the center of mass satisfies $\ddot{Z} + \omega_z^2 Z^2 = 0$, while the z coordinates of individual atoms satisfy

$$\ddot{z}_i + \omega_z^2 z_i = -\frac{1}{m}\sum_{j\neq i}\frac{dV}{dr}(r_{ij})\frac{z_i - z_j}{r_{ij}}, \tag{2.36}$$

where $V(r)$ is the pairwise interaction potential as before. Now we transform to coordinates measured relative to the center of mass, $z_i' = z_i - Z$. The equations of motion remain unchanged because Z solves the homogeneous version of (2.36), and the right hand side depends only on the relative coordinates, $z_i' - z_j' = z_i - z_j$. Therefore the dynamics in the center of mass frame are equivalent to the dynamics of a system at rest. Additionally, one finds that the transformed Hamiltonian $H'(\mathbf{r}_i') = H(\mathbf{r}_i') + E_{\mathrm{cm}}$ differs from the original form of the Hamiltonian by the constant energy E_{cm} of the center of mass, and that the many-body wavefunction, transformed to the center-of-mass frame, satisfies the same Schrödinger equation as in the lab frame [42].

Experimentally, we often work with atomic clouds where the center of mass oscillates along the harmonically confined direction. These oscillations typically arise due to magnetic field ramps during system preparation. The harmonic oscillator theorem ensures that we can analyze the dynamics of atom clouds in the center of mass frame, without risk that the center of mass motion influences these dynamics.

2.4.2 Boltzmann Transport Theory

In the classical and semi-classical descriptions of a many-body system, we specify the number of particles near each point $(\mathbf{r}, \mathbf{p})$ in phase space. We divide phase space into small cells of volume $d^3\mathbf{r}d^3\mathbf{p} = h^3$, and define the distribution function $f(\mathbf{r}, \mathbf{p}, t)$ as the number of particles in the cell containing the point $(\mathbf{r}, \mathbf{p})$ at time t. For N particles, this definition of f gives the normalization

$$N = \int \frac{\mathrm{d}^3 r \, \mathrm{d}^3 p}{h^3} f(\mathbf{r}, \mathbf{p}). \tag{2.37}$$

The density and current density are

$$n(\mathbf{r}) = \int \frac{\mathrm{d}^3 p}{h^3} f(\mathbf{r}, \mathbf{p}) \tag{2.38}$$

$$\mathbf{J}(\mathbf{r}) = \int \frac{\mathrm{d}^3 p}{h^3} \mathbf{v} f(\mathbf{r}, \mathbf{p}) \equiv n(\mathbf{r})\mathbf{v}(\mathbf{r}), \tag{2.39}$$

where $\mathbf{v}(\mathbf{r})$ is the local average velocity. Additionally, the center of mass is

$$\mathbf{R} = \frac{1}{N} \int \frac{\mathrm{d}^3 r \, \mathrm{d}^3 p}{h^3} \mathbf{r} f(\mathbf{r}, \mathbf{p}). \tag{2.40}$$

In the absence of interactions, Liouville's theorem implies that $f(\mathbf{r}(t), \mathbf{p}(t), t)$ is constant along a classical trajectory. The Boltzmann transport equation expresses the rate of change of f along classical trajectories due to collisions,

$$\frac{\mathbf{p}}{m} \cdot \nabla_{\mathbf{r}} f + \mathbf{F} \cdot \nabla_{\mathbf{p}} f + \frac{\partial f}{\partial t} \equiv \left(\frac{df}{dt} \right)_{\mathrm{coll}}, \tag{2.41}$$

where $\mathbf{F} = -\nabla U$ is the external force. The left hand side is just $\mathrm{d}f/\mathrm{d}t$ along a path in phase space, combined with Hamilton's equations. The right hand side expresses the net rate at which particles enter the vicinity of $(\mathbf{r}, \mathbf{p})$ due to collisions. This rate depends on the probability of finding two particles near each other with the correct momenta, and therefore depends on the two-body distribution. We will assume uncorrelated momenta, a condition which holds at high temperatures, but certainly not in a BCS superfluid. Then the two-body distribution becomes a product of two single-body distribution functions. Specializing to the case of fermions in two spin states with only opposite-spin atoms interacting, we use the distribution functions f_α for spins $\alpha = \uparrow, \downarrow$. The rate of particles entering $(\mathbf{r}, \mathbf{p})$ due to collisions, minus the rate leaving, is,

$$\left(\frac{df_\alpha}{dt}\right)_{\text{coll}} = \int d^3\mathbf{p}_2 \, d\Omega \frac{|\mathbf{p} - \mathbf{p}_2|}{m} \frac{d\sigma}{d\Omega} \left[F_\alpha(\mathbf{r}, \mathbf{p}_1', \mathbf{p}_2', \mathbf{p}, \mathbf{p}_2) - F_\alpha(\mathbf{r}, \mathbf{p}, \mathbf{p}_2, \mathbf{p}_1', \mathbf{p}_2')\right], \tag{2.42}$$

where $\mathbf{p}_1'$ and $\mathbf{p}_2'$ are the momenta of two particles after an elastic collision with initial momenta $\mathbf{p}$ and $\mathbf{p}_2$ and a rotation of the relative momentum by $\Omega = (\theta, \phi)$. For uncorrelated momenta, the two-particle functions become

$$F_\alpha(\mathbf{r}, \mathbf{p}_1, \mathbf{p}_2, \mathbf{p}_1', \mathbf{p}_2') = f_{\alpha 1} f_{-\alpha 2}(1 - f_{\alpha 1'})(1 - f_{-\alpha 2'}), \tag{2.43}$$

where $f_{\alpha 1} = f_\alpha(\mathbf{r}, \mathbf{p}_1)$, etc. The $(1-f)$ factors arise due to Pauli blocking for fermions, which requires that the final states in a collision are initially unoccupied.

The Boltzmann transport equation allows us to calculate the evolution of single-body properties using the method of averages [65]. For a quantity $\chi(\mathbf{r}, \mathbf{p})$, the average value over the spin α particles is

$$\langle \chi_\alpha(t) \rangle = \frac{1}{N_\alpha} \int \frac{d^3\mathbf{r} d^3\mathbf{p}}{h^3} \chi(\mathbf{r}, \mathbf{p}) f_\alpha(\mathbf{r}, \mathbf{p}, t). \tag{2.44}$$

For example, the center of mass of spin α is $\mathbf{R}_\alpha = \langle \mathbf{r}_\alpha \rangle$.

Averages evolve under the Boltzmann transport equation (2.41) according to

$$\frac{\mathrm{d}\langle\chi_\alpha\rangle}{\mathrm{d}t} = \left\langle \frac{\mathbf{p}}{m}\cdot\nabla_{\mathbf{r}}\chi_\alpha \right\rangle + \langle \mathbf{F}\cdot\nabla_{\mathbf{p}}\chi_\alpha\rangle + \left\langle \frac{\mathrm{d}\chi_\alpha}{\mathrm{d}t}\right\rangle_{\text{coll}} \tag{2.45a}$$

where

$$\left\langle \frac{\mathrm{d}\chi_\alpha}{\mathrm{d}t}\right\rangle_{\text{coll}} = \frac{1}{N_\alpha}\int \frac{d^3\mathbf{r}d^3\mathbf{p}}{h^3}\chi(\mathbf{r},\mathbf{p})\left(\frac{df_\alpha}{dt}\right)_{\text{coll}}. \tag{2.45b}$$

We will use Eqn. (2.45) to calculate the spin transport coefficients in the classical limit in section 2.5.5. We can save some calculational effort by noting that the rate of change (2.45b) due to collisions gives zero if collisions conserve $\langle\chi_\alpha\rangle$. For example, when χ depends only on position, (2.45b) vanishes because the position of a particle does not change significantly during a collision. Additionally, since the sum of the momentum or energy over both spin states is conserved,

$$\left\langle \frac{\mathrm{d}\mathbf{p}_\uparrow}{\mathrm{d}t}\right\rangle_{\text{coll}} + \left\langle \frac{\mathrm{d}\mathbf{p}_\downarrow}{\mathrm{d}t}\right\rangle_{\text{coll}} = 0, \tag{2.46}$$

and

$$\left\langle \frac{\mathrm{d}p_\uparrow^2}{\mathrm{d}t}\right\rangle_{\text{coll}} + \left\langle \frac{\mathrm{d}p_\downarrow^2}{\mathrm{d}t}\right\rangle_{\text{coll}} = 0. \tag{2.47}$$

On the other hand, since the relative momentum of colliding particles is not conserved,

$$\left\langle \frac{\mathrm{d}\mathbf{p}_\uparrow}{\mathrm{d}t}\right\rangle_{\text{coll}} - \left\langle \frac{\mathrm{d}\mathbf{p}_\downarrow}{\mathrm{d}t}\right\rangle_{\text{coll}} \neq 0. \tag{2.48}$$

The non-conservation of relative momentum causes rapid damping of spin currents.

2.5 Spin Transport Coefficients

When a physical system is slightly perturbed from equilibrium, it usually evolves according to dynamical rules that are linear. The proportionality constants relating the resulting motion in the system to the disturbance that caused it are known as transport coefficients. In the present chapter, we are interested in a perturbation of the spin density, and the resulting spin current. The transport coefficients describ-

ing spin currents are the spin drag coefficient, the spin conductivity, and the spin diffusivity [33, 54].

2.5.1 Spin Drag

In a gas of atoms in two spin states, relative motion of the two spin states defines a spin current. Collisions between atoms of different spin damps the spin current by randomizing the relative velocity of the colliding atoms. The exchange of momentum between the two spin components constitutes a drag force. For small spin currents, the drag force grows linearly with the current, and the proportionality constant gives the drag coefficient.

We will define the spin drag coefficient for a collection of two types of particles, in the sense of Ref. [33]. Suppose the particles of type i have total mass M_i and center of mass velocity v_i, where $i = 1, 2$. For small velocities, we assume that the force F_{21} on the type 2 particles due to collisions with the type 1 particles varies linearly with the velocities, $F_{21} = -\alpha v_2 + \beta v_1$. To determine the relation between α and β, consider a reference frame where the velocity of type 1 particles is zero at some instant in time. In this frame, and at that moment in time, $F_{21} = -\alpha v_2$. Transforming to an arbitrary frame that moves with velocity u relative to the original frame, the velocities become $v_2' = v_2 - u$ and $v_1' = -u$, while the force $F_{21}' = F_{21}$ must remain the same, because it represents an acceleration. This gives $F_{21}' = -\alpha(v_2' + u) = -\alpha(v_2' - v_1')$, and $\beta = \alpha$. Therefore, the drag force depends on the relative velocity of the two components.[2] Since we obtained this result for an arbitrary reference frame, we may drop the primes and write $F_{21} = -\alpha(v_2 - v_1)$. Additionally, due to Newton's third law, $F_{12} = -F_{21} = -\alpha(v_1 - v_2)$.

The coefficient α determines the damping rate of the relative motion between the two components. Assume no external forces act on the system. In that case,

$$\dot{v}_2 - \dot{v}_1 = -\alpha\left(\frac{1}{M_2} + \frac{1}{M_1}\right)(v_2 - v_1) \equiv -\Gamma_{\mathrm{SD}}(v_2 - v_1), \tag{2.49}$$

[2]This expression for the drag force is Galilean-invariant; having obtained it in one reference frame, it was guaranteed to hold in all reference frames.

which motivates the definition of the spin drag coefficient $\Gamma_{\rm SD}$. In terms of the spin drag coefficient, the force law reads,

$$F_{21} = -\frac{M_1 M_2}{M_1 + M_2}\Gamma_{\rm SD}(v_2 - v_1). \tag{2.50}$$

In a system of particles with equal masses m, we can apply (2.50) locally to find the drag force per unit volume

$$\frac{\mathrm{d}\mathbf{F}_{\uparrow\downarrow}}{\mathrm{d}^3 r} = -m\frac{n_\uparrow n_\downarrow}{n_\uparrow + n_\downarrow}\tilde{\Gamma}_{\rm SD}(\mathbf{r})(\mathbf{v}_\uparrow - \mathbf{v}_\downarrow), \tag{2.51}$$

where $\tilde{\Gamma}_{\rm SD}$ is the local value of the spin drag coefficient. Since our experiments involve inhomogeneous systems, we will use $\Gamma_{\rm SD}$ to refer to the global drag coefficient.

The definition of the spin drag coefficient allows the two types of particles to have different masses. For the experiments in this thesis, the two spin states originally have equal masses. However, in spin-imbalanced gases (Section 4.4.1), the spin up and spin down quasiparticles can have different effective masses. A spin-dependent lattice can also modify the effective masses of the two spin states. Moreover, one can apply this definition to describe the drag force between two clouds of different atoms, for example lithium and potassium.

2.5.2 Spin Conductivity

The spin conductivity expresses the linear response of the spin current to an applied spin dependent force. It plays an analogous role for spin systems to the electrical conductivity in charged systems. For current density $\mathbf{J}_\alpha = n_\alpha \mathbf{v}_\alpha$ in spin α, the spin current density and total current density are

$$\mathbf{J}_s = \mathbf{J}_\uparrow - \mathbf{J}_\downarrow \tag{2.52}$$

$$\mathbf{J} = \mathbf{J}_\uparrow + \mathbf{J}_\downarrow \tag{2.53}$$

In a typical electrical conductor, the drag force on the charge carriers varies pro-

portionally to the electric current. By balancing this drag force with an electric field, one establishes a steady-state current, and defines a conductivity. However, the spin drag force (2.51) does not vary exactly in proportion to the spin current (2.52), but instead varies with the relative velocity. We therefore decompose the spin current into a dissipative part that causes drag, and a non-dissipative, or reactive, part,

$$\mathbf{J}_s = \mathbf{J}_s^D + \mathbf{J}_s^R \tag{2.54}$$

with

$$\mathbf{J}_s^D = \frac{2n_\uparrow n_\downarrow}{n}(\mathbf{v}_\uparrow - \mathbf{v}_\downarrow) = \frac{2}{n}(n_\downarrow \mathbf{J}_\uparrow - n_\uparrow \mathbf{J}_\downarrow) \tag{2.55a}$$

$$\mathbf{J}_s^R = \frac{n_s}{n}\mathbf{J}, \tag{2.55b}$$

where $n = n_\uparrow + n_\downarrow$ and $n_s = n_\uparrow - n_\downarrow$. The spin drag force then becomes

$$\frac{\mathrm{d}\mathbf{F}_{\uparrow\downarrow}}{\mathrm{d}^3 r} = -\frac{1}{2}m\tilde{\Gamma}_{\mathrm{SD}}\mathbf{J}_s^D. \tag{2.56}$$

To define the spin conductivity, suppose a spin-dependent force is applied, so that each atom with spin α feels a force $\mathbf{F}_\alpha$. Then let $\mathbf{F}_s = \mathbf{F}_\uparrow - \mathbf{F}_\downarrow$. In steady state, the spin current generates a spin drag force that balances the applied spin-dependent force,

$$0 = m\dot{\mathbf{v}}_\uparrow - m\dot{\mathbf{v}}_\downarrow \tag{2.57}$$

$$= \mathbf{F}_s - \frac{1}{2}m\tilde{\Gamma}_{\mathrm{SD}}\left(\frac{1}{n_\uparrow} + \frac{1}{n_\downarrow}\right)\mathbf{J}_s^D \tag{2.58}$$

and therefore

$$\mathbf{J}_s^D = \sigma_s \mathbf{F}_s, \tag{2.59}$$

with the spin conductivity given by

$$\sigma_s = \frac{2}{m\tilde{\Gamma}_{\mathrm{SD}}}\frac{n_\uparrow n_\downarrow}{n_\uparrow + n_\downarrow}. \tag{2.60}$$

The total spin current in the pressence of a spin-dependent force is therefore

$$\mathbf{J}_s = \sigma_s \mathbf{F}_s + \frac{n_s}{n}\mathbf{J} \tag{2.61}$$

2.5.3 Spin Diffusion

In a two-component system with no external potential, the equilibrium state has uniform densities for the two components. A gradient in the density of either species will result in a current as particles flow from regions of high density to low density. When both species have density gradients in the same direction, the resulting pressure gradient will drive a net current of particles, or mass current. However, when the density gradients in the two species are not equal, the current densities of the two species will differ, leading to a spin current.

To determine the spin current resulting from a non-equilibrium density distribution, we first find the spin response to a gradient in the chemical potential difference $\mu_\uparrow - \mu_\downarrow$. We use the local chemical potentials $\mu_\alpha = \mu_\alpha(n_\uparrow, n_\downarrow, T)$. At equilibrium, in a spin-independent external potential U, the chemical potential difference is constant, i.e. $\nabla(\mu_\uparrow - \mu_\downarrow) = 0$. Therefore, any gradient in $\mu_\uparrow - \mu_\downarrow$ implies a non-equilibrium system, and may lead to a spin current. Suppose a given gradient $\nabla(\mu_\uparrow - \mu_\downarrow)$ induces some spin current $\mathbf{J}_s^{(\mu)}$ in the $\mathbf{J} = 0$ frame. We can cancel this current by applying a spin-dependent potential U_α such that $\nabla U_\alpha = -\nabla\mu_\alpha - \nabla U$, since that is the equilibrium condition for the chemical potentials. The spin-dependent potentials create a spin force $\mathbf{F}_s = -\nabla(U_\uparrow - U_\downarrow) = \nabla(\mu_\uparrow - \mu_\downarrow)$, and according to (2.59), generate a spin current $\mathbf{J}_s^{(F)} = \sigma_s \mathbf{F}_s$. Since the system is now at equilibrium, the spin currents must cancel, $\mathbf{J}_s^{(\mu)} + \mathbf{J}_s^{(F)} = \mathbf{0}$. The spin current due to the chemical potential gradients is therefore $\mathbf{J}_s^{(\mu)} = -\sigma_s \nabla(\mu_\uparrow - \mu_\downarrow)$. From this we conclude that the dissipative part of the spin current due to chemical potential gradients in a spin-independent potential is

$$\mathbf{J}_s^D = -\sigma_s \nabla(\mu_\uparrow - \mu_\downarrow). \tag{2.62}$$

Since a gradient in chemical potential implies a gradient in density, we can use

(2.62) to write the spin current response to a spin density gradient. However, a gradient in spin density does not always lead to a spin current. For example, a trapped system with an un-equal number of atoms in the two spin states has a locally non-zero spin density gradient at equilibrium. We therefore restrict our attention to a simple case. Consider a location where the densities of the two spin states are equal, $n_\uparrow = n_\downarrow$. Further, assume that the two spin states have opposite density gradients, $\nabla n_\uparrow = -\nabla n_\downarrow$. The spin density gradient then varies proportionally to the gradient of the chemical potential difference

$$\nabla(n_\uparrow - n_\downarrow) = \chi_s \nabla(\mu_\uparrow - \mu_\downarrow), \tag{2.63}$$

where χ_s is the spin susceptibility.[3] Using (2.63) in (2.62) gives the spin diffusion equation for this case,

$$\mathbf{J}_s = -D_s \nabla n_s, \tag{2.65}$$

where

$$D_s = \frac{\sigma_s}{\chi_s}. \tag{2.66}$$

Equation (2.66) is known as an Einstein relation, and is an example of the fluctuation-dissipation theorem.

Coupling of Spin and Heat Transport

In deriving the spin current due to a gradient in the chemical potential different (2.62), we implicitly assumed that the system had a uniform temperature–with a non-uniform temperature, we could not impose equilibrium simply by applying external potentials. The assumption of uniform temperatures holds well in our experiments, but interesting effects are predicted to occur when spin and heat flow simultaneously. In particular, Kim and Huse [78] have pointed out that the coupling of spin and heat

[3] In general, the spin susceptibility is defined by

$$\chi_s = \frac{\delta(n_\uparrow - n_\downarrow)}{\delta(\mu_\uparrow - \mu_\downarrow)}, \tag{2.64}$$

where the temperature and total chemical potential $\mu_\uparrow + \mu_\downarrow$ are held constant.

currents should be observable in atomic Fermi gases with non-zero spin polarization. In the presence of a temperature gradient, equation (2.62) becomes [78, 23]

$$\mathbf{J}_s^D = -\sigma_s \nabla(\mu_\uparrow - \mu_\downarrow) - 2S_s \nabla T, \tag{2.67}$$

where S_s is the spin Seebeck coefficient.[4] According to (2.67), applying a temperature gradient should result in an observable spin current for sufficiently large S_s.

2.5.4 Qualitative Behavior of the Spin Transport Coefficients

The universal behavior of the spin transport coefficients of a Fermi gas can be estimated on general grounds. At unitarity, Eqn. (2.13) gives the total scattering cross-section between atoms of opposite spin as $\sigma = \frac{4\pi}{k^2}$. In the degenerate regime, where $T \approx T_F$, the characteristic wavevector is the Fermi wavevector $k_F = (6\pi^2 n)^{1/3}$, with n the density per spin state, and the scattering cross section is approximately $\sigma \sim 1/k_F^2$. The mean free path between collisions is thus $l = 1/n\sigma \sim 1/k_F$ or about one interparticle spacing, the smallest possible mean free path in a gas. The average speed v of atoms is on the order of the Fermi velocity $\hbar k_F/m$. We can then estimate the spin diffusivity with resonant interactions at $T \approx T_F$,

$$D_s \approx vl \sim (\hbar k_F/m)\,(1/k_F) = \frac{\hbar}{m} \tag{2.68}$$

This value for D_s represents a universal quantum limit to spin diffusivity in Fermi gases. Away from resonance, the scattering cross section decreases, increasing D_s. For temperatures T much greater than the Fermi temperature T_F, the scattering cross section will be given by the square of the thermal de Broglie wavelength, and thus decreases as $\sigma \propto 1/T$. The velocity, in turn, will increase as $v \propto \sqrt{T}$, causing D_s to increase as

$$D_s \propto T^{3/2}, \qquad T \gg T_F \tag{2.69}$$

[4] Our definition of σ_s differs from that in [78] by a factor of 2 owning to our use of $\mathbf{J}_s^D = 2\mathbf{j}_{\text{spin}}$, where $\mathbf{j}_{\text{spin}}$ is the dissipative spin current in [78].

An analogous scaling argument applies to the viscosity[22, 51]. Finally, for $T \ll T_F$, the average velocity will remain on the order of the Fermi velocity, but the effective scattering cross section will scale as $\sigma \propto T^2$ due to Pauli blocking, causing D_s to increase like T^{-2} as the temperature is lowered. For a Fermi gas, we thus expect the minimum D_s to occur at degenerate temperatures, before Pauli blocking becomes effective.

The spin drag coefficient Γ_{SD} can be estimated using analogous arguments. Γ_{SD} scales like the collision rate $n\sigma v$. The maximum of Γ_{SD} is expected to occur for degenerate gases at unitarity. The estimates in the previous paragraph for σ and v give

$$\Gamma_{\text{SD}} \sim n\sigma v \sim E_F/\hbar, \tag{2.70}$$

where $E_F = \hbar^2 k_F^2/2m$ is the Fermi energy. Tuning away from unitarity, the scattering cross section decreases, and hence Γ_{SD} decreases. For temperatures much larger and much smaller than the Fermi temperature, Γ_{SD} also decreases. By analogous arguments to those for D_s, the expected high-temperature scaling of Γ_{SD} at unitarity is

$$\Gamma_{\text{SD}} \propto T^{-1/2}, \qquad T \gg T_F \tag{2.71}$$

At low temperatures, $\sigma \propto T^2$ due to Pauli blocking, resulting in $\Gamma_{\text{SD}} \propto T^2$ scaling.

2.5.5 Classical Calculation of Spin Transport Coefficients

We use the Boltzmann transport equation (section 2.4.2) to find the spin drag coefficient in the classical limit. Consider a uniform cloud of spin up and spin down atoms. The relative velocity of the two clouds along an arbitrary axis z evolves according to (2.45) as

$$\frac{\mathrm{d}}{\mathrm{d}t}\left\langle v_{z\uparrow} - v_{z\downarrow}\right\rangle = \left\langle \frac{\mathrm{d}v_{z\uparrow}}{\mathrm{d}t}\right\rangle_{\text{coll}} - \left\langle \frac{\mathrm{d}v_{z\downarrow}}{\mathrm{d}t}\right\rangle_{\text{coll}} \tag{2.72}$$

In light of (2.49), the spin drag coefficient is given by

$$\left\langle \frac{\mathrm{d}v_{z\uparrow}}{\mathrm{d}t}\right\rangle_{\text{coll}} - \left\langle \frac{\mathrm{d}v_{z\downarrow}}{\mathrm{d}t}\right\rangle_{\text{coll}} = -\Gamma_{\text{SD}}\left\langle v_{z\uparrow} - v_{z\downarrow}\right\rangle \tag{2.73}$$

Evaluating the collision integrals therefore gives $\Gamma_{\rm SD}$. The collision integrals can be written

$$\left\langle \frac{\mathrm{d}v_{z\uparrow}}{\mathrm{d}t} \right\rangle_{\rm coll} - \left\langle \frac{\mathrm{d}v_{z\downarrow}}{\mathrm{d}t} \right\rangle_{\rm coll} = \int \frac{\mathrm{d}^3 r \mathrm{d}^3 p_1 \mathrm{d}^3 p_2 \mathrm{d}\Omega}{h^6} \frac{|\mathbf{p}_1 - \mathbf{p}_2|}{m} \frac{d\sigma}{d\Omega} \left[F_\uparrow(1'2'12) - F_\uparrow(121'2')\right] \times \left(\frac{v_{1z}}{N_\uparrow} - \frac{v_{2z}}{N_\downarrow}\right), \quad (2.74)$$

using the property $F_\downarrow(121'2') = F_\uparrow(212'1')$ (see Eqn. 2.43) and the symmetry of the remaining part of the integrand under $1 \leftrightarrow 2$. Further simplification follows by writing

$$\frac{v_{1z}}{N_\uparrow} - \frac{v_{2z}}{N_\downarrow} = (v_{1z} + v_{2z}) \left(\frac{1}{N_\uparrow} - \frac{1}{N_\downarrow}\right) + \frac{v_{1z} - v_{2z}}{2} \left(\frac{1}{N_\uparrow} + \frac{1}{N_\downarrow}\right) \quad (2.75)$$

and noting that the first term integrates to zero due to conservation of momentum (Eqn. 2.46).

We linearize the collision integral (2.74) by expanding the distribution functions about the equilibrium distributions,

$$f_\alpha = f_\alpha^0 + \delta f_\alpha, \quad (2.76)$$

where $f_\alpha^0 = 1/\left(e^{\beta(\epsilon - \mu_\alpha)} + 1\right)$, the Fermi-Dirac distribution. The deviation δf_α will typically have a factor of $\partial f_\alpha^0 / \partial \epsilon = -\beta f_\alpha^0 (1 - f_\alpha^0)$ so we write it as

$$\delta f_\alpha = f_\alpha^0 (1 - f_\alpha^0) \psi_\alpha \quad (2.77)$$

for some function $\psi_\alpha(\mathbf{p})$. Keeping only the leading terms in ψ_α, the collision integral (2.74) becomes

$$\left\langle \frac{\mathrm{d}(v_{z\uparrow} - v_{z\downarrow})}{\mathrm{d}t} \right\rangle_{\rm coll} = \frac{n_\uparrow + n_\downarrow}{2 n_\uparrow n_\downarrow} \int \frac{\mathrm{d}^3 p_1 \mathrm{d}^3 p_2 \mathrm{d}\Omega}{h^6} \frac{d\sigma}{d\Omega} |\mathbf{v}_1 - \mathbf{v}_2| (v_{1z} - v_{2z}) \times (\psi_{1'} + \psi_{2'} - \psi_1 - \psi_2) f_1^0 f_2^0 (1 - f_{1'}^0)(1 - f_{2'}^0). \quad (2.78)$$

On the second line we omit the spin indices; 1 always corresponds to spin up and 2 to spin down. Additionally, we used the assumption of a uniform system to perform

the spatial integral and replace the particle numbers by the densities n_α.

To determine ψ_α we assume the distribution functions differ from equilibrium by a shift in velocity,

$$f_\alpha(\mathbf{v}) = f^0_\alpha(\mathbf{v} - \mathbf{v}_{\mathrm{d},\alpha}) \tag{2.79}$$

$$\approx f^0_\alpha + f^0_\alpha(1 - f^0_\alpha)\beta m \mathbf{v}\cdot\mathbf{v}_{\mathrm{d},\alpha} \tag{2.80}$$

where $\mathbf{v}_{\mathrm{d},\alpha} = \langle \mathbf{v}_\alpha \rangle$ is the average velocity of spin α. Therefore, according to (2.77), $\psi_\alpha(\mathbf{v}) = \beta m \mathbf{v}\cdot\mathbf{v}_{\mathrm{d},\alpha}$. The factor in the linearized collision integral (2.78) involving the ψ_α becomes

$$\psi_{1'} + \psi_{2'} - \psi_1 - \psi_2 = \frac{\beta m}{2}\,\mathbf{u}_\mathrm{d}\cdot(\mathbf{u}' - \mathbf{u}), \tag{2.81}$$

where we have introduced the relative velocities

$$\mathbf{u} = \mathbf{v}_1 - \mathbf{v}_2 \tag{2.82a}$$

$$\mathbf{u}' = \mathbf{v}'_1 - \mathbf{v}'_2 \tag{2.82b}$$

$$\mathbf{u}_d = \mathbf{v}_{\mathrm{d}\uparrow} - \mathbf{v}_{\mathrm{d}\downarrow} \tag{2.82c}$$

and used conservation of momentum $\mathbf{v}_1 + \mathbf{v}_2 = \mathbf{v}'_1 + \mathbf{v}'_2 \equiv 2\mathbf{V}$. The terms in the collision integral proportional to $u_{\mathrm{d},x}$ and $u_{\mathrm{d},y}$ vanish by symmetry. The spin drag coefficient is then given by

$$\Gamma_{\mathrm{SD}} = \beta m \frac{n_\uparrow + n_\downarrow}{4 n_\uparrow n_\downarrow}\left(\frac{m}{h}\right)^6 \int \mathrm{d}^3V \mathrm{d}^3u \mathrm{d}\Omega \frac{d\sigma}{d\Omega} u u_z (u'_z - u_z) \times f^0_1 f^0_2 (1 - f^0_{1'})(1 - f^0_{2'}) \tag{2.83}$$

In the classical limit, $f^0_\alpha = e^{-\beta(\epsilon-\mu_\alpha)} \ll 1$ and we omit the $1 - f$ factors. In terms of the relative velocity, the s-wave scattering cross section (2.13) is,

$$\frac{d\sigma}{d\Omega} = \frac{a^2}{1 + (\frac{mu}{2\hbar})^2 a^2}. \tag{2.84}$$

Carrying out the integrals, the spin drag coefficient is

$$\Gamma_{\rm SD} = \frac{8}{3}(n_1 + n_2)\sigma\left(T/T_a\right)\sqrt{\frac{k_B T}{\pi m}}, \tag{2.85}$$

where the mean scattering cross section is

$$\sigma\left(T/T_a\right) = 4\pi a^2 \int \mathrm{d}u \frac{1}{1+\frac{T}{T_a}u^2} u^5 e^{-u^5}, \tag{2.86}$$

and $T_a = \hbar^2/(k_B m a^2)$. The limiting values of the mean scattering cross section are

$$\sigma(T \ll T_a) = 4\pi a^2 \tag{2.87}$$

$$\sigma(T \gg T_a) = \frac{2\pi\hbar^2}{m k_B T} = \lambda^2, \tag{2.88}$$

where λ is the thermal de-Broglie wavelength. For unitary interactions, $T_a = 0$ and we have

$$\frac{\hbar\Gamma_{\rm SD}}{\bar{E}_F} = \frac{32\sqrt{2}}{9\pi^{3/2}}\sqrt{\frac{\bar{E}_F}{k_B T}} \approx 0.90\sqrt{\frac{\bar{E}_F}{k_B T}}, \tag{2.89}$$

with $\bar{E}_F = \frac{\hbar^2}{2m}(3\pi^2(n_1+n_2))^{2/3}$.

The Einstein relation (2.66) together with the classical result for the spin susceptibility $\chi_s = \beta\bar{n}$ gives the classical spin diffusion coefficient at unitarity,

$$D_s = \frac{9\pi^{3/2}}{32\sqrt{2}}\frac{\hbar}{m}\left(\frac{T}{T_F}\right)^{3/2} \approx 1.1\frac{\hbar}{m}\left(\frac{T}{T_F}\right)^{3/2} \tag{2.90}$$

2.5.6 Kubo Formula for Spin Conduction

The Kubo formula provides a general framework for calculating linear response coefficients. We write the Hamiltonian as $H(t) = H_0 + Af(t)$, where $Af(t)$ is the perturbation due to a weak external field. The change in a quantity B, to leading order in the perturbation, is

$$\langle \delta B(t) \rangle = \int_{-\infty}^{\infty} \chi_{BA}(t-t')f(t')\mathrm{d}t', \tag{2.91}$$

with Fourier transform

$$\langle \delta B(\omega) \rangle = \chi_{BA}(\omega) f(\omega), \tag{2.92}$$

where $f(\omega)$ is the Fourier transform of $f(t)$. The response function $\chi_{BA}(t)$ and its Fourier transform are [86, 161]

$$\chi_{BA}(t) = i\,\theta(t)\,\langle [A(-t), B] \rangle_0 \tag{2.93}$$

and

$$\chi_{BA}(\omega) = i \int_0^\infty \mathrm{d}t\, e^{i\omega t}\,\langle [A(-t), B] \rangle_0\,, \tag{2.94}$$

where $A(t) = e^{iH_0 t} A e^{-iH_0 t}$ is the interaction picture representation of A, and the expectation value is taken over the equilibrium state. Using the relationship between the Fourier transform of a function and its derivative, $\chi_{BA}(\omega)$ can be written [86],

$$\chi_{BA}(\omega) = \frac{1}{\omega} \int_0^\infty \mathrm{d}t\, e^{i\omega t} \left\langle [\dot{A}(-t), B] \right\rangle_0\,, \tag{2.95}$$

where $\dot{A} = i[H_0, A]$.

To obtain an expression for the spin conductivity, we consider a uniform spin-dependent force applied to a system of spin up and spin down atoms. The perturbation to the Hamiltonian is then

$$H' = \frac{1}{2} \int \mathrm{d}^3\mathbf{r} \left\{ \psi_\uparrow^\dagger [-F_s(t) z] \psi_\uparrow + \psi_\downarrow^\dagger [F_s(t) z] \psi_\downarrow \right\} \tag{2.96}$$

$$= -\frac{1}{2} \int \mathrm{d}^3\mathbf{r}\, z\, \hat{n}_s\, F_s(t), \tag{2.97}$$

where $\hat{n}_s$ is the spin density operator. The force has been chosen to lie along the z direction, and the factor of $\frac{1}{2}$ sets $F_\uparrow - F_\downarrow = F_s$. The response function of the spin current is the dynamic spin conductivity,

$$\langle J_{s,z}(\omega) \rangle = \sigma_s(\omega) F_s(\omega). \tag{2.98}$$

Before using the Kubo formula (2.95) to find the spin conductivity, we note that the

continuity equation for the spin density implies

$$-\int \mathrm{d}^3\mathbf{r} z \frac{\partial \hat{n}_s}{\partial t} = \int \mathrm{d}^3\mathbf{r} z \nabla \cdot \mathbf{J}_s = -\int \mathrm{d}^3\mathbf{r}\, J_{s,z} \tag{2.99}$$

Therefore the dynamic spin conductivity is

$$\sigma_s(\omega) = \frac{1}{2\omega}\int_0^\infty \mathrm{d}t\, e^{i\omega t} \int \mathrm{d}^3\mathbf{r}\ \langle [J_{s,z}(0), J_{s,z}(-t)]\rangle_0 \tag{2.100}$$

$$= \frac{1}{2\omega}\int_0^\infty \mathrm{d}t\, e^{i\omega t} \int \mathrm{d}^3\mathbf{r}\ \langle [J_{s,z}(t), J_{s,z}(0)]\rangle_0 \,, \tag{2.101}$$

where the second line uses the fact that the expectation value is taken over the equilibrium state. The Kubo formula (2.101) allows the spin conductivity to be calculated from a microscopic model of the gas at equilibrium. For example, Ref. [50] uses this formula to calculate the spin transport coefficients for the unitary Fermi gas in Luttinger-Ward theory.[5]

[5]The definition of σ_s in Ref. [50] differs from the definition used here by a factor of 2.

Chapter 3

Experimental Techniques for Studying Quantum Gases

3.1 The BEC1 Apparatus

The experiments reported in this thesis were carried out using a dual-species machine that produces quantum-degenerate gases of ^{23}Na and ^{6}Li. This section provides basic information about the experimental setup. Additional details can be found in several publications [67, 66] and theses [149, 136, 150, 171, 75].

The experimental setup consists of a vacuum chamber and supporting optics and electronics. Figure 3-1 shows a schematic of the vacuum system. An atomic beam is generated from hot vapor given off by molten sodium and lithium within the oven chamber. The atomic beam is slowed by laser light as it passes through a Zeeman slower into the main chamber, which is held under ultra-high vacuum (UHV). Atoms are collected in a magneto-optic trap (MOT) in the main chamber for a few seconds and transferred to a Ioffe-Pritchard magnetic trap for evaporative cooling.

Transferring atoms from the MOT to the magnetic trap proceeds by switching off the laser light and magnetic fields that create the MOT, and optically pumping ^{23}Na and ^{6}Li atoms into stretched hyperfine states. We use the low-field seeking states, $\left|F = \frac{3}{2}, m_F = \frac{3}{2}\right\rangle$ for ^{6}Li and $|F = 2, m_F = 2\rangle$ for ^{23}Na. The hyperfine sublevels of the ^{23}Na and ^{6}Li electronic ground states are shown in Fig. 3-2. A weak guide

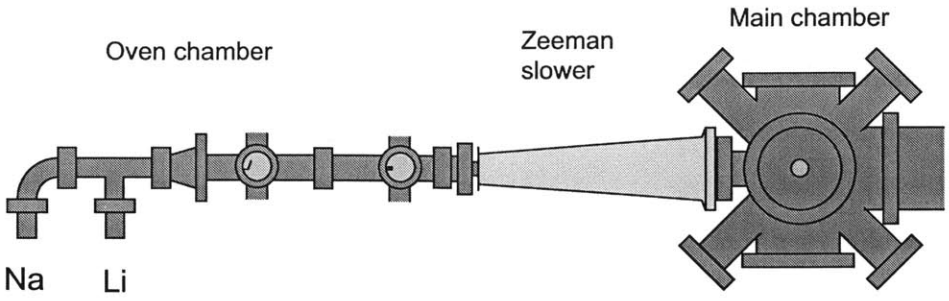

Figure 3-1: Schematic of the vacuum system used for these experiments.

field is applied during optical pumping to define the quantization axis. After optical pumping, the magnetic trap is switched on, producing a magnetic field with a local minimum at the position of the atomic cloud. In the vicinity of the atoms the magnetic field has the form

$$\mathbf{B}(r,z) = \left(B_z + \frac{1}{2}B_z''z^2\right)\hat{\mathbf{z}} + B_r'\mathbf{r}. \tag{3.1}$$

The bias field B_z is set to 80 G at first to weaken the radial confinement, and subsequently lowered to about 4 G. The gas is cooled in the magnetic trap for about 20 s by forced evaporation of the sodium atoms using a microwave field to transfer the most energetic atoms to the $|F = 1, m_F = 1\rangle$ state. Sodium atoms in the $|1,1\rangle$ state are high-field seeking, and leave the trap. Lithium is cooled sympathetically by thermalization with sodium. Without lithium, this method produces a ^{23}Na BEC of about 10^7 atoms. With lithium, full evaporation of the sodium atoms produces a quantum-degenerate gas of a few times 10^7 ^{6}Li atoms.

The spin-polarized ^{6}Li cloud is essentially non-interacting, because fermions in identical spin states do not scatter at low temperatures, as discussed in Section 2.2.1. To allow interactions we must at least create a mixture of two or more hyperfine states. By using combinations of the three lowest hyperfine states, and applying magnetic fields in the 500 to 1000 G range, we access the Feshbach resonances described in Section 2.2.3, allowing us to tune the scattering length.

The lowest three hyperfine states of ^{6}Li are high-field seeking, and cannot be trapped using purely magnetic forces. Additionally, working at high fields would mean increasing B_z in Eqn. (3.1), which weakens the radial confinement. Therefore,

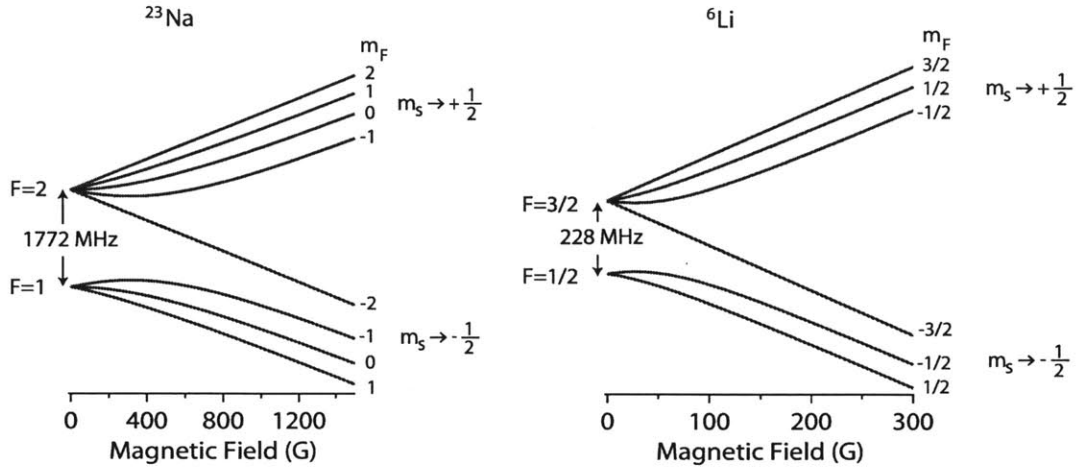

Figure 3-2: Energy sublevels of the electronic ground states of ^{23}Na and ^{6}Li versus magnetic field. Low-field seeking states have a positive slope and are magnetically trappable. At high fields, the electron and nuclear spin decouple and the energy eigenstates approach m_S eigenstates. The $|F = 2, m_F = 2\rangle$ state of ^{23}Na and the $|F = \frac{3}{2}, m_F = \frac{3}{2}\rangle$ state of ^{6}Li are used during evaporative cooling in the magnetic trap. For experiments at high fields, we transfer ^{6}Li into one or more of the three lowest hyperfine states.

after sympathetic cooling, an optical dipole trap (ODT) is ramped up and the radial gradient B_r' is ramped to zero. The optical dipole trap is generated by an infrared laser at 1064 nm, focused to a waist of $w = 120\,\mu$m. The ODT provides confinement along the radial direction, with a potential energy [64]

$$U(r) = \alpha_{\mathrm{Li}} I_0\, e^{-2r^2/w^2}, \tag{3.2}$$

where I_0 is the peak intensity of the laser, and $\alpha_{\mathrm{Li}} = 1.27 \times 10^{-3}\,\mathrm{s}^2/\mathrm{kg}$ expresses the polarizability of ^{6}Li by light with a wavelength of 1064nm. The magnetic field curvature continues to provide confinement in the axial direction. The atoms are now held in a hybrid trap formed by magnetic and optical forces.

After loading lithium atoms into the hybrid trap, we transfer them to the lowest hyperfine state $|1\rangle \equiv |F = \frac{1}{2}, m_F = \frac{1}{2}\rangle$ and raise the magnetic field. The state transfer is performed by applying microwave excitation and sweeping the magnetic field by a few hundred mG to drive a Landau-Zener transition. State $|1\rangle$ is high-field seeking, so we quickly reverse B_z to generate a local maximum in the strength of the magnetic

field and keep the atoms trapped. The bias field is then ramped up to a target value in the range of several hundred gauss. A spin mixture of any combination of the three lowest hyperfine states $|1\rangle$, $|2\rangle$, and $|3\rangle$ is then created using radio-frequency excitation. From here the machine is ready to perform a wide range of experiments on interacting Fermi gases.

3.2 Imaging Atomic Clouds

We obtain information about the atomic gas by sending laser light through the gas and recording a two-dimensional image of the transmitted light intensity on a CCD camera. An imaging system composed of one or more lens pairs focuses the image of the gas onto the plane of the CCD detector. The recorded image provides information about the atomic density distribution.[1] We use two types of imaging: absorption and phase-contrast. Absorption imaging uses light resonant with an electronic transition in the atoms. Phase-contrast imaging uses light detuned by several linewidths.

3.2.1 Absorption Imaging

For absorption imaging, the intensity of light transmitted through a dilute atomic cloud is

$$I_f = I_i e^{-\sigma_0 \tilde{n}}, \tag{3.3}$$

where I_i is the incident intensity and σ_0 is the resonant absorption cross-section. The column density $\tilde{n}$ is the integral of the density distribution n along the line of sight of the camera,

$$\tilde{n} = \int n \mathrm{d}s. \tag{3.4}$$

[1] Although we use a focused imaging system, Ref. [129] shows that a slightly de-focused imaging system can provide information about the spatial fluctuations of the gas density.

We measure the ratio I_f/I_i by taking three separate images, one with atoms, one without atoms, and one dark field image without laser light, giving

$$\frac{I_f}{I_i} = \frac{I_{\mathrm{WA}} - I_{\mathrm{DF}}}{I_{\mathrm{WOA}} - I_{\mathrm{DF}}}, \tag{3.5}$$

where I_{WA}, I_{WOA}, and I_{DF} are signals recorded with atoms, without atoms, and without imaging light, respectively. Resonant imaging light heats the atomic cloud, so we can only take one set of images. Using a camera that can record multiple exposures in rapid succession allows us to image multiple spin states before heating significantly alters the density distribution.

We choose the duration and intensity of the imaging pulses to obtain a high signal-to-noise ratio without disturbing the cloud or incurring non-linearities. Detecting as many photons as possible minimizes the effects of photon shot noise and electronic readout noise. On the other hand, using too high of a light intensity can saturate the atomic transition. Saturation leads to a non-linear response that is complicated to calibrate, although it can be done [167]. Saturation causes an intensity-dependent reduction in the resonant absorption cross-section,

$$\sigma_0(I) = \frac{\sigma_0(0)}{1 + I/I_{\mathrm{SAT}}}, \tag{3.6}$$

where I_{SAT} is the saturation intensity. Through simulations, we find that we can reduce the non-linearity to negligible levels by using $I/I_{\mathrm{SAT}} < 0.1$, with the precise value depending on the error tolerance of the measurement. With limited intensity, using longer pulses allows the capture of more photons, and reduced noise. However, due to the small mass of ^{6}Li atoms, the Doppler shift resulting from scattering multiple photons can cause significant detuning from the atomic transition. The Doppler shift due to the initial velocity distribution of an ultracold gas is negligible. To estimate the Doppler shift we consider an atom initially at rest. During the imaging pulse, the velocity of the atom undergoes a random walk due to photon scattering, resulting in

an average final detuning of

$$\Delta\omega = vk = \frac{\hbar k^2}{m}\sqrt{\frac{N}{3}}, \tag{3.7}$$

where $k = 2\pi/\lambda$ is the wavevector of the imaging light at $\lambda = 671$ nm. The number of scattered photons is

$$N = \frac{1}{2}\frac{I}{I_{\mathrm{SAT}}}\Gamma t_p, \tag{3.8}$$

in the limit of low saturation and short pulse time t_p, with Γ the linewidth. Sufficiently small relative detunings $\Delta\omega/\Gamma$ are obtained using pulse times of 10 μs or less. Pulse times less than 10 μs also keep the distortion of the cloud due to heating below observable levels.

3.2.2 Phase-Contrast Imaging

As an alternative to absorption imaging, phase-contrast imaging uses the phase shift of off-resonant light to produce an image. Because it uses off-resonant light, phase-contrast imaging can potentially produce non-destructive images of the atomic cloud. For phase-contrast imaging, we add a phase plate in the focal plane of the first imaging lens after the vacuum chamber. A 200 μm diameter phase spot at the center of the phase plate adds an additional phase shift of about $\pi/2$ to the light passing through it. Light scattered by the atoms passes through the entire area of the phase plate, while light that does not interact with the atoms focuses on the phase spot and receives an additional phase shift. The two components of the light field interfere on the camera producing an image of the cloud. The intensity detected on the camera is given by [77]

$$I_f = I_i\left[T + 2 - 2\sqrt{2T}\cos\left(\phi + \frac{\pi}{4}\right)\right], \tag{3.9}$$

where T is the transmission coefficient, approximately 1 for far-detuned light, and ϕ is the phase shift due to interaction with the atomic cloud. For imaging multiple spin

states, the total phase shift is

$$\phi = -\frac{\sigma_0}{2}\sum_i \frac{\tilde{n}_i \delta_i}{1+\delta_i^2}, \tag{3.10}$$

where $\tilde{n}_i$ is the column density and $\delta_i = 2\Delta_i/\Gamma$ is the relative detuning of the i-th spin state, with Δ_i the absolute detuning in angular frequency units. Imaging two spin states with light detuned halfway between the two resonances gives a phase shift proportional to the difference in column density between the two spin states, as in Ref. [141]. We used this method to directly measure the density difference of two spin states when studying spin transport in polarized superfluids (Ref. [146] and Section 4.4.2 of this thesis) and for the measurement of spin transport as a function of scattering length (Ref. [145], Supplementary Material, and Figure 4-6 in this thesis).

3.2.3 Obtaining the 3D Density

Images recorded on the CCD camera allow us to directly measure the column density $\tilde{n}$. In order to obtain the three-dimensional density n we must invert the relation (3.4). Due to the cylindrical symmetry of the atomic clouds, integration along a direction perpendicular to the symmetry axis z preserves information about the full density distribution. For imaging along the y axis, the 3D density $n(r,z)$ is related to the column density $\tilde{n}(x,z)$ by

$$\tilde{n}(x) = \int_{-\infty}^{\infty} n\left(\sqrt{x^2+y^2}\right) \mathrm{d}y = 2\int_{|x|}^{\infty} \frac{n(r) r \mathrm{d}r}{\sqrt{r^2-x^2}} \tag{3.11}$$

$$n(r) = -\frac{1}{\pi}\int_r^{\infty} \frac{\partial \tilde{n}}{\partial x}\frac{\mathrm{d}x}{\sqrt{x^2-r^2}}, \tag{3.12}$$

omitting the z dependencies of n and $\tilde{n}$ for clarity. We implement the inverse Abel transform (3.12) numerically to find the density.

3.3 Measurement of the Trapping Potential

We calibrate the trapping potential due to the optical dipole trap using the measured atomic density distribution and the local density approximation. The total trapping potential in the hybrid trap follows

$$U(r,z) = \frac{1}{2}m\omega_z^2\left(z^2 - \frac{1}{2}r^2\right) + U_{\mathrm{ODT}}(r) \tag{3.13}$$

The first term in (3.13) is due to magnetic forces, while the second term is due to the optical dipole trap.

We determine the trapping potential as follows. The axial trapping frequency ω_z is first obtained by measuring the oscillation frequency of the center of mass of an atomic cloud along the z direction. We then image the atomic cloud at equilibrium in the potential (3.13). We repeat the measurement multiple times. For each measurement i, we obtain the density n_i using the inverse Abel transform (3.12). The density n_i follows the local density approximation (LDA) and therefore depends only on the local potential,

$$n_i(r,z) = n_i\left(U(r,z)\right). \tag{3.14}$$

The average also follows an LDA-like relation,

$$n_{\mathrm{avg}}(r,z) = \frac{1}{N_{\mathrm{imgs}}}\sum_i n_i(r,z) = n_{\mathrm{avg}}\left(U(r,z)\right). \tag{3.15}$$

We proceed to invert Eqn. (3.15). Using multiple measurements of the density reduces the noise in this processes.

The known trapping potential $U(0,z)$ at $r = 0$ allows us to determine the function $n_{\mathrm{avg}}(U)$ using

$$n_{\mathrm{avg}}\left(U(0,z)\right) = n_{\mathrm{avg}}(0,z). \tag{3.16}$$

Numerically inverting $n_{\mathrm{avg}}(U)$ gives $U\left(n_{\mathrm{avg}}\right)$. Figure 3-3.a shows an example of $U(n_{\mathrm{avg}})$ determined in this way. We obtain the full trapping potential by evaluating

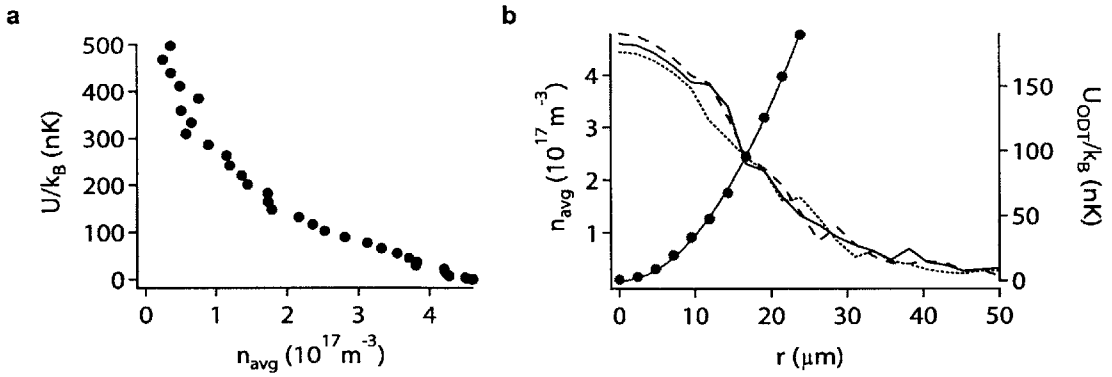

Figure 3-3: Measurement of the trapping potential using the density distribution. **a**, The known axial dependence of the trapping potential allows us to determine the potential U as a function of the density n_{avg} averaged over several images. **b**, The dependence of the density on the radial coordinate r (black curves), together with the function $U(n_{\mathrm{avg}})$, determine the potential energy $U_{\mathrm{ODT}}(r)$ due to the ODT (red points). The solid, dashed, and dotted black curves show the densities versus r for the three rows of pixels nearest to the axial center. The red curve is a fit to $U_{\mathrm{ODT}}(r)$ using Eqn. (3.18)

$U(n_{\mathrm{avg}})$ over the density distribution,

$$U(r,z) = U\left[n_{\mathrm{avg}}(r,z)\right]. \tag{3.17}$$

Subtracting the magnetic potential gives an independent measurement of $U_{\mathrm{ODT}}(r)$ for each value of z. These values are averaged and fit to

$$U_{\mathrm{ODT}}(r) = U_0\left(e^{-2r^2/w^2} - 1\right). \tag{3.18}$$

Figure 3-3.b shows examples of the radial dependence of n_{avg} together with the average $U_{\mathrm{ODT}}(r)$.

Chapter 4

Spin Transport in Strongly Interacting Fermi Gases

Transport experiments serve to characterize condensed matter systems, providing insight into their fundamental properties, and yielding practical information for engineering applications. In ultracold Fermi gases, where we know the microscopic Hamiltonian, but not its exact solution, transport measurements allow us to test many-body theories. Experiments on collective excitations and free expansion, for example, have allowed measurements of the shear viscosity of ultracold Fermi gases [22] and comparisons with theory [18]. In systems with a spin degree of freedom, spin transport provides another set of observables with which to test theories of the many-body state. Additionally, an understanding of spin transport is crucial to the emerging field of spintronics, which aims to use spin currents to create new electronic devices [53, 163, 157, 43]. With these motivations, we set out to measure the spin transport properties of strongly-interacting Fermi gases in the universal regime of s-wave contact interactions. In this chapter, we look at measurements of the spin transport coefficients in a strongly-interacting Fermi gas across the Feshbach resonance and over a wide range of temperatures at unitarity [145] and in highly polarized Fermi gases [146].

4.1 Experimental Realization of Spin Transport

Previous experimental studies of atomic Fermi gases have observed spin transport in the presence of weak interactions [36, 44]. Here, we generate spin currents in the strongly-interacting regime, and from the dynamics we obtain measurements of the spin transport parameters.

Spin transport is generated by exciting the spin dipole mode of the system. The spin dipole mode consists of a separation of the centers of mass of the spin states. The displacement $d = \langle z_\uparrow - z_\downarrow \rangle$ of the centers of mass characterizes the amplitude of a spin dipole excitation. We use a magnetic field gradient to create the spin dipole excitation. When the magnetic moments of spin up and spin down atoms are different, a magnetic field gradient provides a spin dependent force. We use this spin dependent force to separate the spin components, in a variation of Stern-Gerlach separation. Alternative methods are also possible. A radio-frequency pulse on a spin-polarized cloud in the presence of a magnetic field gradient would create a spin wave [44]; a Raman laser pulse on a spin-polarized cloud would create a spin current [130].

The magnetic field gradient is produced by perturbing the trapping potential. The trapping potential varies quadratically along the z axis, with the atoms resting at the potential minimum. The z dependence of the potential results from a current running through coils on either side of the vacuum chamber. Temporarily applying additional current to one set of coils by means of a separate, computer-controlled power supply, shifts the position of the potential minimum and creates a magnetic field gradient at the position of the atoms.

For the magnetic field gradient to separate the spin states, the states must have different magnetic moments. In the vicinity of the Feshbach resonances, however, the magnetic moments of the three lowest hyperfine states of ^{6}Li are almost exactly equal (the Paschen-Bach regime), as they approach eigenstates of electron spin $m_s = -\frac{1}{2}$. To deal with this, we can either transfer one of the spin states to one of the three upper hyperfine levels of the electronic ground state, which have the opposite magnetic moment from the three lower levels, or we can reduce the magnetic field to a value

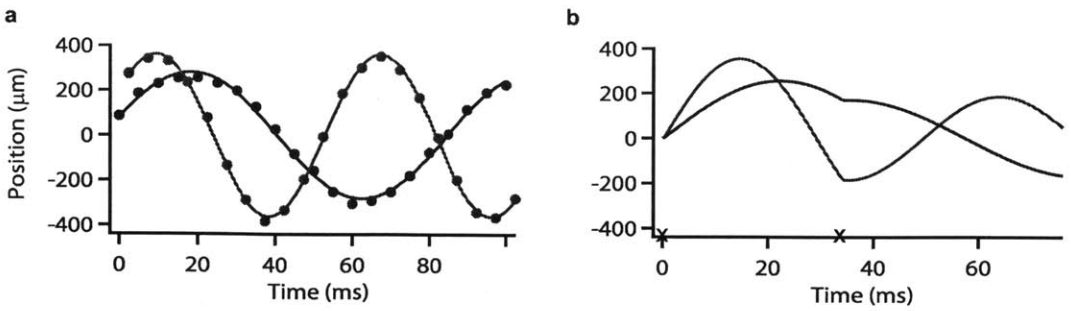

Figure 4-1: A sequence of two magnetic field gradient pulses at 50 G separates the spin components. **a**, After the first gradient pulse, the clouds oscillate at difference frequencies due to their different magnetic moments (data and fits). **b**, A second pulse 34 ms after the first removes most of the velocity of both clouds (simulation; x's mark the times of the pulses).

well bellow the Paschen-Bach regime. We choose the latter, as it promises greater stability. To select the field at which to apply the gradient, we must satisfy two criteria: the magnetic moments must differ significantly, and the scattering length must be small enough to avoid spin drag at this stage.

We find that 50 G meets the above criteria for spin separation. At 50 G, the ratio of the magnetic moments of the lowest two hyperfine states is about 2.5. Consequently, the clouds can be separated using a magnetic field gradient. The scattering length between the two lowest hyperfine states at 50 G is $a_{12} = -27.9\,a_0$, where a_0 is the Bohr radius [9, 169]. For typical densities of about $n = 1 \times 10^{18}\,\mathrm{m}^{-3}$ at this stage, the corresponding mean free path is $l = 1/n\sigma \approx 40$ mm. Since the mean free path greatly exceeds the cloud length of about 0.5 mm, the spin up and spin down clouds easily pass through each other.

We create the spin dipole excitation by applying a pair of magnetic field gradient pulses in the z direction at 50 G. Following the first pulse, the clouds begin to oscillate with differing frequencies and amplitudes (Fig. 4-1.a). After 34 ms of free evolution, the center of mass of the state $|1\rangle$ cloud reaches a position along the z axis that is about opposite to the position of the state $|2\rangle$ center of mass along the z axis. At that moment, we apply a second magnetic field gradient pulse to remove the total center of mass velocity of the clouds (Fig. 4-1.b). The velocities of the two clouds

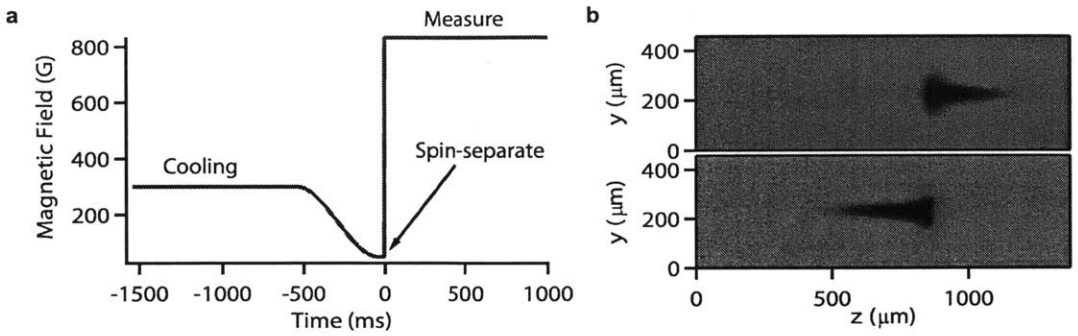

Figure 4-2: **a**, Experimental sequence for spin transport experiments. The spin mixture is created at 300 G. After a 500 ms ramp to 50 G, the spin states are separated using magnetic field gradient pulses. The magnetic field is then quickly ramped to a final value near the Feshbach resonance. **b**, Example of absorption images of clouds in the two lowest hyperfine states at 834G, 7 ms after the final field ramp.

after 34 ms are in the same direction, with magnitudes closely matched to the ratio of the magnetic moments, and the second pulse removes most of the relative velocity as well. The gradient pulse sequence therefore results in the two spin states being displaced symmetrically about $z = 0$, with approximately zero initial velocity.

Before separating the spin states, we must create a 50/50 mixture of the two, as we start with a pure $|1\rangle$ cloud (see Section 3.1). The mixture can, in principle, be performed at 50 G. However, we would like to perform some evaporative cooling before exciting the spin dipole mode, since there is limited time for cooling afterward. Cooling at 50 G is not practical, the collision time being $1/(n\sigma v) \sim 1\,\mathrm{s}$. On the other hand, we cannot cool near the Feshbach resonance, as sweeping the magnetic field down through the BEC regime on the way to 50 G would associate deeply-bound molecules. We therefore prepare the system at 300 G, well away from the Feshbach resonance, where the scattering length is nevertheless sufficiently large ($-288a_0$ [9, 169]) for efficient cooling.

Figure 4-2.a shows the complete sequence of magnetic field ramps. After cooling at 300 G and creating a spin excitation at 50 G, we ramp the magnetic field to a final value near the Feshbach resonance in about 2 ms. At the final field, the trapping potential forces the two clouds to recombine. We then image the clouds after a variable

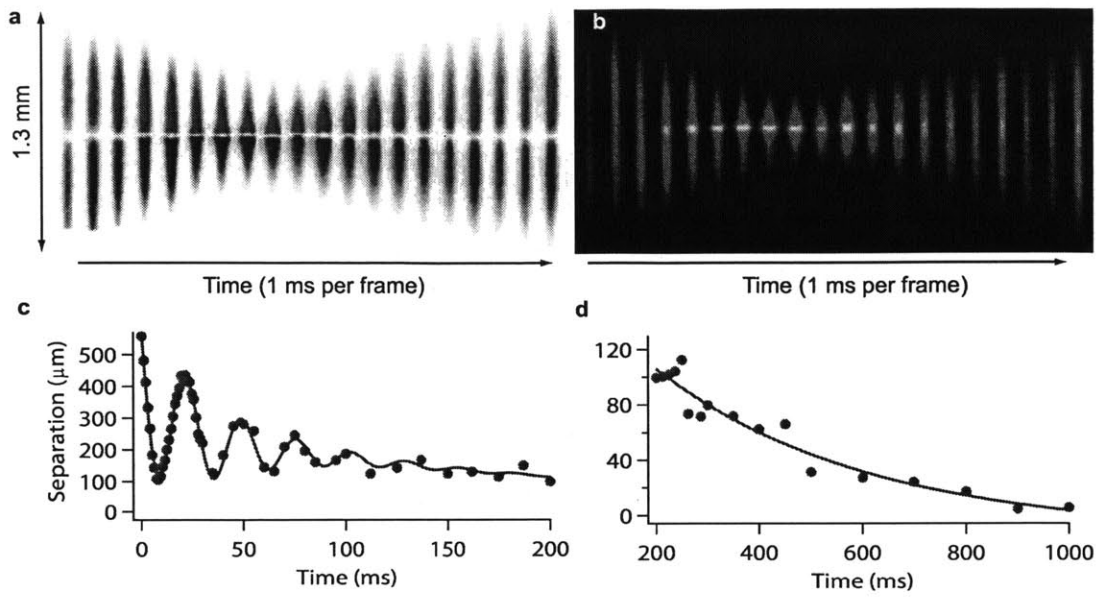

Figure 4-3: Collision of two spin-polarized clouds of fermions in different spin states. (**a**) shows the difference in column densities of the two clouds (red: spin up, blue: spin down) and (**b**) the total column density. Images are shown in 1 ms intervals during the first 20 ms after the magnetic field is set to the Feshbach resonance at 834 G. The collision leads to the formation of a high-density interface between the two spin states. **c**. The separation between the centers of mass of the two spin states initially oscillates at a frequency of 1.63(2) ω_z, where $\omega_z = 2\pi \times 22.8$ Hz is the trap frequency in the axial direction. **d** At later times, as the clouds slowly diffuse into each other, the center of mass separation decays exponentially. Even after half a second, there is still substantial spin separation. The diffusion time indicates a diffusivity on the order of $\hbar/m$.

wait time. Figure 4-2.b shows an absorption image of the two spin components after 7 ms of wait time at the Feshbach resonance. Instead of passing through each other as one might expect of ultra-dilute gases, the clouds collide forcefully, and only slowly diffuse into each other. In the next sections we study this collision and the slow process of diffusion. We will see how the macroscopic behavior of the system gives insight into the fundamental, quantum-limited spin transport properties of the system.

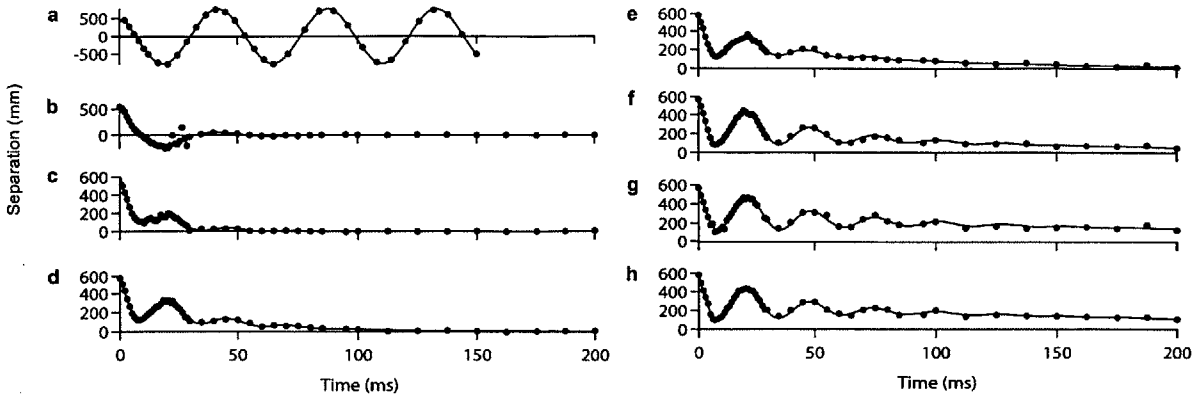

Figure 4-4: Collision between spin up and spin down clouds with varying interaction strength. After separating the spin components, the magnetic field is ramped to a variable value near the Feshbach resonance to reach different interaction strengths. The interaction parameter $k_F a$, with $k_F = (6\pi^2 n)^{1/3}$ and n the central density per spin component, was determined by averaging the values of k_F obtained from images taken after 200 ms of evolution time (not shown). The values of $k_F a$ are (**a**) 0, (**b**) 0.08, (**c**) 0.13, (**d**) 0.19, (**e**) 0.26, (**f**) 1.2, (**g**) ∞, and (**h**) -1.5

4.2 Fermi Gas Collisions

Having separated the two spin states (which we will refer to as spin up and spin down), we can observe the collision of the two clouds for different interaction strengths. Figure 4-3 shows the collision of spin up and spin down clouds at the Feshbach resonance. As the centers of mass approach each other, density builds up at the center of the trap, the clouds acting as essentially impenetrable objects. After a few milliseconds, pressure gradients overcome the trapping forces and the center of mass velocities reverse. After the centers of mass move apart, the trap then forces the centers of mass back together, and the process repeats. The clouds bounce off each other several times, gradually dissipating energy. Going away from resonance, the bouncing damps more quickly (Fig.4-4). For weak interactions, the clouds pass through each other, undergoing a damped oscillation in the trap (Fig. 4-4.b).

The dynamics of the bouncing clouds consists of two modes. The oscillatory part of the motion constitutes an axial compression (breathing) mode of the total density [153]. In this mode the cloud shrinks axially while growing radially, and vice

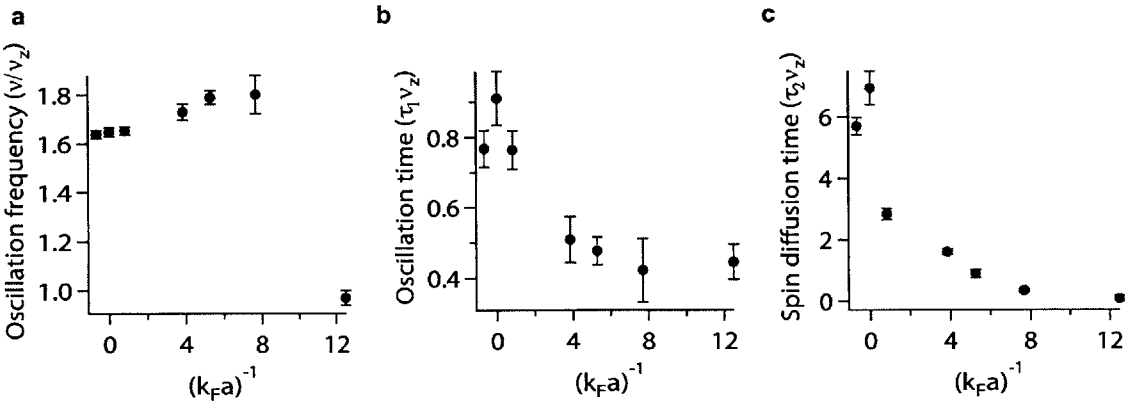

Figure 4-5: Parameters fitted to the Fermi gas collision data in Fig. 4-3, normalized by the axial trap frequency ν_z. The oscillation frequency (**a**) is intermediate between the hydrodynamic and collisionless limits for the axial breathing mode of a trapped gas, but switches to the dipole frequency ν_z for sufficiently weak interactions. The damping times (**b**) and (**c**) attain their maximum values at the Feshbach resonance, with the diffusive damping time (**c**) significantly exceeding the damping time of the breathing mode (**b**).

versa. The viscosity in the region where the two spin states overlap causes damping of the breathing mode. The second mode is the spin dipole mode. The spin dipole mode consists of relative motion of the spin up and spin down centers of mass. The breathing mode couples to the spin dipole mode because the spin states are separated, generating a non-dissipative spin current (J_s^R in section 2.5.2). Additionally, the spin up and spin down clouds diffuse into one another, following a dissipative spin current that increases the overlap of the two clouds.

We fit the measured center of mass separation $d = \langle z_\uparrow - z_\downarrow \rangle$ to

$$d(t) = A_1 \sin(2\pi\nu(t - t_0))e^{-t/\tau_1} + A_2 e^{-t/\tau_2} + A_3 e^{-t/\tau_3}. \tag{4.1}$$

The first term describes the contribution of the breathing mode, while the second term describes the dissipative part of the spin transport. The third term has a short time scale ($\tau_3 = 5-10$ ms) and accounts for rapid dissipation during the first collision, likely due to atoms spilled out of the trap.

Figure 4-5 shows the fitted oscillation frequency ν and the damping times τ_1 and

τ_2 for the data in Fig. 4-3.b-h, normalized by the trap frequency. Near the Feshbach resonance, the oscillation frequency is intermediate between the hydrodynamic value[1] at unitarity [153, 10] of $\sqrt{12/5}\nu_z = 1.55\nu_z$ and the collisionless value $2\nu_z$. At the unitarity point, we find $\nu = 1.63(2)\nu_z$. Going away from unitarity, the oscillation frequency increases, approaching the collisionless limit. However, as the scattering cross section is reduced further (Fig. 4-3.b), the frequency switches to about ν_z as the character of the oscillation changes from an axial breathing mode to an underdamped spin dipole mode.

Near the Feshbach resonance, the spin diffusion time τ_2 exceeds the lifetime τ_1 of the breathing mode by almost an order of magnitude (Fig. 4-5.b,c). Both time scales reach their maxmimum values at unitarity. For the breathing mode lifetime this indicates a minimum in the viscosity on resonance, in agreement with measurements of the axial breathing mode in unpolarized gases [10]. The maximum in the spin diffusion time at resonance indicates a minimum in the spin diffusivity at resonance, which we will explore next.

4.3 Measuring Spin Transport in a Trapped Fermi Gas

The spin diffusion time τ_2 of the previous section gives a measure of the spin transport parameters of the system. To obtain a more formal measurement of the spin transport properties, and to control the temperature, we now begin the measurement only after the breathing mode has damped out. Working in the absence of the breathing mode allows us to define spin transport coefficients for trapped gases that relate more clearly to the intrinsic spin transport properties of a homogeneous gas.

[1]The hydrodynamic limit depends on the equation of state. For a unitary Fermi gas, at all temperatures, the axial breathing mode frequency is $\sqrt{12/5}\nu_z$ [153, 10, 154]. In the BEC limit it is $\sqrt{5/2}\nu_z$=1.58ν_z [152].

4.3.1 Definition of Spin Transport Coefficients for Trapped Gases

Due to the inhomogeneous density of trapped gases, the transport properties that we measure are related to the values for homogeneous gases by an average over the trap. To this end, we define the equilibrium trap average of a function $G(\mathbf{r})$ as

$$\langle G \rangle_0 = \frac{1}{N_0} \int \mathrm{d}^3 r \, G(\mathbf{r}) \, n_0(\mathbf{r}), \tag{4.2}$$

where $n_0 = n_\uparrow = n_\downarrow$ is the density per spin state at equilibrium and $N_0 = N_\uparrow = N_\downarrow$ is the number of atoms per spin state.

After the breathing mode damps, the separation d of the centers mass of the two clouds decays exponentially. From eqn. (2.50) for the spin drag force, the spin dipole excitation evolves according to

$$\ddot{d} + \Gamma_{\mathrm{SD}} \dot{d} + \omega_z^2 d = 0, \tag{4.3}$$

where Γ_{SD} is the global spin drag coefficient for the trapped gas. Near equilibrium, the global spin drag coefficient is related to the local value $\tilde{\Gamma}_{\mathrm{SD}}$ by

$$\Gamma_{\mathrm{SD}} = \frac{\left\langle \tilde{\Gamma}_{\mathrm{SD}} u_{\mathrm{d},z} \right\rangle_0}{\langle u_{\mathrm{d},z} \rangle_0}, \tag{4.4}$$

where $u_{\mathrm{d},z} = v_{\uparrow,z} - v_{\downarrow,z}$ is the z-component of the difference in the local average velocities of the two spin states. Equation (4.4) is obtained by integrating (2.51) over the cloud to find the total spin drag force.

We measure the spin drag coefficient by fitting the separation of the spin up and spin down centers of mass to

$$d(t) = d_0 e^{-t/\tau}. \tag{4.5}$$

The relaxation time τ is analogous to the parameter τ_2 of Section 4.2. From the

equation of motion (4.3), the spin drag coefficient is

$$\Gamma_{\mathrm{SD}} = \omega_z^2 \tau + 1/\tau. \tag{4.6}$$

In the overdamped regime applicable to most of the experiments, $\omega_z \tau \gg 1$, and (4.6) becomes $\Gamma_{\mathrm{SD}} = \omega_z^2 \tau$. In practice, we use the full expression (4.6) to find Γ_{SD}.

Including an additional piece of information, the spin density gradient, gives a measure of the spin diffusivity accessible in trapped gases. The spin diffusivity $\tilde{D}_s$ is defined by the spin diffusion equation (2.65),

$$\mathbf{J}_s = -\tilde{D}_s \nabla n_s. \tag{4.7}$$

The spin diffusion equation holds locally at the total center of mass (the trap center[2]). At the trap center, the z-component of the spin current density is $J_{s,z}(0) = \bar{n}(0) u_{\mathrm{d},z}(0)$, where $\bar{n}(0) \equiv (n_\uparrow(0) + n_\downarrow(0))/2 = n_\uparrow(0) = n_\downarrow(0)$. To estimate the spin current at the trap center, we replace the unknown local relative velocity $u_{\mathrm{d},z}(0)$ with the trap average, $\langle u_{\mathrm{d},z} \rangle = \dot{d} = -d/\tau$. Using this we construct an estimate of the spin diffusivity,

$$D_s = \frac{\bar{n}(0) d}{g \tau}, \tag{4.8}$$

where $g = \partial_z n_s(0)$ is the spin density gradient at the trap center. The measured spin diffusivity is related to the spin diffusivity of a homogeneous gas $\tilde{D}_s$ by the ratio of the average relative velocity to the local relative velocity at the trap center,

$$D_s = \tilde{D}_s(0) \frac{\langle u_{\mathrm{d},z} \rangle}{u_{\mathrm{d},z}(0)}. \tag{4.9}$$

4.3.2 Spin Transport Measurements

We first look at the dependence of the spin transport coefficients on interaction strength. After preparing the spin excitation at 50 G, the magnetic field is set to

[2]In the lab frame, the total center of mass oscillates about the trap center. Here we work in the center of mass frame, where the effective potential has its center located at the total center of mass, according to the harmonic potential theorem of Section 2.4.1

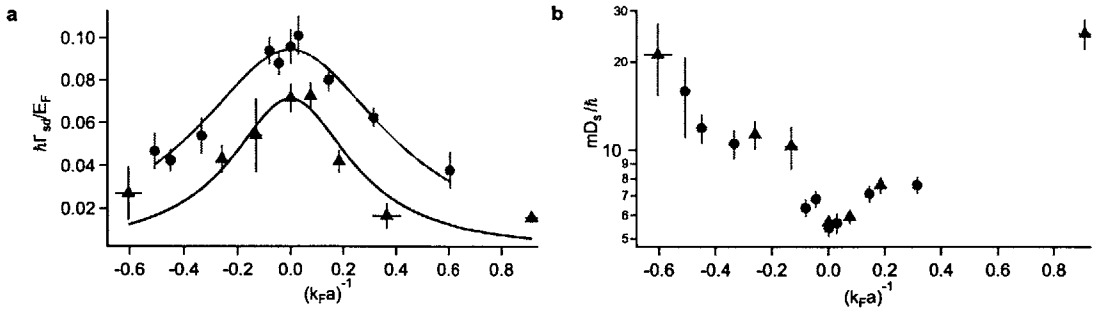

Figure 4-6: Spin transport coefficients as a function of interaction strength. The system was evaporatively cooled to one of two different trap depths. Red circles: higher depth, blue triangles: lower depth. At unitarity, cooling to the higher trap depth gives $T/T_F = 0.32(1)$, while cooling to the lower trap depth gives $T/T_F = 0.16(2)$. The spin drag coefficient (**a**) attains it maximum value on resonance. Solid lines show Lorentzian fits. The spin diffusivity (**b**) is minimum on resonance, and shows no dependence on temperature in this range.

a variable value near the Feshbach resonance, to set the scattering length for the measurement. We use the time during which the breathing mode damps to apply a variable amount of cooling to the clouds. Cooling is applied by reducing the depth of the optical dipole trap. The time available for cooling is limited by the relaxation of the spin dipole excitation to a few hundred milliseconds.

Figure 4-6 shows the spin drag coefficient and spin diffusivity over a range of interaction strengths. The spin drag coefficient is maximal at the Feshbach resonance, while the spin diffusivity is minimal there. This makes sense, as the collision rate is highest at the scattering resonance, leading to maximum spin drag and minimal spin diffusion. Data are taken for cooling to two different trap depths. The blue triangles in Fig. 4-6 show measurements made using the lower trap depth, while the red circles show measurements made using the higher trap depth. On resonance, the lower depth gives a temperature of $0.16(2)\ T_F$, and the higher depth gives $0.32(1)\ T_F$, where T_F is the central Fermi temperature. Comparing the two data sets, the spin drag coefficient is greater at the higher temperature, while the spin diffusivity shows no dependence on temperature in this range.

To further observe the effect of temperature on the spin transport coefficients,

we work at unitarity and vary the temperature. We can reach a wide range of temperatures by varying the duration and depth of the cooling ramps both at unitarity and during the preparation phase at 300 G. Rapid, inefficient, evaporation at 300 G allows us to increase T/T_F to about 1. To go beyond $T/T_F \sim 1$, we heat the cloud further by releasing it from the optical dipole trap and recapturing it, using a relatively deep trap. The final trap depth is chosen so as to maintain a constant temperature, by allowing a small amount of evaporation during the measurement, to counteract extrinsic and intrinsic heating sources. The decrease in atom number during the measurement is typically 10-30%. We reach temperatures ranging from about 0.14 T_F to 11 T_F.

The spin transport coefficients as a function of temperature at unitarity are shown in Fig. 4-7. The spin drag coefficient reaches a maximum value of approximately $0.1\, E_F/\hbar$ for $T \approx T_F$. At higher temperatures, the spin drag coefficient scales as $T^{-1/2}$, in agreement with the expected high-temperature scaling for resonant interactions, $\Gamma_{\mathrm{SD}} \propto n\sigma v \propto \frac{E_F}{\hbar}(T/T_F)^{-1/2}$, discussed in Section 2.5.4. For $T/T_F > 2$, we find $\Gamma_{\mathrm{SD}} = 0.16(1)\frac{E_F}{\hbar}(T/T_F)^{-1/2}$. The crossover from classical $T^{-1/2}$ scaling to the plateau around T_F shows the effects of quantum degeneracy: as the temperature is lowered towards T_F, the characteristic velocity ceases to drop with decreasing temperature, and becomes fixed to the Fermi velocity.

Below T_F, the spin drag coefficient begins to decrease with decreasing temperature. This is expected in Fermi liquids due to Pauli blocking, which predicts that the spin drag coefficient should eventually exhibit T^2 scaling as $T \to 0$ [160, 117, 17, 16]. However, the effective collision rate for density excitations is predicted to increase at low temperatures due to pairing correlations [127]. This contrast suggests that the effect of pairing on spin and density excitations may be qualitatively different. In a simple picture, spin currents require the flow of unpaired atoms, whereas collective density excitations affect paired and unpaired atoms alike.

The temperature dependence of the spin diffusivity is shown in Fig. 4-7.b. At high temperatures, we find $D_s = 5.8(2)\frac{\hbar}{m}(T/T_F)^{3/2}$ for $T/T_F > 2$. This scaling agrees with the expected classical behavior for resonant interactions, $D_s \propto v/n\sigma \propto T^{3/2}$. For

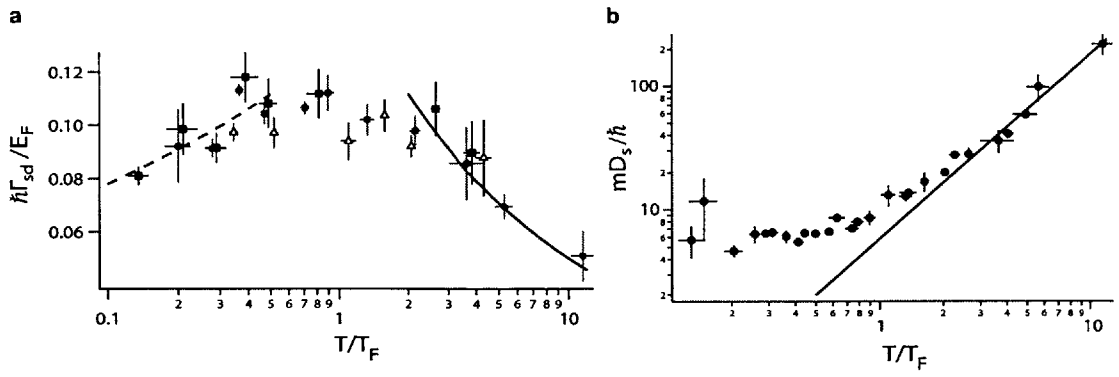

Figure 4-7: Spin transport coefficients as a function of temperature at unitarity. The spin drag coefficient (**a**), normalized by the Fermi energy at the trap center, exhibits a broad maximum around $T = T_F$. We find agreement between measurements taken at three different axial trapping frequencies, 22.8 Hz (red circles), 37.5 Hz (blue triangles) and 11.2 Hz (black squares). The spin diffusivity (**b**) reaches a constant minimum value of $6.3(3)\,\hbar/m$ at low temperatures. The solid lines show fits to the classical scaling laws for $T/T_F > 2$.

temperatures below T_F, the spin diffusivity reaches a minimum value of $6.3(3)\,\hbar/m$. The spin diffusivity in Fermi liquids is expected increase with decreasing temperature as T^{-2} for sufficiently low temperatures [16]. The temperatures reached here may not be low enough to see the expected low-temperature upturn of D_s. A recent calculation [50] of the spin diffusivity in the unitary fermi gas based on the Luttinger-Ward formalism shows a very small upturn in D_s in this temperature range, consistent with the uncertainty in our measurements.

While the high-temperature scalings of the data agree with the classical calculations for homogeneous gases, the absolute values differ by a multiplicative factor. In section 2.5.5 we found the high-temperature limits $\tilde{\Gamma}_{\mathrm{SD}} = 0.90\frac{E_F}{\hbar}\sqrt{\frac{\tilde{E}_F}{k_B T}}$ and $\tilde{D}_s = 1.1\frac{\hbar}{m}\left(\frac{T}{T_F}\right)^{3/2}$. The measured spin drag coefficient at high temperatures is smaller by a factor of 5.6(4), while the measured spin diffusivity is larger by about the same factor, 5.3(2). We attribute these factors to the inhomogeneous density and velocity distributions of the trapped system. The relation (4.4) between the local and global spin drag coefficients yields a simple expression for this multiplicative factor

in the high-temperature limit,

$$\Gamma_{\mathrm{SD}} = \tilde{\Gamma}_{\mathrm{SD}}(0)/\alpha, \tag{4.10}$$

with

$$\alpha = n_0(0)\frac{\int n_0 u_{\mathrm{d},z}\mathrm{d}^3r}{\int n_0^2 u_{\mathrm{d},z}\mathrm{d}^3r}, \tag{4.11}$$

where we have used $\tilde{\Gamma}_{\mathrm{SD}} \propto n$ in the high-temperature regime. For a uniform system α reduces to 1, while for a harmonically trapped system with a uniform drift velocity $\alpha = 2^{3/2} = 2.8$. However, the drift velocity profile cannot be uniform: even if it starts out uniform, spin currents would get damped faster in the center of the overlap region of the two clouds, where the collision rate is high, than in the wings, where it is low. A non-uniform drift velocity profile will develop. For example, a quadratic drift velocity profile $u_{\mathrm{d},z}(\mathbf{r}) = ax^2 + by^2 + cz^2$ will result in $\alpha = 2^{5/2} \approx 5.7$. Close to the trap center, by symmetry the drift velocity will behave like a constant plus a quadratic function of position. The actual value of α should therefore lie between 2.8 and 5.7.

For the spin diffusivity, the effect of the trap can in general involve a different multiplicative factor. Equation (4.9) gives

$$D_s = \tilde{D}_s(0)\alpha', \tag{4.12}$$

where

$$\alpha' = \frac{\langle u_{\mathrm{d},z}\rangle}{u_{\mathrm{d},z}(0)}, \tag{4.13}$$

which can in general be different from α. However, by considering the Euler equations in the high-temperature regime, one can show that $\alpha' \approx \alpha$ (see [145], Supplementary Information).

The measurements of spin transport shown here offer a first detailed look at the spin transport properties of ultracold Fermi gases. As one of the fundamental dissipative processes in a Fermi gas, spin transport provides a new set of physical properties against which to test many-body theories. For example, the Luttinger-Ward

formalism, proven to be accurate at calculating the equation of state [69, 70, 85] and viscosity [51, 22] of the unitary Fermi gas, has since been extended to calculate the spin transport coefficients of the unitary Fermi gas, showing good qualitative agreement with the results reported here [50]. The high-temperature regime of our measurement also poses an interesting theoretical challenge, namely to use the known local properties of the system to predict its global behavior. This challenge has been undertaken analytically [15], using a starting point analogous to Eqn. (2.62) to obtain the spin relaxation time, and numerically, using a simulation of the Boltzmann transport equation [59, 60, 61].

4.4 Spin Transport in Polarized Fermi Gases

Spin imbalance provides an important degree of freedom in experiments on ultracold Fermi gases. By increasing the spin imbalance beyond the Pauli (or Clogston-Chandrasekhar) limit for superfluidity, strongly-interacting Fermi gases can remain normal down to zero temperature [29, 24, 172, 141, 105]. This allows access to the low-temperature normal phase, a realization of a strongly-interacting Fermi liquid. Conversely, using a small spin imbalance, below the Clogston limit, allows one to directly observe the superfluid transition through the phase separation of the polarized normal phase and the un-polarized superfluid phase [173]. In this section we look at spin transport in spin-imbalanced gases with resonant interactions. For high spin imbalance, we measure spin transport in the polaron regime, while for small spin imbalance we observe spin transport in the superfluid phase [146].

4.4.1 Highly-Polarized Fermi Gases

In the limit where the number of spin down (minority) atoms is vanishingly small compared to the number of spin up (majority) atoms, the minority atoms form polaron quasiparticles [26, 31, 120, 132], where minority atoms are dressed by the majority Fermi sea. The energy of a single polaron in a zero-temperature Fermi sea of spin $\uparrow$

atoms has been described using the effective Hamiltonian [97, 17, 124]

$$H = -\alpha\mu_\uparrow + \frac{\mathbf{p}^2}{2m^*}, \tag{4.14}$$

where $\mathbf{p}$ is the momentum of the polaron, m^* is the polaron effective mass, $\mu_\uparrow$ is the local spin $\uparrow$ chemical potential, and α characterizes the polaron binding energy. The parameters α and m^*/m, where m is the bare mass of spin $\uparrow$ and spin $\downarrow$ fermions, have been measured experimentally [142, 132, 105, 104] and calculated theoretically [97, 30, 119, 116], giving $\alpha = 0.62$ and $m^*/m \approx 1.2$ at zero temperature.

As before, we consider the problem of spin transport induced by a spin dipole excitation along the z direction. Equation (2.50) gives the local spin drag force exerted on the minority cloud,

$$\frac{\mathrm{d}F_{\downarrow\uparrow}}{\mathrm{d}^3\mathbf{r}} = -m^* \int \mathrm{d}^3r\, n_\downarrow \tilde{\Gamma}_{\mathrm{SD}} \mathbf{v}_\downarrow, \tag{4.15}$$

using m^* as the effective mass of the spin down atoms.

In the limit $N_\downarrow \ll N_\uparrow$, the motion of the spin $\uparrow$ cloud due to momentum absorbed from the spin $\downarrow$ cloud may be neglected. The equation of motion of the spin $\downarrow$ center of mass $Z_\downarrow$ is then [17]

$$m^*\ddot{Z}_\downarrow + (1+\alpha)m\omega_z^2 Z_\downarrow + \frac{m^*}{N_\downarrow}\int \mathrm{d}^3r\, n_\downarrow(\mathbf{r})\frac{v_\downarrow(\mathbf{r})}{\tau_P(\mathbf{r})} = 0, \tag{4.16}$$

where the factor of $(1+\alpha)$ is due to the attraction of the minority fermions to the majority cloud. The the momentum relaxation rate $1/\tau_P$ is equivalent to the local spin drag coefficient. We use the notation $1/\tau_P$ for consistency with earlier work on polarized Fermi gases [17].

Experimentally, we find that the spin dipole excitation is strongly damped. As before, we fit the separation of the spin up and spin down centers of mass to $d(t) = d_0 e^{-t/\tau}$. For each time series, we obtain the dimensionless relaxation time

$$\tilde{\tau} = \hbar\omega_z^2\tau/E_{F\uparrow}. \tag{4.17}$$

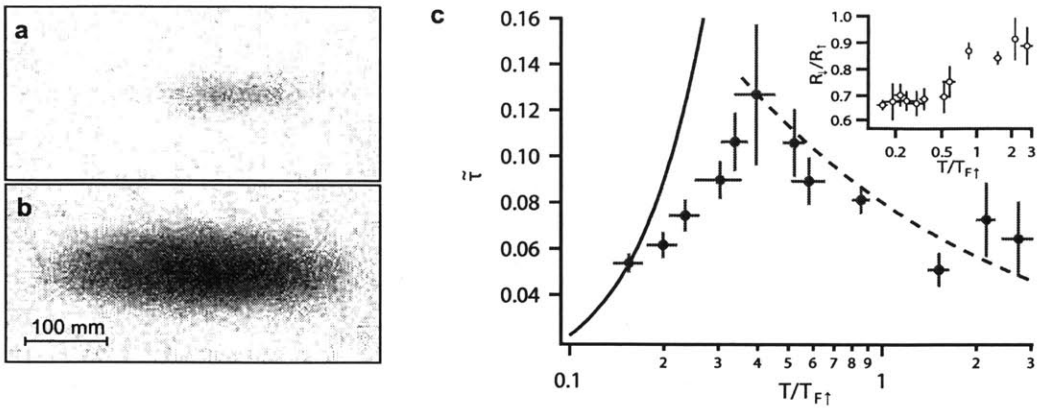

Figure 4-8: Spin transport in highly-polarized Fermi gases. **(a)** and **(b)** show two-dimensional column density images of the minority and majority spin state, respectively, obtained using resonant absorption imaging in one run of the experiment. The distance between the centers of mass in **(a)** and **(b)** is 34 μm. **c**, Normalized relaxation time of the spin dipole mode of a highly-polarized Fermi gas as a function of the reduced temperature $T/T_{F\uparrow}$. The solid curve is the low temperature limit from [17], given by equation (4.20). The dashed curve is the expression $0.08\sqrt{\frac{T_{F\uparrow}}{T}}$. Inset: ratio of the minority cloud size to the majority clouds size as a function of the reduced temperature $T/T_{F\uparrow}$.

$\tilde{\tau}$ relates to the fundamental properties of the gas as

$$\tilde{\tau} = \frac{m^*/m}{1+\alpha} \cdot \frac{1/\hat{\tau}_P}{E_{F\uparrow}/\hbar}, \tag{4.18}$$

where

$$\frac{1}{\hat{\tau}_P} = \frac{\int \mathrm{d}^3 r \, n_\downarrow(\mathbf{r}) v_\downarrow(\mathbf{r})/\tau_P(\mathbf{r})}{\int \mathrm{d}^3 r \, n_\downarrow(\mathbf{r}) v_\downarrow(\mathbf{r})} \tag{4.19}$$

is the global momentum relaxation rate, equivalent to the global spin drag coefficient Γ_{SD}. We have used the overdamped limit $(\omega_z \tau)^2 \gg 1$ to obtain Eqn. (4.18) by neglecting the second time derivative in Eqn. (4.16). This limit holds well in our experiments, where τ is always greater than 100 ms, and $(\omega_z \tau)^2 > 200$.

Figure 4-8 shows the measured values of the dimensionless relaxation time $\tilde{\tau}$ as a function of the reduced temperature $T/T_{F\uparrow}$. $\tilde{\tau}$ increases at low temperatures before reaching a maximum of $0.13(3)E_{F\uparrow}$ for $T/T_{F\uparrow} = 0.40(6)$, and decreases at higher temperatures. We interpret the behavior of the relaxation time at low temperatures as

a consequence of Pauli blocking: as the temperature is lowered significantly below the majority Fermi temperature, the phase space available for a minority atom to scatter goes to zero. The reduction of spin drag at low temperatures observed here is more pronounced than the reduction observed in the previous section, where the number of spin up and spin down atoms was equal. In the highly-polarized case, spin drag at $T/T_F \approx 0.15$ reduces by 51(6)% from the maximum value, while in the equal-number case, spin drag reduces by only 26(4)%. The difference in the amount of reduction may indicate the effects of pairing correlations in the non-polarized gas [127].

As in the previous section, the global effect of spin drag depends on the density and velocity distribution of the clouds. In the spin-imbalanced case, the ratio of the cloud sizes changes going from the low temperature regime, where the cloud sizes depend on the number of atoms, to the high temperature regime, where the cloud sizes depend only on the temperature. The inset in Fig. 4-8 shows the ratio of the cloud sizes $R_\downarrow/R_\uparrow$ as a function of the reduced temperature, where $R_{\uparrow(\downarrow)}$ is the 1/e width in the z direction from a two-dimensional gaussian fit to the majority (minority) column density. The ratio $R_\downarrow/R_\uparrow$ increases with increasing $T/T_{F\uparrow}$. Even at the lowest temperatures, $R_\downarrow/R_\uparrow$ remains significant, attaining a value of 0.7, due to the finite minority fraction $N_\downarrow/N_\uparrow \approx 0.1$. The effect of inhomogeneity is therefore reduced at low temperatures, but should remain present.

We can compare our results for $\tilde{\tau}$ at low temperatures to the low temperature limit in Ref. [17],

$$\frac{1/\tau_P(\mathbf{0})}{E_{F\uparrow}/\hbar} = \mathrm{c}\frac{\alpha^2}{1+\alpha}\left(\frac{m^*}{m}\right)^2\left(\frac{T}{T_{F\uparrow}}\right)^2 \tag{4.20}$$

for temperatures $T \ll T_{F\uparrow}$. The prefactor c changes slightly from $\mathrm{c} = \frac{2\pi^3}{9} = 6.89\ldots$ to $\mathrm{c} \approx 6.0$ as the temperature rises from far below $T_{F\downarrow}$, where even the minority cloud is degenerate, to temperatures where $T_{F\downarrow} \ll T \ll T_{F\uparrow}$ and the minority is a classical gas [17]. In our coldest data, $T \approx 0.5T_{F\downarrow}$ and $T_{F\downarrow} \approx 0.3T_{F\uparrow}$, assuming $m^* = 1.2\,m$. To compare our data to Ref. [17] using (4.20) we set $\mathrm{c} = \frac{2\pi^3}{9}$, $\alpha = 0.6$ and $m^* = 1.2\,m$. The comparison is affected by the inhomogeneous trapping potential in the experiment, as Eqn. (4.20) gives the local value of $1/\tau_P$ at the center of the majority cloud.

The experimental data agree with the value from Eqn. (4.20) at the lowest temperatures measured (see Fig. 4-8). The deviation at higher temperatures is expected as the $T \ll T_{F\uparrow}$ limit becomes inapplicable. The convergence of the experimental data to the theoretical value at low temperature despite the inhomogeneity of the system may be partly due to the reduced minority cloud size at low temperatures, which reduces the effects of inhomogeneity, as discussed above. Additionally, the variation of the momentum relaxation rate with density will to some extent cancel at moderately low temperatures, as $1/\tau_P$ changes from increasing with increasing density at high reduced temperatures to decreasing with increasing density due to Pauli blocking at low reduced temperatures. The crossing of the experimental curve with the predictions for a uniform system at low temperatures therefore does not necessarily indicate that the inhomogeneity is negligible at low temperatures in this measurement.

At high temperatures $T \gg T_{F\uparrow,\downarrow}$, the spin transport properties of a trapped system can be calculated from the Boltzmann transport equation. In the $n_\downarrow \ll n_\uparrow$ limit, the classical result (2.89) for the spin drag coefficient becomes

$$\frac{1/\tau_P}{E_{F\uparrow}/\hbar} = \frac{16\sqrt{2}}{9\pi^{3/2}}\sqrt{\frac{T_{F\uparrow}}{T}}. \tag{4.21}$$

For a harmonic trap, the normalized relaxation rate follows,

$$\tilde{\tau} = \frac{8}{9\pi^{3/2}\,\epsilon}\sqrt{\frac{T_{F\uparrow}}{T}} \approx \frac{0.16}{\epsilon}\sqrt{\frac{T_{F\uparrow}}{T}}, \tag{4.22}$$

where ϵ expresses the effect of the non-uniform velocity distribution, and follows

$$\epsilon = \frac{\int \mathrm{d}^3 r\, v_\downarrow(\frac{\mathbf{r}}{\sqrt{2}}) e^{-\beta U}}{\int \mathrm{d}^3 r\, v_\downarrow(\mathbf{r}) e^{-\beta U}}, \tag{4.23}$$

where U is the trapping potential (here assumed to be quadratic). For a quadratic velocity profile, $v_\downarrow(\mathbf{r}) = ax^2 + by^2 + cz^2$, the predicted $\tilde{\tau}$ is reduced by factor of $\epsilon = 2$. We find that the high temperature result (4.22) with $\epsilon = 2$ leads to close agreement with our experimental results (Fig. 4-8.c). This model for the velocity profile is interesting because it estimates the effect of the inhomogenous velocity distribution.

However, the velocity should remain non-zero everywhere, rather than going to zero at the origin as in the quadratic case. The actual velocity profile may have deviations from quadratic dependence at larger distances from the trap center that compensate for the non-zero velocity at the center.

4.4.2 Spin-Imbalanced Superfluids

We extend the method of the previous section to study spin transport in Fermi gases with resonant interactions and small spin imbalance. When the global polarization $\frac{N_\uparrow - N_\downarrow}{N_\uparrow + N_\downarrow}$ is less than about 75% in a harmonically trapped Fermi gas at low temperature and with resonant interactions, the system phase separates into a superfluid core surrounded by a polarized normal state region [172, 141, 105]. The superfluid core is visible as a sharp reduction in the density difference of the two spin states [141]. The transition between the superfluid and the imbalanced normal regions forms a sharp interface below a tricritical point, where the density imbalance jumps between the two regions [143]. Scattering and spin transport at the interface between a normal and superfluid Fermi gas have been considered theoretically in Refs. [159, 110].

To observe spin transport in an imbalanced gas containing a superfluid, we prepare a spin mixture with a global polarization of 17(3)%. Phase contrast imaging is used to enhance the sensitivity to small differences in density. An imaging pulse tuned halfway between the resonance frequencies of the two states directly measures the difference in the column densities (Fig. 4-9.a) while a second pulse, red-detuned from both states (Fig. 4-9.b), provides additional information needed to reconstruct the total column density in each state [143]. From the column densities of each state we obtain three-dimensional density distributions using the inverse Abel transformation.

The two-dimensional spin density (Fig. 4-9.a) and three-dimensional spin density (Fig. 4-9.c) show a reduction near the center of the trap, with the three-dimensional density going to zero, characteristic of the superfluid core in imbalanced Fermi gases [141]. We have checked that the shell structure remains even after the spin density reaches equilibrium. Additionally, estimates of the temperature confirm that it is cold enough to contain a superfluid [146, 85].

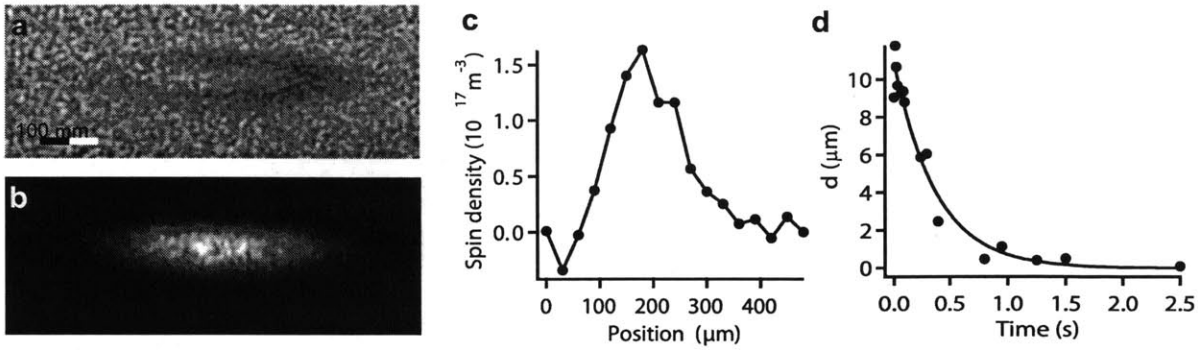

Figure 4-9: Spin transport in a superfliud Fermi gas. Phase contrast images are taken with imaging light detuned **(a)** halfway between the resonance frequencies of the two states and **(b)** at large red detuning from both states. The image in **(a)** is proportional to the difference in column densities of the two states. The depletion of the density difference in the center of the cloud indicates the superfluid region. It is displaced from the center of the majority due to the spin dipole excitation.**(c)** shows the difference in reconstructed three-dimensional densities of the spin up and spin down clouds as a function of the z coordinate for $z > 0$. The depletion in the center again indicates pairing and superfluidity [141]. An elliptical average over a narrow range of the radial coordinate ρ is used to increase the signal to noise ratio. **d**, The displacement of the spin up and spin down centers of mass relaxes exponentially, indicating strong spin drag despite the presence of a superfluid.

Even in the presence of the superfluid core, we observe strong damping of the spin dipole mode. Figure 4-9.d shows that the displacement d between the majority and minority centers of mass along the z axis relaxes gradually to zero, rather than oscillating as would be expected in a dissipationless system. The 1/e relaxation time $\tau = 360$ ms corresponds to a spin drag coefficient of $\omega_z^2 \tau = 0.06(1) E_{F\uparrow}/\hbar$, close to the maximum spin drag coefficient in non-polarized trapped Fermi gases at unitarity (Section 4.3.2).

Chapter 5

Evolution of Pairing From Three to Two Dimensions

A great variety of interesting condensed matter systems arise in two dimensions (2D). Examples include the fractional quantum Hall effect and the Berezinskii-Kosterlitz-Thouless (BKT) transition [82, 83]. In two dimensions, closed paths partition space into distinct subsets, leading to new topological effects, such as anyon quasiparticles [106]. Two-dimensional solid-state systems arise at surfaces and in bulk crystal structures. In the latter case, the system consists of an array of coupled 2D planes. Examples include some organic superconductors [88, 144] and the cuprate superconductors [155].

With ultracold atom experiments, we can tune the dimensionality of the system by applying an external potential, allowing explorations of physics in reduced dimensions. For example, the BKT transition has been studied using bosonic atoms in an optical lattice potential [68]. In this chapter we study the physics of fermions in two dimensions, and in the dimensional crossover from three to two dimensions, where the system is three-dimensional (3D) but anisotropic. The dimensionality is tuned using an optical lattice potential. We measure the binding energy of strongly-interacting fermion pairs as a function of lattice depth, observing the evolution from three to two dimensions. The anisotropic 3D regime presents greater challenges to describe theoretically, but also may provide access to new phases of matter [39, 40].

The two-dimensional limit restores some simplicity by eliminating the anisotropy as a parameter, but at the same time allows more precise comparisons with theory.

5.1 Dimensional Crossover in a 1D Lattice

5.1.1 Single-Particle Physics in a 1D Lattice

Strongly confining a three-dimensional gas along one direction produces an essentially two-dimensional system by freezing out motion along the third direction. This confinement can be provided using, for example, a strong harmonic potential [45], or using a one-dimensional (1D) lattice [100]. We use a 1D standing-wave optical lattice generated by retroreflecting a 1064 nm laser beam. This produces a periodic potential,

$$V_L(z) = V_0 \sin^2(\pi z/d), \tag{5.1}$$

with depth V_0 and lattice spacing $d = 532$ nm. The solutions to the Schrödinger equation for a single particle in the potential (5.1) are free in the x and y directions and follow Bloch's theorem along the z direction: $\phi_{n,q}(z) = u_{n,q}(z)e^{iqz}$, where $u_{nq}(z)$ is periodic with period d, q is the lattice momentum, and the index $n = 0, 1, 2, 3\ldots$ labels the energy band. The energies $\epsilon_{n,q}$ are periodic in q with period $2\pi/d$, so q is chosen to lie in $[-\pi/d, \pi/d]$. As the lattice depth increases, the energy $\epsilon_{0,q}$ of the first Bloch band becomes flat, and the group velocity goes to zero. Wavepacket centered at a given lattice site will then tend to remain at that site. Atoms therefore become localized in the z direction when the lattice depth is large.

The 2D limit corresponds to deep lattices, where the gas is confined to an array of 2D layers. In the pressence of a 1D lattice there are two degrees of freedom associated with motion in the z direction: the index of the Bloch band and the tunneling between lattice planes. We will load atoms into the first Bloch band, so the tunneling rate remains as the free parameter that we tune to interpolate from 3D to 2D. We parametrize the tunneling rate using the lattice depth, normalized by the

recoil energy,

$$E_R = \frac{\hbar^2 \pi^2}{2md^2}. \tag{5.2}$$

A deep lattice corresponds to $V_0/E_R \gg 1$, with a flat dispersion $\epsilon_{0,q}$ and a low tunneling rate.

For sufficiently large V_0/E_R, the atoms see only the local minima of the lattice potential, and system becomes equivalent to a quasi-2D gas confined by a strong harmonic trap in the z direction. The corresponding harmonic oscillator frequency follows by expanding (5.1) to leading order in z,

$$\hbar\omega_z = 2\sqrt{V_0 E_R}. \tag{5.3}$$

We will use $\hbar\omega_z$ from (5.3) to compare our measurements in deep lattices to predictions for harmonicaly confinemed gases.

Band Structure Calculation

Understanding our measurements often requires us to solve the single-particle Schrödinger equation in the lattice potential (5.1). We compute the eigenstates and energies using the Schrödinger equation in momentum space,

$$\left(\frac{\hbar^2 k^2}{2m} + \frac{V_0}{2}\right)\tilde{\phi}(k) - \frac{V_0}{4}\left[\tilde{\phi}\left(k - \frac{2\pi}{d}\right) + \tilde{\phi}\left(k + \frac{2\pi}{d}\right)\right] = E\tilde{\phi}(k) \tag{5.4}$$

where $\tilde{\phi}(k)$ is the Fourier transform of the wavefunction $\phi(z)$. For a state with lattice momentum q, $\tilde{\phi}(k)$ is non-zero for $k = q + 2\pi j/d$, for any integer j. The wavefunction is then

$$\phi_q(z) = \sum_{j=-\infty}^{\infty} c_j e^{i(q+2\pi j/d)z} \tag{5.5}$$

and the Schrödinger equation (5.4) becomes, after dividing by E_R,

$$\left[\left(\frac{qd}{\pi} + 2j\right)^2 + \frac{V_0}{2}\right] c_j - \frac{V_0}{4}(c_{j-1} + c_{j+1}) = \frac{E_q}{E_R} c_j. \tag{5.6}$$

The Hamiltonian for each q corresponds to a tridiagonal matrix. The eigenvalues gives the band energies $\epsilon_{n,q}$. We find the eigenvalues numerically by restricting $|j| \leq j_{\max}$. For lattice depths $V_0 \leq 30E_R$, the lower eigenvalues converge to high precision for $j_{\max} > 5$.

5.1.2 Bound States and Scattering in Two Dimensions

For $V_0/E_R \gg 1$, we approximate the lattice potential as a harmonic potential with frequency ω_z and harmonic oscillator length $l_z = \sqrt{\frac{\hbar}{m\omega_z}}$. In the 2D limit, a bound state exists for all values of the s-wave scattering length a between fermions of unequal spin. The binding energy is given by [115, 12]

$$E_{\mathrm{b}}^{\mathrm{2D}} = \hbar\omega_z \, F_2 \left(l_z/a\right), \tag{5.7}$$

where F_2 is found by inverting the relation

$$\frac{l_z}{a} = \int_0^\infty \frac{\mathrm{d}u}{\sqrt{4\pi u^3}} \left(1 - \frac{2ue^{-\epsilon u}}{1 - e^{-2u}}\right), \tag{5.8}$$

with $\epsilon = \frac{E_{\mathrm{b}}^{\mathrm{2D}}}{\hbar\omega_z}$. In particular, at the Feshbach resonance, where $l_z/a = 0$, the binding energy becomes $E_{\mathrm{b}}^{\mathrm{2D}} = 0.244\hbar\omega_z$ [12]. In contrast, the binding energy in 3D is $E_{\mathrm{b}}^{\mathrm{3D}} = \frac{\hbar^2}{ma^2}$, which vanishes when $1/a = 0$.

The binding energy determines the s-wave scattering amplitude in 2D. For collisions with relative momentum $\hbar k$, the scattering amplitude is [115]

$$f(k) = \frac{2\pi}{-\ln(ka_{\mathrm{2D}}) + i\pi/2}, \tag{5.9}$$

where $a_{\mathrm{2D}} = \hbar/\sqrt{mE_{\mathrm{b}}}$. The scattering cross-section in 2D has units of length and is given by [115]

$$\sigma(k) = \frac{|f(k)|^2}{4k}. \tag{5.10}$$

5.1.3 Two-Body Physics in a 1D Lattice

The two-body problem in free space reduces to a one-body problem for the relative motion (Section 2.2.1). In a harmonic trap, the relative motion again decouples from the center of mass motion. This can be seen by writing the potential energy of two colliding particles in terms of the center of mass and relative coordinates,

$$V_h(z_1) + V_h(z_2) = \frac{1}{2}m\omega_z^2(z_1^2 + z_2^2) = \frac{1}{2}m_r\omega_z^2 z^2 + \frac{1}{2}M\omega_z^2 Z^2, \tag{5.11}$$

where $z = z_1 - z_2$, $Z = (z_1 + z_2)/2$, $m_r = m/2$, and $M = 2m$. In the pressense of a 1D lattice, however, the relative and center of mass coordinates no longer decouple,

$$V_L(z_1) + V_L(z_2) = V_0\left[\sin^2(\pi z_1/d) + \sin^2(\pi z_2/d)\right] \tag{5.12}$$

$$= V_0\left[\sin^2(\pi(z + Z/2)/d) + \sin^2(\pi(z - Z/2)/d)\right] \tag{5.13}$$

In this case one must retain both the relative coordinates $\mathbf{r} = \mathbf{r}_1 - \mathbf{r}_2$ and the center of mass Z along the z axis when solving the two-body problem. Reference [109] solves the two-body problem in a 1D lattice, finding the binding energy

$$\frac{E_b}{E_R} = F_L\left(V_0/E_R, d/a\right). \tag{5.14}$$

in terms of a dimensionless function F_L. As expected, Ref. [109] finds that F_L increases with V_0/E_R for fixed d/a because the binding energy is greater in the 2D limit than in 3D.

5.1.4 Mean-Field Theory in Two Dimensions

As in 3D, the mean-field approximation for the Hamiltonian of a fermionic system near the ground state is [155, 103, 123, 133]

$$H_{\mathrm{MF}} - \mu N = E_G(\mu) + \sum_k E_k(\gamma_{k\uparrow}^\dagger\gamma_{k\uparrow} + \gamma_{k\downarrow}^\dagger\gamma_{k\downarrow}), \tag{5.15}$$

where $\gamma_{k,\alpha}$ are the Bogoliubov operators and the excitation spectrum is

$$E_k = \sqrt{(\epsilon_k - \mu)^2 + \Delta^2}, \tag{5.16}$$

with $\epsilon_k = \frac{\hbar^2 k^2}{2m}$.

In 2D, Refs. [103, 123] find

$$\Delta = \sqrt{2 E_F E_\mathrm{b}} \tag{5.17}$$

and

$$\mu = E_F - E_\mathrm{b}/2, \tag{5.18}$$

where E_F is the Fermi energy and E_b is the binding energy at zero density.

Removing one particle from the many-body ground state and adding it to the vacuum leaves behind a quasiparticle excitation. The corresponding change in energy is [155]

$$\Delta E(k) = (E_G + E_k - \mu + \epsilon_k) - E_G = E_k - (\mu - \epsilon_k). \tag{5.19}$$

The minimum energy cost occurs at $k = 0$, and is given by

$$\Delta E(0) = \sqrt{\mu^2 + \Delta^2} - \mu = E_\mathrm{b}. \tag{5.20}$$

Remarkably, the energy cost to break a pair in 2D mean-field theory is given exactly by the binding energy of two particles in vacuum.

As in 3D, mean-field theory describes a smooth crossover from BEC to BCS superfluidity. The crossover is parametrized by the 2D interaction parameter $\ln(k_F a_{2\mathrm{D}})$. The BEC side of the crossover corresponds to $\ln(k_F a_{2\mathrm{D}}) < 0$, while the BCS side corresponds to $\ln(k_F a_{2\mathrm{D}}) > 0$ [123]. When $|\ln(k_F a_{2\mathrm{D}})| < 1$, the scattering amplitude (5.9) at the Fermi surface is large and one expects the mean-field approximation to become inaccurate.

5.2 Measurement of Binding Energies in a 1D Lattice

We measure the binding energy of fermion pairs in a 1D lattice using RF spectroscopy. To minimize final state interaction effects we use states $|1\rangle$ and $|3\rangle$ as the initial states for spectroscopy.

5.2.1 Experimental Procedure

We start with a spin polarized cloud of ^{6}Li atoms in the lowest hyperfine state $|1\rangle$ after sympathetic cooling with ^{23}Na. After raising the magnetic field to 568 G, where the scattering lengths between all three lowest hyperfine states of ^{6}Li are less than 200 a_0, and in particular where $a_{13} \approx 0$ [169], we create an equal mixture of states $|1\rangle$ and $|3\rangle$ using a 50% Landau-Zener transfer to $|2\rangle$, followed by a 100% transfer from $|2\rangle$ to $|3\rangle$. Working at $a_{13} \approx 0$ allows the $2 \rightarrow 3$ transition to proceed without decoherence due to final state interactions.

After creating the 1-3 mixture, we raise the magnetic field to a final value in the vicinity of a broad Feshbach resonance centered at 690 G. The gas is then cooled by lowering the depth of the optical dipole trap and the optical lattice is ramped up over 100 ms. The optical lattice crosses the optical dipole trap at an angle of about 0.5 degrees, allowing the optical lattice to be retroreflected after the chamber while the dipole trap beam is dumped. An RF pulse is applied to probe the gas on either the 1-2 transition or the 3-2 transition. We mainly use a pulse duration of 1 ms but also tested shorter and longer pulses. We then image state 2 and either state 1 or state 3. The fraction of atoms transfered to state 2 is obtained from each run of the experiment. The experiment is repeated with different pulse frequencies to obtain a spectrum. For the magnetic field range used here (650-834 G), the 1-2 transition is located at about 76 MHz and the 2-3 transition is at about 82 MHz. The probe frequency is scanned over a few hundred kHz to observe the spectral features associated with bound states and pairing.

To ensure loading into the first Bloch band, the Fermi energy and temperature of the cloud are kept below the energy of the second band. The 2D Fermi energy $E_F^{2D} = \frac{2\pi\hbar^2\bar{n}}{m}$, with $\bar{n}$ the 2D density per spin state at the center of the cloud, is typically $h \cdot 10$ kHz. The bottom of the second band is at least one recoil energy $E_R = h \cdot 29.3$ kHz above the bottom of the first band in shallow lattices, and up to about $h \cdot 300$ kHz for the deepest lattices. The temperature is estimated by fitting to the atomic density distribution after free expansion and found to be on the order of the Fermi energy.

Lattice Calibration

To measure the depth V_0 of the lattice, we use Kaptiza-Dirac diffraction or lattice modulation spectroscopy.[1] For Kaptiza-Dirac diffraction, the lattice is pulsed on for a short time t_p, imprinting a phase grating on the atomic wavefunctions. When the pulse is short compared to the recoil time $t_R = h/E_R = 34\,\mu$s and the atomic momentum distribution is well-localized in k-space, discrete diffraction orders appear after a few milliseconds of free expansion (Fig. 5-1.a). The fractional population in the n-th diffraction order is given by

$$P_n = J_n^2\left(\frac{\pi t_p V_0}{h}\right), \tag{5.21}$$

where J_n is the Bessel function of order n. In practice, the populations of the diffraction orders are measured for several lattice depths and the signal V_{PD} from a monitoring photodiode is recorded for each lattice depth. The data is then fit to $P_n = J_n^2(\alpha V_{\mathrm{PD}})$, where α is a fit parameter (Fig. 5-1.b). The lattice depth for a given photodiode value is then $V_0 = \frac{\alpha h}{\pi t_p} V_{\mathrm{PD}}$. Before using Kapitza-Dirac diffraction for calibration, the alignment of the optical lattice relative to the optical dipole trap is checked to ensure that the atoms sit at the center of the lattice beam during the pulse. Because of the requirement that the atomic momentum distribution be localized in k-space, it is necessary to use a BEC or fermion pair condensate in order to obtain

[1] We at first used Kapitza-Dirac diffraction, and later began using lattice modulation spectroscopy, which we judged to be more precise.

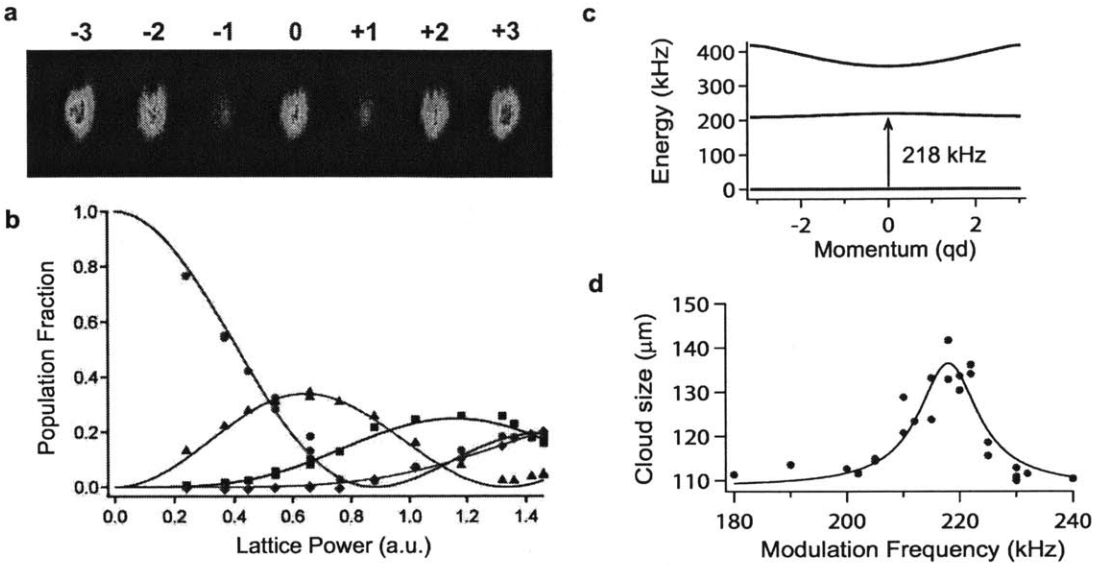

Figure 5-1: The depth of the optical lattice potential is calibrated using Kapitza-Dirac diffraction (**a** and **b**) and modulation spectroscopy (**c** and **d**). For Kapitza-Dirac diffraction, the lattice is pulsed on for 2 μs and the fraction of atoms in each diffraction order (**a**) is measured and plotted as a function of the control voltage for the lattice power (**b**). Fitting Bessel functions provides a calibration of the absolute depth of the lattice (curves in **b**). For modulation spectroscopy, the lattice depth is modulated by a few percent for 300 ms, driving transitions from the first to the second Bloch band (**c**). Increased tunneling in the second band causes the cloud to grow along the lattice axis, with a maximum at the resonant frequency (**d**).

a strong signal. We mostly used a ^{23}Na BEC but have also performed Kapitza-Dirac diffraction using $^6Li_2$ molecular condensates. To obtain clean separation between diffraction orders with a $^6Li_2$ condensate, we found it necessary to ramp the magnetic field near to the zero crossing of the scattering length.

Lattice modulation spectroscopy offers some benefits over Kapitza-Dirac diffraction for the purposes of lattice depth calibration. Modulation spectroscopy consists of modulating the intensity of the lattice laser to resonantly drive transitions to higher Bloch bands (Fig. 5-1.c). Exciting the higher bands results in an increased cloud size due to tunneling along the lattice axis (Fig. 5-1.d). Resonant excitation occurs when the modulation frequency matches the frequency of the transition from the lowest band to one of the higher bands. For example, to drive the 0 to 1 transition, we modulate at a frequency of $\hbar\omega_m = \epsilon_{1q} - \epsilon_{0q}$, where q is the quasimomentum of the

atoms to be excited. A further refinement of this technique is to apply band-mapping by ramping down the lattice linearly over about 1 ms and then allowing the cloud to expand freely for a few ms. The Bloch states are then adiabatically mapped to momentum eigenstates, and one can resolve the momentum dependence of the transition frequency to obtain a more precise determination of the lattice depth.

5.2.2 RF Spectra in a 1D Lattice

When the system absorbs an RF photon of energy $h\nu_{\mathrm{rf}}$, the hyperfine state of one of the atoms is changed to $|2\rangle$. The change in energy of the system, not including the hyperfine energy $h\nu_{\mathrm{hf}}$, is then $h\nu = \pm h(\nu_{\mathrm{rf}} - \nu_{\mathrm{hf}})$, where the plus symbol corresponds to a $|1\rangle \rightarrow |2\rangle$ transition, and the minus symbol to a $|3\rangle \rightarrow |2\rangle$ transition. We refer to ν as the RF offset (relative to the hyperfine frequency ν_{hf}).

An RF offset near zero flips the spin of unpaired atoms, while a sufficiently large positive offset can break pairs. For a two-body system, the threshold for breaking a pair is the two-body binding energy E_{b}. In the many-body state this pair-breaking threshold may differ from the two-body binding energy. However, in Section 5.1.4 we saw that the pair-breaking threshold in the mean-field approximation in 2D remains equal to the two body binding energy. We will regard the threshold measured experimentally as a generalized binding energy E_{b} that may depend on density.

Figure 5-2 shows an example of an RF spectrum. At negative RF offset we see a peak corresponding to a bound-to-bound transition. This occurs at an RF offset of

$$h\nu_{\mathrm{bb}} = E_{\mathrm{b}} - E'_{\mathrm{b}}, \tag{5.22}$$

where E_{b} is the binding energy in the initial state, and E'_{b} is the binding energy in the final state. Since we use the 1-3 mixture, the final state binding enegy is always significantly greater than the initial state binding energy in the range of magnetic fields used. This is because the scattering length in the final state is a_{23} or a_{12}, depending on whether we probe the $1 \rightarrow 2$ or $3 \rightarrow 2$ transition, and both are positive but smaller than $|a_{13}|$. Consequently, $E'_{\mathrm{b}} > E_{\mathrm{b}}$ and the bound-to-bound transition

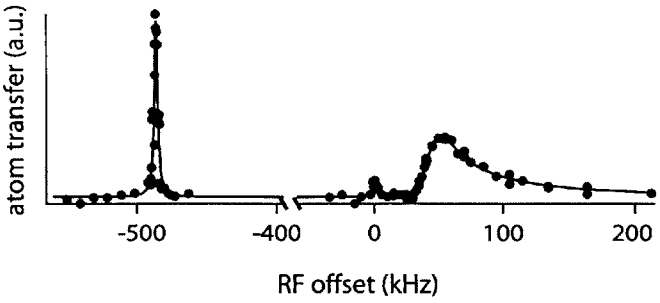

Figure 5-2: Example of an RF Spectrum of strongy-interacting fermions in a 1D lattice. Here the lattice depth is 9.59(7) E_R and the interacting parameter d/a is -0.01(4), corresponding to resonant interactions in 3D. The spectrum shows three features, a bound-to-bound transition at negative RF offset, a free-to-free transition at zero offset, and a bound-to-free transition at positive offset.

occurs at negative RF offset. At $\nu = 0$ we see a peak due to transfer of unpaired atoms. The broad asymmetric feature at positive RF offset is the pair dissociation spectrum. The long high-frequency tail results from breaking pairs into free atoms with non-zero momentum. The threshold of the dissociation spectrum determines the binding energy.

RF spectra are recorded for various lattice depths and interaction strengths. Figure 5-3 shows examples of spectra over a range of lattice depths at the 3D Feshbach resonance and on the BCS-side of the resonance at 721 G, where fermion pairing in 3D is a purely many-body effect. At the lowest lattice depths, the spectra show only a single peak, shifted to positive offset frequencies due to many-body interactions. This is similar to the case without a lattice [137, 131]. However, as the lattice depth is raised, the single peak splits into two and a clear pairing gap emerges.

5.2.3 Observed Binding Energies

Binding energies are determined from the frequency of the pairing threshold. To obtain a simple estimate of the threshold, one could fit a line to the steep part of the dissociation spectrum, and obtain the zero-crossing. However, this leads to an under-estimate of the binding energy due to experimental broadening mechanisms. To obtain a more accurate measurement of E_b, we fit the measured spectrum to the

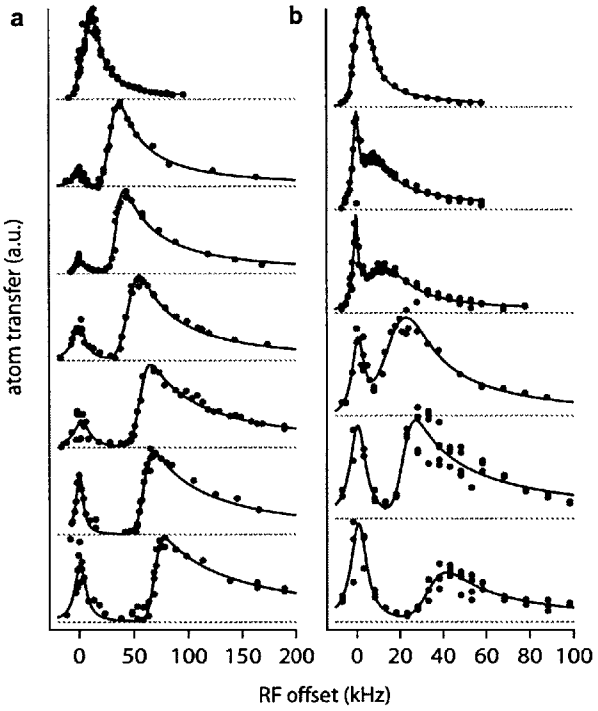

Figure 5-3: Evolution of fermion pairing in the 3D-to-2D crossover in a one-dimensional optical lattice, observed via RF spectroscopy. Shown is the transferred atom number versus RF offset frequency relative to the atomic hyperfine splitting. **a**, Spectra at the Feshbach resonance at 690.7(1) G with $d/a = -0.01(4)$. Lattice depths from top to bottom in units of E_R: 1.84(3), 4.8(2), 6.1(2), 9.9(4), 12.2(4), 18.6(7), and 19.5(7). **b**, Spectra on the BCS side at 720.7(1) G, $d/a = -1.15(2)$. Lattice depths in units of ER: 2.75(5), 4.13(7), 4.8(1), 6.0(2), 10.3(2), and 18.1(4).

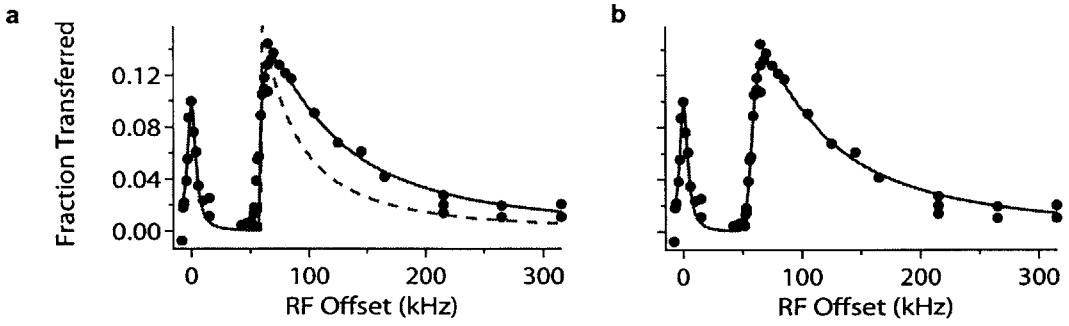

Figure 5-4: Fitting the lineshape for bound-to-free spectra in 2D. The spectrum shown here is obtained with a lattice depth of 18.6(7) E_R, $d/a = -0.01(4)$, and a final state binding energy of 574 kHz. **a**, The lineshape without final state interactions (orange dashed curve) predicts a discontinuous onset and a more rapid decay with increasing frequency than observed. Including the correction due to final state interactions (blue curve) results in a successful fit. **b**, We convolve the theoretical lineshape with a gaussian function of variable width to account for experimental broadening. In this case the optimal gaussian has a width of $w_m = 3.6(4)$ kHz.

predicted lineshape for dissociation of molecules in 2D [89],

$$I(\nu) \propto \frac{\theta(h\nu - E_\mathrm{b})}{\nu^2} \frac{\ln^2(E_\mathrm{b}/E'_\mathrm{b})}{\ln^2((h\nu - E_\mathrm{b})/E'_\mathrm{b}) + \pi^2}. \tag{5.23}$$

The first factor matches the spectrum one finds by applying Fermi's golden rule to the bound state and assuming a non-interacting final state, while the second factor is due to interactions in the final state. In 3D, final state interactions having large E'_b affect the high-frequency tail of the pair dissociation spectrum but have a vanishing effect near threshold [28]. However, in 2D, Eqn. (5.23) shows that the large energy scale of the final state interactions has an observable effect even near the threshold.

Figure 5-4.a compares the theoretical lineshapes with and without the final state correction to one of our spectra. Final state interactions cause the spectrum to rise continuously from zero rather than discontinuously jumping to the maximum value, as it would without final state interactions. The behavior of the high-frequency tail is observably modified by the final state interaction. Fitting our spectra with a pure power law tail typically gives a $1/\nu^{1.5}$ law rather than $1/\nu^2$. However, $1/\nu^2$ with the logarithmic correction as in (5.23) yields a good fit. Including the final state

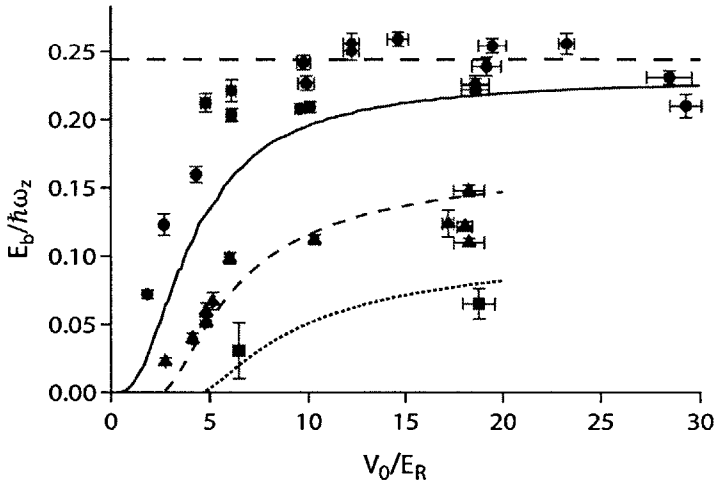

Figure 5-5: Binding energy E_b versus lattice depth V_0 at several values of the 3D scattering length a. E_b is normalized via the lattice frequency ω_z. Red circles: results from spectra at 690.7(1) G and $d/a = -0.01(4)$. Green triangles: 720.7(1) G, $d/a = -1.15(2)$. Blue squares: 800.1(1) G, $d/a = -2.69(1)$. Curves show predictions from Orso *et al.* [109]. Black dashed line: harmonic approximation result for $1/a = 0$.

interaction requires knowing E_b', which we obtain from spectra where a bound-to-bound peak was measured, using a preliminary estimate of E_b for subtraction in Eqn. (5.22).

The spectra are slightly broadened due to decoherence and a finite pulse time. The broadening is mostly noticable at the pairing threshold. We account for the broadening by convolving the theoretical lineshape (5.23) with a gaussian function of width w_m (Fig. 5-4.b). The parameters E_b and w_m are determined by a least-squares fit to the measured spectrum. Typical spectra have w_m of 5 kHz, consistent with our estimates of broadening based on collisions and three-body losses. The Fourier broadening is 1 kHz. Power broadening is about 5 kHz on the free to free transition, and less than 1 kHz on the bound to free transition due to the reduced wavefunction overlap. At low lattice depths, the 2D form for the paired spectrum should differ from the exact shape that interpolates between the 3D and 2D limits. In the case where the shape of the spectrum is given by the 3D limit, fitting to the 2D form overestimates the binding energy by 8%.

Figure 5-5 shows the measured binding energies as function of V_0/E_R for several

interaction strengths. The measured binding energies grow with increasing lattice depth, and agree reasonably well with theoretical predictions for two-body bound pairs in a 1D lattice [109]. The binding energy at the 3D resonance approaches a constant multiple of $\hbar\omega_z$ as the lattice depth increases, as expected from the 2D limit [115, 12]. Figure 5-6.a compares the binding energies measured in lattices deeper than $17E_R$ to predictions in the harmonic quasi-2D limit [115, 12]. At the 3D Feshbach resonance, we find $E_\mathrm{b} = 0.232(16)\hbar\omega_z$ for deep lattices. This value is close to the harmonic confinement result of $0.244\hbar\omega_z$ [12]. The exact calculation [109] predicts a constant downward shift of the binding energy by $0.2E_R$ for deep lattices due to the anharmonicity of the sinusoidal potential. For V_0 of about $20E_R$, this gives a prediction of $0.22\hbar\omega_z$, also close to the measured value.

The upward deviation of the measured binding energies with resonant interactions at low lattice depths (red circles in Fig. 5-5) relative to the two-body prediction of Ref. [109] is likely due to many-body effects. When interactions are resonant, the pair dissociation threshold in 3D occurs at about $0.5E_F$ [131]. In shallow lattices we expect that the threshold continues to receive an upward shift due to the Fermi energy. On the 3D BCS-side, the many-body shift of the threshold is expected to be smaller due to a smaller value of Δ in Eqn. (5.20). This is consistent with the data at 721 G (green triangles in Fig. 5-5), which only shows a significant upward shift for the lowest lattice depth measured.

Figure 5-6.b shows the binding energy measured in deep lattices normalized by the exact two-body result [109] versus the many-body interaction parameter $\ln(k_F a_{2\mathrm{D}})$. For $|\ln(k_F a_{2\mathrm{D}})| > 1$, the binding energies are close to the two-body value, as predicted by zero-temperature mean-field theory [123]. The data show a slight downward deviation for the strongest coupling, where $|\ln(k_F a_{2\mathrm{D}})| < 1$. At fixed reduced temperature T/T_F, the relationship should be universal and would be interesting to study further.

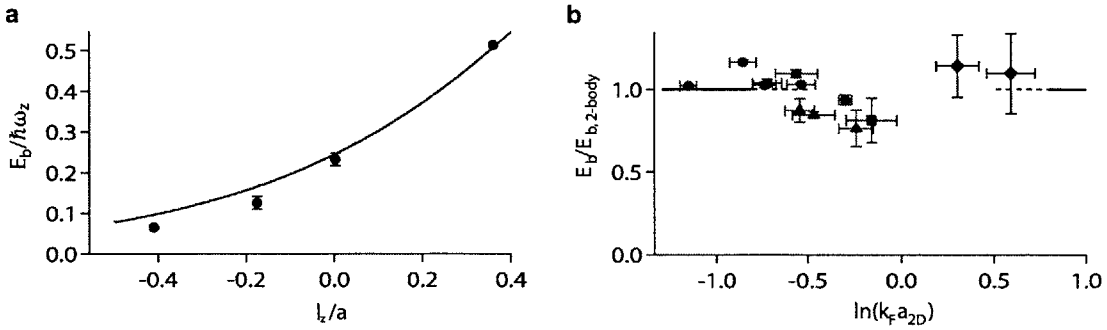

Figure 5-6: **a**, Binding energy of fermion pairs versus interaction strength l_z/a for deep lattices ($V_0 > 17E_R$). Solid curve: theoretical prediction in the 2D harmonic limit [115, 12]. **b**, Ratio of the measured binding energy to the two-body result [109] versus $\ln(k_F a_{2D})$ for $V_0 > 17E_R$. Black diamonds: binding energy determined from the bound to bound transition with resonant final state interactions. Other data symbols: see Fig. 5-5. Horizontal line: zero-temperature mean-field theory [123].

5.3 Conclusions on Fermion Pairing in the 3D-to-2D Crossover

In conclusion, we have measured the binding energy of fermion pairs along the crossover from 3D to 2D in a one-dimensional optical lattice. Measurements were performed at several lattice depths and scattering lengths, allowing quantitative comparison with theoretical predictions. Overall, the measured binding energies agree well with the two-body binding energy calculated in Ref. [109]. In 2D, this agreement is expected from mean-field theory [123]. Deviations from the two-body binding energy in deep lattices are found to be largest in the strong-coupling regime, where mean-field theory is expected to become inaccurate. While these measurements have addressed pairing, superfluidity in a one-dimensional lattice will be an exciting topic for future studies.

Chapter 6

Solitons in Superfluid Fermi Gases

Solitons are localized, non-linear excitations of fluids that propagate without dispersing. In superfluids, solitons occur when the phase of the order parameter jumps over a short distance. In a dark soliton, the phase jump is accompanied by a reduction in the superfluid density, while in a bright soliton it is accompanied by an increase in the density. Solitons move through the superfluid with a velocity that depends on the phase jump. Unlike sound waves, soliton excitations maintain their shape as they evolve dynamically, are more localized, and move at speeds less than the speed of sound. In this chapter, I describe experiments in which we create dark solitons in a superfluid Fermi gas, and measure the soliton oscillation period over a range of interaction strengths, from the BEC limit to unitarity.

6.1 Solitons in Superfluids

6.1.1 Soliton Solution of the Gross-Pitaevskii Equation

Although we perform these measurements using fermionic atoms, we can gain some intuition for solitons in superfluids from the bosonic case. The order parameter of a superfluid Bose gas is

$$\langle \psi(\mathbf{r},t) \rangle = \phi(\mathbf{r},t) e^{-i\mu t}, \tag{6.1}$$

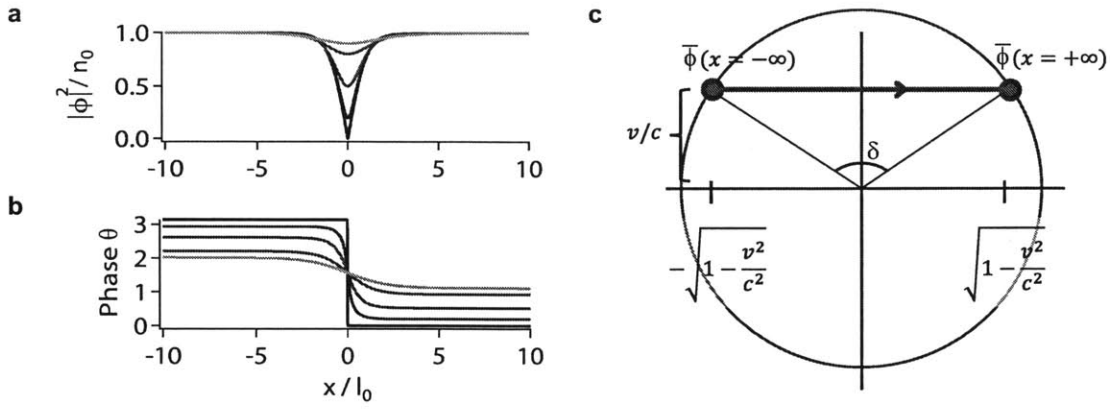

Figure 6-1: Soliton solution to the Gross-Pitaevskii equation. Plots show the spatial structure of the macroscopic wavefunction at fixed time $t = 0$. **a**, Density normalized by the background density n_0. **b**, Phase of the macroscopic wavefunction. Colors from orange to black correspond to velocities $v/c = 0.9, 0.8, 0.5, 0.2, 0$. **c**, The normalized wavefunction $\bar{\phi} = \phi/\sqrt{n_0}$ traces a chord across the unit circle in the complex plane as x goes from $-\infty$ to ∞.

where ϕ is the macroscopic wavefunction and μ is the chemical potential. In a weakly-interacting Bose gas at zero temperature, the density is $n = |\phi|^2$. In terms of the phase θ, the macroscopic wavefunction can be written $\phi = \sqrt{n}e^{i\theta}$. The order parameter evolves according to the time-dependent Gross-Pitaevskii (GP) equation,

$$i\partial_t\phi = \left[-\frac{\hbar^2}{2m}\nabla^2 + g\,|\phi|^2 - \mu + U(\mathbf{r})\right]\phi. \tag{6.2}$$

Here $U(\mathbf{r})$ is the external potential, m is the mas of the bosons, and g is an interaction parameter. For contact interactions with s-wave scattering length $a \ll n^{-1/3}$, the interaction parameter is $g = 4\pi\hbar^2 a/m$. For a homogeneous system, equation (6.2) gives the equation of state $\mu = gn$. The characteristic length scale in equation (6.2) is the healing length l_0,

$$l_0 = \hbar/\sqrt{mng} = 1/\sqrt{4\pi an}. \tag{6.3}$$

The speed of sound is

$$c = \frac{\hbar}{ml_0} = \sqrt{\mu/m}. \tag{6.4}$$

Solving the GP equation (6.2) in 1D with $U = 0$ for solutions of the form $\phi(x,t) =$

$\phi(x - vt)$, one finds [52, 168]

$$\phi(x,t) = \sqrt{n_0}\left[i\frac{v}{c} + \sqrt{1-\frac{v^2}{c^2}}\tanh\left(\sqrt{1-\frac{v^2}{c^2}}\frac{x-vt}{l_0}\right)\right], \tag{6.5}$$

where $l_0 = \hbar/\sqrt{mn_0g}$ and $c = \frac{\hbar}{ml_0}$. Figure 6-1 illustrates the solution (6.5) as a function of x at $t = 0$. The minimum density occurs at $x = vt$ and is $n_{\min} = n_0(v/c)^2$. Defining the phase jump δ as

$$\delta = \theta(\infty) - \theta(-\infty), \tag{6.6}$$

one sees from Fig. 6-1.c that the velocity is related to the phase jump by

$$v = -c\,\mathrm{sign}(\delta)\cos(\delta/2)\,. \tag{6.7}$$

The wavefunction (6.5) describes a large-amplitude excitation of a non-linear equation. Larger values of the non-linearity parameter g in the GP equation (6.2) lead to a smaller healing length (6.3) and therefore a more localized excitation. This excitation is considered a soliton because it is a non-linear excitation that propagates without dispersing, its form being stabilized by the non-linear dynamics.

As a dark soliton propagates through a trapped atomic gas, it slows down toward the edges of the cloud an eventually turns around. Using a Thomas-Fermi approximation for the gas density, one finds the oscillation period of the solitons to be [52]

$$T_s^{\mathrm{BEC}} = \sqrt{2}T_z, \tag{6.8}$$

where T_z is the trapping period in the direction of the soliton motion, here labeled z.

As an excited state, the soliton should eventually decay to allow the system to reach equilibrium. The snake instability is a dynamic, non-dissipative, instability where the soliton plane becomes deformed, and evolves into vortices [3]. Sufficiently strong confinement of the gas parallel to the soliton plane can suppress this instability [139]. Solitons decay dissipatively by emitting phonons. This leads to an

acceleration of the soliton, until it reaches the speed of sound and vanishes [52]. The lifetime of a soliton due to dissipation is therefore determined by the dissipation rate, and the initial velocity of the soliton. An initially slow soliton will take longer before reaching the speed of sound and disappearing.

6.1.2 Solitons in fermionic superfluids

For a fermion-pair superfluid with field operators $\psi_\uparrow(\mathbf{r})$ and $\psi_\downarrow(\mathbf{r})$, the order parameter is

$$\Delta = \langle \psi_\uparrow \psi_\downarrow \rangle. \tag{6.9}$$

Dark solitons in superfluid Fermi gases have been predicted to occur due to a jump in the phase of $\Delta(\mathbf{r})$ across a plane [46, 6, 93]. The field Δ therefore plays an analogous role in the description of solitons in Fermi superfluids to the macroscopic wavefunction ϕ in Bose superfluids. We can again write the order parameter in terms of its phase, $\Delta = |\Delta| e^{i\theta}$. As in the bosonic case, a phase jump of π is predicted to correspond to a stationary soliton [6]. The dynamics of solitons in Fermi superfluids have been studied using the Bogoliubov de Gennes mean-field equations [93, 138, 139]. The soliton oscillation period is expected to grow from the BEC limit (6.8) to $\sqrt{3}T_z$ at unitarity.

6.2 Creating Solitons by Phase Imprinting

We create solitons in superfluid Fermi gases by directly imprinting a phase jump onto the superfluid order parameter. A similar technique was used to create solitons in Bose-Einstein condensates [19]. The phase jump is imprinted by applying a conservative potential $U_G(\mathbf{r})$ for a short time t_p, using a pulse of a 532 nm (green) light. For sufficiently short pulse times, the kinetic energy of the gas is negligible, and the Heisenberg field operators pick up a phase factor,

$$\psi_\alpha(\mathbf{r}, t_p) = e^{-i U_G(\mathbf{r}) t_p} \psi_\alpha(\mathbf{r}, 0). \tag{6.10}$$

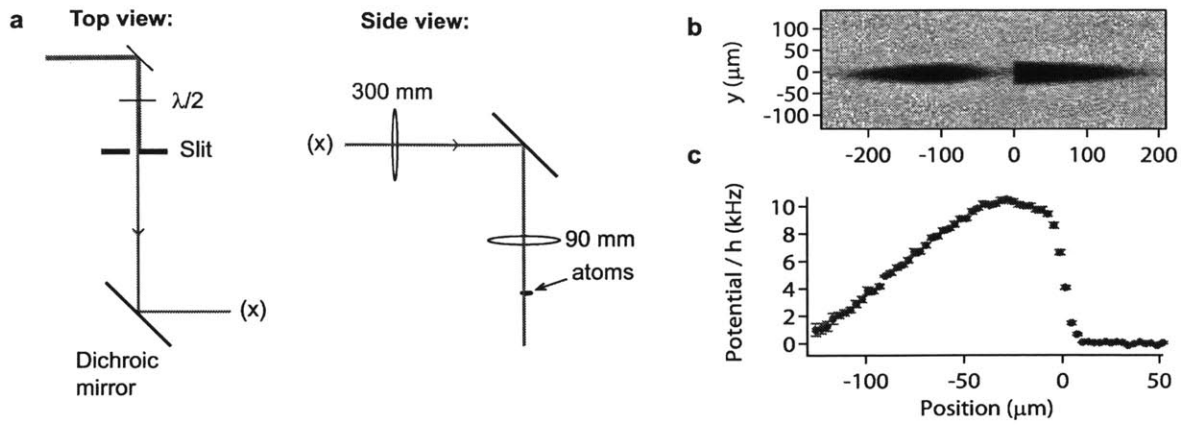

Figure 6-2: Phase-imprinting technique. **a**, Optical setup for preparing the phase-imprinting beam. **b**, Absorption image of an atomic gas loaded adiabatically into the phase-imprinting beam, showing the sharp change in the potential. **c**, Potential energy due to the phase-imprinting beam (scaled to full power) as a function of position in the axial direction.

The order parameter picks up twice the phase,

$$\Delta(\mathbf{r}, t) = e^{-2i\,U_G(\mathbf{r})t_p} \tag{6.11}$$

To generate a soliton, we use U_G with a sharp jump δU_G at the center of the atomic cloud. To create a soliton, the imprinted phase must meet three requirements. First, the duration t_p of the pulse must be sufficiently short so that the gas cannot respond during the pulse. The pulse duration should therefore be approximately h/μ or less, where μ is the chemical potential. For typical atomic densities near the Feshbach resonance this gives about 50 μs. The second condition is that the jump in the applied potential must occur over a length scale l_G on the order of or smaller than the coherence length of the superfluid, a few micrometers. Finally, the total phase difference $2\delta U_G t_p$ must be on the order of π in order to generate a deep soliton. Numerical simulations of the GP equation show that creating solitons by phase imprinting is not 100% efficient. The soliton depth achieved is always less than one would expect based on the applied phase. The efficiency increases as l_G and t_p are decreased. A low efficiency can be somewhat compensated by increasing the strength of the applied potential U_G, although at the cost of creating multiple solitons and

sound waves.

Figure 6-2.a shows the optical setup for phase imprinting. A sharp jump in the phase-imprinting beam intensity is created by blocking half of the beam with an adjustable metal slit. The slit is imaged onto the atoms using a high-resolution imaging system. The imaging system is shared with the 671 nm light used for measuring the atomic density distribution, described in Section 3.2. Figure 6-2.b shows an absorption image of the atomic cloud loaded adiabatically into the green light potential $U_G(\mathbf{r})$. The sharp jump in density indicates the sharp jump in the potential. Using lower light intensities to keep the atomic density finite, we measure the potential energy created by the green light, employing a method similar to that described in Section 3.3. Figure 6-2.c shows the measured potential, scaled up to full intensity.

The imprinting process creates two sound waves, as well as one or more dark solitons. The sound waves propagate to the edges of the cloud and vanish, while the dark soliton(s) remain. We use pulses that are sufficiently weak to create only a single long-lived soliton. For our setup, this corresponds to pulse times of about 30-50 μs, and an imprinted phase of about 1.0 to 1.6 π. Due to the imperfect efficiency of phase imprinting, although the applied phase is greater than π, the phase jump remaining after the soliton has formed is still less than π. For example, as we reduce the pulse time to zero, the initial velocity of the soliton monotonically increases until no soliton is created.

For these experiments, we prepare a superfluid gas of fermionic ^{6}Li atoms in an equal mixture of the lowest two hyperfine states, with 2×10^5 to 5×10^5 atoms per state. The scattering length is tuned by varying the total magnetic field in the vicinity of a broad s-wave Feshbach resonance centered at 832 G. We find that soliton creation is more efficient in the BEC regime, so for measurements at fields $B < 760$ G we first apply a phase imprinting pulse at 760 G and then ramp the magnetic field up to the final field over about two trapping periods.

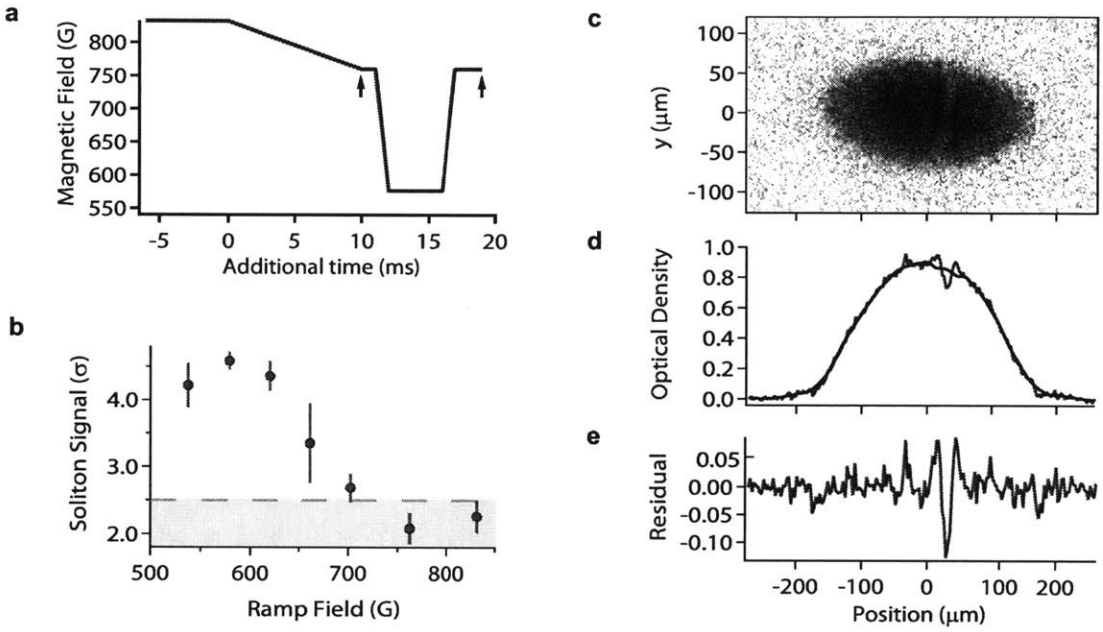

Figure 6-3: Detection of solitons in a superfluid Fermi gas. **a**, Magnetic field ramps used for imaging solitons using the rapid-ramp technique. **b**, Soliton signal (residual depth) normalized by the standard deviation of background fluctuations, versus the rapid-ramp field. **c**, Absorption image of an atomic cloud containing a soliton, after rapid-ramp. **d**, Integrated optical density (red) and running average (black), from the image in (**c**). **e**, Difference between the integrated optical density and its running average (residual).

6.3 Detection of Solitons

Because of the small width of the soliton plane, we cannot observe solitons *in situ*. We increase the length scale and density depletion (depth) of the soliton by ramping the total magnetic field into the deep BEC regime, and turning off the trapping potential to allow the cloud to expand. A similar method has been applied to observe vortices in superfluid Fermi gases [170]. Ramping to the BEC regime converts Cooper pairs into tightly bound, weakly-interacting molecules, and increases the coherence length. The magnetic field ramps used for detecting solitons are shown in Fig. 6-3.a. After a few ms of expansion in the deep BEC regime, we then ramp the magnetic field to 760 G for imaging. Fig. 6-3.b shows the strength of the observed soliton signal relative to the background fluctuations as a function of the magnetic field used to access the deep BEC regime. We use 577 G, where the signal is maximized.

We image parallel to the plane of the soliton and detect the soliton as a reduction in the column density along a line, as shown in Fig. 6-3.c. To extract the position of the soliton plane, we integrate the column density to obtain a one-dimensional density (Fig. 6-3).d. The one-dimensional density is then filtered using a running average (black curve in Fig. 6-3.d). We subtract the running average from the one-dimensional density to obtain a residual (Fig. 6-3.e). The minimum value of the residual indicates the position of the soliton.

6.4 Measurement of the Soliton Oscillation Period

We track the position of the soliton as a function of time, observing several oscillations in the trap (Fig. 6-4). In some cases, in addition to sinusoidal motion, we observe an increase in the oscillation amplitude over time (Fig. 6-5.a). The position at each time is extracted and fit to a sinusoidal function with exponentially increasing amplitude. The oscillation period determined from the fit is shown in Fig. 6-6, normalized by the trap period T_z. We use three different trapping frequencies $\nu_z = 5$, 10, and 22 Hz, to check for systematic effects. Within each class of trapping frequencies, the precise

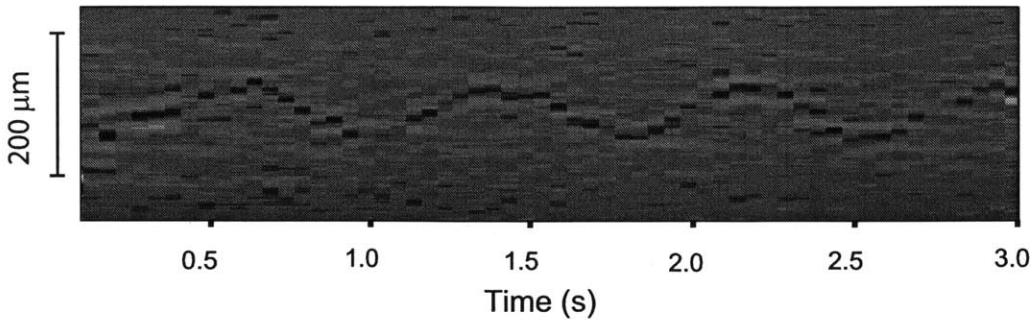

Figure 6-4: Periodic oscillation of a dark soliton in a superfluid Fermi gas. Shown is a false-color image of the density residual as a function of time. Each column of pixels comes from a different run of the experiment. The example shown here is taken at 760 G, with $k_F a = 1.4(1)$

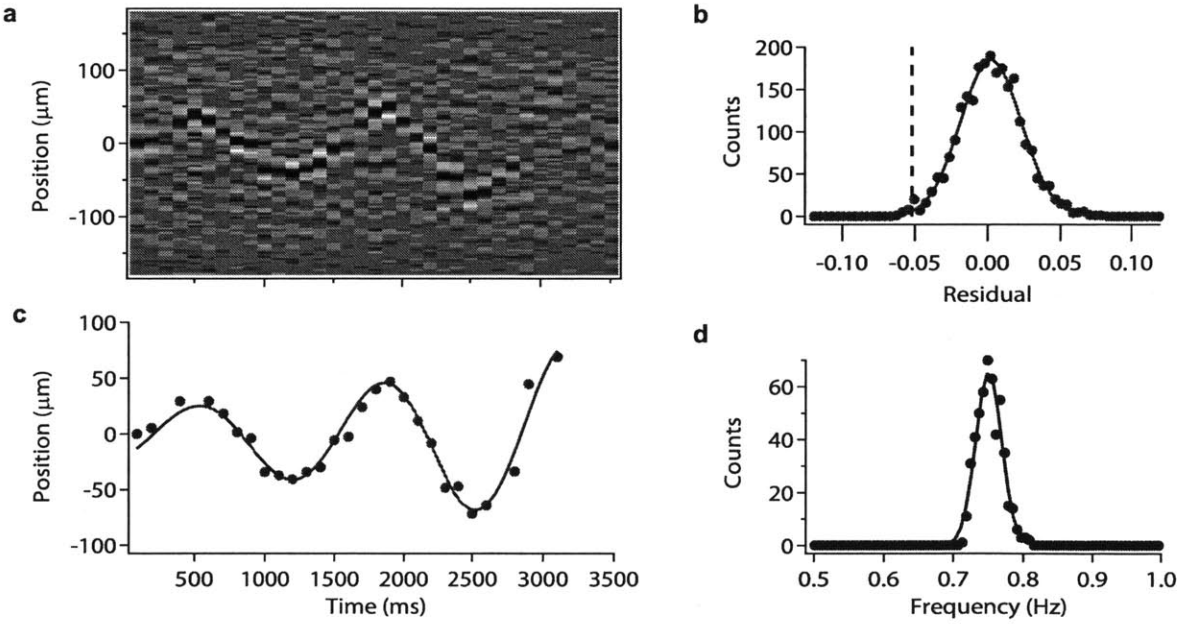

Figure 6-5: Measurement of dark soliton oscillation period. (**a**) Shows an example of a dark soliton in a unitary Fermi gas. Dissipation causes an observable increase in the oscillation amplitude. To identify solitons, we require that the density residual be less than a critical value of -2.5σ, where σ is the standard deviation of the residual due to background fluctuations. (**b**) shows a histogram of the background fluctuations. The vertical dashed line shows -2.5σ. The positions extracted from (**a**) are shown in (**c**) along with a fit to determine the oscillation period. (**d**) shows a histogram of the fitted oscillation frequency determined using bootstrap resampling.

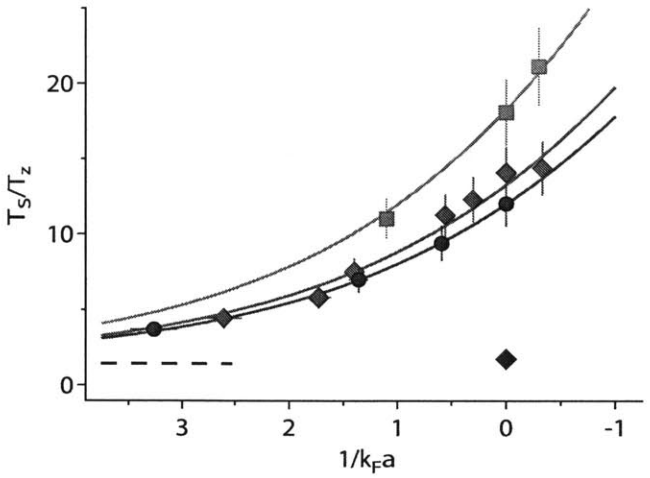

Figure 6-6: Dark soliton oscillation period as a function of interaction strength, normalized by the trapping period T_z. Data are shown for three different trapping frequencies, 22 Hz (orange), 10 Hz (red), and 5 Hz (black). Dashed line: BEC limit of $\sqrt{2}$. Purple diamond: mean-field prediction at unitarity of $\sqrt{3}$. The 10 Hz (red) points at $1/k_Fa$ =1.7,1.4,0.56, and 0 are averages over several measurements. The vertical and horizontal error bars show 12.3% and 6.6% error, respectively, coming from the standard deviation of five measurements at 760 G.

value of the trapping frequency varies slightly depending on the total magnetic field used. For example, in the 10 Hz class, the trapping frequency is 10.22(2) Hz at 700 G and 10.87(1) Hz at 832 G. We measure the trapping frequencies precisely for each magnetic field by exciting a center of mass oscillation, and normalize by the trapping frequency measured at each field.

We see that the oscillation period greatly exceeds the predictions of mean-field theory. At unitarity, for the 5 Hz trap, we observe $T_s/T_z = 12(2)$, a factor of 7 greater than the predicted value of $\sqrt{3}$. The 10 Hz and 22 Hz traps give $T_s/T_z = 14(2)$ and 18(2), respectively. The farthest point on the BEC side has $1/k_Fa = 3.3(2)$ and $T_s/T_z = 3.7(5)$, a factor of 2.6(4) higher than the BEC limit of $\sqrt{2}$. The closer mutual agreement between values measured at trapping frequencies of 5 and 10 Hz compared to values measured at 10 and 22 Hz suggest that the 5 Hz measurements are close to the limit of a highly-elongated cloud.

Although our measurements disagree with mean-field theory quantitatively, one thing is consistent: the soliton oscillation period increases going from the BEC limit

to unitarity. The physics behind this increases offers a clue as to what causes the extremely large oscillation periods seen here. In mean-field theory, the increase in the oscillation period is due to the soliton gaining mass as it "fills up" with localized fermionic excitations (Andreev bound states) [6, 139]. However, mean-field theory misses a second class of excitations, bosonic excitations of the order parameter due to quantum fluctuations.

To approach this problem, one can first consider the case of a strongly-interacting Bose gas. Indeed, even on the BEC-side of the Feshbach resonance ($1/a > 0$), we see significant enhancement of the oscillation period relative to the mean-field prediction. In a Bose gas, the dynamics of the order parameter couple to quantum fluctuations of the field operator, $\psi - \langle\psi\rangle$. Fluctuation modes localized at the soliton are predicted to occur [52, 47, 48]. Significant occupation of these modes may account for the observed enhancement of the oscillation period. The equations coupling these modes to the order parameter are similar to the coupled equations for bright-dark solitons in BECs [20], where long oscillation periods have also been observed [11]. The quantum fluctuations may therefore act like a second species of atoms, as in the dark-bright soliton case, to fill up the soliton and slow it down.

Chapter 7

Conclusion

We have performed experiments studying several new phenomena in strongly-interacting Fermi gases. Spin transport has been measured over a wide range of temperatures and interaction strengths. The spin transport coefficients are seen to attain universal limiting values in degenerate gases at unitarity, with the spin diffusivity reaching a minimum value of 6.3(3) $\hbar/m$. These measurements have provided new tests of theoretical descriptions of strongly-interacting Fermi gases. In a second set of measurements we studied the evolution of fermion pairing from three to two dimensions. We observed the dependence of the pair binding energy on the confinement along one direction. Deviations from the two-body binding energy provided a novel probe of beyond-mean-field physics. We have also studied the lineshapes of the pair dissociation spectra, showing the anomalously strong sensitivity to short-range physics in 2D. In a third set of measurements, we produced dark soliton excitations in a superfluid Fermi gas. We measured the oscillation period of solitons in trapped gases and found them to exceed theoretical predictions by an order of magnitude. This unexpected behavior suggests that quantum fluctuations localized in the soliton plane strongly modify the soliton mass. These observations should allow sensitive tests of theories beyond the mean-field level.

Appendix A

Universal Spin Transport in a Strongly Interacting Fermi Gas

This appendix contains a reprint of Ref. [145]: Ariel Sommer, Mark Ku, Giacomo Roati, and Martin W. Zwierlein, *Universal Spin Transport in a Strongly Interacting Fermi Gas*, Nature **472**, 201-204 (2011).

LETTER

doi:10.1038/nature09989

Universal spin transport in a strongly interacting Fermi gas

Ariel Sommer[1,2,3], Mark Ku[1,2,3], Giacomo Roati[4,5] & Martin W. Zwierlein[1,2,3]

Transport of fermions, particles with half-integer spin, is central to many fields of physics. Electron transport runs modern technology, defining states of matter such as superconductors and insulators, and electron spin is being explored as a new carrier of information[1]. Neutrino transport energizes supernova explosions following the collapse of a dying star[2], and hydrodynamic transport of the quark–gluon plasma governed the expansion of the early Universe[3]. However, our understanding of non-equilibrium dynamics in such strongly interacting fermionic matter is still limited. Ultracold gases of fermionic atoms realize a pristine model for such systems and can be studied in real time with the precision of atomic physics[4]. Even above the superfluid transition, such gases flow as an almost perfect fluid with very low viscosity when interactions are tuned to a scattering resonance[3,5–8]. In this hydrodynamic regime, collective density excitations are weakly damped[6,7]. Here we experimentally investigate spin excitations in a Fermi gas of ^{6}Li atoms, finding that, in contrast, they are maximally damped. A spin current is induced by spatially separating two spin components and observing their evolution in an external trapping potential. We demonstrate that interactions can be strong enough to reverse spin currents, with components of opposite spin reflecting off each other. Near equilibrium, we obtain the spin drag coefficient, the spin diffusivity and the spin susceptibility as a function of temperature on resonance and show that they obey universal laws at high temperatures. In the degenerate regime, the spin diffusivity approaches a value set by $\hbar/m$, the quantum limit of diffusion, where $\hbar$ is Planck's constant divided by 2π and m the atomic mass. For repulsive interactions, our measurements seem to exclude a metastable ferromagnetic state[9–11].

Understanding the transport of spin, as opposed to the transport of charge, is highly relevant to the novel field of spintronics[1]. Whereas charge currents are unaffected by electron–electron scattering owing to momentum conservation, spin currents are intrinsically damped owing to collisions between electrons of opposite spin, as their relative momentum is not conserved. This phenomenon is known as spin drag[12,13]. It is expected to contribute significantly to the damping of spin currents in doped semiconductors[14]. The random collision events also lead to spin diffusion—the tendency for spin currents to flow in such a way as to even out spatial gradients in the spin density—which has been studied in high-temperature superconductors[15] and in liquid ^{3}He–^{4}He mixtures[16,17].

Creating spin currents poses a major challenge in electronic systems, where mobile spins are scattered by their environment and by each other. However, in ultracold atomic gases, we have the freedom to first prepare an essentially non-interacting spin mixture, separate atoms spatially by using magnetic field gradients, and only then induce strong interactions. Past observations of spin currents in ultracold Fermi gases[18,19] were made in the weakly interacting regime. Here we access the regime near a Feshbach resonance[4], where interactions are as strong as allowed by quantum mechanics (the unitarity limit). We measure spin transport properties, namely the spin drag coefficient Γ_{sd} and the spin diffusivity D_s, of a strongly interacting Fermi gas composed of an equal number of atoms in two different spin states. In the strongly interacting regime, spin drag is expected to reach a universal maximum value, and spin diffusion is expected to reach a universal minimum.

The universal behaviour of the spin transport coefficients of a Fermi gas can be estimated on general grounds. At the Feshbach resonance, the scattering cross-section σ between atoms of opposite spin is given by the square of the de Broglie wavelength. In the degenerate regime (that is, below the Fermi temperature T_F) $\sigma \approx 1/k_F^2$, where $k_F = (6\pi^2 n)^{1/3}$ is the Fermi wavevector and n is the density of atoms in each spin state. The mean free path between collisions is thus $l = 1/(n\sigma) \approx 1/k_F$, or about one interparticle spacing, which is the smallest possible mean free path in a gas. The average speed v of atoms is of the order of the Fermi velocity, $\hbar k_F/m$. In estimating the spin diffusivity $D_s \approx vl$, the density-dependent factors cancel, giving $D_s \approx \hbar/m$. This value for D_s represents a universal quantum limit to spin diffusivity in Fermi gases. Away from resonance, the scattering cross-section decreases, increasing D_s. For temperatures T much greater than T_F, the scattering cross-section will be given by the square of the thermal de Broglie wavelength, and thus decreases as $\sigma \propto 1/T$. The velocity, in turn, will increase as $v \propto \sqrt{T}$, causing D_s to increase as $D_s \propto T^{3/2}$. An analogous scaling argument applies to the viscosity[7,8]. Finally, in a degenerate Fermi gas, the average velocity will remain of the order of the Fermi velocity, but the effective scattering cross-section will scale as $\sigma \propto T^2$ owing to Pauli blocking, causing D_s to increase as T^{-2} as the temperature is lowered. For a Fermi gas, we thus expect the minimum D_s to occur near T_F, before Pauli blocking becomes effective. Correspondingly, the coefficient Γ_{sd} characterizing spin drag is expected to reach a universal maximum value, given by the Fermi rate $E_F/\hbar$, where $E_F = \hbar^2 k_F^2/2m$ is the Fermi energy.

In our experiment, we prepare an equal mixture of the two lowest hyperfine states ('spin up' and 'spin down') of fermionic ^{6}Li in a cylindrically symmetric atom trap[4,20,21]. The confinement along the axis of symmetry is harmonic, with frequency ω_z. We separate the two spin components along the axis of symmetry of the trap (see Methods Summary), and turn on strong interactions between unequal spins by quickly increasing the magnetic field to a Feshbach resonance located at 834 G. The confining potential of the trap forces the two clouds of opposite-spin atoms to propagate towards each other, establishing a spin current. Measurements are made by selectively imaging the two spin components.

Figure 1 shows the collision between the two spin domains on resonance. The clouds bounce off each other and essentially completely repel each other. Owing to the axial trapping potential, the clouds return after the collision, and we observe several oscillations in the displacement $d = \langle z_\uparrow \rangle - \langle z_\downarrow \rangle$, where $\langle z_{\uparrow(\downarrow)} \rangle$ is the centre of mass of the spin-up (spin-down) cloud. After the oscillations have decayed, the displacement decreases to zero monotonically, on a timescale of the

[1]Department of Physics, Massachusetts Institute of Technology, Cambridge, Massachusetts 02139, USA. [2]MIT-Harvard Center for Ultracold Atoms, Massachusetts Institute of Technology, Cambridge, Massachusetts 02139, USA. [3]Research Laboratory of Electronics, Massachusetts Institute of Technology, Cambridge, Massachusetts 02139, USA. [4]INO-CNR, University of Florence, 50019 Sesto Fiorentino, Italy. [5]LENS, University of Florence, 50019 Sesto Fiorentino, Italy.

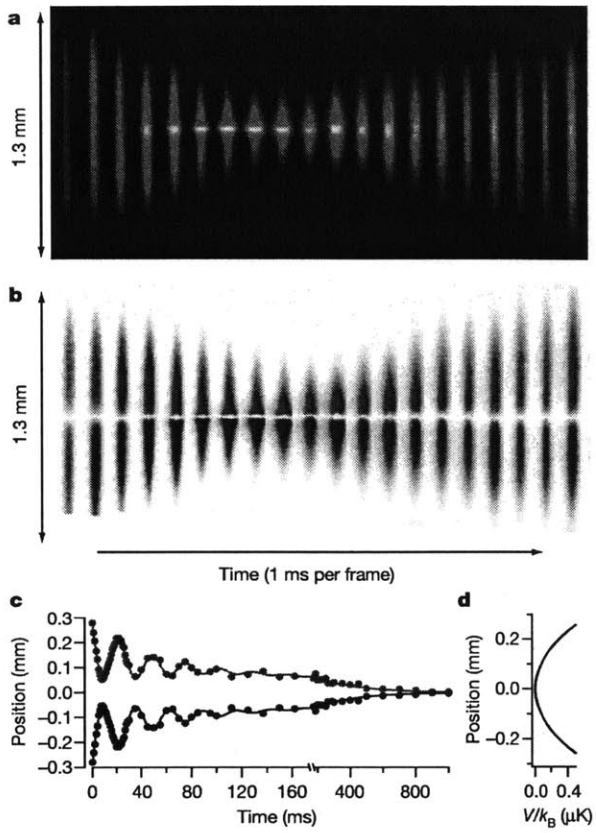

Figure 1 | Observation of spin current reversal in a resonant collision between two oppositely spin-polarized clouds of fermions. a, b, Total column density (**a**) and the difference in column densities (**b**: red, spin up; blue, spin down) during the first 20 ms after the collision. The central column densities here are typically 7×10^9 cm^{-2}. Strong repulsion is observed that leads to a high-density interface. **c,** The centre of mass separation initially oscillates at 1.63(2) times the axial trap frequency of 22.8 Hz (see Supplementary Information) before decaying exponentially at later times. The initial atom number per spin state is 1.2×10^6, and the temperature 200 ms after the collision and later is $0.5T_F$, with T_F the Fermi temperature at the centre of each cloud. **d,** The trapping potential V is harmonic along the symmetry axis.

order of one second, which is an extremely long time compared to the trapping period (44 ms). The underlying explanation for spin current reversal and the slow relaxation can be found in the extremely short mean free path and the high collision rate between opposite-spin atoms at unitarity. According to the above estimate, the spin diffusivity is approximately $\hbar/m$, which for ^{6}Li is (100 μm)^2 s^{-1}. The atom clouds in the experiment have a length of the order of 100 μm, and it takes them of the order of a second to diffuse through each other. So we are indeed observing quantum-limited spin diffusion. The initial bounces will occur when the mean free path of a spin-up atom in the spin-down cloud is smaller than the spin-down cloud size, that is, when the mixture is hydrodynamic. Instead of quickly diffusing into the spin-down region, it is then more likely that the spin-up atom is scattered back into the spin-up region, where it can propagate ballistically.

After long evolution times, the oscillations shown in Fig. 1 have been damped out, and the displacement between the centres of mass is much smaller than the widths of the clouds. The relaxation dynamics can then be described by linear response theory, giving access to the spin transport coefficients. The spin drag coefficient Γ_{sd} is defined as the rate of momentum transfer between opposite-spin atoms[12,14], and is therefore related to the collision rate. From the Boltzmann transport equation, the relaxation of the displacement d near equilibrium follows the differential equation[22]

$$\Gamma_{sd}\dot{d} + \omega_z^2 d = 0$$

in the case of strongly overdamped motion realized here. Fitting an exponential with decay time τ to the displacement gives the spin drag coefficient of the trapped system as $\Gamma_{sd} = \omega_z^2\tau$. In the deeply degenerate regime, the relationship between the measured and the microscopic spin drag coefficient might be affected by a weak enhancement of the effective mass[23] and the attractive interaction energy between the clouds[10,22,24].

The spin drag coefficient is found to be greatest on resonance, and thus spin conduction is slowest on resonance (see Supplementary Information). On resonance, Γ_{sd} in a homogeneous system must be given by a function of the reduced temperature T/T_F times the Fermi rate $E_F/\hbar$. At high temperatures, we expect the spin drag coefficient to obey a universal scaling $\Gamma_{sd} \propto n\sigma v \propto \frac{E_F}{\hbar}(T/T_F)^{-1/2}$. In Fig. 2 we show the spin drag coefficient as a function of T/T_F; Γ_{sd} is normalized by $E_F/\hbar$, where E_F and T_F are the local values at the centre of total mass. We observe $T^{-1/2}$ scaling for $T/T_F > 2$, finding $\Gamma_{sd} = 0.16(1)\frac{E_F}{\hbar}(T/T_F)^{-1/2}$. At lower temperatures, we observe a crossover from classical to non-classical behaviour as the spin drag coefficient reaches a maximum of approximately $0.1E_F/\hbar$ near the Fermi temperature. We interpret this saturation of the spin drag coefficient as a consequence of Fermi statistics and unitarity[4,5], as σ and v approach values determined by the Fermi wavevector k_F. The spin drag coefficient is inversely proportional to the spin conductivity, which describes the spin current response to an external spin-dependent force. Near the Fermi temperature, the maximum spin drag coefficient corresponds to a minimum spin conductivity of the order of $k_F/\hbar$. This is the slowest spin conduction possible in three dimensions in the absence of localization.

At low temperatures, the spin drag coefficient decreases with decreasing temperature. Reduced spin drag at low temperatures is expected in Fermi liquids owing to Pauli blocking[11,18,22,24,25], and is also expected in one-dimensional Fermi gases[26]. In the case of collective density (rather than spin) excitations, it was shown that pairing correlations enhance the effective collision rate dramatically as the temperature is lowered[6]. The effect of pairing on the spin drag coefficient may be qualitatively different. In a simple picture, spin currents require the flow of unpaired atoms, whereas collective density excitations affect paired and unpaired atoms alike.

Comparing the relaxation rate to the gradient in spin density allows us to also measure the spin diffusivity D_s. At the centre of the trap, the spin current density J_s is given by the spin diffusion equation[27]

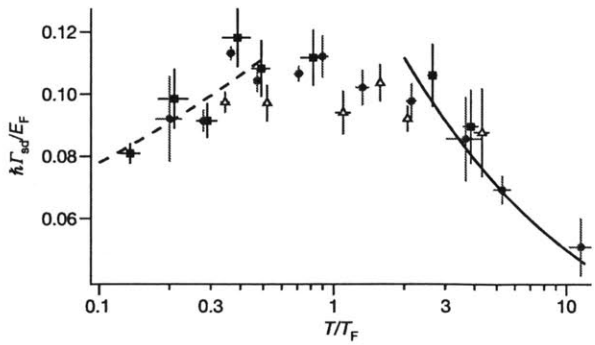

Figure 2 | Spin drag coefficient of a trapped Fermi gas with resonant interactions. The spin drag coefficient Γ_{sd} is normalized by the Fermi rate $E_F/\hbar$ at the trap centre, whereas the temperature is normalized by $T_F = E_F/k_B$. We find agreement between measurements taken at three different axial trapping frequencies, 22.8 Hz (red circles), 37.5 Hz (blue triangles) and 11.2 Hz (black squares). The data for $T/T_F > 2$ fit to a $T^{-1/2}$ law (solid line). Dashed line, a power law fit for $T/T_F < 0.5$ to show the trend. Each point is a mean from typically three determinations of Γ_{sd}, each obtained from a time series of about 30 experimental runs and weighted according to the standard deviation from fitting error and shot to shot fluctuations. Error bars, ±1s.e.

$$J_s = -D_s \frac{\partial(n_\uparrow - n_\downarrow)}{\partial z}$$

where $n_{\uparrow(\downarrow)}$ is the density of spin-up (spin-down) atoms. We calculate J_s using the trap-averaged velocity as $J_s = \frac{1}{2}(n_\uparrow + n_\downarrow)\dot{d}$, where the densities are evaluated at the centre of total mass.

We find that the spin diffusivity is at a minimum when interactions are resonant (see Supplementary Information). The increase in spin diffusivity for positive scattering length a, as well as the decrease in spin drag, argues against the existence of a ferromagnetic state in repulsive Fermi gases, for which diffusion should stop entirely[9,11]. Figure 3 reports the measured spin diffusivity as a function of temperature at unitarity. In the high-temperature limit on resonance, one expects $D_s \propto v/n\sigma \propto T^{3/2}$. At high temperatures, we indeed find this temperature dependence, with a fit giving $D_s = 5.8(2)\frac{\hbar}{m}(T/T_F)^{3/2}$ for $T/T_F > 2$. In the degenerate regime, the spin diffusivity is seen to attain a limiting value of $6.3(3)\hbar/m$.

When comparing these results to theoretical calculations, it is important to account for the inhomogeneous density distributions and velocity profiles. For a homogeneous system on resonance, and at high temperatures compared to the Fermi temperature, we predict $D_s = 1.11\frac{\hbar}{m}(T/T_F)^{3/2}$ and $\Gamma_{sd} = 0.90\frac{E_F}{\hbar}(T/T_F)^{-1/2}$ (see Supplementary Information). The measured spin drag coefficient is smaller by a factor of 0.90/0.16(1) = 5.6(4) while the spin diffusivity is larger by about the same factor, 5.8(2)/1.11 = 5.3(2), compared to a homogeneous system at the density of the centre of total mass. These factors reflect the inhomogeneity of the system and agree with an estimate from the Boltzmann transport equation (see Supplementary Information). The emergence of a superfluid core at our lowest temperatures will further modify the ratio of trap-averaged to local transport coefficients.

Finally, the measured transport coefficients give for the first time access to the temperature dependence of the spin susceptibility, $\chi_s(T)$, in strongly interacting Fermi gases. Defined as $\chi_s = \frac{\partial(n_\uparrow - n_\downarrow)}{\partial(\mu_\uparrow - \mu_\downarrow)}$, the spin susceptibility describes the spin response to an infinitesimal effective magnetic field or chemical potential difference $\mu_\uparrow - \mu_\downarrow$ applied to the gas, and is a crucial quantity that can discriminate between different states of matter[10]. In a magnetic field gradient, particles with opposite spin are forced apart at a rate determined by the spin conductivity σ_s, while diffusion acts to recombine them. The balance between the processes of diffusion and conduction therefore determines the resulting magnetization gradient, a connection expressed in the Einstein relation[11] $\chi_s = \sigma_s/D_s$. Assuming the standard relation[11,14] $\sigma_s = n/(m\Gamma_{sd})$,

$$\chi_s = \frac{1}{md\omega_z^2}\frac{\partial(n_\uparrow - n_\downarrow)}{\partial z}$$

where $\frac{\partial(n_\uparrow - n_\downarrow)}{\partial z}$ is evaluated near the trap centre. The inhomogeneous trapping potential does not affect the measurement of χ_s in the hydrodynamic limit at high temperatures (see Supplementary Information). Close to the transition to superfluidity, interaction effects may modify the relation between σ_s and Γ_{sd}.

Figure 4 reports our findings for the spin susceptibility at unitarity, as a function of the dimensionless temperature T/T_F. At high temperatures, we observe the Curie law $\chi_s = n/(k_B T)$, where k_B is Boltzmann's constant. In this classical regime of uncorrelated spins, the susceptibility equals the (normalized) compressibility of the gas $n^2\kappa = \partial n/\partial\mu$ that we also directly obtain from our profiles. At degenerate temperatures, the measured spin susceptibility becomes smaller than the normalized compressibility. This is expected for a Fermi liquid, where $\chi_s = \frac{3n}{2E_F}\frac{1}{1+F_0^a}$ and $\kappa = \frac{3}{2nE_F}\frac{1}{1+F_0^s}$ with Landau parameters F_0^s and F_0^a describing the density (s) and spin (a) response[10]. The spin susceptibility is expected to strongly decrease at sufficiently low temperatures in the superfluid phase, as pairs will form that will not break in the presence of an infinitesimal magnetic field. It is currently debated whether the strongly interacting Fermi gas above the superfluid transition temperature is a Fermi liquid[23] or a state with an excitation gap (pseudogap)[28,29]. The opening of a gap in the excitation spectrum would be revealed as a downturn of the spin susceptibility below a certain temperature. Such a downturn is not observed in χ_s down to $T/T_F \approx 0.2$, and therefore our spin susceptibility data agree down to this point with the expected behaviour for a Fermi liquid.

In conclusion, we have studied spin transport in strongly interacting Fermi gases. The spin diffusivity was found to attain a limiting value of about $6.3\hbar/m$, establishing the quantum limit of diffusion for strongly interacting Fermi gases. Away from resonance, the diffusivity increases.

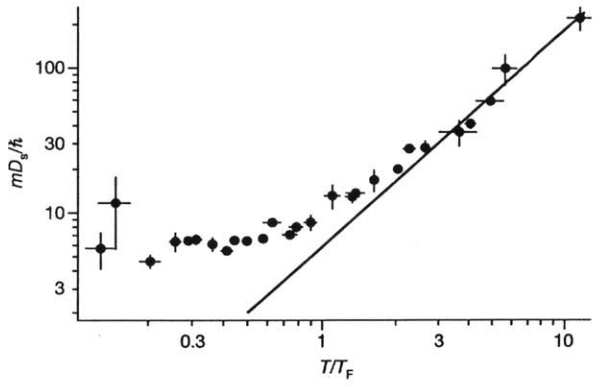

Figure 3 | Spin diffusivity of a trapped Fermi gas. Shown is the spin diffusivity on resonance (D_s, normalized by $\hbar/m$; filled circles) as a function of the dimensionless temperature T/T_F. At high temperatures, D_s obeys the universal $T^{3/2}$ behaviour (solid line). At low temperatures, D_s approaches a constant value of $6.3(3)\hbar/m$ for temperatures below about $0.5T_F$, establishing the quantum limit of spin diffusion for strongly interacting Fermi gases. Error bars, ±1s.e.

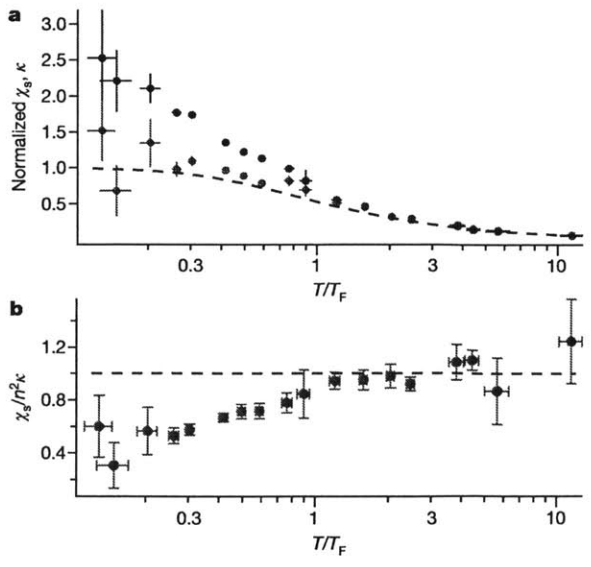

Figure 4 | Spin susceptibility on resonance. **a**, Spin susceptibility (χ_s, open red circles) and isothermal compressibility (κ, filled blue circles), normalized by the values for an ideal Fermi gas at zero temperature. For temperatures below T_F, χ_s becomes suppressed relative to κ, owing to interactions between opposite-spin atoms. Dashed line, χ_s of a non-interacting Fermi gas for comparison. **b**, Red circles, χ_s divided by the value of $n^2\kappa$ obtained from the same clouds. At temperatures above T_F, the ratio of χ_s to $n^2\kappa$ approaches unity (dashed line). Error bars, ±1s.e.

This casts doubt on the possibility of stabilizing a ferromagnetic gas on the repulsive side of the Feshbach resonance[9], which would require a vanishing diffusivity[11]. The observed slow relaxation of spin excitations is a likely explanation for the surprising—possibly non-equilibrium[27]—profiles in spin-imbalanced Fermi gases reported in ref. 30, which did not agree with equilibrium measurements by other workers[20,21,31]. Our measurements of the temperature dependence of the spin susceptibility are consistent with a Fermi liquid picture, and do not reveal a pseudogap. An interesting subject for further study is whether spins are still able to diffuse through the superfluid, or whether they travel around it, avoiding the superfluid owing to the pairing gap.

METHODS SUMMARY

The spin mixture is initially prepared at 300 G. To separate the spin components, we reduce the magnetic field to 50 G, where the magnetic moments of the two spin states are unequal, and apply two magnetic field gradient pulses. We then bring the total magnetic field to the Feshbach resonance in about 2 ms.

To reach low temperatures during the approach to equilibrium, evaporative cooling is applied, at 834 G, by gradually lowering the depth of the optical dipole trap. To reach high temperatures, we heat the atoms by switching off the optical dipole trap for up to 3 ms to allow the atom clouds to expand before recapturing them. We then set the final depth of the dipole trap so that the atom number and the temperature remain nearly constant during the approach to equilibrium.

Spin selective imaging is performed by means of *in situ* absorption or phase contrast imaging using two 4-μs imaging pulses separated by 6 μs. These images give the column densities of each spin state, from which we obtain the three-dimensional densities by way of an inverse Abel transform[21]. The gradient in the spin density is obtained from a linear fit to the polarization versus z.

We determine the temperature of the clouds by fitting the density versus potential energy in the vicinity of $z = 0$ (but for all values of the radial coordinate r) to the equation of state of the unitary Fermi gas, measured recently by our group[32]. The trapping potential itself is determined by summing the densities of hundreds of clouds, using the known axial, harmonic trapping potential to convert equidensity lines to equipotential lines and fitting the result to an analytic model.

Received 4 January; accepted 4 March 2011.

1. Wolf, S. A. Spintronics: a spin-based electronics vision for the future. *Science* **294,** 1488–1495 (2001).
2. Burrows, A. Neutrinos from supernova explosions. *Annu. Rev. Nucl. Part. Sci.* **40,** 181–212 (1990).
3. Schäfer, T. & Teaney, D. Nearly perfect fluidity: from cold atomic gases to hot quark gluon plasmas. *Rep. Prog. Phys.* **72,** 126001 (2009).
4. Inguscio, M., Ketterle, W. & Salomon, C. (eds) *Ultracold Fermi Gases* (Proc. Int. School of Physics 'Enrico Fermi', Course CLXIV, IOS, 2008).
5. O'Hara, K. M., Hemmer, S. L., Gehm, M. E., Granade, S. R. & Thomas, J. E. Observation of a strongly interacting degenerate Fermi gas of atoms. *Science* **298,** 2179–2182 (2002).
6. Riedl, S. *et al.* Collective oscillations of a Fermi gas in the unitarity limit: temperature effects and the role of pair correlations. *Phys. Rev. A* **78,** 053609 (2008).
7. Cao, C. *et al.* Universal quantum viscosity in a unitary Fermi gas. *Science* **331,** 58–61 (2011).
8. Enss, T., Haussmann, R. & Zwerger, W. Viscosity and scale invariance in the unitary Fermi gas. *Ann. Phys.* **326,** 770–796 (2011).
9. Jo, G.-B. *et al.* Itinerant ferromagnetism in a Fermi gas of ultracold atoms. *Science* **325,** 1521–1524 (2009).
10. Stringari, S. Density and spin response function of a normal Fermi gas at unitarity. *Phys. Rev. Lett.* **102,** 110406 (2009).
11. Duine, R. A., Polini, M., Stoof, H. T. C. & Vignale, G. Spin drag in an ultracold Fermi gas on the verge of ferromagnetic instability. *Phys. Rev. Lett.* **104,** 220403 (2010).
12. D'Amico, I. & Vignale, G. Theory of spin Coulomb drag in spin-polarized transport. *Phys. Rev. B* **62,** 4853–4857 (2000).
13. Weber, C. P. *et al.* Observation of spin Coulomb drag in a two-dimensional electron gas. *Nature* **437,** 1330–1333 (2005).
14. D'Amico, I. & Vignale, G. Coulomb interaction effects in spin-polarized transport. *Phys. Rev. B* **65,** 085109 (2002).
15. Gedik, N., Orenstein, J., Liang, R., Bonn, D. A. & Hardy, W. N. Diffusion of nonequilibrium quasi-particles in a cuprate superconductor. *Science* **300,** 1410–1412 (2003).
16. Garwin, R. L. & Reich, H. A. Self-diffusion and nuclear relaxation in He^3. *Phys. Rev.* **115,** 1478–1492 (1959).
17. Anderson, A. C., Edwards, D. O., Roach, W. R., Sarwinski, R. E. & Wheatley, J. C. Thermal and magnetic properties of dilute solutions of He^3 in He^4 at low temperatures. *Phys. Rev. Lett.* **17,** 367–372 (1966).
18. DeMarco, B. & Jin, D. S. Spin excitations in a Fermi gas of atoms. *Phys. Rev. Lett.* **88,** 040405 (2002).
19. Du, X., Luo, L., Clancy, B. & Thomas, J. E. Observation of anomalous spin segregation in a trapped Fermi gas. *Phys. Rev. Lett.* **101,** 150401 (2008).
20. Zwierlein, M. W., Schirotzek, A., Schunck, C. H. & Ketterle, W. Fermionic superfluidity with imbalanced spin populations. *Science* **311,** 492–496 (2006).
21. Shin, Y., Zwierlein, M., Schunck, C., Schirotzek, A. & Ketterle, W. Observation of phase separation in a strongly interacting imbalanced Fermi gas. *Phys. Rev. Lett.* **97,** 030401 (2006).
22. Vichi, L. & Stringari, S. Collective oscillations of an interacting trapped Fermi gas. *Phys. Rev. A* **60,** 4734–4737 (1999).
23. Nascimbène, S., Navon, N., Jiang, K. J., Chevy, F. & Salomon, C. Exploring the thermodynamics of a universal Fermi gas. *Nature* **463,** 1057–1060 (2010).
24. Bruun, G. M., Recati, A., Petchick, C. J., Smith, H. & Stringari, S. Collisional properties of a polarized Fermi gas with resonant interactions. *Phys. Rev. Lett.* **100,** 240406 (2008).
25. Bruun, G. M. Spin diffusion in Fermi gases. *New J. Phys.* **13,** 035005 (2011).
26. Polini, M. & Vignale, G. Spin drag and spin-charge separation in cold Fermi gases. *Phys. Rev. Lett.* **98,** 266403 (2007).
27. Parish, M. M. & Huse, D. A. Evaporative depolarization and spin transport in a unitary trapped Fermi gas. *Phys. Rev. A* **80,** 063605 (2009).
28. Gaebler, J. P. *et al.* Observation of pseudogap behavior in a strongly interacting Fermi gas. *Nature Phys.* **6,** 569–573 (2010).
29. Perali, A. *et al.* Evolution of the normal state of a strongly interacting Fermi gas from a pseudogap phase to a molecular Bose gas. *Phys. Rev. Lett.* **106,** 060402 (2011).
30. Partridge, G. B., Li, W., Kamar, R. I., Liao, Y. & Hulet, R. G. Pairing and phase separation in a polarized Fermi gas. *Science* **311,** 503–505 (2006).
31. Nascimbène, S. *et al.* Collective oscillations of an imbalanced Fermi gas: axial compression modes and polaron effective mass. *Phys. Rev. Lett.* **103,** 170402 (2009).
32. Ku, M. *et al.* Equation of state of a strongly interacting atomic Fermi gas. *Bull. Am. Phys. Soc.* **55,** abstr. W6. 00001 (2010); available at ⟨http://meetings.aps.org/link/BAPS.2010.DAMOP.W6.1⟩ (2010).

Supplementary Information is linked to the online version of the paper at www.nature.com/nature.

Acknowledgements We thank G. Bruun, C. Pethick, D. Huse, R. Duine and W. Zwerger for discussions, and A. Schirotzek for help with the early stages of the experiment. This work was supported by the NSF, AFOSR-MURI, ARO-MURI, ONR, DARPA YFA, a grant from the Army Research Office with funding from the DARPA OLE programme, the David and Lucille Packard Foundation and the Alfred P. Sloan Foundation.

Author Contributions All authors contributed to the experimental work. A.S. analysed the data. M.K. developed the algorithm for thermometry. M.W.Z. performed theoretical calculations. A.S. and M.W.Z wrote the manuscript.

Author Information Reprints and permissions information is available at www.nature.com/reprints. The authors declare no competing financial interests. Readers are welcome to comment on the online version of this article at www.nature.com/nature. Correspondence and requests for materials should be addressed to A.S. (atsommer@mit.edu).

SUPPLEMENTARY INFORMATION

doi:10.1038/nature09989

Supplementary Discussion and Figures: Dependence on Interaction Strength

We study the dependence of the spin transport properties of the system on interaction strength by ramping to a variable field in the vicinity of the Feshbach resonance and measuring the subsequent evolution of the system. Supplementary Figure 1 shows the results of colliding two clouds at different fields, revealing the transition from transmission of the clouds through each other to reflection of the clouds as the mean free path becomes smaller than the cloud size. When the scattering length is set to zero (Sup. Fig. 1**a**), the center of mass separation oscillates at the trap frequency ω_z. On resonance (Sup. Fig. 1**g**), the observed oscillation frequency is $1.63(2)\,\omega_z$, where the error estimate is one standard deviation of fitting error from a fit to a phenomenological function. This frequency is intermediate between the frequency $1.55\,\omega_z$ of the axial breathing mode of a unitary Fermi gas in the hydrodynamic limit[1] and the non-interacting value of $2\,\omega_z$, as the system contains a hydrodynamic region at the center, and is non-interacting in the spin-polarized wings.

From Supplementary Figure 1 it is clear that the spin separation is most long-lived near resonance (Sup. Fig. 1**f-h**). There it is possible to measure the spin transport coefficients quantitatively after waiting for the oscillations in the center of mass separation to damp out. During that time, evaporative cooling is applied by reducing the depth of the optical dipole trap before raising it to an intermediate value and beginning the measurement. Data series are taken for cooling to two different trap depths. On resonance, the lower depth yields temperatures of $0.16(2)\,T_F$, and the higher depth yields temperatures of $0.32(1)\,T_F$, where T_F is the central Fermi temperature and the error estimates are one standard deviation. The spin drag coefficient exhibits a maximum on resonance (Sup. Fig. 2**a**), while the spin diffusivity is minimum on resonance (Sup. Fig. 2**b**). way from resonance, accurate thermometry becomes more difficult as the equation of state is not known. However, estimates from the edges of the clouds suggest that the temperature does not vary significantly for different fields at the higher trap depth, while at the lower trap depth the temperature is about $0.25\,T_F$ at $(k_F a)^{-1} = -0.6$ and 0.9. t each value of the interaction strength, the spin drag coefficient is found to be larger for the higher trap depth, where the temperature is higher, while the spin diffusion coefficient shows no significant temperature dependence.

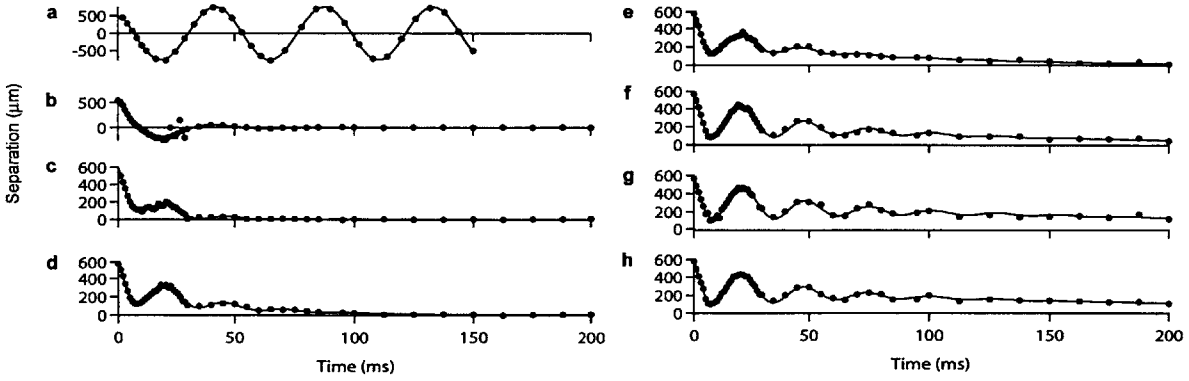

Supplementary Figure 1 | Collision between spin up and spin down clouds at varying interaction strength. After separating the spin components, the magnetic field was ramped to a variable value in the vicinity of the Feshbach resonance to reach different interaction strengths. The interaction parameter $k_F a$, with $k_F = (6\pi^2 n)^{1/3}$ and n the central density per spin component, was determined by averaging the values of k_F obtained for $t > 200$ ms of evolution time (not shown). The values of $k_F a$ are (**a**) 0, (**b**) 0.08, (**c**) 0.13, (**d**) 0.19, (**e**) 0.26, (**f**) 1.2, (**g**) ∞, and (**h**) -1.5. For $t > 200$ ms the temperature is about $0.5\,T_F$, with T_F the Fermi temperature at the center of each cloud. The initial atom number is about 1×10^6. The solid lines show phenomenological fits.

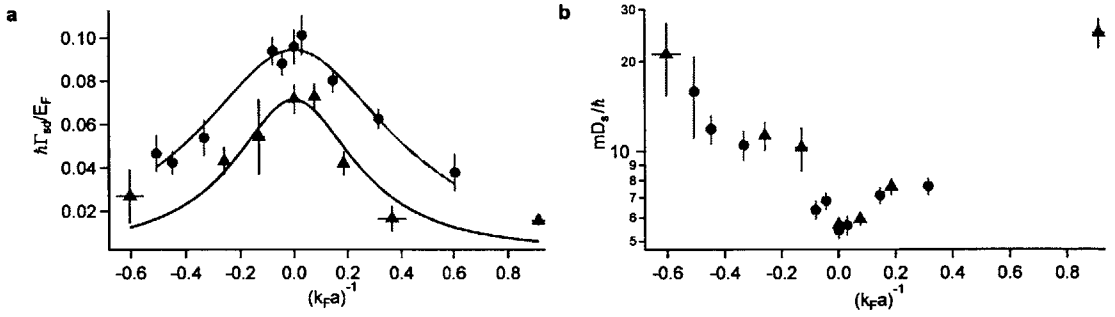

Supplementary Figure 2 | Spin transport coefficients across the Feshbach resonance. The system was evaporatively cooled to one of two different trap depths (blue triangles: lower trap depth, red circles: higher trap depth) before beginning the measurement. Temperature estimates are given in the text. **a**, spin drag coefficient and **b**, spin diffusivity, for varying interaction strength. The largest spin drag and smallest spin diffusivity occur at the Feshbach resonance, where $1/k_F a = 0$. The solid lines in **a** show Lorentzian fits. Each data point shows the result from one time series. Error bars show the standard deviation due to fitting error and shot to shot fluctuations within the time series.

Supplementary Methods

The experiment takes place in a trapping potential of the form

$$V(r,z) = \frac{1}{2}m\omega_z^2 z^2 + V_r(r),$$

where $r = \sqrt{x^2+y^2}$. Here z is the symmetry axis of the trap, and we image along the y axis. The radial potential $V_r(r)$ is the sum of a gaussian potential due to the optical dipole trap plus a weak quadratic anti-trapping potential from the magnetic field. The effective radial trapping frequency, defined using the aspect ratios of the atomic clouds, varies from 80 Hz at the low optical trap depths used for the low temperature measurements to 250 Hz at the high optical trap depths used for the high temperature measurements.

From each run of the experiment we obtain two-dimensional column densities $n_\sigma^{2\mathrm{d}}(x,z)$ of both spin states $\sigma = \uparrow, \downarrow$. Fitting a two-dimensional Gaussian to each column density provides a measurement of the center of mass of each spin state. We subtract the z components of the centers of mass of the two spin states to obtain the separation parameter $d = \langle z_\uparrow \rangle - \langle z_\downarrow \rangle$. The three-dimensional densities $n_\sigma(r,z)$ are obtained using a numerical implementation of the inverse Abel transformation[2]:

$$n_\sigma(r_i,z) = \sum_{j=i}^{j_{\max}} \frac{n_\sigma^{2\mathrm{d}}(x_{j+1},z) - n_\sigma^{2\mathrm{d}}(x_j,z)}{x_{j+1}-x_j} \ln\left[\frac{j+1+\sqrt{(j+1)^2-i^2}}{j+\sqrt{j^2-i^2}}\right],$$

For each line of constant z, the values of $n_\sigma(r_i,z)$ with small i are sensitive to noise in $n_\sigma^{2\mathrm{d}}(x_j,z)$ for small j. To reduce noise, we fit a one-dimensional Gaussian to $n_\sigma^{2\mathrm{d}}(x_j,z)$, for each value of z and for $j < 3$ (corresponding to $|x| < 7$ μm), and use this fit (with sub-resolution sampling to reduce discretization error) in the above formula.

The temperature is determined by analyzing the densities $n_\sigma(r,z)$ for $|z| < 60$ μm (as the 1/e radii of the clouds range from 100 to 400 μm, this restriction excludes the more polarized, large z, regions of the clouds). We obtain the temperature of each cloud by fitting the density versus potential energy V to

$$n = \lambda^{-3} f(\beta\mu - \beta V),$$

where $\beta = \frac{1}{k_B T}$, $\lambda = \sqrt{\frac{2\pi\hbar^2}{m k_B T}}$, T is the temperature, μ is the global chemical potential, and f is a universal function defining the equation of state of the unitary Fermi gas[3], with μ and T as the fit parameters. The equation of state function f was obtained by extending the third-order Virial expansion to low temperatures using measured density distributions in a known trapping potential[3].

Supplementary Equations: Measurement of Transport oefficients

Near equilibrium, d decays exponentially, and we fit the measured values to

$$d(t) = d_0 \mathrm{e}^{-t/\tau}.$$

The spin drag coefficient is then

$$\Gamma_{\mathrm{sd}} = \omega_z^2 \tau.$$

To non-dimensionalize this quantity we multiply by $\hbar$ and divide by the Fermi energy $E_F = \frac{\hbar^2}{2m}(6\pi^2 n(\vec{0}))^{2/3}$, where $n(\vec{0}) = (n_\uparrow(\vec{0}) + n_\downarrow(\vec{0}))/2$ is the average three-dimensional density at $(r, z) = (0, 0)$.

fter fitting to $d(t)$ to obtain τ, we obtain the spin diffusivity from each spin up-spin down image pair as

$$D_{\mathrm{s}} = \frac{n(\vec{0})d}{g\tau},$$

where $g = \frac{\partial(n_\uparrow - n_\downarrow)}{\partial z}|_{z=0,r=0}$ is the spin density gradient. The spin density gradient is obtained from the slope b of a linear fit to the polarization $p(z) = \frac{n_\uparrow - n_\downarrow}{n_\uparrow + n_\downarrow}$ as a function of z at $r = 0$ using the formula

$$g = b \cdot (n_\uparrow(\vec{0}) + n_\downarrow(\vec{0})).$$

The Einstein relation provides the spin susceptibility as

$$\begin{aligned}\chi_{\mathrm{s}} = \sigma_s / D_{\mathrm{s}} &= \frac{n(\vec{0})}{m\, D_{\mathrm{s}}\, \Gamma_{\mathrm{sd}}} \\ &= \frac{g}{m\, d\, \omega_z^2}.\end{aligned}$$

lthough derived using transport coefficients, the final expression for χ_{s} does not actually depend on the relaxation time τ, so it gives an independent value of χ_{s} from each run of the experiment.

We obtain the isothermal compressibility $\kappa = \frac{1}{n^2}\frac{\partial n}{\partial \mu}$ at the center of mass for near-equilibrium clouds within the local density approximation as

$$\kappa = -\frac{1}{mn^2\omega_z^2}\frac{\partial^2 n}{\partial z^2},$$

where the second derivative $\partial^2 n/\partial z^2$ of the density is determined from a Gaussian fit to $n(r = 0, z)$ from $z = 0$ to the half maximum.

Supplementary Equations: Relation to Homogeneous Values

The measured spin drag coefficient and spin diffusivity are related to the values for a homogeneous system through averages over the trapped cloud. Define the trap average of a function $G(\vec{r})$ of position $\vec{r}$ as

$$\langle G \rangle = \frac{1}{N}\int \mathrm{d}^3 r\, G(\vec{r})\, n(\vec{r}),$$

where $N = N_\uparrow = N_\downarrow$ and $n = \frac{1}{2}(n_\uparrow + n_\downarrow)$.

Near equilibrium, where $n \approx n_\uparrow \approx n_\downarrow$, the center of mass separation $d(t)$ evolves according to

$$\ddot{d} + \omega_z^2 d = -\langle \tilde{\Gamma}_{\mathrm{sd}} u_{z,\mathrm{rel}} \rangle = -\Gamma_{\mathrm{sd}} \dot{d},$$

where $u_{z,\mathrm{rel}}$ is the z component of the local relative velocity between spin up and spin down atoms and $\tilde{\Gamma}_{\mathrm{sd}}(\vec{r})$ is the local spin drag coefficient. s $\dot{d} = \langle u_{z,\mathrm{rel}} \rangle$,

$$\Gamma_{\mathrm{sd}} = \frac{\langle \tilde{\Gamma}_{\mathrm{sd}} u_{z,\mathrm{rel}} \rangle}{\langle u_{z,\mathrm{rel}} \rangle}.$$

This relation neglects the modification of the transport equations due to quasiparticle effective mass and interaction energy corrections. Under the same conditions, the measured spin diffusivity D_s is related to the local spin diffusivity $\tilde{D}_s$ at the trap center by

$$D_s = \tilde{D}_s(0)\frac{\langle u_{z,\mathrm{rel}}\rangle}{u_{z,\mathrm{rel}}(0)}.$$

The the local spin susceptibility $\tilde{\chi}_s$ at the trap center is given by

$$\tilde{\chi}_s(0) = \tilde{\sigma}_s(0)/\tilde{D}_s(0) = \left(\frac{n(0)}{m\tilde{\Gamma}_{\mathrm{sd}}(0)}\right)\left(\frac{g}{n(0)u_{z,\mathrm{rel}}(0)}\right),$$

with the local spin conductivity $\tilde{\sigma}_s$. Note that the density n cancels in the above expression, so it remains true even when n is replaced by an effective density of mobile atoms in the presence of pairing. The measured spin susceptibility χ_s is therefore related to the local value by

$$\chi_s = \frac{\tilde{\Gamma}_{\mathrm{sd}}(0)u_{z,\mathrm{rel}}(0)}{\omega_z^2 d}\tilde{\chi}_s(0).$$

For small spin correlations, i.e. $\tilde{\chi}_s - n^2\kappa \approx 0$, we expect $\chi_s \approx \tilde{\chi}_s(0)$. Consider a volume element of spin up atoms with z coordinate Z. The motion of the volume element satisfies the Euler equation,

$$\ddot{Z} = \partial_t u_{z,\uparrow} + (\vec{u}_\uparrow \cdot \nabla)u_{u,\uparrow} = -\omega_z^2 Z - \frac{1}{2}\tilde{\Gamma}_{\mathrm{sd}}\, u_{z,\mathrm{rel}} - \frac{\partial_z P_\downarrow}{m n_\uparrow},$$

where $u_{z,\sigma}$ is the z component of the local average velocity $\vec{u}_\sigma$ of atoms with spin σ, and P_σ is the partial pressure of atoms with spin σ. similar equation holds for the spin down cloud. Subtracting them gives

$$\tilde{\Gamma}_{\mathrm{sd}}u_{z,\mathrm{rel}} = \frac{1}{m}\left(\frac{\partial_z P_\uparrow}{n_\downarrow} - \frac{\partial_z P_\downarrow}{n_\uparrow}\right),$$

where the $\ddot{Z}$ terms have been omitted because they are negligible in the case of overdamped motion applicable to our experiment. We now assume that, close to equilibrium, the density distribution of the spin up (down) atoms is equal to the equilibrium density distribution but shifted in the positive (negative) z direction by $d/2$. This is reasonable for $\tilde{\chi}_s - n^2\kappa \approx 0$. Using the Gibbs-Duhem relation $dP_\sigma = n_\sigma d\mu_\sigma$ one then finds $\tilde{\Gamma}_{\mathrm{sd}}(0)u_{z,\mathrm{rel}}(0) = \omega_z^2 d$, i.e. $\chi_s = \tilde{\chi}_s(0)$.

Supplementary Equations: Theoretical alculation of Transport oefficients

Neglecting effective mass corrections and the interaction energy between the spins, the coefficients for spin transport may be calculated using the Boltzmann transport equation, describing the evolution of the semi-classical distribution functions $f_\sigma(\vec{r},\vec{v},t)$, with $\sigma = \uparrow,\downarrow$:

$$\frac{\partial f_\sigma}{\partial t} + \vec{v}\cdot\nabla_r f_\sigma + \frac{\vec{F}}{m}\cdot\nabla_v f_\sigma = I_{\sigma\mathrm{coll}}[f_\uparrow, f_\downarrow]$$

with $\vec{F}$ an external force, and $I_{\uparrow\mathrm{coll}}$ ($I_{\downarrow\mathrm{coll}}$) the collision integral for spin up (down) atoms,

$$I_{\uparrow\mathrm{coll}}[f_\uparrow, f_\downarrow] = -\int\frac{\mathrm{d}^3 p_\downarrow}{(2\pi\hbar)^3}\int \mathrm{d}\Omega\frac{\mathrm{d}\sigma}{\mathrm{d}\Omega}\,|\vec{v}_\uparrow - \vec{v}_\downarrow|\left[(1-f_\uparrow)(1-f_\downarrow)f'_\uparrow f'_\downarrow - f_\uparrow f_\downarrow(1-f'_\uparrow)(1-f'_\downarrow)\right].$$

The integral describes the scattering of particles $\uparrow$ and $\downarrow$ into new states $\uparrow'$ and $\downarrow'$. Ω is the solid angle between the incoming and outgoing relative momenta $(\vec{p}_\uparrow - \vec{p}_\downarrow)$ and $(\vec{p}'_\uparrow - \vec{p}'_\downarrow)$, and $\frac{\mathrm{d}\sigma}{\mathrm{d}\Omega}$ is the differential scattering cross section for scattering between up and down spins. We will first derive the diffusion coefficient and the spin drag coefficient for the homogeneous case, in the absence of an external trapping potential, using a standard variational approach[4]. ssume density gradients n'_σ along z for spin up and spin down, causing a spin density gradient $g = \partial(n_\uparrow - n_\downarrow)/\partial z = n'_\uparrow - n'_\downarrow$.

This causes a change in the distribution functions $\partial f_\sigma/\partial z = n'_\sigma f_\sigma/n$. Linearizing the Boltzmann equation, writing $f_\sigma = f^0 + f^0(1-f^0)\psi_\sigma$, with f^0 the equilibrium distribution, we have for spin up

$$X \equiv v_z \frac{g}{n} = \frac{I_{\uparrow\mathrm{coll}}[\psi] - I_{\downarrow\mathrm{coll}}[\psi]}{f^0(1-f^0)}$$

where the linearized collisional integral for spin up particles is

$$I_{\uparrow\mathrm{coll}}[\psi] = -\int \frac{\mathrm{d}^3 p_\downarrow}{(2\pi\hbar)^3} \int \mathrm{d}\Omega \frac{\mathrm{d}\sigma}{\mathrm{d}\Omega} \left|\vec{v}_\uparrow - \vec{v}_\downarrow\right| \left(\psi_\uparrow + \psi_\downarrow - \psi_{\uparrow'} - \psi_{\downarrow'}\right) f^0_\uparrow f^0_\downarrow (1-f^0_{\uparrow'})(1-f^0_{\downarrow'}).$$

The induced spin current is

$$j_s = \int \frac{\mathrm{d}^3 p}{(2\pi\hbar)^3} v_z (f_\uparrow - f_\downarrow) = \int \frac{\mathrm{d}^3 p}{(2\pi\hbar)^3} v_z f^0(1-f^0)\psi \equiv \langle v_z, \psi \rangle$$

where a scalar product has been defined, and $\psi = \psi_\uparrow - \psi_\downarrow$. The Boltzmann equation now gives

$$j_s = \langle v_z, \psi \rangle = -\frac{n}{g} \langle X, \psi \rangle = -\frac{n}{g} \langle \psi, H\psi \rangle = -D_s g$$

and thus $D_s = \frac{n}{g^2} \langle \psi, H\psi \rangle$. Here, $H\psi = (I_{\uparrow\mathrm{coll}}[\psi] - I_{\downarrow\mathrm{coll}}[\psi])/f^0(1-f^0)$. The expression for D_s allows for a variational calculation, noting that $\langle \psi, H\psi \rangle \geq \langle U, H\psi \rangle^2 / \langle U, HU \rangle = \langle U, X \rangle^2 / \langle U, HU \rangle$ for trial functions U. In the classical regime at non-degenerate temperatures, the $1/r^5$ force law allows an exact solution to Boltzmann's equation with $\psi = X$. For other force laws $1/r^n$ with $n > 5$ and the hard sphere, the choice $U = X$ yields transport coefficients accurate to within a few percent[4]. We thus have in the non-degenerate regime $\langle X, X \rangle = g^2 k_B T/nm$ and $D_s \geq \frac{k_B T}{m\Gamma_{\mathrm{sd}}}$ with the variational result for the spin drag coefficient

$$\Gamma_{\mathrm{sd}} \equiv \frac{\langle X, H, X \rangle}{\langle X, X \rangle} = \frac{m}{n k_B T} \int \frac{\mathrm{d}^3 p_\uparrow}{(2\pi\hbar)^3} \int \frac{\mathrm{d}^3 p_\downarrow}{(2\pi\hbar)^3} \int \mathrm{d}\Omega \frac{\mathrm{d}\sigma}{\mathrm{d}\Omega} \left|\vec{v}_\uparrow - \vec{v}_\downarrow\right| (v_{\uparrow z} - v_{\downarrow z}) \left(v_{\uparrow z} - v_{\downarrow z} - v'_{\uparrow z} + v'_{\downarrow z}\right) f^0_\uparrow f^0_\downarrow$$

The collision integral can be calculated (for details, see for example[4]) and yields

$$\Gamma_{\mathrm{sd}} = \frac{16}{3} n \sigma(T/T_a) \left(\frac{k_B T}{\pi m}\right)^{1/2}$$

with

$$\sigma(T/T_a) = 4\pi a^2 \int \mathrm{d}u \frac{1}{1 + \frac{T}{T_a} u^2} u^5 e^{-u^2}$$

and $T_a = \frac{\hbar^2}{k_B m a^2}$ is the temperature scale associated with the scattering length a. The limiting values of the temperature-dependent average scattering cross section $\sigma(T/T_a)$ are

$$\sigma(T \ll T_a) = 4\pi a^2$$

and

$$\sigma(T \gg T_a) = \frac{2\pi\hbar^2}{m k_B T} = \lambda^2,$$

with the thermal de Broglie-wavelength λ. For unitary interactions, $T_a = 0$, and the latter limit applies. With the Fermi energy $E_F = \frac{\hbar^2}{2m}(6\pi^2 n)^{2/3}$, we find in the unitary limit where $\sigma = \lambda^2$

$$\frac{\hbar\Gamma_{\mathrm{sd}}}{E_F} = \frac{32\sqrt{2}}{9\pi^{3/2}} \sqrt{\frac{E_F}{k_B T}} = 0.90 \sqrt{\frac{E_F}{k_B T}}.$$

The spin diffusivity then obeys the variational bound

$$D_s \geq \frac{k_B T}{m\Gamma_{\rm sd}} = \frac{9\pi^{3/2}}{32\sqrt{2}}\frac{\hbar}{m}\left(\frac{T}{T_F}\right)^{3/2} = 1.1\frac{\hbar}{m}\left(\frac{T}{T_F}\right)^{3/2}.$$

The spin susceptibility follows either from $\chi_s = \sigma_s/D_s = \frac{n}{m\Gamma_{\rm sd}D_s} = \frac{n}{k_BT}$ or directly from the definition $\chi_s = \frac{\partial(n_\uparrow - n_\downarrow)}{\partial(\mu_\uparrow - \mu_\downarrow)}$. s $n_\sigma = \frac{1}{\lambda^3}e^{\overline{\mu}+\sigma\delta\mu/2}$ with the average chemical potential $\overline{\mu} = (\mu_\uparrow+\mu_\downarrow)/2$ and the difference $\delta\mu = \mu_\uparrow - \mu_\downarrow$, one obtains $\chi_s = \lim(\delta\mu \to 0)\frac{\partial(n_\uparrow - n_\downarrow)}{\partial\delta\mu} = \frac{n}{k_BT}$.

We now turn to the trapped case with inhomogeneous densities. Define the joint distribution function $f(\vec{r}_\uparrow, \vec{r}_\downarrow, \vec{v}_\uparrow, \vec{v}_\downarrow) = f_\uparrow(\vec{r}_\uparrow, \vec{v}_\uparrow) f_\downarrow(\vec{r}_\downarrow, \vec{v}_\downarrow)$. ny quantity of the form $\chi(\vec{r}_\uparrow, \vec{r}_\downarrow, \vec{v}_\uparrow, \vec{v}_\downarrow)$ can be averaged[5] over f:

$$\langle\chi\rangle = \frac{1}{N_\uparrow N_\downarrow}\int {\rm d}^3r_\uparrow {\rm d}^3r_\downarrow {\rm d}^3v_\uparrow {\rm d}^3v_\downarrow (\chi f),$$

where N_σ is the number of atoms with spin σ. We generalize to arbitrary scattering length a, and non-uniform drift velocity, the calculation by Vichi and Stringari [6] of the equation of motion for the relative coordinates of the two spin components in a harmonic trap of angular frequency ω_z along the z axis. From the Boltzmann equation,

$$\partial_t \langle z_\uparrow - z_\downarrow\rangle = \langle v_{z\uparrow} - v_{z\downarrow}\rangle$$

and

$$\partial_t \langle v_{z\uparrow} - v_{z\downarrow}\rangle = -\langle v_{z\uparrow} - v_{z\downarrow}\rangle \Gamma_{\rm sd} - \omega_z^2 \langle z_\uparrow - z_\downarrow\rangle,$$

where the spin drag coefficient is

$$\Gamma_{\rm sd} = \frac{\langle (v_{z\uparrow} - v_{z\downarrow}) I_{\rm coll}[f]\rangle}{\langle v_{z\uparrow} - v_{z\downarrow}\rangle}.$$

with

$$\langle (v_{z\uparrow} - v_{z\downarrow}) I_{\rm coll}[f]\rangle = -\int {\rm d}^3r \int \frac{{\rm d}^3p_\uparrow}{(2\pi\hbar)^3}\int \frac{{\rm d}^3p_\downarrow}{(2\pi\hbar)^3}\int {\rm d}\Omega \frac{{\rm d}\sigma}{{\rm d}\Omega}|\vec{v}_\uparrow - \vec{v}_\downarrow|(v_{z\uparrow} - v_{z\downarrow})\times$$
$$\left[(1-f_\uparrow)(1-f_\downarrow)f'_\uparrow f'_\downarrow - f_\uparrow f_\downarrow (1-f'_\uparrow)(1-f'_\downarrow)\right].$$

We assume that the distribution functions near equilibrium are $f_\sigma(\vec{r},\vec{v}) = f^0(\vec{r}, \vec{v} - \vec{v}_{\sigma,\rm drift})$ and $\vec{v}_{\sigma,\rm drift} = \pm v_{\rm d}(\vec{r})\hat{z}$ is the drift velocity of spin σ. This again corresponds to the choice $\psi = X$ in the homogeneous calculation, just now for every position $\vec{r}$ in the trap. The momentum part of the collision integral can be calculated as before, and we obtain $\Gamma_{\rm sd} = \tilde{\Gamma}_{\rm sd}(0)/\alpha$ with

$$\alpha = n_0(\vec{0})\frac{\int n_0 v_{\rm d}\, {\rm d}^3r}{\int n_0^2 v_{\rm d}\, {\rm d}^3r},$$

$n_0 = \int f^0 {\rm d}^3v$ is the equilibrium density of each spin state. For a uniform system $\alpha = 1$, while for a harmonically trapped system with a uniform drift velocity we find $\alpha = 2^{3/2} = 2.8$. However, the drift velocity profile cannot be uniform: even if it started out uniform, spin currents would get damped faster in the center of the overlap region of the two clouds, where the collision rate is high, than in the wings, where it is low. non-uniform drift velocity profile will develop. For example, a quadratic drift velocity profile $v_{\rm d}(\vec{r}) = ax^2 + by^2 + cz^2$ will result in $\alpha = 2^{5/2} \approx 5.7$. Close to the trap center, by symmetry the drift velocity will behave like a constant plus a quadratic function of position. The actual value of α may thus lie between 2.8 and 5.7. full theoretical calculation of the spin current density and the drift velocity profile is beyond the scope of this supplementary material. The spin diffusivity measured in our experiment for $T \gg T_F$ is

$$D_s = \tilde{D}_s\alpha = 1.1\alpha\frac{\hbar}{m}\left(\frac{T}{T_F}\right)^{3/2}.$$

The bulk value for $\alpha = 1$ represents a lower bound on the diffusivity. The effect of inhomogeneities in a harmonic, cylindrically symmetric trap can increase the diffusivity by $\alpha \approx 5.7$. The high-temperature result for the diffusivity has been obtained independently by Georg Bruun [7].

1. Inguscio, M., Ketterle, W. & Salomon, C. (eds.) *Ultracold Fermi Gases*. Proceedings of the International School of Physics "Enrico Fermi", Course CLXIV, Varenna, 20 - 30 June 2006 (msterdam: IOS, 2008).

2. Bockasten, K. Transformation of observed radiances into radial distribution of the emission of a plasma. *J. Opt. Soc. m.* **51**, 943–947 (1961).

3. Ku, M. *et al.* Equation of state of a strongly interacting atomic Fermi gas. Conference abstract at ⟨http://meetings.aps.org/link/B PS.2010.D MOP.W6.1⟩ (2010).

4. Smith, H. & Jensen, H. H. *Transport Phenomena* (New York: Oxford, 1989).

5. Guéry-Odelin, D., Zambelli, F., Dalibard, J. & Stringari, S. Collective oscillations of a classical gas confined in harmonic traps. *Phys. Rev.* **60**, 4851 (1999).

6. Vichi, L. & Stringari, S. Collective oscillations of an interacting trapped Fermi gas. *Phys. Rev.* **60**, 4734 (1999).

7. Bruun, G. M. Spin diffusion in Fermi gases. Preprint at ⟨http://arxiv.org/abs/1012.1607⟩ (2010).

Appendix B

Spin Transport in Polaronic and Superfluid Fermi Gases

This appendix contains a reprint of Ref. [146]: Ariel Sommer, Mark Ku, and Martin W. Zwierlein, *Spin Transport in Polaronic and Superfluid Fermi Gases*, New J. Phys. **13**, 055009 (2011).

New Journal of Physics
The open-access journal for physics

Spin transport in polaronic and superfluid Fermi gases

Ariel Sommer[1], **Mark Ku and Martin W Zwierlein**
Department of Physics, MIT-Harvard Center for Ultracold Atoms, MIT, Cambridge, MA 02139, USA
and
Research Laboratory of Electronics, MIT, Cambridge, MA 02139, USA
E-mail: atsommer@mit.edu

New Journal of Physics **13** (2011) 055009 (14pp)
Received 10 February 2011
Published 24 May 2011
Online at http://www.njp.org/
doi:10.1088/1367-2630/13/5/055009

Abstract. We present measurements of spin transport in ultracold gases of fermionic ^{6}Li in a mixture of two spin states at a Feshbach resonance. In particular, we study the spin-dipole mode, where the two spin components are displaced from each other against a harmonic restoring force. We prepare a highly imbalanced, or polaronic, spin mixture with a spin-dipole excitation and we observe strong, unitarity-limited damping of the spin-dipole mode. In gases with small spin imbalance, below the Pauli limit for superfluidity, we observe strongly damped spin flow even in the presence of a superfluid core. This indicates strong mutual friction between superfluid and polarized normal spins, possibly involving Andreev reflection at the superfluid–normal interface.

Contents

1. **Introduction** 2
2. **Highly imbalanced Fermi gases** 3
3. **A superfluid with small spin polarization** 9
4. **Conclusions** 11
Acknowledgments 12
References 12

[1] Author to whom any correspondence should be addressed.

1. Introduction

The quality of transport is one of the most important properties distinguishing states of matter. Of great technical importance, electrons in condensed matter materials can flow as currents or supercurrents, or be localized in an insulator, or even switch their state of conductivity through controllable parameters like an applied magnetic field. It is the task of many-body physics to develop models that may explain the observed transport properties in a system. Dilute atomic gases cooled to quantum degeneracy provide ideal systems for testing many-body theories. In particular, Feshbach resonances [1] in atomic Fermi gases allow experimental control over the strength of two-body interactions, giving access to the Bose–Einstein condensation to Bardeen–Cooper–Schrieffer superfluid (BEC–BCS) crossover regime [2, 3]. Transport properties have played an important role in characterizing strongly interacting Fermi gases in the BEC-BCS crossover, with the observation of hydrodynamic flow indicating nearly perfect fluidity [4, 5], the measurement of collective excitation frequencies probing the equation of state [6–8], and the observation of vortex lattices in rotating gases demonstrating superfluidity [9]. The first observations of spin transport in Fermi gases were obtained in the weakly interacting regime, and showed the onset of Pauli blocking of collisions [10], and the transition from collisionless to hydrodynamic behavior [11]. Spin excitations have also been observed in Fermi gases as long-lived spin waves near zero scattering length [12].

Here we study spin transport in strongly interacting two-component Fermi gases. Spin currents are strongly damped in such systems due to the high collision rate between opposite spin atoms: as two-body scattering does not conserve relative momentum, each scattering event on average reduces the net spin current [13]. At the Feshbach resonance, scattering is maximal, with a mean-free path between collisions of opposite spins that can be as short as one interparticle spacing—the smallest possible in a three-dimensional (3D) gas. Measurements of spin transport in strongly interacting Fermi gases with an equal number of atoms in two spin states were recently reported [14]. Interactions were shown to be strong enough to reverse spin currents, with two clouds of opposite spin almost perfectly repelling each other. The spin diffusivity was found to reach a lower limit of the order of $\hbar/m$ at unitarity, the quantum limit of diffusion. Here, we consider the case where the number of atoms in the two states is unequal, and study spin transport in the polaron and phase-separated superfluid regimes. In highly polarized systems that remain non-superfluid down to zero temperature [15–17], spin currents are expected to become undamped due to Pauli blocking [18–20]. In this imbalanced regime, a high-frequency mode observed after a compressional excitation was interpreted as a weakly damped spin quadrupole (or breathing) mode [21]. The question of the damping properties of the spin excitation and its temperature dependence was left open. Spin transport properties of ultracold Fermi gases have been investigated theoretically most recently in [18–20], [22–24], allowing comparison between theory and experiment.

In section 2, we present measurements of the damping rate of spin excitations in highly polarized Fermi gases as a function of temperature. We show that damping is maximal at finite temperatures. In section 3, we study smaller spin polarizations, below the Pauli limit of superfluidity [15], just enough to reveal the presence of a superfluid core in the system. We show that the spin-dipole mode is strongly damped in the presence of the superfluid. In a partially polarized Fermi gas, damping of spin motion is expected to persist at low temperatures due to Andreev reflection [20].

2. Highly imbalanced Fermi gases

Fermi gases with resonant interactions can remain normal down to zero temperature if the spin imbalance exceeds the Pauli (or the Clogston–Chandrasekhar) limit [15, 16, 21, 25, 26, 39]. We refer to the spin state with the larger population of atoms as the majority, or spin-up state, and the state with fewer atoms as the minority, or spin-down state. Radio-frequency (RF) spectroscopy [17] on such systems confirms the quasi-particle picture [27–29] where minority atoms are dressed by the majority Fermi sea, forming a quasi-particle known as the Fermi polaron. The energy of a single polaron in a zero-temperature Fermi sea of spin-up atoms has been described using the effective Hamiltonian [18, 19, 30],

$$H = -\alpha\mu_\uparrow + \frac{\mathbf{p}^2}{2m^*}, \tag{1}$$

where $\mathbf{p}$ is the momentum of the polaron, m^* is the polaron effective mass, $\mu_\uparrow$ is the local spin-up chemical potential and α characterizes the polaron binding energy. The parameters α and m^*/m, where m is the bare mass of spin-up and spin-down fermions, have been measured experimentally [17, 21, 31, 32] and calculated theoretically [30], [33–35], giving $\alpha = 0.62$ and $m^*/m \approx 1.2$ at zero temperature.

We consider a mixture of $N_\uparrow$ spin-up fermions and $N_\downarrow$ spin-down fermions at temperature T with equal masses and resonant interactions, held in a spin-independent potential of the form

$$V(\rho, z) = \tfrac{1}{2}m\omega_z^2 z^2 + V_\rho(\rho), \tag{2}$$

where $\rho^2 = x^2 + y^2$. The spin-up (down) clouds have density $n_{\uparrow(\downarrow)}(\mathbf{r})$ at position $\mathbf{r}$. The minority cloud is initially displaced by a small amount $Z_\downarrow(0)$ along the z-axis and is allowed to relax to its equilibrium position.

In the limit $N_\downarrow \ll N_\uparrow$, the motion of the spin-up cloud due to momentum absorbed from the spin-down cloud may be neglected. The equation of motion of the spin-down center of mass $Z_\downarrow$ is then [18]

$$m^*\ddot{Z}_\downarrow + (1+\alpha)m\omega_z^2 Z_\downarrow + \frac{m^*}{N_\downarrow}\int \mathrm{d}^3 r\, n_\downarrow(\mathbf{r})\frac{v_\downarrow(\mathbf{r})}{\tau_P(\mathbf{r})} = 0, \tag{3}$$

where the factor of $(1+\alpha)$ is due to the attraction of the minority fermions to the majority cloud, $1/\tau_P$ is the local momentum relaxation rate due to collisions [18] and is equivalent to the spin drag coefficient [13, 22], and $v_\downarrow$ is the local drift velocity of spin-down atoms. By dimensional analysis, $\hbar/\tau_P(\mathbf{r})$ must be given by the local majority Fermi energy times a universal dimensionless function of the local reduced temperature $T/T_{\mathrm{F}\uparrow}^{\mathrm{local}}(\mathbf{r})$ and the local ratio $T_{\mathrm{F}\downarrow}^{\mathrm{local}}(\mathbf{r})/T_{\mathrm{F}\uparrow}^{\mathrm{local}}(\mathbf{r})$ of the Fermi temperatures, where $T_{\mathrm{F}\uparrow(\downarrow)}^{\mathrm{local}}(\mathbf{r})$ is the local majority (minority) Fermi temperature. The first two terms in (3) follow from (1), (2) and the local density approximation, while the third term is due to damping and is not captured in (1). Equation (3) neglects a possible back-action of the minority on the majority atoms that might deform the majority density profile.

In our experimental realization of this transport problem, we use a gas of ultracold fermionic ^{6}Li atoms. The ^{6}Li atoms are cooled sympathetically with ^{23}Na [36] and loaded into a hybrid optical and magnetic trap with an adjustable bias magnetic field [37]. The magnetic field curvature provides essentially perfect harmonic confinement along the axial (z) direction, while the optical dipole trap (laser wavelength 1064 nm, waist 115 μm) provides trapping in the radial

directions, with negligible contribution to the axial confinement. With this system, we perform a collection of time series measurements. In each time series, we prepare the system in a chosen initial state and observe its evolution.

At the Feshbach resonance at 834 G, the magnetic moments of 'spin-up' and 'spin-down' atoms, the two lowest hyperfine states of ^{6}Li, are equal to 1 part in 1000, since their electron spin is in fact aligned with the magnetic field. Inducing a spin current is therefore extremely challenging on resonance. However, at lower fields, their magnetic moments differ, allowing separation of the two gas clouds by a magnetic field gradient. Our experimental procedure for producing these separated clouds is as follows.

We prepare the system starting with about 1×10^7 atoms of ^{6}Li in the lowest hyperfine state, at a total magnetic field of 300 G. A small fraction of atoms are transferred to the second-lowest hyperfine state using a RF Landau–Zener sweep. The mixture is then evaporatively cooled for a variable amount of time by lowering the depth of the optical dipole trap from $k_B \times 7\,\mu$K to a variable final depth between $k_B \times 0.5\,\mu$K and $k_B \times 1\,\mu$K, where k_B is the Boltzmann constant. The optical dipole trap depth is then raised to $k_B \times 6\,\mu$K, where the zero-temperature Fermi energy in the majority state is between $k_B \times 0.8\,\mu$K and $k_B \times 1.3\,\mu$K.

After the spin mixture is prepared at 300 G, the total magnetic field is reduced gradually over 500 ms to 50 G, where the ratio of the magnetic moments of the two states is 2.5 and interactions are very weak. A magnetic field gradient is applied along the z-direction for about 4 ms, imparting a linear momentum of the same sign but a different magnitude to each spin state. The clouds are then allowed to evolve for about 30 ms, and they execute about half of an oscillation period at different amplitudes and frequencies (the frequency ratio is 1.6 between spin-up and spin-down). When the clouds have returned to the center of the trap, their centers of mass are displaced from each other by about 200 μm (for comparison, the $1/e$ radius of the majority cloud in the z-direction is between 200 and 300 μm at this point). A second gradient pulse is applied along the same direction to remove the relative velocity of the two clouds. The second pulse also removes most of the total center-of-mass motion. The total magnetic field is then ramped to the Feshbach resonance at 834 G in about 5 ms. At resonance, the two spin states have identical trapping frequencies of 22.8 Hz.[2]

To reach low temperatures, we apply a variable amount of evaporative cooling by lowering the depth of the optical dipole trap after reaching 834 G. The time available for evaporative cooling is limited to about 0.4 s by the relaxation time of the spin excitation. To reach high temperatures, we prepare a hotter cloud at 300 G and heat the system further at 834 G by releasing the atoms from the optical dipole trap and recapturing them. The depth of the optical dipole trap is then ramped gradually to a final value in 80 ms. The final depth is chosen to keep the number of atoms and the temperature approximately constant during the subsequent evolution, and it corresponds to an effective radial trap frequency ranging from 80 Hz for the low-temperature data to 250 Hz for the high-temperature data. After preparing the system at the chosen temperature and with a nonzero spin-dipole moment, we are left with typically $N_\uparrow \approx 4 \times 10^5$ atoms in the majority state and $N_\downarrow \approx 4 \times 10^4$ atoms in the minority state. We then allow the system to evolve for a variable wait time t before measuring the densities of the spin-up and spin-down clouds using resonant absorption imaging. Note that we limit the

[2] The system as a whole oscillates harmonically along the z-direction at 22.8 Hz due to the residual center-of-mass energy. This motion does not affect the dynamics in the total center-of-mass frame because the trapping potential is harmonic in the z-direction, and therefore, according to Kohn's theorem, the dynamics in the total center-of-mass frame are equivalent to the dynamics of a system at rest [38].

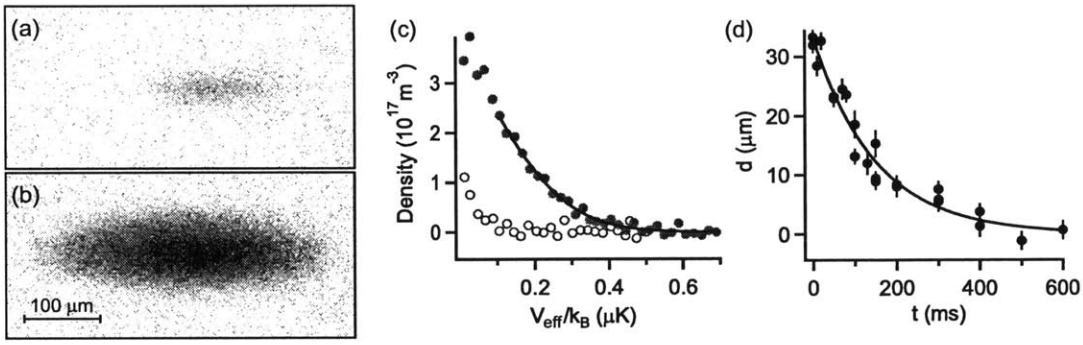

Figure 1. Measuring the spin-dipole mode of a highly polarized Fermi gas. (a) and (b) show 2D column density images of the minority and majority spin state, respectively, obtained using resonant absorption imaging in one run of the experiment. The imaging pulses are each 4 μs in duration and separated by 6 μs. The distance between the centers of mass in (a) and (b) is 34 μm. (c) Density of the majority (solid red circles) and minority (open blue circles) versus the effective potential energy $V_{\rm eff}$ defined in the text, obtained from the images in (a) and (b). The temperature of the cloud is found by fitting the non-interacting Fermi gas equation of state (solid line) to the region of the majority density where the minority fraction is 5% or less. (d) Displacement d of the minority center of mass relative to the majority center of mass as a function of time t. This time series includes the run displayed in (a–c). Error bars are from fitting uncertainty (one std. dev.). The curve shows an exponential fit.

population of the majority cloud to ensure that the central optical density is less than 2, allowing for accurate density measurements.

Figures 1(a) and (b) show typical 2D column densities of the two spin states after evaporative cooling on resonance. From the column densities, we reconstruct the 3D densities $n_\sigma(\rho, z)$ of each state $\sigma = \uparrow, \downarrow$ using the inverse Abel transformation. The temperature of the system is determined by fitting the majority density as a function of potential energy to the equation of state of a non-interacting Fermi gas [37] (figure 1(c)): $n_{\uparrow,\rm FG} = -\lambda^{-3}\zeta_{3/2}(-e^{\beta(\mu - V_{\rm eff})})$, where $\lambda = \sqrt{2\pi\hbar^2/mk_BT}$ is the thermal de Broglie wavelength, $\beta = 1/k_BT$, the fit parameters are the chemical potential μ and the temperature T, $\zeta_{3/2}$ is the polylogarithm of order 3/2, and $V_{\rm eff} = V(\rho, z - Z_\uparrow)$ is the effective potential energy. The fit is restricted to $z < Z_\uparrow$ and to the outer edges of the majority cloud, where $n_\downarrow/n_\uparrow < x_c$. We used a cut-off minority fraction of $x_c = 0.05$ for all clouds with $T < 0.5T_{F\uparrow}$. For some of the data with $0.5 < T/T_{F\uparrow} < 1$, x_c was increased to 0.08 to increase the available signal, while for the data with $T > 2T_{F\uparrow}$, x_c was increased to 0.15 for the same reason. These increases in x_c should not affect the accuracy of the thermometry because the system interacts less strongly at high $T/T_{F\uparrow}$ [3]. This is demonstrated by our spin susceptibility measurements for the balanced case in [14] that agree with the compressibility above $T/T_F \approx 1$, showing the absence of spin correlations in this temperature regime. For normalization, the central densities $n_\sigma(0)$ of each species are recorded and used to define the central Fermi energies $E_{F\sigma} = \hbar^2 k_{F\sigma}^2/2m_\sigma$, with $k_{F\sigma} = (6\pi^2 n_\sigma(0))^{1/3}$, $m_\uparrow = m$, and $m_\downarrow = m^*$, and Fermi temperatures $T_{F\sigma} = E_{F\sigma}/k_B$.

Spin transport is measured by observing the time evolution of the center-of-mass separation $d(t) = Z_\downarrow(t) - Z_\uparrow(t)$ (figure 1(d)), with $Z_{\uparrow(\downarrow)}(t)$ the center of mass of the majority (minority) cloud along the z-axis at time t, determined from a 2D Gaussian fit to the column density. We find that d relaxes exponentially to zero, corresponding to an overdamped spin-dipole mode, and fit the evolution to an exponential function $d(t) = d_0 e^{-t/\tau}$. We report the dimensionless relaxation time $\tilde{\tau} = \hbar\omega_z^2\tau/E_{F\uparrow}$. Equation (3) implies that $\tilde{\tau}$ is mostly independent of the absolute scales set by the density and the trapping frequency. Defining the average momentum relaxation rate as

$$\frac{1}{\hat{\tau}_P} = \frac{\int d^3r\, n_\downarrow(\mathbf{r}) v_\downarrow(\mathbf{r})/\tau_P(\mathbf{r})}{\int d^3r\, n_\downarrow(\mathbf{r}) v_\downarrow(\mathbf{r})}, \tag{4}$$

and making the approximation that $\hat{\tau}_P$ is constant in time relates $\tilde{\tau}$ to fundamental properties of the system as

$$\tilde{\tau} \approx \frac{m^*/m}{(1+\alpha)} \cdot \frac{1/\hat{\tau}_P}{\hbar/E_{F\uparrow}}, \tag{5}$$

in the limit $(\omega_z\tau)^2 \gg 1$ realized in our measurements, where τ is always at least 100 ms, and so $(\omega_z\tau)^2 > 200$.

Figure 2 shows the measured values of the dimensionless relaxation time $\tilde{\tau}$ as a function of the reduced temperature $T/T_{F\uparrow}$. $\tilde{\tau}$ increases at low temperatures before reaching a maximum of $0.13(3)E_{F\uparrow}$ for $T/T_{F\uparrow} = 0.40(6)$, and decreases at higher temperatures. We interpret the behavior of the relaxation time at low temperatures as a consequence of Pauli blocking: as the temperature is lowered significantly below the majority Fermi temperature, the phase space available for a minority atom to scatter goes to zero. The reduction in $\tilde{\tau}$ at high temperatures is expected: at high temperatures, $1/\hat{\tau}_P$ is essentially given by the collision rate in the gas [40], $1/\hat{\tau}_P \sim n\sigma v$. The scattering cross-section σ on resonance for $T \gg T_{F\uparrow}$ is given by the square of the de Broglie wavelength and is thus proportional to $1/T$, while the average speed v of the particles is proportional to $\sqrt{T}$. Hence, $\tilde{\tau}$ is expected to decrease like $\hbar n\sigma v/E_{F\uparrow} \propto \sqrt{T_{F\uparrow}/T}$. We observed behavior similar to figure 2 in 3D Fermi gases with resonant interactions and equal spin populations in [14], although we see more significant Pauli blocking here than in [14] at comparable temperatures.

The systematic uncertainties of the measured values have been estimated, and are comparable to or less than the statistical errors. The temperature measurement uses knowledge of the potential energy (2). The radial potential energy function $V_\rho(\rho)$ is assumed to have the form

$$V_\rho(\rho) = \frac{2aP}{\pi w_0^2}(1 - e^{-2\rho^2/w_0^2}) - \frac{1}{4}m\omega_z^2\rho^2, \tag{6}$$

where a is a known constant expressing the polarizability of the atoms, P is the optical power of the dipole trap and w_0 is the waist of the trapping beam, and $\omega_z = 2\pi \times 22.8$ Hz is the axial trapping frequency. Direct measurements give P and w_0 with 5–10% accuracy. To refine the trap model, we sum the 3D densities of the majority atom clouds for each value of P used in the experiment, taking only $t > 190$ ms, and use the known axial potential together with the local density approximation to obtain $V_\rho(\rho)$. The model (6) is then fit to the experimentally measured $V_\rho(\rho)$ with w_0 as a free parameter, giving $w_0 = 115\,\mu$m. Equivalently, P could have been used as the free parameter; the difference in the two approaches adds less than 1% uncertainty to the potential energy. The uncertainty in the potential energy is dominated by noise in the images of

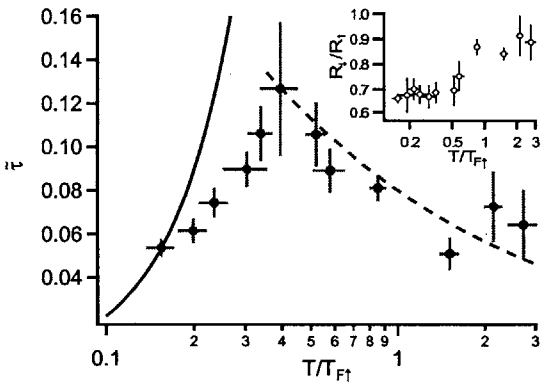

Figure 2. Normalized relaxation time of the spin-dipole mode of a highly polarized Fermi gas as a function of the reduced temperature $T/T_{F\uparrow}$. $T_{F\uparrow}$ is the local Fermi temperature at the center of the majority cloud. The solid curve is the low-temperature limit from [18], given by equation (7). The dashed curve is the expression $0.08\sqrt{\frac{T_{F\uparrow}}{T}}$. The inset shows the average ratio of the minority cloud size to the majority cloud size as a function of the reduced temperature $T/T_{F\uparrow}$. The cloud sizes are defined as the $1/e$ radii along the z-axis, estimated by fitting a 2D Gaussian function to the column densities of the two spin states. In both figures, each point is a weighted average of the results from 1 to 3 time series, with each time series containing on average 30 spin-up–spin-down image pairs. The error bars give standard deviations due to statistical fluctuations within a time series. Where the results of more than one time series are averaged, the error bars show the standard deviation of the weighted mean, determined from the standard deviations from each time series.

the clouds, giving an uncertainty in w_0 of about $2\,\mu$m. This implies a 7% systematic error on the potential energy at $\rho = 40\,\mu$m (a typical value of ρ in the outer region of the cloud). The resulting systematic uncertainty on the temperature is 10% at the lowest temperatures, and 5% for temperatures near T_F or higher. Measurements of density are affected by the laser linewidth, imperfect polarization of the imaging light, and nonlinearities from saturation of the imaging transition, Doppler shifting of atoms scattered by the imaging light and pumping into transparent final states. The density measurement is calibrated using equilibrium low-temperature clouds with large spin imbalance. The systematic uncertainty in the density is 10%. This leads to a total systematic error in the reduced temperatures of 8–12%, and a systematic error in $\tilde{\tau}$ of 6%. The magnification of the imaging system is calibrated to 0.5% and does not contribute significantly to the uncertainties in w_0 or d.

It would be interesting to have available a calculation of spin transport coefficients such as $1/\tau_P$ at arbitrary temperatures for comparison with our data. A full solution is available for Fermi gases with equal populations in one spatial dimension [22, 23] and shows qualitative features similar to our data, with a maximum of the spin drag coefficient (analogous to $\tilde{\tau}$) at finite temperatures of the order of T_F.

We expect our data to differ quantitatively from predictions for a homogeneous system. The measured quantity $\tilde{\tau}$ is a global property of the trapped system, while the momentum relaxation

rate $1/\tau_P$ is a local quantity. For $T \gg T_{F\uparrow}$, $1/\tau_P \propto n_\uparrow$, and $1/\tau_P$ increases with increasing majority density, while for $T \ll T_{F\uparrow}$, due to Pauli blocking $1/\tau_P \propto E_{F\uparrow}(T/T_{F\uparrow})^2 \propto n_\uparrow^{-2/3}$, and $1/\tau_P$ decreases with increasing majority density. Additionally, the variation in $1/\tau_P$ should cause the spin current to be non-uniform. The effect of inhomogeneity should be greater at high reduced temperatures, where the minority cloud size approaches the majority cloud size. The inset in figure 2 shows the ratio of the cloud sizes $R_\downarrow/R_\uparrow$ as a function of the reduced temperature, where $R_{\uparrow(\downarrow)}$ is the 1/e width in the z-direction from a 2D Gaussian fit to the majority (minority) column density. Indeed, $R_\downarrow/R_\uparrow$ increases with increasing $T/T_{F\uparrow}$. Even at the lowest temperatures, $R_\downarrow/R_\uparrow$ remains significant, attaining a value of 0.7, due to the finite minority fraction $N_\downarrow/N_\uparrow \approx 0.1$. The effect of inhomogeneity is therefore reduced at low temperatures, but should remain present.

We compare our results for $\tilde{\tau}$ at low temperatures to the low-temperature limit in [18], which can be written as

$$\frac{1/\tau_P(0)}{E_{F\uparrow}/\hbar} = c\frac{\alpha^2}{1+\alpha}\left(\frac{m^*}{m}\right)^2\left(\frac{T}{T_{F\uparrow}}\right)^2, \tag{7}$$

for temperatures $T \ll T_{F\uparrow}$.[3] The prefactor c changes slightly from $c = \frac{2\pi^3}{9} = 6.89\ldots$ to c ≈ 6.0 as the temperature rises from far below $T_{F\downarrow}$, where even the minority cloud is degenerate, to temperatures where $T_{F\downarrow} \ll T \ll T_{F\uparrow}$ and the minority is a classical gas [18]. In our coldest data, $T \approx 0.5T_{F\downarrow}$ and $T_{F\downarrow} \approx 0.3T_{F\uparrow}$, assuming $m^* = 1.2\,m$. To compare our data with [18], using (7), we set $c = \frac{2\pi^3}{9}$, $\alpha = 0.6$ and $m^* = 1.2m$. The comparison is affected by the inhomogeneous trapping potential in the experiment, as equation (7) gives the local value of $1/\tau_P$ at the center of the majority cloud. The experimental data agree with the value from equation (7) at the lowest temperatures measured (see figure 2). The deviation at higher temperatures is expected as the $T \ll T_{F\uparrow}$ limit becomes inapplicable. The convergence of the experimental data to the theoretical value at low temperature despite the inhomogeneity of the system may be partly due to the reduced minority cloud size at low temperatures, which reduces the effects of inhomogeneity, as discussed above. Additionally, the variation in the momentum relaxation rate with density will to some extent cancel at moderately low temperatures, as $1/\tau_P$ changes from increasing with increasing density at high reduced temperatures to decreasing with increasing density due to Pauli blocking at low reduced temperatures. The crossing of the experimental curve with the predictions for a uniform system at low temperatures therefore does not necessarily indicate that the inhomogeneity is negligible at low temperatures in this measurement.

At high temperatures $T \gg T_{F\uparrow,\downarrow}$, the spin transport properties of a trapped system can be calculated from the Boltzmann transport equation. For vanishing minority fraction, we find (now with $\alpha = 0$ and $m^* = m$ and assuming harmonic trapping in all three directions) [14]

$$\tilde{\tau} = \frac{8}{9\pi^{3/2}\epsilon}\sqrt{\frac{T_{F\uparrow}}{T}} \approx \frac{0.16}{\epsilon}\sqrt{\frac{T_{F\uparrow}}{T}}, \tag{8}$$

where $\epsilon = 1$ when the minority drift velocity distribution $v_\downarrow$ is uniform. This result features the expected dependence $\propto \sqrt{\frac{T_{F\uparrow}}{T}}$ on temperature. The relative velocity between the two spin states

[3] We omit a term due to the relative velocity of the spin up and spin-down clouds, which produces a correction of less than 1% in the overdamped, finite-temperature regime accessed in this experiment.

cannot be truly constant in space but has to be depressed in the center, where the density is highest and the momentum relaxation is fastest. In general,

$$\epsilon = \frac{\int \mathrm{d}^3 r v_\downarrow(\frac{\vec{r}}{\sqrt{2}})\mathrm{e}^{-\beta V}}{\int \mathrm{d}^3 r v_\downarrow(\vec{r})\mathrm{e}^{-\beta V}}, \tag{9}$$

where V is the trapping potential (here assumed to be quadratic). For example, for a quadratic drift velocity profile, $v_\downarrow(\vec{r}) = ax^2 + by^2 + cz^2$, the predicted $\tilde{\tau}$ is reduced by factor of $\epsilon = 2$. We find that the high-temperature result (8) with $\epsilon = 2$ leads to close agreement with our experimental results (figure 2). This model is interesting because it estimates the effects of inhomogeneous density and velocity distributions, but it has shortcomings. The drift velocity should remain non-zero everywhere, rather than going to zero at the origin as in the quadratic case, and should have a radial component. A full quantitative description of the overdamped spin-dipole motion in the high-temperature limit in an external trapping potential will therefore be more complex.

3. A superfluid with small spin polarization

We extend the method of the previous section to study spin transport in Fermi gases with resonant interactions and small spin imbalance. When the global polarization $\frac{N_\uparrow - N_\downarrow}{N_\uparrow + N_\downarrow}$ is less than about 75% in a harmonically trapped Fermi gas at low temperature and with resonant interactions, the system phase separates into a superfluid core surrounded by a polarized normal state region [15, 16, 21]. The superfluid core is visible as a sharp reduction in the density difference of the two spin states [16]. The transition between the superfluid and the imbalanced normal regions forms a sharp interface below a tricritical point, where the density imbalance jumps between the two regions [39]. Scattering and spin transport at the interface between a normal and superfluid Fermi gas have been considered theoretically in [20, 41].

To observe spin transport in an imbalanced gas containing a superfluid, we prepare a spin mixture with a global polarization of 17(3)%. The gas is cooled at 300 G and again at 834 G after creating the spin-dipole excitation as described in the previous section. Two off-resonant phase contrast images are taken to measure the densities of each spin state. An imaging pulse tuned halfway between the resonance frequencies of the two states directly measures the difference in the column densities (figure 3(a)), while a second pulse, red-detuned from both states (figure 3(b)), provides additional information needed to reconstruct the total column density in each state [39]. From the column densities of each state, we obtain 3D density distributions using the inverse Abel transformation.

The 2D spin density (figure 3(a)) and 3D spin density (figure 3(c)) show a reduction near the center of the trap, with the 3D density going to zero, characteristic of the superfluid core in imbalanced Fermi gases [16]. We have checked that the shell structure remains even after the spin density reaches equilibrium. Additionally, we estimate the temperature T of the system to confirm that it is cold enough to contain a superfluid. In unpolarized systems, the superfluid transition is predicted to occur at about $T_c/T_F = 0.173(6)$ [42], where $k_B T_F = E_F = \hbar^2(6\pi^2 n(0))^{2/3}/2m$ and n is the density per spin state. This theoretical value agrees well with a determination of T_c/T_F by our group. Fitting the equation of state of a unitary Fermi gas at zero imbalance [43] to the majority (minority) density gives an estimate $T_{\uparrow(\downarrow)}$ of the temperature. The fits are restricted to $V_{\sigma,\mathrm{eff}} > 0.3\,\mu$K, where $V_{\sigma,\mathrm{eff}} = V(\rho, z - Z_\sigma)$, to exclude

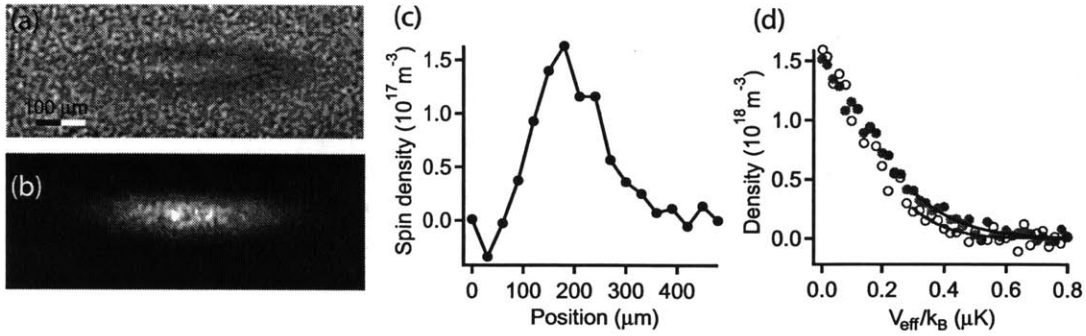

Figure 3. Spin-dipole mode of an imbalanced Fermi gas with a superfluid core. Phase contrast images are taken with imaging light detuned (a) halfway between the resonance frequencies of the two states and (b) at large red detuning from both states. The image in (a) is proportional to the difference in column densities of the two states. The depletion of the density difference in the center of the cloud indicates the superfluid region. It is displaced from the center of the majority due to the spin-dipole excitation. Panel (c) shows the difference in reconstructed 3D densities of the spin up and spin-down clouds as a function of the z coordinate for $z > 0$. The depletion in the center again indicates pairing and superfluidity [16]. An elliptical average over a narrow range of the radial coordinate ρ is used to increase the signal-to-noise ratio. (d) The temperature is estimated from the 3D densities of the two states as a function of the effective potential V_{eff} defined in the text. Solid red circles: majority density, open blue circles: minority density. The curves are fits to the densities using the equation of state of a unitary Fermi gas at zero imbalance to get upper and lower bounds on the temperature.

the putative superfluid region. Compared to a balanced gas at unitarity with $N'_\uparrow = N'_\downarrow = N_\uparrow$, and at the same temperature T, the majority cloud should have a larger size because the interaction energy between the spin-up and spin-down atoms is attractive. We therefore expect that $T_\uparrow$ is an overestimate of T. Likewise, we expect $T_\downarrow < T$, and we consider $T_\uparrow$ and $T_\downarrow$ to provide approximate upper and lower bounds on T.

Figure 4(a) shows the temperature bounds during the approach to equilibrium. Time-averaging gives $0.12(1) < T/T_F < 0.15(2)$, where $T_F \equiv T_{F\uparrow} \approx T_{F\downarrow}$. The error estimates include the standard error of the mean and the systematic error from uncertainty in the potential energy and in the density. These temperature bounds confirm that the system is in the vicinity of the superfluid transition.

Even in the presence of the superfluid core, we still observe strong damping of the spin-dipole mode. Figure 4(b) shows that the displacement d between the majority and minority centers of mass along the z-axis relaxes gradually to zero, rather than oscillating as would be expected in a dissipationless system. The $1/e$ relaxation time $\tau = 360$ ms corresponds to a spin drag coefficient [13, 22] of $\omega_z^2 \tau = 0.06(1) E_{F\uparrow}/\hbar$, close to the maximum spin drag coefficient in non-polarized trapped Fermi gases at unitarity [14].

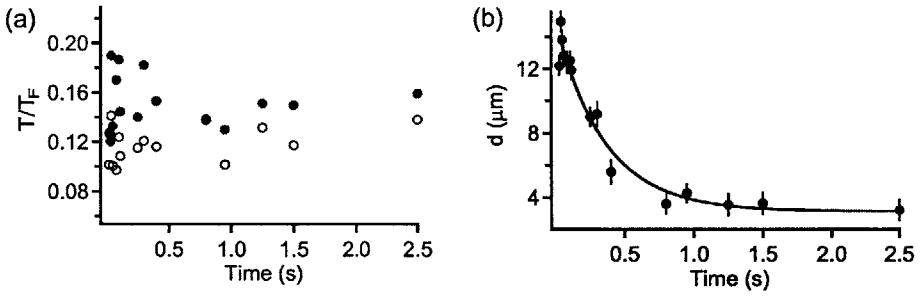

Figure 4. (a) Reduced temperature as a function of time during relaxation of the spin-dipole excitation in a spin-polarized Fermi gas containing a superfluid region. Red solid (blue open) circles: $T_{\uparrow(\downarrow)}/T_{F\uparrow(\downarrow)}$ from a fit to the edge of the majority (minority) spin state using the equation of state of an unpolarized unitary Fermi gas, giving an upper (lower) limit to true temperature. (b) The displacement of the spin-up and spin-down centers of mass relaxes exponentially, indicating strong spin drag despite the presence of a superfluid. Error bars: one std. dev. from fitting error.

The strong damping is reminiscent of the friction between the normal and superfluid component in liquid helium [44] and in atomic Bose–Einstein condensates [46]. In the latter case, out-of-phase oscillations between the condensate and the thermal component are strongly damped. Even at low temperatures, currents in superfluids as well as in 1D superconducting wires are still damped due to phase slips [46–48]. In the presented case of a partially polarized Fermi gas, Andreev reflection of unpaired atoms at the normal-to-superfluid interface should cause spin current decay even at the lowest temperatures [20, 41]. At higher temperatures or if the majority chemical potential in the normal state region can overcome the pairing gap, the microscopic velocity of majority atoms will significantly exceed the critical velocity of the superfluid of about $0.3v_F$ [49, 50], causing strong dissipation of spin currents. The relative importance of dissipation at the interface versus dissipation inside the superfluid could be determined by whether a spin current flows through the superfluid or around it. However, we are not able to determine the spatial distribution of the spin current with our current data.

4. Conclusions

In this work, we presented our measurements on the damping of the spin-dipole mode in a highly polarized Fermi gas with resonant interactions, over a wide range of temperatures. The damping is seen to become weaker at temperatures significantly less than the majority Fermi energy, as expected from Pauli blocking, i.e. the fact that quasi-particles in a Fermi liquid become long lived at sufficiently low temperatures. These measurements provide the first quantitative test of theoretical calculations of the spin transport properties of highly polarized Fermi gases. We also observe spin transport in a Fermi gas with low spin polarization containing a superfluid region. It is found that the spin-dipole motion remains strongly damped, revealing the importance of friction between the superfluid and the normal component, possibly accompanied by reflection processes at the interface.

Acknowledgments

This work was supported by the NSF, AFOSR-MURI, AFOSR-YIP, ARO-MURI, ONR, DARPA YFA, a grant from the Army Research Office with funding from the DARPA OLE program, the David and Lucille Packard Foundation and the Alfred P Sloan Foundation. The authors thank André Schirotzek, Giacomo Roati and Peyman Ahmadi for experimental assistance and David Huse for interesting discussions.

References

[1] Chin C, Grimm R, Julienne P and Tiesinga E 2010 Feshbach resonances in ultracold gases *Rev. Mod. Phys.* **82** 1225–86

[2] Ketterle W and Zwierlein M W 2008 Making, probing and understanding ultracold Fermi gases *Ultracold Fermi Gases, Proc. Int. School of Physics 'Enrico Fermi', Course CLXIV (Varenna, 20–30 June 2006)* ed M Inguscio, W Ketterle and C Salomon (Amsterdam: IOS Press) pp 1–462

[3] Giorgini S, Pitaevskii L P and Stringari S 2008 Theory of ultracold atomic Fermi gases *Rev. Mod. Phys.* **80** 1215–60

[4] Cao C, Elliott E, Joseph J, Wu H, Petricka J, Schäfer T and Thomas J E 2010 Universal quantum viscosity in a unitary Fermi gas *Science* **331** 58–61

[5] O'Hara K M, Hemmer S L, Gehm M E, Granade S R and Thomas J E 2002 Observation of a strongly interacting degenerate Fermi gas of atoms *Science* **298** 2179

[6] Kinast J, Hemmer S L, Gehm M E, Turlapov A and Thomas J E 2004 Evidence for superfluidity in a resonantly interacting Fermi gas *Phys. Rev. Lett.* **92** 150402

[7] Bartenstein M, Altmeyer A, Riedl S, Jochim S, Chin C, Hecker-Denschlag J and Grimm R 2004 Collective excitations of a degenerate gas at the BEC-BCS crossover *Phys. Rev. Lett.* **92** 203201

[8] Altmeyer A, Riedl S, Kohstall C, Wright M J, Geursen R, Bartenstein M, Chin C, Hecker J Denschlag and Grimm R 2007 Precision measurements of collective oscillations in the BEC-BCS crossover *Phys. Rev. Lett.* **98** 040401

[9] Zwierlein M W, Abo-Shaeer J R, Schirotzek A, Schunck C H and Ketterle W 2005 Vortices and superfluidity in a strongly interacting Fermi gas *Nature* **435** 1047–51

[10] DeMarco B and Jin D S 2002 Spin excitations in a Fermi gas of atoms *Phys. Rev. Lett.* **88** 040405

[11] Gensemer S D and Jin D S 2001 Transition from collisionless to hydrodynamic behavior in an ultracold Fermi gas *Phys. Rev. Lett.* **87** 173201

[12] Du X, Luo L, Clancy B and Thomas J E 2008 Observation of anomalous spin segregation in a trapped Fermi gas *Phys. Rev. Lett.* **101** 150401

[13] D'Amico I and Vignale G 2000 Theory of spin Coulomb drag in spin-polarized transport *Phys. Rev.* B **62** 4853–7

[14] Sommer A, Ku M, Roati G and Zwierlein M W 2011 Universal spin transport in a strongly interacting Fermi gas *Nature* **472** 201–4

[15] Zwierlein M W, Schirotzek A, Schunck C H and Ketterle W 2006 Fermionic superfluidity with imbalanced spin populations *Science* **311** 492–6

[16] Shin Y, Zwierlein M W, Schunck C H, Schirotzek A and Ketterle W 2006 Observation of phase separation in a strongly interacting imbalanced Fermi gas *Phys. Rev. Lett.* **97** 030401

[17] Schirotzek A, Wu C-H, Sommer A and Zwierlein M W 2009 Observation of Fermi polarons in a tunable Fermi liquid of ultracold atoms *Phys. Rev. Lett.* **102** 230402–4

[18] Bruun G M, Recati A, Petchick C J, Smith H and Stringari S 2008 Collisional properties of a polarized Fermi gas with resonant interactions *Phys. Rev. Lett.* **100** 240406

[19] Recati A, Lobo C and Stringari S 2008 Role of interactions in spin-polarized atomic Fermi gases at unitarity *Phys. Rev.* A **78** 023633

[20] Parish M M and Huse D A 2009 Evaporative depolarization and spin transport in a unitary trapped Fermi gas *Phys. Rev.* A **80** 063605

[21] Nascimbène S, Navon N, Jiang K J, Tarruell L, Teichmann M, McKeever J, Chevy F and Salomon C 2009 Collective oscillations of an imbalanced Fermi gas: axial compression modes and polaron effective mass *Phys. Rev. Lett.* **103** 170402–4

[22] Polini M and Vignale G 2007 Spin drag and spin-charge separation in cold Fermi gases *Phys. Rev. Lett.* **98** 266403

[23] Rainis D, Polini M, Tosi M P and Vignale G 2008 Spin-drag relaxation time in one-dimensional spin-polarized Fermi gases *Phys. Rev.* B **77** 035113

[24] Duine R A, Polini M, Stoof H T C and Vignale G 2010 Spin drag in an ultracold Fermi gas on the verge of ferromagnetic instability *Phys. Rev. Lett.* **104** 220403

[25] Clogston A M 1962 Upper limit for the critical field in hard superconductors *Phys. Rev. Lett.* **9** 266

[26] Chandrasekhar B S 1962 A note on the maximum critical field of high-field superconductors *Appl. Phys. Lett.* **1** 7

[27] Chevy F 2006 Universal phase diagram of a strongly interacting Fermi gas with unbalanced spin populations *Phys. Rev.* A **74** 063628

[28] Combescot R, Recati A, Lobo C and Chevy F 2007 Normal state of highly polarized Fermi gases: simple many-body approaches *Phys. Rev. Lett.* **98** 180402

[29] Prokof'ev N and Svistunov B 2008 Fermi-polaron problem: diagrammatic Monte Carlo method for divergent sign-alternating series *Phys. Rev.* B **77** 020408

[30] Lobo C, Recati A, Giorgini S and Stringari S 2006 Normal state of a polarized Fermi gas at unitarity *Phys. Rev. Lett.* **97** 200403

[31] Shin Y-I 2008 Determination of the equation of state of a polarized Fermi gas at unitarity *Phys. Rev.* A **77** 041603

[32] Nascimbène S, Navon N, Jiang K J, Chevy F and Salomon C 2010 Exploring the thermodynamics of a universal Fermi gas *Nature* **463** 1057–60

[33] Combescot R and Giraud S 2008 Normal state of highly polarized Fermi gases: full many-body treatment *Phys. Rev. Lett.* **101** 050404

[34] Prokof'ev N V and Svistunov B V 2008 Bold diagrammatic Monte Carlo: a generic sign-problem tolerant technique for polaron models and possibly interacting many-body problems *Phys. Rev.* B **77** 125101

[35] Pilati S and Giorgini S 2008 Phase separation in a polarized Fermi gas at zero temperature *Phys. Rev. Lett.* **100** 030401

[36] Hadzibabic Z, Gupta S, Stan C A, Schunck C H, Zwierlein M W, Dieckmann K and Ketterle W 2003 Fifty-fold improvement in the number of quantum degenerate fermionic atoms *Phys. Rev. Lett.* **91** 160401

[37] Zwierlein M W, Schunck C H, Schirotzek A and Ketterle W 2006 Direct observation of the superfluid phase transition in ultracold Fermi gases *Nature* **442** 54–8

[38] Dobson J F 1994 Harmonic-potential theorem: implications for approximate many-body theories *Phys. Rev. Lett.* **73** 2244

[39] Shin Y-I, Schunck C H, Schirotzek A and Ketterle W 2008 Phase diagram of a two-component Fermi gas with resonant interactions *Nature* **451** 689–93

[40] Vichi L and Stringari S 1999 Collective oscillations of an interacting trapped Fermi gas *Phys. Rev.* A **60** 4734

[41] Van Schaeybroeck B and Lazarides A 2007 Normal-superfluid interface scattering for polarized fermion gases *Phys. Rev. Lett.* **98** 170402

[42] Goulko O and Wingate M 2010 Thermodynamics of balanced and slightly spin-imbalanced Fermi gases at unitarity *Phys. Rev.* A **82** 053621

[43] Ku M, Schirotzek A, Sommer A, Zwierlein M, Van K Houcke, Werner F, Kozik E, Prokofev N and Svistunov B 2010 equation of state of a strongly interacting atomic Fermi gas, available at http://meetings.aps.org/link/BAPS.2010.DAMOP.W6.1

[44] Vinen W F 1957 Mutual friction in a heat current in liquid helium ii. iii theory of mutual friction *Proc. R. Soc.* A **242** 493–515

[45] Stamper-Kurn D M, Miesner H-J, Inouye S, Andrews M R and Ketterle W 1998 Collisionless and hydrodynamic excitations of a Bose–Einstein condensate *Phys. Rev. Lett.* **81** 500–3

[46] Langer J S and Michael Fisher E 1967 Intrinsic critical velocity of a superfluid *Phys. Rev. Lett.* **19** 560–3

[47] Langer J S and Ambegaokar V 1967 Intrinsic resistive transition in narrow superconducting channels *Phys. Rev.* **164** 498–510

[48] McKay D, White M, Pasienski M and DeMarco B 2008 Phase-slip-induced dissipation in an atomic Bose–Hubbard system *Nature* **453** 76–80

[49] Miller D E, Chin J K, Stan C A, Liu Y, Setiawan W, Sanner C and Ketterle W 2007 Critical velocity for superfluid flow across the BEC-BCS crossover *Phys. Rev. Lett.* **99** 070402

[50] Combescot R, Kagan M Yu and Stringari S 2006 Collective mode of homogeneous superfluid Fermi gases in the BEC-BCS crossover *Phys. Rev.* A **74** 042717

Appendix C

Revealing the Superfluid Lambda Transition in the Universal Thermodynamics of a Unitary Fermi Gas

This appendix contains a reprint of Ref. [85]: Mark J. H. Ku, Ariel T. Sommer, Lawrence W. Cheuk, Martin W. Zwierlein, *Revealing the Superfluid Lambda Transition in the Universal Thermodynamics of a Unitary Fermi Gas*, Science **335**, 563-567 (2012).

will slow down their spin rates with time after the RLDP. However, they cannot explain the apparent difference in spin distributions between AXMSPs and radio MSPs, because radio MSPs, which have weak surface magnetic field strengths, could not spin down by the required amount even in a Hubble time. The true age of a pulsar (*23*) is given by $t = P/((n-1)\dot{P})[1-(P_0/P)^{n-1}]$. Assuming an evolution with a braking index $n = 3$ and $B = 1.0\times 10^8$ G, the time scale t is larger than 10 Gy, using $P_0 = \langle P\rangle_{AXMSP} = 3.3$ ms and $P(t) = \langle P\rangle_{MSP} = 5.5$ ms. To make things worse, one has to add the main-sequence lifetime of the LMXB donor star, which is typically 3 to 12 Gy, thereby reaching unrealistic large total ages. Although the statistics of AXMSPs still has its basis in small numbers and care must be taken for both detection biases (such as eclipsing effects of radio MSPs) and comparison between various subpopulations (*8*), it is evident from both observations and theoretical work that the RLDP effect presented here plays an important role for the spin distribution of MSPs.

The RLDP effect may also help explain a few other puzzles, for example, why characteristic (or spin-down) ages of radio MSPs often largely exceed cooling age determinations of their white dwarf companions (*24*). It has been suggested that standard cooling models of white dwarfs may not be correct (*25*–*27*), particularly for low-mass helium white dwarfs. These white dwarfs avoid hydrogen shell flashes at early stages and retain thick hydrogen envelopes, at the bottom of which residual hydrogen burning can continue for several billion years after their formation, keeping the white dwarfs relatively hot (~10^4 K) and thereby appearing much younger than they actually are. However, it is well known that the characteristic age is not a trustworthy measure of true age (*28*), and the RLDP effect exacerbates this discrepancy even further. In the model calculation presented in Fig. 1, it was assumed that $B = 1.0\times 10^8$ G and $\varphi = 1.0$. However, P_0 and τ_0 depend strongly on both B and φ. This is shown in Fig. 2, where I have calculated the RLDP effect for different choices of B and φ by using the same stellar donor model [i.e., same $\dot{M}(t)$ profile] as before. The use of other LMXB donor star masses, metallicities, and initial orbital periods would lead to other $\dot{M}(t)$ profiles (*16*, *17*) and hence different evolutionary tracks. The conclusion is that recycled MSPs can basically be born with any characteristic age. Thus, we are left with the cooling age of the white dwarf companion as the sole reliable, although still not accurate, measure as an age indicator.

A final puzzle is why no sub-millisecond pulsars have been found among the 216 radio MSPs detected in total so far. Although modern observational techniques are sensitive enough to pick up sub-millisecond radio pulsations, the fastest spinning known radio MSP, J1748−2446ad (*29*), has a spin frequency of only 716 Hz, corresponding to a spin period of 1.4 ms. This spin rate is far from the expected minimum equilibrium spin period (*8*) and the physical mass shedding limit of about 1500 Hz. It has been suggested that gravitational wave radiation during the accretion phase halts the spin period above a certain level (*30*, *31*). The RLDP effect presented here is a promising candidate for an alternative mechanism, in case a sub-millisecond AXMSP is detected (*8*).

References and Notes

1. M. A. Alpar, A. F. Cheng, M. A. Ruderman, J. Shaham, *Nature* **300**, 728 (1982).
2. D. Bhattacharya, E. P. J. van den Heuvel, *Phys. Rep.* **203**, 1 (1991).
3. L. Bildsten *et al.*, *Astrophys. J. Suppl. Ser.* **113**, 367 (1997).
4. R. Wijnands, M. van der Klis, *Nature* **394**, 344 (1998).
5. J. W. T. Hessels *et al.*, *AIP Conf. Proc.* **1068**, 130 (2008).
6. The Roche lobe of a binary star is the innermost equipotential surface passing through the first Lagrangian point, L1. If a star fills its Roche lobe, the unbalanced pressure at L1 will cause mass transfer to the other star (*2*).
7. A. M. Archibald *et al.*, *Science* **324**, 1411 (2009); 10.1126/science.1172740.
8. Materials and methods are available as supporting material on *Science* Online.
9. F. K. Lamb, C. J. Pethick, D. A. Pines, *Astrophys. J.* **184**, 271 (1973).
10. P. Ghosh, F. K. Lamb, *NATO Sci. Ser.* **377**, 487 (1992).
11. J. Frank, A. King, D. J. Raine, *Accretion Power in Astrophysics* (Cambridge Univ. Press, Cambridge, 2002).
12. A. F. Illarionov, R. A. Sunyaev, *Astron. Astrophys.* **39**, 185 (1975).
13. M. Ruderman, J. Shaham, M. Tavani, *Astrophys. J.* **336**, 507 (1989).
14. R. F. Webbink, S. Rappaport, G. J. Savonije, *Astrophys. J.* **270**, 678 (1983).
15. S. Rappaport, Ph. Podsiadlowski, P. C. Joss, R. Di Stefano, Z. Han, *Mon. Not. R. Astron. Soc.* **273**, 731 (1995).
16. T. M. Tauris, G. J. Savonije, *Astron. Astrophys.* **350**, 928 (1999).
17. Ph. Podsiadlowski, S. Rappaport, E. D. Pfahl, *Astrophys. J.* **565**, 1107 (2002).
18. The magnetospheric coupling parameter, $0.5 < \varphi < 1.4$ is a numerical factor of order unity depending on the accretion flow, the disk model, and the magnetic inclination angle of the pulsar (*10*, *11*, *32*–*34*).
19. S. L. Shapiro, S. A. Teukolsky, *Black Holes, White Dwarfs, and Neutron Stars: The Physics of Compact Objects* (Wiley-Interscience, New York, 1983).
20. S. A. Rappaport, J. M. Fregeau, H. C. Spruit, *Astrophys. J.* **606**, 436 (2004).
21. L. Burderi *et al.*, *Astrophys. J.* **560**, L71 (2001).
22. This "turn-off problem" has previously been debated elsewhere (*13*, *33*, *35*).
23. R. N. Manchester, J. H. Taylor, *Pulsars* (Freeman, San Francisco, CA, 1977).
24. D. R. Lorimer, A. G. Lyne, L. Festin, L. Nicastro, *Nature* **376**, 393 (1995).
25. F. Alberts, G. J. Savonije, E. P. J. van den Heuvel, O. R. Pols, *Nature* **380**, 676 (1996).
26. L. A. Nelson, E. Dubeau, K. A. MacCannell, *Astrophys. J.* **616**, 1124 (2004).
27. M. H. van Kerkwijk, C. G. Bassa, B. A. Jacoby, P. G. Jonker, in *Binary Radio Pulsars*, F. A. Rasio, I. H. Stairs, Eds. [Astronomical Society of the Pacific (ASP) Conference Series, San Francisco, CA, 2005], vol. 328, pp. 357–370.
28. This is the case if the pulsar spin period, P, is close to its initial spin period, P_0.
29. J. W. T. Hessels *et al.*, *Science* **311**, 1901 (2006).
30. L. Bildsten, *Astrophys. J.* **501**, L89 (1998).
31. D. Chakrabarty *et al.*, *Nature* **424**, 42 (2003).
32. Y.-M. Wang, *Astrophys. J.* **475**, L135 (1997).
33. F. Lamb, W. Yu, in *Binary Radio Pulsars*, F. A. Rasio, I. H. Stairs, Eds. (ASP Conference Series, San Francisco, CA, 2005), vol. 328, pp. 299–310.
34. C. R. D'Angelo, H. C. Spruit, *Mon. Not. R. Astron. Soc.* **406**, 1208 (2010).
35. M. Ruderman, J. Shaham, M. Tavani, D. Eichler, *Astrophys. J.* **343**, 292 (1989).
36. A. Patruno, *Astrophys. J.* **722**, 909 (2010).
37. I. S. Shklovskii, *Sov. Astron.* **13**, 562 (1970).

Acknowledgments: I gratefully thank N. Langer and M. Kramer for discussions and funding and without whom these results would not be possible and R. Eatough for helpful comments on the SOM. This work was partly supported by the Cluster of Excellence proposal EXC 1076, "The nature of forces and matter," at the University of Bonn. Radio pulsar data has been obtained from the *ATNF Pulsar Catalogue* (www.atnf.csiro.au/research/pulsar/psrcat/).

Supporting Online Material

www.sciencemag.org/cgi/content/full/335/6068/561/DC1
Materials and Methods
SOM Text
Figs. S1 and S2
References (*38*–*54*)

8 November 2011; accepted 6 January 2012
10.1126/science.1216355

Revealing the Superfluid Lambda Transition in the Universal Thermodynamics of a Unitary Fermi Gas

Mark J. H. Ku, Ariel T. Sommer, Lawrence W. Cheuk, Martin W. Zwierlein*

Fermi gases, collections of fermions such as neutrons and electrons, are found throughout nature, from solids to neutron stars. Interacting Fermi gases can form a superfluid or, for charged fermions, a superconductor. We have observed the superfluid phase transition in a strongly interacting Fermi gas by high-precision measurements of the local compressibility, density, and pressure. Our data completely determine the universal thermodynamics of these gases without any fit or external thermometer. The onset of superfluidity is observed in the compressibility, the chemical potential, the entropy, and the heat capacity, which displays a characteristic lambda-like feature at the critical temperature $T_c/T_F = 0.167(13)$. The ground-state energy is $\frac{3}{5}\xi N E_F$ with $\xi = 0.376(4)$. Our measurements provide a benchmark for many-body theories of strongly interacting fermions.

Phase transitions are ubiquitous in nature: Water freezes into ice, electron spins suddenly align as materials turn into magnets, and metals become superconducting. Near the transitions, many systems exhibit critical behavior, reflected by singularities in thermodynamic quantities: The magnetic susceptibility diverges at a ferromagnetic transition, and the specific heat

shows a jump at superconducting and superfluid transitions (*1*, *2*), resolved as the famous lambda peak in ^{4}He (*3*). A novel form of superfluidity has been realized in trapped, ultracold atomic gases of strongly interacting fermions, particles with half-integer spin (*4*–*7*). Thanks to an exquisite control over relevant system parameters, these gases have recently emerged as a versatile system well suited to solve open problems in many-body physics (*7*).

Initial measurements on the thermodynamics of strongly interacting Fermi gases have focused on trap-averaged quantities (*8*–*10*) in which the superfluid transition is inherently difficult to observe. The emergence of the condensate of fermion pairs in a spin-balanced Fermi gas is accompanied by only minute changes in the gas density (*5*). Quantities that involve integration of the density over the local potential, such as the energy E (*11*) and the pressure P (*12*), are only weakly sensitive to the sudden variations in the thermodynamics of the gas expected near the superfluid phase transition (*13*).

For a neutral gas, thermodynamic quantities involving the second derivative of the pressure P are expected to become singular at the second-order phase transition into the superfluid state. An example is the isothermal compressibility $\kappa = \frac{1}{n}\frac{\partial n}{\partial P}|_T$, the relative change of the gas density n due to a change in the pressure P. Because the change in pressure is related to the change in chemical potential μ of the gas via $dP = n\, d\mu$ at constant temperature, $\kappa = \frac{1}{n^2}\frac{\partial^2 P}{\partial \mu^2}|_T$ is a second derivative of the pressure, and thus should reveal a clear signature of the transition.

The general strategy to determine the thermodynamic properties of a given substance is to measure an equation of state (EoS), such as the pressure $P(\mu,T)$ as a function of the chemical potential μ and the temperature T. Equivalently, replacing the pressure by the density $n = \frac{\partial P}{\partial \mu}|_T$, one can determine the density EoS $n(\mu,T)$. We directly measure the local gas density $n(V)$ as a function of the local potential V from in situ absorption images of a trapped, strongly interacting Fermi gas of ^{6}Li atoms at a Feshbach resonance (*5*). The trapping potential is cylindrically symmetric, with harmonic confinement along the axial direction; this symmetry allows us to find the three-dimensional (3D) density through the inverse Abel transform of the measured column density (*14*, *15*). The local potential is directly determined from the atomic density distribution and the accurately known harmonic potential along the axial direction.

The compressibility κ follows as the change of the density n with respect to the local potential V experienced by the trapped gas. The change in the local chemical potential is given by the negative change in the local potential, $d\mu = -dV$, and hence the local compressibility is $\kappa = -\frac{1}{n^2}\frac{dn}{dV}|_T$. We can then replace the unknown chemical potential μ in the density EoS $n(\mu,T)$ by the known variation of n with μ in the atom trap, given by κ. Instead of the a priori unknown temperature T, we determine the pressure $P(V) = \int_{-\infty}^{\mu} d\mu' n(\mu') = \int_V^{\infty} dV' n(V')$ given by the integral of the density over the potential (*16*). The resulting equation of state $n(\kappa,P)$ contains only quantities that can be directly obtained from the density distribution. This represents a crucial advance over previous methods that require the input of additional thermodynamic quantities, such as the temperature T and the chemical potential μ, whose determination requires the use of a fitting procedure or an external thermometer, as in (*11*, *12*).

We normalize the compressibility and the pressure by the respective quantities at the same local density for a noninteracting Fermi gas at $T = 0$, $\kappa_0 = \frac{3}{2}\frac{1}{nE_F}$, and $P_0 = \frac{2}{5}nE_F$, where $E_F = \frac{\hbar^2(3\pi^2 n)^{2/3}}{2m}$ is the local Fermi energy and m is the particle mass, yielding $\tilde{\kappa} \equiv \kappa/\kappa_0$ and $\tilde{p} \equiv P/P_0$. For dilute gases at the Feshbach resonance, the scattering length diverges and is no longer a relevant length scale. In the absence of an interaction-dependent length scale, the thermodynamics of such resonant gases are universal (*17*), and $\tilde{\kappa}$ is a universal function of $\tilde{p}$ only. Every experimental profile $n(V)$, irrespective of the trapping potential, the total number of atoms, or the temperature, must produce the same universal curve $\tilde{\kappa}$ versus $\tilde{p}$. By averaging many profiles, one obtains a low-noise determination of $\tilde{\kappa}(\tilde{p})$.

Our method has been tested on the noninteracting Fermi gas that can be studied in two independent ways: in spin-balanced gases near the zero-crossing of the scattering length and in the wings of highly imbalanced clouds at unitarity, where only one spin state is present locally. Both determinations yield the same noninteracting compressibility EoS (Fig. 1).

Figure 1 also shows the compressibility equation of state $\tilde{\kappa}(\tilde{p})$ for the unitary Fermi gas. In the high-temperature ($\tilde{p} >> 1$) regime, the pressure, and hence all other thermodynamic quantities, allow for a Virial expansion in terms of the fugacity $e^{\beta\mu}$ (*18*): $P\,\beta\lambda^3 = 2\sum_j b_j e^{j\beta\mu}$, with the nth-order Virial coefficients b_n. It is known that $b_1 = 1$, $b_2 = 3\sqrt{2}/8$, and $b_3 = -0.29095295$ (*18*); our data show good agreement with the third-order Virial expansion. Fixing b_2 and b_3, our measurement yields a prediction for $b_4 = +0.065(10)$, in agreement with (*12*), but contradicting a recent four-body calculation that gives a negative sign (*19*).

At degenerate temperatures ($\tilde{p} \lesssim 1$), the normalized compressibility rises beyond that of a noninteracting Fermi gas, as expected for an attractively interacting gas. A sudden rise of the compressibility at around $\tilde{p} = 0.55$, followed by a decrease at lower temperatures marks the superfluid transition. The expected singularity of the compressibility at the transition is rounded off by the finite resolution of our imaging system. Below the transition point, the decrease of the compressibility is consistent with the expectation from Bardeen-Cooper-Schrieffer (BCS) theory, in which

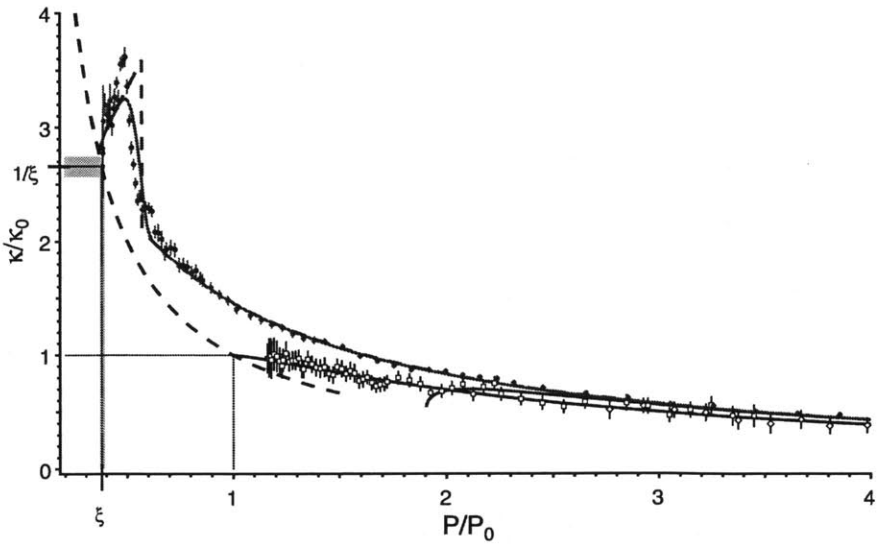

Fig. 1. Normalized compressibility κ/κ_0 versus normalized pressure P/P_0 of the unitary Fermi gas (red solid circles). Each data point is the average of between 30 and 150 profiles. The error bars show mean ± SD, including systematic errors from image calibration (*13*). Blue solid line: third-order Virial expansion. Black open squares (black open diamonds): data for a noninteracting Fermi gas obtained with a highly spin-imbalanced mixture at the Feshbach resonance (spin-balanced gas near zero-crossing of the scattering length). Black solid curve: theory for a noninteracting Fermi gas. Black dashed curve: the relation $\tilde{\kappa} = 1/\tilde{p}$ that must be obeyed at zero temperature both for the noninteracting gas ($\tilde{\kappa} = 1/\tilde{p} = 1$) and the unitary gas ($\tilde{\kappa} = 1/\tilde{p} = 1/\xi$) (dotted lines). Gray band: the uncertainty region for the $T = 0$ value of $\tilde{\kappa} = 1/\xi$ and $\tilde{p} = \xi$. Blue dashed curve: model for the EoS of the unitary Fermi gas [above T_c: interpolation from the Monte Carlo calculation (*34*); below T_c: BCS theory, including phonon and pair-breaking excitations]. Green solid curve: effect of 2 μm optical resolution on the model EoS.

Department of Physics, Massachusetts Institute of Technology (MIT), MIT Harvard Center for Ultracold Atoms, and Research Laboratory of Electronics, MIT, Cambridge, MA 02139, USA.

*To whom correspondence should be addressed. E-mail: zwierlein@mit.edu

single-particle excitations freeze out and pairs form (see model in Fig. 1).

As $T \to 0$, the Fermi energy E_F is the only intensive energy scale, so the chemical potential must be related to E_F by a universal number, $\mu = \xi E_F$, where ξ is known as the Bertsch parameter (*6*, *7*). It follows that at $T = 0$, $\tilde{\kappa} = 1/\tilde{p} = 1/\xi$ (*13*). The extrapolation of the low-temperature experimental data for $\tilde{\kappa}(\tilde{p})$ toward the curve $\tilde{\kappa} = 1/\tilde{p}$ gives $\xi = 0.37(1)$, a value that we find consistently for the normalized chemical potential, energy, and free energy at our lowest temperatures.

From the universal function $\tilde{\kappa}(\tilde{p})$, we obtain all other thermodynamic quantities of the unitary gas. First, to find the normalized temperature T/T_F (where $k_B T_F = E_F$), note that the change in pressure with T/T_F at constant temperature is related to the compressibility. One finds $\frac{d\tilde{p}}{d(T/T_F)} = \frac{5}{2}\frac{T_F}{T}\left(\tilde{p} - \frac{1}{\tilde{\kappa}}\right)$, so by integration (*13*)

$$\frac{T}{T_F} = \left(\frac{T}{T_F}\right)_i exp\left\{\frac{2}{5}\int_{\tilde{p}_i}^{\tilde{p}} d\tilde{p}\frac{1}{\tilde{p} - \frac{1}{\tilde{\kappa}}}\right\} \quad (1)$$

where $(T/T_F)_i$ is the normalized temperature at an initial normalized pressure $\tilde{p}_i$ that can be chosen to lie in the Virial regime validated above.

Thanks to the relation $E = \frac{3}{2}PV$, valid at unitarity (*17*), we can also directly obtain the heat capacity per particle at constant volume $\mathcal{V}$ (*13*),

$$\frac{C_V}{k_B N} \equiv \frac{1}{k_B N}\frac{\partial E}{\partial T}|_{N,\mathcal{V}} = \frac{3}{5}\frac{d\tilde{p}}{d(T/T_F)} = \frac{3}{2}\frac{T_F}{T}\left(\tilde{p} - \frac{1}{\tilde{\kappa}}\right) \quad (2)$$

Figure 2 shows the normalized compressibility and the specific heat as a function of T/T_F. At high temperatures, the specific heat approaches that of a noninteracting Fermi gas and eventually $C_V = \frac{3}{2} N k_B$, the value for a Boltzmann gas. A dramatic rise is observed for T/T_F at around 0.16, followed by a steep drop at lower temperatures. Such a λ-shaped feature in the specific heat is characteristic of second-order phase transitions, as in the famous λ transition in ^{4}He (*3*). Jumps in the specific heat are well known from superconductors (*1*) and ^{3}He (*2*). In experiments on atomic gases, such jumps had only been inferred from derivatives to fit functions that implied a jump (*20*, *21*). We do not expect to resolve the critical behavior very close to T_c. Because of the spatially varying chemical potential in our trapped sample, the critical region is confined to a narrow shell.

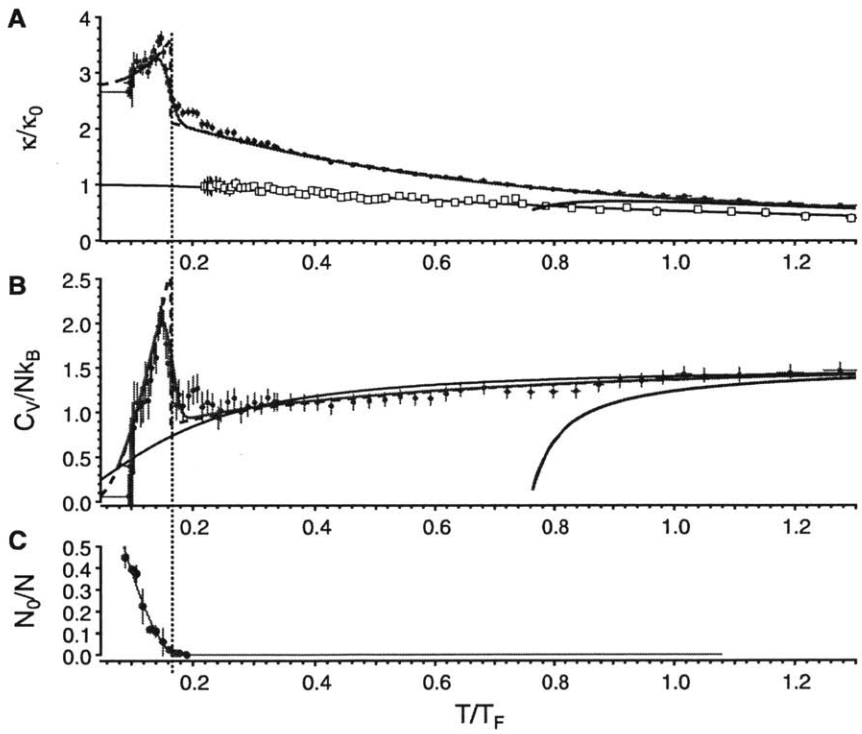

Fig. 2. (A) Normalized compressibility $\tilde{\kappa} = [2/3]\kappa\, n\, E_F$ and **(B)** specific heat per particle C_V/Nk_B of a unitary Fermi gas as a function of reduced temperature T/T_F (solid red circles). Black solid curve: theory for a noninteracting Fermi gas. Blue solid curve: third-order Virial expansion for the unitary gas. Black open squares: data for the normalized compressibility as a function of T/T_F of a noninteracting Fermi gas (combining data from both highly imbalanced gases at unitarity and balanced gases near zero-crossing). Blue dashed (green solid) curve: model from Fig. 1, excluding (including) the effect of finite imaging resolution. **(C)** Global condensate fraction at unitarity as determined from a rapid ramp to the molecular side of the Feshbach resonance, plotted as a function of local T/T_F at the trap center. The onset of condensation coincides with the sudden rise of the specific heat. Error bars, mean ± SD.

Based on the estimate in (*22*), the thickness of the critical shell is 1% of the cloud size. The finite resolution of our imaging system (2 μm or about 5% of the cloud size in the radial direction) suffices to explain the rounding of the singularity expected from criticality. The rounding also reduces the observed jump in the heat capacity at the transition. We obtain a lower bound $\Delta C/C_n \equiv (C_s - C_n)/C_n \geq 1.0^{+4}_{-1}$, where C_s/N (C_n/N) is the specific heat per particle at the peak (the onset of the sudden rise). Considering the strong interactions, this is surprisingly close to the BCS value of 1.43 (*1*). Below T_c, the specific heat is expected to decrease as $\sim \exp(-\Delta_0/k_B T)$ due to the pairing gap Δ_0. At low temperatures, $T \ll T_c$, the phonon contribution $\propto T^3$ dominates (*23*). This behavior is consistent with our data, but the phonon regime is not resolved.

To validate our in situ measurements of the superfluid phase transition, we have employed the rapid ramp method to detect fermion pair condensation (*24*, *25*). The results (Fig. 2C) show that the onset of condensation and the sudden rise in specific heat and compressibility all occur at the same critical temperature, within the error bars. Unlike previous experimental determinations of T_c/T_F for the homogeneous unitary Fermi gas (*11*, *12*), we determine T_c/T_F directly from the density profiles, finding a sudden rise in the specific heat and the onset of condensation at $T_c/T_F = 0.167(13)$. This value is determined as the midpoint of the sudden rise, and the error is assessed as the shift due to the uncertainty of the Feshbach resonance (*13*). This is in very good agreement with theoretical determinations, such as the self-consistent T-matrix approach that gives $T_c/T_F \approx 0.16$ (*23*), and Monte Carlo calculations that give $T_c/T_F = 0.171(5)$ (*26*) and 0.152(7) (*27*). There is a current debate on the possibility of a pseudogap phase of preformed pairs above T_c (*12*, *28*). A pairing gap for single-particle excitations above the transition should be signaled by a downturn of the specific heat above T_c, which is not observed in our measurements.

From the definition of the compressibility $\kappa = \frac{1}{n^2}\frac{\partial n}{\partial \mu}|_T$, we can obtain the reduced chemical potential μ/E_F as a function of the T/T_F (Fig. 3A) (*13*). This function is here obtained from measured quantities, rather than from numerical derivatives of data that involved uncontrolled thermometry (*11*). In the interval of T/T_F from around 0.25 to 1, the chemical potential is close to that of a noninteracting Fermi gas, shifted by $(\xi_n - 1)E_F$ because of interactions present in the normal state, with $\xi_n \approx 0.45$. Unlike a normal Fermi gas, the chemical potential attains a maximum of $\mu/E_F = 0.42(1)$ at $T/T_F = 0.171(10)$, and then decreases at lower temperatures, as expected for a superfluid of paired fermions (*23*). As the temperature is increased from zero in a superfluid, first the emergence of phonons (sound excitations) and then the breaking of fermion pairs contribute to increasing the chemical potential. At T_c, the singular compressibility implies a sharp change in slope for μ/E_F, in agreement with our observa-

tion and theory (*23*). At low temperatures, the reduced chemical potential μ/E_F saturates to the universal value ξ. As the internal energy E and the free energy F satisfy $E(T) > E(0) = \frac{3}{5}N\xi E_F = F(0) > F(T)$ for all T, the reduced quantities $f_E \equiv \frac{5}{3}\frac{E}{NE_F} = \tilde{p}$ and $f_F \equiv \frac{5}{3}\frac{F}{NE_F} = \frac{5}{3}\frac{\mu}{E_F} - \frac{2}{3}\tilde{p}$ (Fig. 3A) provide upper and lower bounds for ξ (*29*). Taking the coldest points of these three curves and including the systematic error due to the effective interaction range, we find $\xi = 0.376(4)$. The uncertainty in the Feshbach resonance is expected to shift ξ by at most 2% (*13*). This value is consistent with a recent upper bound $\xi < 0.383(1)$ from (*30*), is close to $\xi = 0.36(1)$ from a self-consistent T-matrix calculation (*23*), and agrees with $\xi = 0.367(9)$ from an epsilon expansion (*31*). It lies below earlier estimates $\xi = 0.44(2)$ (*32*) and $\xi = 0.42(1)$ (*33*) from fixed-node quantum Monte Carlo calculation that provides upper bounds on ξ. Our measurement agrees with several less accurate experimental determinations (*6*) but disagrees with the most recent experimental value 0.415(10) that was used to calibrate the pressure in (*12*).

From the energy, pressure, and chemical potential, we can obtain the entropy $S = \frac{1}{T}(E + P\mathcal{V} - \mu N)$, and hence the entropy per particle $S/Nk_B = \frac{T_F}{T}\left(\tilde{p} - \frac{\mu}{E_F}\right)$ as a function of T/T_F (Fig. 3B). At high temperatures, S is close to the entropy of an ideal Fermi gas at the same T/T_F. Above T_c, the entropy per particle is nowhere small compared with k_B. Also, the specific heat C_V is not linear in T in the normal phase. This shows that the normal regime above T_c cannot be described in terms of a Landau Fermi Liquid picture, although some thermodynamic quantities agree surprisingly well with the expectation for a Fermi liquid [see (*12*) and (*13*)]. Below about $T/T_F = 0.17$, the entropy starts to strongly fall off compared with that of a noninteracting Fermi gas, which we again interpret as the freezing out of single-particle excitations as a result of the formation of fermion pairs. Far below T_c, phonons dominate. They only have a minute contribution to the entropy (*23*), less than 0.02 k_B at $T/T_F = 0.1$, consistent with our measurements. At the critical point, we obtain $S_c = 0.73(13)\,Nk_B$, in agreement with theory (*23*). It is encouraging for future experiments with fermions in optical lattices that we obtain entropies less than 0.04 $N\,k_B$, far below critical entropies required to reach magnetically ordered phases.

From the chemical potential μ/E_F and $T/T_F = \frac{4\pi}{(3\pi^2)^{2/3}}\frac{1}{(n\lambda^3)^{2/3}}$, we finally obtain the density EoS $n(\mu,T) \equiv \frac{1}{\lambda^3}f_n(\beta\mu)$, with the de Broglie wavelength $\lambda = \sqrt{\frac{2\pi\hbar^2}{mk_BT}}$. The pressure EoS follows as $P(\mu,T) \equiv \frac{k_BT}{\lambda^3}f_P(\beta\mu)$, with $f_P = \frac{2}{5}\frac{T_F}{T}\tilde{p}f_n(\beta\mu)$. Figure 4 shows the density and pressure normalized by their noninteracting counterparts at the same chemical potential and temperature. For the normal state, a concurrent theoretical calculation employing a new Monte Carlo method agrees excellently with our data (*34*). Our data deviate from a previous experimental determination of the pressure EoS (*12*) that was calibrated with an independently measured value of $\xi = 0.415(10)$ (*35*) and disagree with the energy measurement in (*11*) that used a thermometry inconsistent with the Virial expansion (*10*). Around

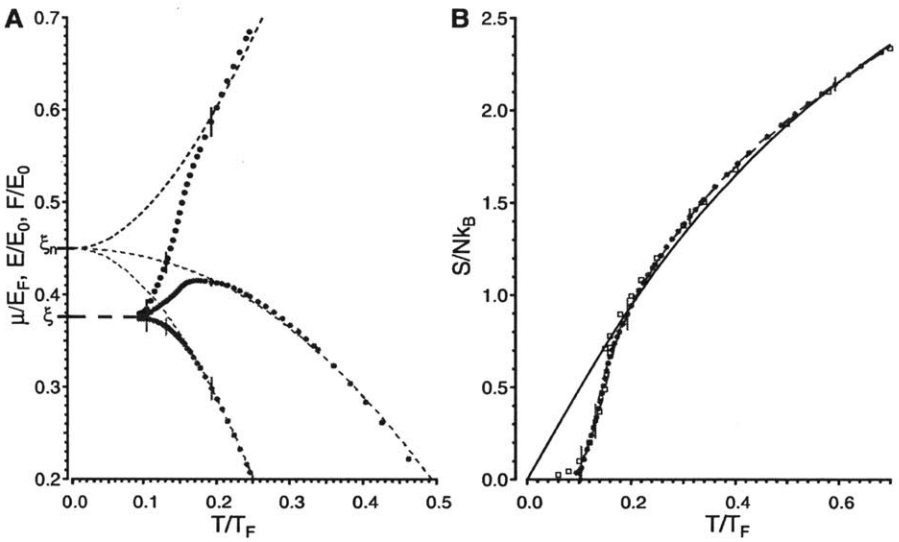

Fig. 3. (**A**) Chemical potential μ, energy E, and free energy F of the unitary Fermi gas versus T/T_F. μ (red solid circles) is normalized by the Fermi energy E_F, and E (black solid circle) and F (green solid circle) are normalized by $E_0 = \frac{3}{5}N\,E_F$. At high temperatures, all quantities approximately track those for a noninteracting Fermi gas, shifted by $\xi_n - 1$ (dashed curves). The peak in the chemical potential signals the onset of superfluidity. In the deeply superfluid regime at low temperatures, μ/E_F, E/E_0, and F/F_0 all approach ξ (blue dashed line). (**B**) Entropy per particle. At high temperatures, the entropy closely tracks that of a noninteracting Fermi gas (black solid curve). The open squares are from the self-consistent T-matrix calculation (*23*). A few representative error bars are shown, representing mean ± SD.

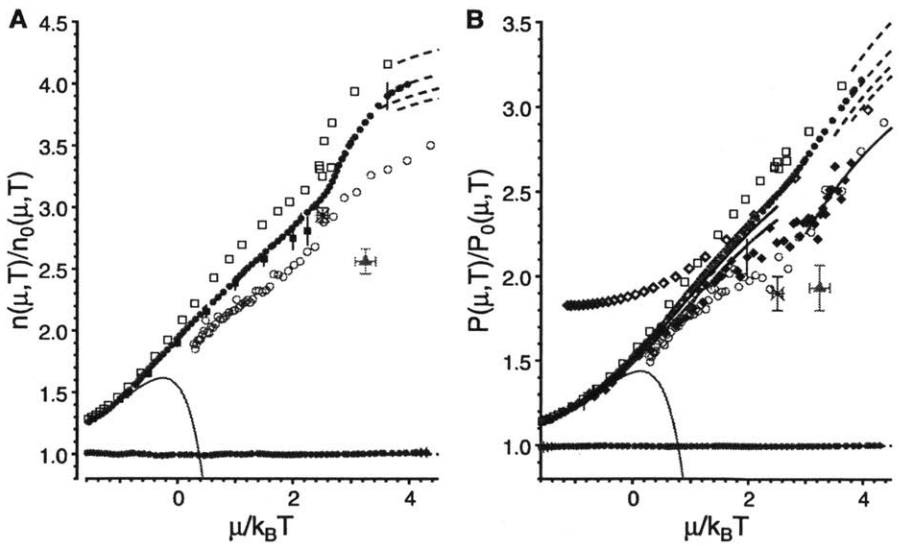

Fig. 4. (**A**) Density and (**B**) pressure of a unitary Fermi gas versus μ/k_BT, normalized by the density and pressure of a noninteracting Fermi gas at the same chemical potential μ and temperature T. Red solid circles: experimental EoS. Blue dashed curves: low-temperature behavior with $\xi = 0.364$ (upper), 0.376 (middle), and 0.388 (lower). Black dashed curve: low-temperature behavior with ξ at upper bound of 0.383 from (*30*). Green solid circles (black fine dashed line): MIT experimental data (theory) for the ideal Fermi gas. Blue solid squares (blue curve): diagrammatic Monte Carlo calculation (*34*) for density (pressure, with blue dashed curves denoting the uncertainty bands). Solid green line: third-order Virial expansion. Open black squares: self-consistent T-matrix calculation (*23*). Open green circles: lattice calculation (*36*). Orange star and blue triangle: critical point from the Monte Carlo calculations (*26*) and (*27*), respectively. Solid diamonds: Ecole Normale Supérieure experiment (*12*). Purple open diamonds: Tokyo experiment (*11*).

the critical point, the density shows a strong variation, whereas the pressure, the integral of the density over μ at constant T, is naturally less sensitive to the superfluid transition.

In conclusion, we have performed thermodynamic measurements of the unitary Fermi gas across the superfluid phase transition at the level of uncertainty of a few percent, without any fits or input from theory, enabling validation of theories for strongly interacting matter. Similar unbiased methods can be applied to other systems, for example, two-dimensional Bose and Fermi gases or fermions in optical lattices.

References and Notes

1. M. Tinkham, *Introduction to Superconductivity* (Dover, Mineola, New York, ed. 2, 2004).
2. D. Vollhardt, P. Wölfle, *The Superfluid Phases of Helium 3* (Taylor & Francis, London, 1990).
3. J. A. Lipa, J. A. Nissen, D. A. Stricker, D. R. Swanson, T. C. P. Chui, *Phys. Rev. B* **68**, 174518 (2003).
4. M. W. Zwierlein, J. R. Abo-Shaeer, A. Schirotzek, C. H. Schunck, W. Ketterle, *Nature* **435**, 1047 (2005).
5. W. Ketterle, M. Zwierlein, *Riv. Nuovo Cim.* **31**, 247 (2008).
6. S. Giorgini, L. P. Pitaevskii, S. Stringari, *Rev. Mod. Phys.* **80**, 1215 (2008).
7. I. Bloch, J. Dalibard, W. Zwerger, *Rev. Mod. Phys.* **80**, 885 (2008).
8. J. Kinast *et al.*, *Science* **307**, 1296 (2005).
9. J. T. Stewart, J. P. Gaebler, C. A. Regal, D. S. Jin, *Phys. Rev. Lett.* **97**, 220406 (2006).
10. L. Luo, B. Clancy, J. Joseph, J. Kinast, J. E. Thomas, *Phys. Rev. Lett.* **98**, 080402 (2007).
11. M. Horikoshi, S. Nakajima, M. Ueda, T. Mukaiyama, *Science* **327**, 442 (2010).
12. S. Nascimbène, N. Navon, K. J. Jiang, F. Chevy, C. Salomon, *Nature* **463**, 1057 (2010).
13. Materials and methods are available as supporting material on *Science* Online.
14. Y. Shin, M. W. Zwierlein, C. H. Schunck, A. Schirotzek, W. Ketterle, *Phys. Rev. Lett.* **97**, 030401 (2006).
15. G. B. Partridge *et al.*, *Phys. Rev. Lett.* **97**, 190407 (2006).
16. C.-H. Cheng, S.-K. Yip, *Phys. Rev. B* **75**, 014526 (2007).
17. T.-L. Ho, *Phys. Rev. Lett.* **92**, 090402 (2004).
18. X.-J. Liu, H. Hu, P. D. Drummond, *Phys. Rev. Lett.* **102**, 160401 (2009).
19. D. Rakshit, K. M. Daily, D. Blume, Thermodynamics of two-component Fermi gas with large scattering length: Fourth- and higher-order virial coefficients, preprint arXiv:1106.5958; available at http://arxiv.org/abs/1106.5958.
20. J. R. Ensher, D. S. Jin, M. R. Matthews, C. E. Wieman, E. A. Cornell, *Phys. Rev. Lett.* **77**, 4984 (1996).
21. L. Luo, J. Thomas, *J. Low Temp. Phys.* **154**, 1 (2009).
22. L. Pollet, N. V. Prokof'ev, B. V. Svistunov, *Phys. Rev. Lett.* **104**, 245705 (2010).
23. R. Haussmann, W. Rantner, S. Cerrito, W. Zwerger, *Phys. Rev. A* **75**, 023610 (2007).
24. C. A. Regal, M. Greiner, D. S. Jin, *Phys. Rev. Lett.* **92**, 040403 (2004).
25. M. W. Zwierlein *et al.*, *Phys. Rev. Lett.* **92**, 120403 (2004).
26. O. Goulko, M. Wingate, *Phys. Rev. A* **82**, 053621 (2010).
27. E. Burovski, N. Prokof'ev, B. Svistunov, M. Troyer, *Phys. Rev. Lett.* **96**, 160402 (2006).
28. J. P. Gaebler *et al.*, *Nat. Phys.* **6**, 569 (2010).
29. Y. Castin, F. Werner, *The BCS-BEC Crossover and the Unitary Fermi Gas*, W. Zwerger, ed. (Springer-Verlag, Berlin, 2012), chap. 5.
30. M. M. Forbes, S. Gandolfi, A. Gezerlis, *Phys. Rev. Lett.* **106**, 235303 (2011).
31. P. Arnold, J. E. Drut, D. T. Son, *Phys. Rev. A* **75**, 043605 (2007).
32. J. Carlson, S.-Y. Chang, V. R. Pandharipande, K. E. Schmidt, *Phys. Rev. Lett.* **91**, 050401 (2003).
33. G. E. Astrakharchik, J. Boronat, J. Casulleras, A. S. Giorgini, *Phys. Rev. Lett.* **93**, 200404 (2004).
34. K. Van Houcke *et al.*, Feynman diagrams versus Fermi-gas Feynman quantum emulator, preprint arXiv:1110.3747 (2011); available at http://arxiv.org/abs/1110.3747.
35. S. Nascimbène, Thermodynamics of ultracold Fermi gases, thesis, Ecole Normale Supérieure, Paris (2010).
36. A. Bulgac, J. E. Drut, P. Magierski, *Phys. Rev. Lett.* **96**, 090404 (2006).

Acknowledgments: We thank B. Svistunov, N. Prokof'ev, and F. Werner for fruitful discussions; Z. Hadzibabic for a critical reading of the manuscript; the authors of (*11*, *12*, *23*, *26*, *27*, *36*) for kindly providing us with their data; and André Schirotzek for help during the early stages of the experiment. M.J.H.K. acknowledges financial support from NSERC. This work was supported by the NSF, Air Force Office of Scientific Research (AFOSR) - Multidisciplinary Research Program of the University Research Initiative (MURI), Army Research Office (ARO) - MURI, Office of Naval Research, Defense Advanced Research Projects Agency (DARPA) Young Faculty Award, a grant from the ARO with funding from the DARPA Optical Lattice Emulator program, an AFOSR Presidential Early Career Award in Science and Engineering, the David and Lucile Packard Foundation, and the Alfred P. Sloan Foundation.

Supporting Online Material

www.sciencemag.org/cgi/content/full/science.1214987/DC1
Materials and Methods
Figs. S1 to S4
References (*37–45*)

7 October 2011; accepted 3 January 2012
Published online 12 January 2012;
10.1126/science.1214987

Iron Catalysts for Selective Anti-Markovnikov Alkene Hydrosilylation Using Tertiary Silanes

Aaron M. Tondreau,[1] Crisita Carmen Hojilla Atienza,[1] Keith J. Weller,[2] Susan A. Nye,[2] Kenrick M. Lewis,[3] Johannes G. P. Delis,[4] Paul J. Chirik[1]*

Alkene hydrosilylation, the addition of a silicon hydride (Si-H) across a carbon-carbon double bond, is one of the largest-scale industrial applications of homogeneous catalysis and is used in the commercial production of numerous consumer goods. For decades, precious metals, principally compounds of platinum and rhodium, have been used as catalysts for this reaction class. Despite their widespread application, limitations such as high and volatile catalyst costs and competing side reactions have persisted. Here, we report that well-characterized molecular iron coordination compounds promote the selective anti-Markovnikov addition of sterically hindered, tertiary silanes to alkenes under mild conditions. These Earth-abundant base-metal catalysts, coordinated by optimized bis(imino)pyridine ligands, show promise for industrial application.

Metal-catalyzed olefin hydrosilylation, which forms alkylsilanes by cleaving a silicon-hydrogen bond and adding the fragments across a carbon-carbon double bond (*1*, *2*), finds widespread application in the commercial manufacture of silicone-based surfactants, fluids, molding products, release coatings, and pressure-sensitive adhesives (*3*, *4*). Consequently, hydrosilylation has emerged as one of the largest-scale applications of homogeneous catalysis (*5–9*). For more than three decades, precious metal compounds with Pt, Pd, Ru, and Rh have been used almost exclusively as catalysts. Platinum compounds such as Karstedt's and Speier's catalysts, $Pt_2\{[(CH_2{=}CH)SiMe_2]_2O\}_3$ (Me, methyl) and $H_2PtCl_6{\cdot}6H_2O/^iPrOH$ (^{i}Pr, isopropyl), respectively, are the most widely used industrial catalysts (*1*, *10–12*), though they suffer from chemical limitations such as intolerance to amino-substituted olefins and a tendency to catalyze competing isomerization of the terminal alkenes to internal isomers. Undesired isomerization often necessitates subsequent purification steps that are both energy and cost intensive. Furthermore, decomposition of the catalyst to colloidal platinum contributes to unwanted side reactions and also causes discoloration of the final products.

It has been estimated that the worldwide silicone industry consumed ~180,000 troy ounces (5.6 metric tons) of platinum in 2007 and most is not recovered (*13*). The high cost, coupled with the increasing demands on precious metals due to fuel-cell and other emerging technologies, has increased the volatility of the platinum market (*14*). The combination of chemical, economic, and political challenges inspires the exploration of inexpensive and Earth-abundant catalysts using iron, manganese, and cobalt (*15*). At the core of this challenge is suppressing tendencies of first-row transition metals toward one-electron redox processes in favor of the two-electron chemistry associated with the heavier metals that probably make up the fundamental steps in a catalytic cycle for alkene hydrosilylation.

[1]Department of Chemistry, Princeton University, Princeton, NJ 08544, USA. [2]Momentive Performance Materials, 260 Hudson River Road, Waterford, NY 12188, USA. [3]Momentive Performance Materials, 769 Old Saw Mill River Road, Tarrytown, NY 10591, USA. [4]Momentive Performance Materials bv, Plasticslaan 1, 4612PX Bergen op Zoom, Netherlands.

*To whom correspondence should be addressed. E-mail: pchirik@princeton.edu

Appendix D

Evolution of Fermion Pairing from Three to Two Dimensions

This appendix contains a reprint of Ref. [147]: Ariel T. Sommer, Lawrence W. Cheuk, Mark J. H. Ku, Waseem S. Bakr, and Martin W. Zwierlein, *Evolution of Fermion Pairing from Three to Two Dimensions*, Phys. Rev. Lett. **108**, 045302 (2012).

Evolution of Fermion Pairing from Three to Two Dimensions

Ariel T. Sommer, Lawrence W. Cheuk, Mark J. H. Ku, Waseem S. Bakr, and Martin W. Zwierlein

Department of Physics, MIT-Harvard Center for Ultracold Atoms, and Research Laboratory of Electronics, MIT, Cambridge, Massachusetts 02139, USA

(Received 13 October 2011; published 23 January 2012)

We follow the evolution of fermion pairing in the dimensional crossover from three-dimensional to two-dimensional as a strongly interacting Fermi gas of ^{6}Li atoms becomes confined to a stack of two-dimensional layers formed by a one-dimensional optical lattice. Decreasing the dimensionality leads to the opening of a gap in radio-frequency spectra, even on the Bardeen-Cooper-Schrieffer side of a Feshbach resonance. The measured binding energy of fermion pairs closely follows the theoretical two-body binding energy and, in the two-dimensional limit, the zero-temperature mean-field Bose-Einstein-condensation to Bardeen-Cooper-Schrieffer crossover theory.

DOI: 10.1103/PhysRevLett.108.045302 PACS numbers: 67.85.−d, 03.75.Lm, 05.30.Fk, 32.30.Bv

Interacting fermions in coupled two-dimensional (2D) layers present unique physical phenomena and are central to the description of unconventional superconductivity in high-transition-temperature cuprates [1] and layered organic conductors [2]. Experiments on ultracold gases of fermionic atoms have allowed access to the crossover from Bose-Einstein condensation (BEC) of tightly bound fermion pairs to Bardeen-Cooper-Schrieffer (BCS) superfluidity of long-range Cooper pairs in three spatial dimensions [3,4] and, more recently, the confinement of interacting Fermi gases to two spatial dimensions [5–9]. A fermionic superfluid loaded into a periodic potential should form stacks of two-dimensional superfluids with tunable interlayer coupling [10–13], an ideal model for Josephson-coupled quasi-2D superconductors [1,14]. For deep potentials in the regime of uncoupled 2D layers, increasing the temperature of the gas is expected to destroy superfluidity through the Berezinskii-Kosterlitz-Thouless mechanism [15–17], while more exotic multiplane vortex loop excitations are predicted for a three-dimensional (3D) anisotropic BCS superfluid near the critical point [18].

In this Letter, we study fermion pairing across the crossover from 3D to 2D in a periodic potential of increasing depth. To form a bound state in 3D, the attraction between two particles in a vacuum must exceed a certain threshold. However, if the two particles interact in the presence of a Fermi sea, the Cooper mechanism allows pairing for arbitrarily weak interactions [19]. In 2D, even two particles in a vacuum can bind for arbitrarily weak interactions. Surprisingly, the mean-field theory of the BEC-BCS crossover in 2D predicts that the binding energy of fermion pairs in the many-body system is identical to the two-body binding energy E_b [20]. Indeed, to break a pair and remove one pairing partner from the system costs an energy [21] $E_{b,\mathrm{MF}} = \sqrt{\mu^2 + \Delta^2} - \mu$ within mean-field theory, where μ is the chemical potential and Δ is the pairing gap. In 2D, one finds [20] $\mu = E_F - E_b/2$ and $\Delta^2 = 2E_F E_b$, where E_F is the Fermi energy, and thus $E_{b,\mathrm{MF}} = E_b$; i.e., the many-body and two-body binding energies are predicted to be identical throughout the BEC-BCS crossover.

We realize a system that is tunable from 3D to 2D with a gas of ultracold fermionic ^{6}Li atoms trapped in an optical trap and a standing-wave optical lattice. The lattice produces a periodic potential along the z direction,

$$V(z) = V_0 \sin^2(\pi z/d), \tag{1}$$

with depth V_0 and lattice spacing $d = 532$ nm. Together with the optical trap, the lattice interpolates between the 3D and 2D limits. It gradually freezes out motion along one dimension and confines particles in increasingly uncoupled layers. Features characteristic of the 2D system appear as the strength of the periodic potential is increased. The threshold for pairing is reduced, allowing pairs to form for weaker attractive interactions than in the 3D system. The effective mass of particles increases along the confined direction, and the center of mass and relative degrees of freedom of an atom pair become coupled [11]. For a deep potential that suppresses interlayer tunneling, the system is an array of uncoupled two-dimensional layers. Here, the center of mass and relative motion decouple and fermion pairs form for the weakest interatomic attraction [11,22,23].

In the experiment, the appearance of bound fermion pairs is revealed using radio-frequency (rf) spectroscopy. The atomic gas consists of an equal mixture of ^{6}Li atoms in the first and third hyperfine states (denoted as $|1\rangle$ and $|3\rangle$), chosen to minimize final-state interaction effects in the rf spectra [24]. Interactions between atoms in states $|1\rangle$ and $|3\rangle$ are greatly enhanced by a broad Feshbach resonance at 690.4(5) G [25]. An rf pulse is applied to transfer atoms from one of the initial hyperfine states to the unoccupied second hyperfine state (denoted as $|2\rangle$). In previous work on rf spectroscopy of ^{40}K fermions in a deep one-dimensional (1D) lattice [8], an rf pulse transferred atoms from an initially weakly interacting state into a strongly interacting spin state, likely producing polarons [26]. In

our Letter, the initial state is the strongly interacting, largely paired Fermi gas in equilibrium, and the final state is weakly interacting.

An asymmetric dissociation peak (the bound-to-free transition) in the rf spectrum indicates the presence of fermion pairs. For two-particle binding, the pair dissociation line shape in the 3D and 2D limits is proportional to $\rho(h\nu - E_b)/\nu^2$, with ρ the free-particle density of states and $\nu = \pm(\nu_{\rm rf} - \nu_{\rm hf})$ the offset of the rf frequency $\nu_{\rm rf}$ from the hyperfine splitting $\nu_{\rm hf}$ (plus symbol: $|1\rangle \rightarrow |2\rangle$ transition; minus symbol: $|3\rangle \rightarrow |2\rangle$ transition). This form can be obtained from Fermi's golden rule and the bound-state wave function in momentum space; see also Refs. [21,27]. In 2D, the expected dissociation line shape is then proportional to

$$I(\nu) \propto \frac{\theta(h\nu - E_b)}{\nu^2}. \quad (2)$$

In addition to the pairing peak, at finite temperature one expects a peak in the rf spectrum due to unbound atoms (the free-to-free transition). A narrow bound-to-bound transition can also be driven at an offset frequency $\nu_{bb} = (E_b - E_b')/h$ that transfers one spin state of the initial bound pair with binding energy E_b into a bound state of $|2\rangle$ with $|1\rangle$ or $|3\rangle$, of binding energy E_b'. For a $|1\rangle - |3\rangle$ mixture near the Feshbach resonance, $E_b \ll E_b'$ [24], so the bound-to-bound peak is well-separated from the bound-to-free and free-to-free peaks. As very recently calculated [28], final-state interactions and the anomalous nature of scattering in 2D introduce an additional factor of $\frac{\ln^2(E_b/E_b')}{\ln^2[(h\nu - E_b)/E_b'] + \pi^2}$ into Eq. (2), causing a rounding off of the sharp peak expected from the step function.

In a 1D lattice, the binding energy for two-body pairs is determined by the lattice spacing d, the depth V_0, and the 3D scattering length a. In the 2D limit $V_0 \gg E_R$, with recoil energy $E_R = \frac{\hbar^2\pi^2}{2md^2}$, the scattering properties of the gas are completely determined by E_b [22,23]. In that limit, the lattice wells can be approximated as harmonic traps with level spacing $\hbar\omega_z = 2\sqrt{V_0 E_R}$ and harmonic oscillator length $l_z = \sqrt{\frac{\hbar}{m\omega_z}}$. In a many-particle system in 2D, the ratio of the binding energy to the Fermi energy determines the strength of interactions. The 2D scattering amplitude $f(E_F) = \frac{2\pi}{-\ln(k_F a_{2D}) + i\pi/2}$ for collisions with energy E_F is parametrized by $\ln(k_F a_{2D})$, where $k_F = \sqrt{2mE_F}/\hbar$ and $a_{2D} = \hbar/\sqrt{mE_b}$. It is large when $|\ln(k_F a_{2D})| \lesssim 1$ [22,23], corresponding to the strong-coupling regime [28,29]. The BEC side of the BEC-BCS crossover corresponds to negative values of $\ln(k_F a_{2D})$, while the BCS side corresponds to positive values [20].

The experimental sequence proceeds as follows. An ultracold gas of ^{6}Li is produced by sympathetic cooling with ^{23}Na as described previously [21]. The ^{6}Li atoms are transferred from a magnetic trap to an optical dipole trap (wavelength 1064 nm, waist 120 μm), with axial harmonic confinement (frequency 22.8 Hz) provided by magnetic field curvature. With ^{6}Li polarized in state $|1\rangle$, the magnetic bias field is raised to 568 G, and an equal mixture of hyperfine states $|1\rangle$ and $|3\rangle$ is created using a 50% rf transfer from $|1\rangle$ to $|2\rangle$ followed by a full transfer from $|2\rangle$ to $|3\rangle$. The field is then raised to the final value, and evaporative cooling is applied by lowering the depth of the optical dipole trap, resulting in a fermion pair condensate with typically 5×10^5 atoms per spin state. The lattice is then ramped up over 100 ms. The retro-reflected lattice beam (wavelength 1064 nm) is at an angle of 0.5 degrees from the optical dipole trap beam, enough to selectively reflect only the lattice beam. The depth of the lattice is calibrated using Kapitza-Dirac diffraction of a ^{23}Na BEC and a $^6Li_2$ molecular BEC and by lattice modulation spectroscopy on the ^{6}Li cloud. The magnetic field and hyperfine splitting are calibrated using rf spectroscopy on spin-polarized clouds. After loading the lattice, the rf pulse is applied for a duration of typically 1 ms. Images of state $|2\rangle$ and either $|1\rangle$ or $|3\rangle$ are recorded in each run of the experiment.

To ensure loading into the first Bloch band, the Fermi energy and temperature of the cloud are kept below the second band. The 2D Fermi energy $E_F^{\rm 2D} = \frac{2\pi\hbar^2 n}{m}$, with n the 2D density per spin state, is typically $h \times 10$ kHz. The bottom of the second band is at least one recoil energy $E_R = h \times 29.3$ kHz above the bottom of the first band in shallow lattices and up to about $h \times 300$ kHz for the deepest lattices. The temperature is estimated to be on the order of the Fermi energy.

rf spectra are recorded for various lattice depths and interaction strengths. Figure 1 shows examples of spectra over a range of lattice depths at the 3D Feshbach resonance and on the BCS side of the resonance at 721 G, where fermion pairing in 3D is a purely many-body effect. At the lowest lattice depths, the spectra show only a single peak, shifted to positive offset frequencies due to many-body interactions. This is similar to the case without a lattice [24,30]; to discern a peak due to fermion pairs from a peak due to unbound atoms would require locally resolved rf spectroscopy of imbalanced Fermi gases [30]. However, as the lattice depth is raised, the single peak splits into two and a clear pairing gap emerges. The narrow peak at zero offset is the free-to-free transition, and the asymmetric peak at positive offset is the pair dissociation spectrum. The pair spectrum, especially on resonance, shows a sharp threshold and a long tail corresponding to dissociation of fermion pairs into free atoms with nonzero kinetic energy.

Binding energies are determined from the offset frequency of the pairing threshold. Although the line shape in Eq. (2) jumps discontinuously from zero to its maximum value, the spectra are observed to be broadened. This is to a large part due to the logarithmic corrections [28] noted above, which predict a gradual rise at the threshold $h\nu = E_b$, and a spectral peak that is slightly shifted from

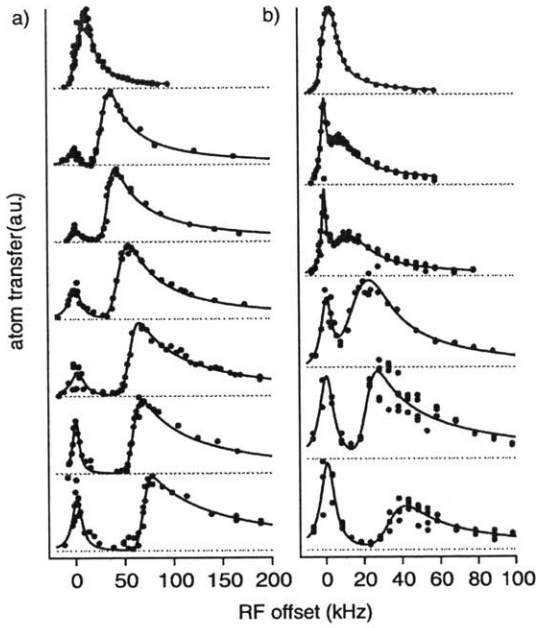

FIG. 1 (color online). Evolution of fermion pairing in the 3D-to-2D crossover in a one-dimensional optical lattice, observed via rf spectroscopy. Shown is the transferred atom number versus rf offset frequency relative to the atomic hyperfine splitting. (a) Spectra at the Feshbach resonance at 690.7(1) G with $d/a = -0.01(4)$. Lattice depths from top to bottom in units of E_R: 1.84(3), 4.8(2), 6.1(2), 9.9(4), 12.2(4), 18.6(7), and 19.5 (7). (b) Spectra on the BCS side at 720.7(1) G, $d/a = -1.15(2)$. Lattice depths in units of E_R: 2.75(5), 4.13(7), 4.8(1), 6.0(2), 10.3 (2), and 18.1(4).

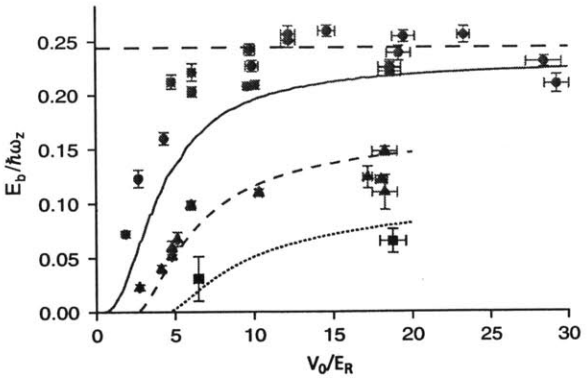

FIG. 2 (color online). Binding energy E_b versus lattice depth V_0 at several values of the 3D scattering length a. E_b is normalized via the lattice frequency ω_z. Red circles: results from spectra at 690.7(1) G and $d/a = -0.01(4)$. Green triangles: 720.7(1) G, $d/a = -1.15(2)$. Blue squares: 800.1(1) G, $d/a = -2.69(1)$. Curves show predictions from Orso *et al.* [11]. Horizontal black dashed line: harmonic approximation result for $1/a = 0$.

E_b. We include possible additional broadening by convolving the theoretical line shape, including the logarithmic correction, with a Gaussian function of width w_m. The parameters E_b and w_m are determined by a least-squares fit to the measured spectrum. Typical spectra have w_m of 5 kHz, consistent with our estimates of broadening based on collisions and three-body losses. The Fourier broadening is 1 kHz. Power broadening is about 5 kHz on the free-to-free transition and less than 1 kHz on the bound-to-free transition due to the reduced wave function overlap. Inclusion of the logarithmic correction is found to be necessary in order for the fit function to reproduce the observed behavior of the high-frequency tail. The final-state binding energy used in the logarithmic correction for fitting is obtained from spectra where both a bound-to-bound and a bound-to-free peak were measured. At low lattice depths, the 2D form for the paired spectrum should differ from the exact shape that interpolates between the 3D and 2D limits. In the case where the shape of the spectrum is given by the 3D limit, fitting to the 2D form overestimates the binding energy by 8%.

Figure 2 shows the measured binding energies as function of V_0/E_R for several interaction strengths. The binding energies are normalized by $\hbar\omega_z \equiv 2\sqrt{V_0 E_R}$, which equals the level spacing in the harmonic approximation to the lattice potential. The measured binding energies grow with increasing lattice depth and agree reasonably well with theoretical predictions for two-body bound pairs in a 1D lattice [11]. The binding energy at the 3D resonance approaches a constant multiple of $\hbar\omega_z$ as the lattice depth increases, as expected from the 2D limit [22,23]. Figure 3(a) compares the binding energies measured in lattices deeper than $17E_R$ to predictions in the harmonic quasi-2D limit [22,23]. At the 3D Feshbach resonance, we find $E_b = 0.232(16)\hbar\omega_z$ for deep lattices. The error bar refers to the standard error on the mean. This value is close to the harmonic confinement result of $0.244\hbar\omega_z$ [23]. The exact calculation [11] predicts a constant downward shift of the binding energy by $0.2E_R$ for deep lattices due to the anharmonicity of the sinusoidal potential. For V_0 of about $20E_R$, this gives a prediction of $0.22\hbar\omega_z$, also close to the measured value.

Figure 3(b) shows the binding energy measured in deep lattices normalized by the exact two-body result [11] versus the many-body interaction parameter $\ln(k_F a_{2D})$. Overall, the binding energies are close to the two-body value, even in the strong-coupling regime for $|\ln(k_F a_{2D})| < 1$, as predicted by zero-temperature mean-field theory [20]. The data show a slight downward deviation for the strongest coupling. At fixed reduced temperature T/T_F, the relationship should be universal. It will thus be interesting to see in future work whether the binding energy depends significantly on temperature.

The bound-to-bound transition is seen in Fig. 4 as a narrow peak at negative offset frequencies. In the regime where E_b can be found from the pair dissociation spectrum,

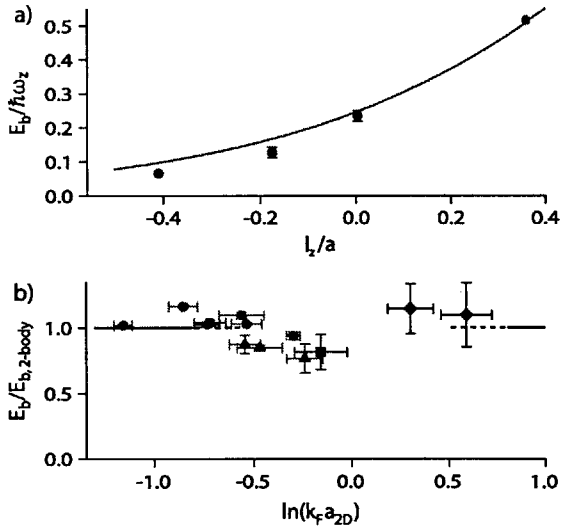

FIG. 3 (color online). (a) Binding energy of fermion pairs versus interaction strength l_z/a for deep lattices ($V_0 > 17E_R$). Solid curve: theoretical prediction in the 2D harmonic limit [22,23]. (b) Ratio of the measured binding energy to the two-body result [11] versus $\ln(k_F a_{2D})$ for $V_0 > 17E_R$. Black diamonds: binding energy determined from the bound-to-bound transition with resonant final-state interactions. Other data symbols: see Fig. 2. Horizontal line: zero-temperature mean-field theory [20].

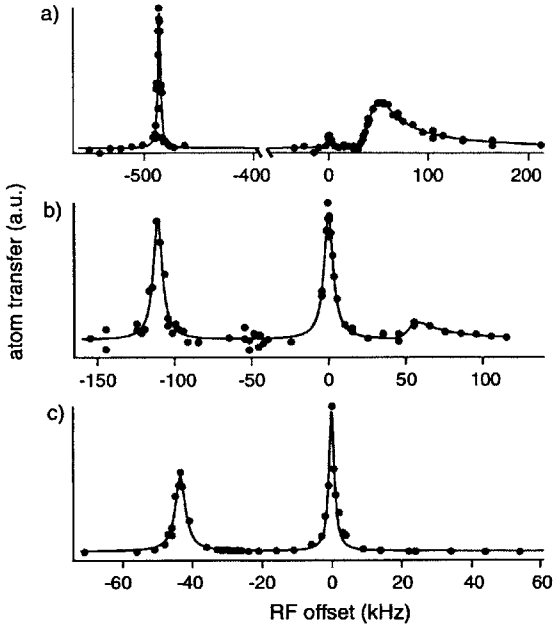

FIG. 4 (color online). Spectra including the bound-to-bound transition, a narrow peak at negative rf offset. Shown are spectra at magnetic fields of (a) 690.7(1) G, (b) 751.1(1) G, and (c) 834.4(1). The interaction parameters d/a are (a) $-0.01(4)$, (b) $-1.91(1)$, and (c) $-3.06(1)$. Lattice depths in units of E_R are (a) 9.59(7), (b) 26.1(4), and (c) 26.4(3). The bound-to-free transition is not visible in (c). The transfer is from $|1\rangle$ to $|2\rangle$ in (a) and (b) and from $|3\rangle$ to $|2\rangle$ in (c).

the bound-to-bound peak position directly yields the binding energy in the final state E_b'. For example, the spectrum in Fig. 4(a), taken at the 3D $|1\rangle - |3\rangle$ resonance at 690.7(1) G and $V_0/E_R = 9.59(7)$, gives $E_b'/E_R = 18.0(1)$ at a final-state interaction of $d/a' = 8.41(2)$. Likewise, the spectrum in Fig. 4(b) at $V_0/E_R = 26.1(4)$ and a magnetic field of 751.1(1) G, where $d/a' = 2.55(1)$, gives $E_b'/E_R = 5.3(1)$. An independent measurement for $d/a = 2.55(2)$ using the bound-to-free spectrum at 653.55 G yields $E_b/E_R = 5.25(2)$, showing that bound-to-bound transitions correctly indicate binding energies.

The BCS side of the 2D BEC-BCS crossover is reached in Fig. 4(c) by increasing the number of atoms to increase E_F and increasing the magnetic field to reach a lower binding energy. In Fig. 4(c), the central Fermi energy is $h \times 43(6)$ kHz and $T/T_F = 0.5(2)$. The magnetic field is set to 834.4(1) G, where $d/a = -3.06(1)$, and the final-state interactions between $|1\rangle$ and $|2\rangle$ are resonant, with $d/a' = -0.01(3)$. The lattice depth is $V_0/E_R = 26.4(3)$. Thus, we know that $E_b' = 0.232(16)\hbar\omega_z = 2.4(2)E_R$ at this lattice depth. From the bound-to-bound transition in Fig. 4(c), we can then directly determine the binding energy of $|1\rangle - |3\rangle$ fermion pairs to be $E_b/E_R = 0.9(2)$. The theoretical prediction [11] for two-body binding gives $E_b/E_R = 0.82(1)$. The measured binding energy gives a many-body interaction parameter of $\ln(k_F a_{2D}) = 0.6(1)$, on the BCS side but within the strongly interacting regime, where one expects many-body effects beyond mean-field BEC-BCS theory [26,29]. It is therefore interesting that the measured binding energy is close to the expected two-body binding energy to much better than the Fermi energy, as predicted by mean-field theory [20].

In conclusion, we have measured the binding energy of fermion pairs along the crossover from 3D to 2D in a one-dimensional optical lattice. Measurements were performed at several lattice depths and scattering lengths, allowing quantitative comparison with theoretical predictions. Considering the fact that the gas is a strongly interacting many-body system, the close agreement with two-body theory is surprising, especially in the strong-coupling regime. While mean-field BEC-BCS theory in 2D predicts this behavior [20], it misses other important features of the many-body system, most strikingly the interaction between fermion pairs [13]. Superfluidity in a one-dimensional lattice will be an exciting topic for future studies. Stacks of weakly coupled, superfluid 2D layers would constitute a basic model of the geometry found in high-temperature superconductors.

The authors would like to thank G. Orso for providing his code to calculate binding energies and M. Köhl and W. Zwerger for stimulating discussions. This work was supported by the NSF, AFOSR-MURI, ARO-MURI, ONR, DARPA YFA, a grant from the Army Research Office with

funding from the DARPA OLE program, the David and Lucile Packard Foundation, and the Alfred P. Sloan Foundation.

[1] M. Tinkham, *Introduction to Superconductivity* (Dover, Mineola, NY, 2004), 2nd ed., p. 318.
[2] J. Singleton and C. Mielke, Contemp. Phys. **43**, 63 (2002).
[3] *Ultracold Fermi Gases*, Proceedings of the International School of Physics "Enrico Fermi," Course CLXIV, edited by M. Inguscio, W. Ketterle, and C. Salomon (Elsevier, Amsterdam, 2008).
[4] S. Giorgini, L. P. Pitaevskii, and S. Stringari, Rev. Mod. Phys. **80**, 1215 (2008).
[5] K. Günter, T. Stöferle, H. Moritz, M. Köhl, and T. Esslinger, Phys. Rev. Lett. **95**, 230401 (2005).
[6] X. Du, Y. Zhang, and J. E. Thomas, Phys. Rev. Lett. **102**, 250402 (2009).
[7] K. Martiyanov, V. Makhalov, and A. Turlapov, Phys. Rev. Lett. **105**, 030404 (2010).
[8] B. Fröhlich, M. Feld, E. Vogt, M. Koschorreck, W. Zwerger, and M. Köhl, Phys. Rev. Lett. **106**, 105301 (2011).
[9] P. Dyke, E. D. Kuhnle, S. Whitlock, H. Hu, M. Mark, S. Hoinka, M. Lingham, P. Hannaford, and C. J. Vale, Phys. Rev. Lett. **106**, 105304 (2011).
[10] G. Orso and G. V. Shlyapnikov, Phys. Rev. Lett. **95**, 260402 (2005).
[11] G. Orso, L. P. Pitaevskii, S. Stringari, and M. Wouters, Phys. Rev. Lett. **95**, 060402 (2005).
[12] L. Salasnich, Phys. Rev. A **76**, 015601 (2007).
[13] W. Zhang, G.-D. Lin, and L.-M. Duan, Phys. Rev. A **77**, 063613 (2008).
[14] S. T. Ruggiero, T. W. Barbee, and M. R. Beasley, Phys. Rev. Lett. **45**, 1299 (1980).
[15] J. M. Kosterlitz and D. Thouless, J. Phys. C **5**, L124 (1972).
[16] D. S. Petrov, M. A. Baranov, and G. V. Shlyapnikov, Phys. Rev. A **67**, 031601 (2003).
[17] W. Zhang, G.-D. Lin, and L.-M. Duan, Phys. Rev. A **78**, 043617 (2008).
[18] M. Iskin and C. A. R. Sá de Melo, Phys. Rev. Lett. **103**, 165301 (2009).
[19] L. N. Cooper, Phys. Rev. **104**, 1189 (1956).
[20] M. Randeria, J.-M. Duan, and L. Y. Shieh, Phys. Rev. Lett. **62**, 981 (1989).
[21] W. Ketterle and M. Zwierlein, Riv. Nuovo Cimento Soc. Ital. Fis. **31**, 247 (2008).
[22] D. S. Petrov and G. V. Shlyapnikov, Phys. Rev. A **64**, 012706 (2001).
[23] I. Bloch, J. Dalibard, and W. Zwerger, Rev. Mod. Phys. **80**, 885 (2008).
[24] C. Schunck, Y. Shin, A. Schirotzek, and W. Ketterle, Nature (London) **454**, 739 (2008).
[25] M. Bartenstein, A. Altmeyer, S. Riedl, R. Geursen, S. Jochim, C. Chin, J. H. Denschlag, R. Grimm, A. Simoni, E. Tiesinga, C. J. Williams, and P. S. Julienne, Phys. Rev. Lett. **94**, 103201 (2005).
[26] V. Pietila, D. Pekker, Y. Nishida, and E. Demler, arXiv:1110.0494.
[27] C. Chin and P. S. Julienne, Phys. Rev. A **71**, 012713 (2005).
[28] C. Langmack, M. Barth, W. Zwerger, and E. Braaten, arXiv:1111.0999.
[29] G. Bertaina and S. Giorgini, Phys. Rev. Lett. **106**, 110403 (2011).
[30] A. Schirotzek, Y.-i. Shin, C. H. Schunck, and W. Ketterle, Phys. Rev. Lett. **101**, 140403 (2008).

Appendix E

Spin-Injection Spectroscopy of a Spin-Orbit Coupled Fermi Gas

This appendix contains a reprint of Ref. [25]: Lawrence W. Cheuk, Ariel T. Sommer, Zoran Hadzibabic, Tarik Yefsah, Waseem S. Bakr, and Martin W. Zwierlein, *Spin-Injection Spectroscopy of a Spin-Orbit Coupled Fermi Gas*, Phys. Rev. Lett. **109**, 095302 (2012).

Spin-Injection Spectroscopy of a Spin-Orbit Coupled Fermi Gas

Lawrence W. Cheuk,[1] Ariel T. Sommer,[1] Zoran Hadzibabic,[1,2] Tarik Yefsah,[1] Waseem S. Bakr,[1] and Martin W. Zwierlein[1]

[1]*Department of Physics, MIT-Harvard Center for Ultracold Atoms, and Research Laboratory of Electronics, MIT, Cambridge, Massachusetts 02139, USA*

[2]*Cavendish Laboratory, University of Cambridge, J. J. Thomson Avenue, Cambridge CB3 0HE, United Kingdom*

(Received 25 June 2012; published 27 August 2012)

The coupling of the spin of electrons to their motional state lies at the heart of recently discovered topological phases of matter. Here we create and detect spin-orbit coupling in an atomic Fermi gas, a highly controllable form of quantum degenerate matter. We directly reveal the spin-orbit gap via spin-injection spectroscopy, which characterizes the energy-momentum dispersion and spin composition of the quantum states. For energies within the spin-orbit gap, the system acts as a spin diode. We also create a spin-orbit coupled lattice and probe its spinful band structure, which features additional spin gaps and a fully gapped spectrum. In the presence of s-wave interactions, such systems should display induced p-wave pairing, topological superfluidity, and Majorana edge states.

DOI: 10.1103/PhysRevLett.109.095302 PACS numbers: 67.85.Lm, 03.65.Vf, 03.65.Wj, 03.75.Ss

Spin-orbit coupling is responsible for a variety of phenomena, from the fine structure of atomic spectra to the spin Hall effect, topological edge states, and, in the presence of interactions, the predicted phenomenon of topological superconductivity [1,2]. In electronic systems, spin-orbit coupling arises from the relativistic transformation of electric fields into magnetic fields in a moving reference frame. In the reference frame of an electron moving with wave vector $\mathbf{k}$ in an electric field, the motional magnetic field couples to the electron spin through the magnetic dipole interaction. In a two-dimensional semiconductor heterostructure, the electric field can arise from structure or bulk inversion asymmetry [3], leading to magnetic fields of the form $\mathbf{B}^{(R)} = \alpha(-k_y, k_x, 0)$ or $\mathbf{B}^{(D)} = \beta(k_y, k_x, 0)$, respectively known as the Rashba [4] and Dresselhaus [5] contributions. Including a possible momentum-independent Zeeman field $\mathbf{B}^{(Z)} = (0, B_y^{(Z)}, B_z^{(Z)})$, the Hamiltonian of the electron takes the form

$$\mathcal{H} = \frac{\hbar^2 k^2}{2m} - \frac{g\mu_B}{\hbar}\mathbf{S}\cdot(\mathbf{B}^{(D)} + \mathbf{B}^{(R)} + \mathbf{B}^{(Z)}), \quad (1)$$

where g is the electron g factor, μ_B is the Bohr magneton, and $\mathbf{S}$ is the electron spin.

The energy-momentum dispersion and the associated spin texture of the Hamiltonian in Eq. (1) are shown in Fig. 1(a) for $B_y^{(Z)} = 0$ and $\alpha = \beta$. In the absence of a perpendicular Zeeman field $B_z^{(Z)}$, the spectrum consists of the parabolic free particle dispersions for the two spin states that are shifted relative to each other in k space owing to the spin-orbit interaction. For a nonzero field $B_z^{(Z)}$, a gap opens in the spectrum. This gap, known as the spin-orbit gap, has been recently observed in one-dimensional quantum wires [6,7]. The two energy bands are spinful in the sense that the spin of an atom is locked to its momentum.

In this work, we engineer the Hamiltonian in Eq. (1) with equal Rashba and Dresselhaus strengths in an optically trapped, degenerate gas of fermionic lithium atoms via Raman dressing of atomic hyperfine states [8,9]. Raman fields have previously been used to generate spin-orbit coupling and gauge fields in pioneering work on Bose-Einstein condensates [10–12] and, recently, spin-orbit coupling in Fermi gases [13]. Here, we directly measure the spinful band structure of Eq. (1), as well as the rich band structure of a spin-orbit coupled lattice. For this, we introduce spin-injection spectroscopy, which is capable of completely characterizing the quantum states of spin-orbit coupled fermions, including the energy-momentum dispersion and the associated spin texture. By tracing the evolution of quantum states in the Brillouin zone, this method can be extended to directly measure topological invariants, such as the Chern number in a two-dimensional system [1,2,14].

Spin-orbit coupling is generated by using a pair of laser beams that connects the second and third lowest hyperfine levels in ^{6}Li, labeled $|\downarrow\rangle$ and $|\uparrow\rangle$, via a two-photon Raman transition, as shown in Figs. 1(b) and 1(c). The Raman process imparts momentum $\hbar Q\hat{x}$ to an atom while changing its spin from $|\downarrow\rangle$ to $|\uparrow\rangle$ and momentum $-\hbar Q\hat{x}$ while changing the spin from $|\uparrow\rangle$ to $|\downarrow\rangle$. Defining a quasimomentum $q = k_x + \frac{Q}{2}$ for spin $|\downarrow\rangle$ and $q = k_x - \frac{Q}{2}$ for spin $|\uparrow\rangle$, one obtains the Hamiltonian of the form given in Eq. (1) [10]. In this mapping, $B_z^{(Z)} = \hbar\Omega_R/g\mu_B$, where Ω_R is the two-photon Rabi frequency, $B_y^{(Z)} = \hbar\delta/g\mu_B$, where δ is the two-photon detuning, and $\alpha = \beta = \frac{\hbar^2 Q}{2mg\mu_B}$. In addition to providing spin-orbit coupling, the Raman beams lead to spontaneous photon scattering. For our experimental setup, the spontaneous scattering rate is ~240 times smaller than Ω_R, slow enough to permit accurate spin-injection spectroscopy (see Supplemental Material [15]).

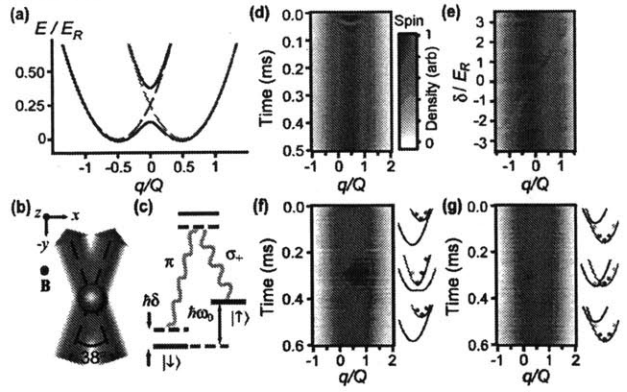

FIG. 1 (color online). Realization of spin-orbit coupling in an atomic Fermi gas. (a) Energy bands as a function of quasimomentum q for Raman coupling strength of $\hbar\Omega_R = 0.25E_R$ and $\hbar\delta = 0E_R$. Energy bands for $\hbar\Omega_R = \hbar\delta = 0E_R$ are shown with dashed lines. Color indicates spin composition of the states. (b) A pair of Raman beams at $\pm 19°$ relative to the $\hat{y}$ axis couples states $|\downarrow, k_x = q\rangle$ and $|\uparrow, k_x = q + Q\rangle$. A bias magnetic field $\mathbf{B}$ in the $\hat{z}$ direction provides the quantization axis. (c) Energy level diagram of states coupled by the Raman fields: $\hbar\delta$ is the two-photon detuning. The hyperfine interaction splits $|\uparrow\rangle$ and $|\downarrow\rangle$ by $\hbar\omega_0$, and the relevant polarization components are π and σ_+. (d) Momentum-dependent Rabi oscillations for $\hbar\Omega_R = 0.71(2)E_R$ and $\hbar\delta = -0.25(1)E_R$. Atoms are prepared in $|\downarrow\rangle$ (red) and are subsequently projected into a superposition of eigenstates as the Raman field is pulsed on. (e) A π pulse for the resonant momentum class is applied at different $\hbar\delta$ for $\hbar\Omega_R = 0.035(5)E_R$. (f),(g) Adiabatic loading and unloading of atoms into the upper (lower) band with $\hbar\Omega_R = 0.53(5)E_R$. The Raman beams are turned on with $\delta = \mp 8.5\Omega_R$, which is then swept linearly to $\delta = 0$ and back at a rate of $|\dot{\delta}| = 0.27(5)\Omega_R^2$.

We sympathetically cool ^{6}Li atoms with ^{23}Na in a magnetic trap down to a temperature of $T < 0.1T_F$, where T_F is the Fermi temperature [16]. After removal of Na atoms, the Li atoms are transferred into an optical dipole trap formed by two orthogonal 1064 nm beams. To separate the atomic hyperfine levels, we apply a magnetic field of 11.6 G. At this field, the interactions between states $|\uparrow\rangle$ and $|\downarrow\rangle$ (scattering length $20a_0$) are negligible in the experiment.

When the spin-orbit gap is opened suddenly, an atom prepared in the state $|\downarrow, k_x = q - Q/2\rangle$ oscillates between $|\downarrow, k_x = q - Q/2\rangle$ and $|\uparrow, k_x = q + Q/2\rangle$ with a momentum-dependent frequency $\Delta(q)/h$, where $\Delta(q)$ is the energy difference between the bands at quasimomentum q. Such Rabi oscillations correspond to Larmor precession of the pseudospin in the effective magnetic field $\mathbf{B}^{(SO)} = \mathbf{B}^{(D)} + \mathbf{B}^{(R)} + \mathbf{B}^{(Z)}$. We have observed these oscillations by starting with atoms in $|\downarrow\rangle$, pulsing on the Raman field for a variable duration τ, and imaging the atoms spin-selectively after time-of-flight expansion from the trap. Time-of-flight maps momentum to real space, allowing direct momentum resolution of the spin populations. As a function of pulse duration, we observe oscillations of the spin polarization with momentum-dependent frequencies, as shown in Fig. 1(d). Since our Fermi gas occupies a large range of momentum states with near-unity occupation, each image at a given pulse duration τ contains information for a large range of momenta q. The observation of momentum-dependent oscillations demonstrates the presence of a spin-orbit gap and shows that the atomic system is coherent over many cycles. To highlight the momentum selectivity of this process, we prepare an equal mixture of atoms in states $|\uparrow\rangle$ and $|\downarrow\rangle$ and pulse on the Raman fields for a time $t = \pi/\Omega_R$ for different two-photon detunings δ. This inverts the spin for atoms with momentum q where $\Delta(q)$ is minimal and equals $\hbar\Omega_R$. The resonant momentum class depends linearly on δ due to the Doppler shift $\propto k_x Q$, as shown in Fig. 1(e).

Instead of pulsing on the Raman field and projecting the initial state into a superposition of states in the two bands, one can introduce the spin-orbit gap adiabatically with respect to band populations. This is achieved by starting with a spin-polarized Fermi gas and sweeping the two-photon detuning δ from an initial value δ_i to a final detuning δ_f. The magnitude of the initial detuning $|\delta_i|$ is much larger than the two-photon recoil energy $E_R = \hbar^2 Q^2/2m$, so that the effective Zeeman field is almost entirely parallel with the spins. Depending on the direction of the sweep, this loads atoms into either the upper or the lower dressed band. We interrupt the sweep at various times and image the spin-momentum distribution. This reveals that the spin texture follows the effective Zeeman field. We verify that the process is reversible by sweeping the detuning back to δ_i and observing that full spin polarization is restored, as shown in Figs. 1(f) and 1(g).

Having demonstrated the ability to engineer spin-orbit coupling in a Fermi gas, we introduce a general approach to measure the eigenstates and energies of fermions at each quasimomentum q and thus resolve the band structure and the spin texture of spin-orbit coupled atomic systems. Our approach yields similar information to spin and angle-resolved photoemission spectroscopy (spin-ARPES), a powerful technique recently developed in condensed matter physics [17]. Spin-ARPES is particularly useful for studying magnetic and quantum spin Hall materials; it has been used, for example, to directly measure topological quantum numbers in the $Bi_{1-x}Sb_x$ series, revealing the presence of topological order and chiral properties [18].

Our spectroscopic technique uses radio frequency (rf) spin injection of atoms from a free Fermi gas into an empty spin-orbit coupled system using photons of a known energy, as shown in Fig. 2(a). After injection, the momentum and spin of the injected atoms are analyzed by using time of flight [19] combined with spin-resolved detection. Atoms are initially loaded into one of two free "reservoir" atomic states $|\downarrow\rangle_R$ and $|\uparrow\rangle_R$, for which we use the first and fourth lowest hyperfine states of ^{6}Li. State $|\downarrow\rangle_R$ can be

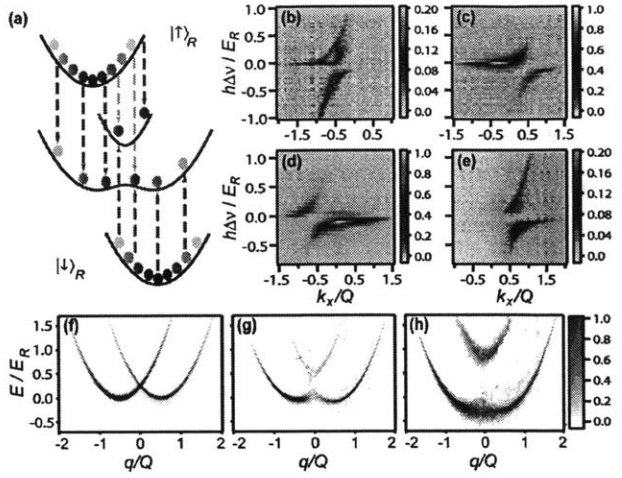

FIG. 2 (color online). Spin-injection spectroscopy. (a) An rf pulse injects atoms from the reservoir states (shown in black) $|\uparrow\rangle_R$ and $|\downarrow\rangle_R$ into the spin-orbit coupled system (shown in red and blue). Injection occurs when the rf photon energy equals the energy difference between the reservoir state and the spin-orbit coupled state at quasimomentum q. (b),(c) Spin-resolved $|\downarrow\rangle$ and $|\uparrow\rangle$ spectra, respectively, when transferring out of $|\uparrow\rangle_R$. Here, $\hbar\Omega_R = 0.43(5)E_R$ and $\hbar\delta = 0.00(3)E_R$. (d),(e) Spin-resolved $|\downarrow\rangle$ and $|\uparrow\rangle$ spectra, respectively, when transferring out of $|\downarrow\rangle_R$ for the same Raman strength $\hbar\Omega_R$. (f), (g), and (h) The reconstructed spinful dispersions for $\hbar\delta = 0.00(3)E_R$ and $\hbar\Omega_R = 0E_R$, $\hbar\Omega_R = 0.43(5)E_R$, and $\hbar\Omega_R = 0.9(1)E_R$, respectively.

coupled via rf to the state $|\downarrow\rangle$, as this connects the first and second lowest hyperfine states. Similarly, an atom in state $|\uparrow\rangle_R$ can be transferred to $|\uparrow\rangle$. rf spin injection does not impart momentum to the atom and occurs when the frequency of the rf pulse matches the energy difference between the spin-orbit coupled bands and the initial reservoir state, as shown in Fig. 2(a). Spin injection from $|\downarrow\rangle_R$ ($|\uparrow\rangle_R$) populates mostly the region of the spin-orbit coupled bands with a strong admixture of $|\downarrow\rangle$ ($|\uparrow\rangle$) states. Thus, the use of two reservoir states allows us to measure both the $|\downarrow\rangle$-rich and the $|\uparrow\rangle$-rich parts of the spin-orbit coupled bands. Following the injection process, the Raman beams are switched off, and the atoms are simultaneously released from the trap. By counting the number of atoms of a given spin and momentum as a function of injection energy after time of flight, we determine the dispersion of the spin-orbit coupled bands along with their spin texture. Note that, while spin-ARPES and previous momentum-resolved spectroscopic techniques in ultracold atoms probe the occupied states of a given system, our spin-injection method probes the unoccupied states. In the case of fermionic superfluids, this would reveal the excited branch of the quasiparticle dispersion.

The topological characteristics of the bands, which are encoded in the eigenstates, can be extracted from the spin and momentum composition. For our spin-orbit system with $\delta = 0$, the spin of the eigenstates is confined to the y-z plane on the Bloch sphere, because the effective magnetic field has no $\hat{x}$ component. More general couplings may not restrict the spin to a great circle on the Bloch sphere, in which case at least two spin components must be measured for a complete characterization of the bands. This can be achieved by rotating the different spin components onto the measurement basis with an rf pulse.

Applying spin-injection spectroscopy, we have measured the band structure of the equal-part Rashba-Dresselhaus Hamiltonian at $\delta = 0$ for several Ω_R. Figures 2(b)–2(e) show spin- and momentum-resolved spin-injection spectra obtained with atoms starting in the $|\uparrow\rangle_R$ reservoir (top row) and starting in the $|\downarrow\rangle_R$ reservoir (bottom row), for the case $\hbar\Omega_R = 0.43(5)E_R$ and $\delta = 0$. The $(q, \uparrow) \leftrightarrow (-q, \downarrow)$ symmetry of the system can be seen in the spectra in Fig. 2. The energy at each quasimomentum is found by adding the energy injected into the system by the rf pulse to the initial kinetic energy of the free particle in the reservoir. Figures 2(f)–2(h) show the dispersion and spin texture of the bands obtained from the data. As Ω_R is increased, we observe the opening of a spin-orbit gap at $q = 0$. The spin composition of the bands evolves from purely $|\uparrow\rangle$ or $|\downarrow\rangle$ away from the spin-orbit gap to a mixture of the two spin states in the vicinity of the spin-orbit gap, where the spin states are resonantly coupled.

A Fermi gas with the above dispersion has a spinful semimetallic behavior when the Fermi energy lies within the spin-orbit gap. When the Fermi energy is outside the spin-orbit gap, there is a fourfold degeneracy of states at the Fermi surface. Inside the gap, however, the degeneracy is halved. Furthermore, propagation of spin up particles at the Fermi energy can occur only in the positive q direction, while spin down fermions can propagate only in the opposite direction. For energies within the gap, the system thus acts as a spin-current diode.

An even richer band structure involving multiple spinful bands separated by fully insulating gaps can arise in the presence of a periodic lattice potential. This has been realized for Bose-Einstein condensates by adding rf coupling between the Raman-coupled states $|\uparrow\rangle$ and $|\downarrow\rangle$ [20]. Using a similar method, we create a spinful lattice for ultracold fermions and use spin-injection spectroscopy to probe the resulting spinful band structure. The combined Raman-rf coupling scheme is shown in Fig. 3(a). The Raman field couples the states $|\downarrow, k_x = q\rangle$ and $|\uparrow, k_x = q + Q\rangle$ with strength Ω_R, whereas the rf field couples the states $|\downarrow, k_x = q\rangle$ and $|\uparrow, k_x = q\rangle$ with strength Ω_{RF}. As a result, the set of coupled states for a given quasimomentum q, shown in the repeated Brillouin scheme in Fig. 3(b), is $|\sigma, k_x = q + nQ\rangle$ for integer n and $\sigma = \uparrow, \downarrow$. The lowest four bands are degenerate at the band center $q = 0$ when $\Omega_R = \Omega_{\mathrm{RF}} = 0$. The Raman field splits the degeneracy between the first and fourth bands, leaving the other two degenerate. The remaining degeneracy, which is a Dirac point, is removed with the addition of the rf field. Thus,

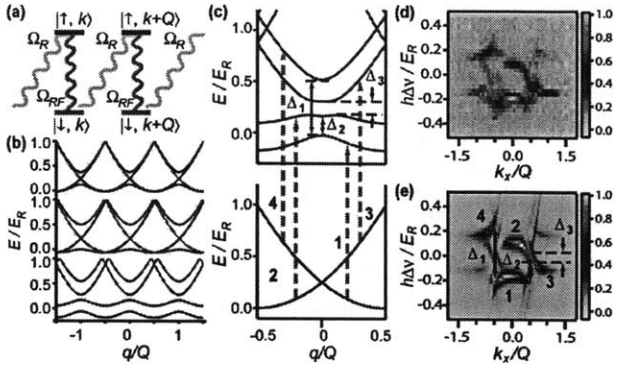

FIG. 3 (color online). Creating and probing a spin-orbit coupled lattice. (a) The addition of a radio frequency field allows momentum transfer of any multiple of Q, producing a spinful lattice band structure. (b) The band structure of the Raman-rf system in the repeated zone scheme. Band structures from top to bottom correspond to $\hbar\Omega_{\mathrm{RF}} = 0$ and $\hbar\Omega_R = 0.25E_R$, $\hbar\Omega_R = 0.5E_R$ and $\hbar\Omega_{\mathrm{RF}} = 0$, and $\hbar\Omega_R = 0.5E_R$ and $\hbar\Omega_{\mathrm{RF}} = 0.25E_R$. In the bottommost band, all degeneracies are lifted. (c) Spin injection from free particle bands to spinful lattice bands, starting from $|\downarrow\rangle_R$. Transitions near zero rf detuning ($h\Delta\nu \sim 0$) that give rise to dominant spectral features are identified. (d) Experimental spectrum of the Raman-rf system with $\hbar\Omega_R = 0.40(5)E_R$ and $\hbar\Omega_{\mathrm{RF}} = 0.28(2)E_R$ in the spin $|\downarrow\rangle$ channel after injection from reservoir $|\downarrow\rangle_R$. (e) The theoretical spectra corresponding to (d). Features corresponding to the gaps and transitions identified in (c) are labeled.

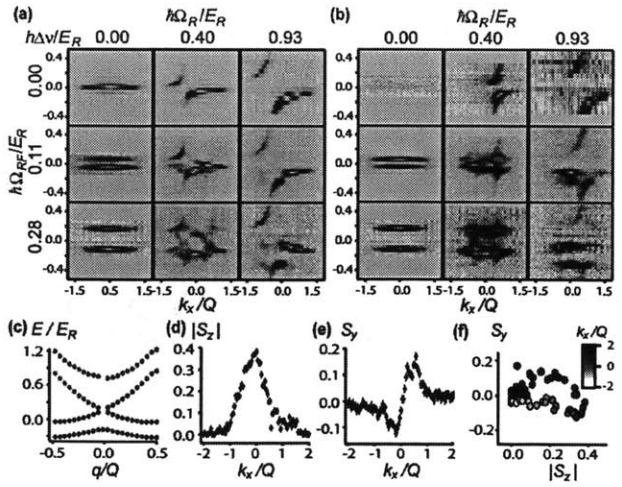

FIG. 4 (color online). Evolution of spin-textured energy bands of a spin-orbit coupled lattice. (a),(b) Experimental Raman-rf spin-injection spectra for injection from $|\downarrow\rangle_R$ for channels $|\downarrow\rangle$ and $|\uparrow\rangle$, respectively. The color map used is the same as Figs. 2(b) and 2(e) after rescaling to the maximum intensity. Interaction effects between $|\uparrow\rangle$ with $|\downarrow\rangle_R$ (see Fig. S4) makes only the dominant features resolvable in $|\uparrow\rangle$, while finer features are visible in $|\downarrow\rangle$. (c) Reconstructed band structure for $\hbar\Omega_R = 0.93(7)E_R$ and $\hbar\Omega_{\mathrm{RF}} = 0.28(2)E_R$. Color indicates the spin texture. (d)–(f) Experimentally measured spin components S_y and $|S_z|$ as a function of momentum k_x for the lattice wave functions corresponding to the bottommost band in (c).

when the system is filled up to the top of the second band, it is an insulator. Furthermore, when Ω_{RF} is large enough, a band gap also opens between the first and second bands.

Figure 3(d) shows the $|\downarrow\rangle$ channel of the spin-injection spectra, measured with fermions initially in reservoir state $|\downarrow\rangle_R$. Spectra with injection from $|\downarrow\rangle_R$ is sufficient to reconstruct the full band structure given the $(q,\uparrow) \leftrightarrow (-q,\downarrow)$ symmetry of the Hamiltonian. The transitions between the reservoir and the spin-orbit coupled bands for $\hbar\Omega_R = 0.40(5)E_R$ and $\hbar\Omega_{\mathrm{RF}} = 0.28(2)E_R$ are shown in Fig. 3(c). The experimental spectrum in Fig. 3(d) is compared to the theoretically calculated spectrum, shown in Fig. 3(e). The spectrum exhibits four prominent features separated by three energy gaps, labeled Δ_1, Δ_2, and Δ_3 in Fig. 3(e). The gaps giving rise to these features are shown on the band structure in Fig. 3(c). The gap Δ_1 is opened by the spin-orbit coupling, while Δ_2 is opened by a direct rf coupling, and Δ_3 is opened by a second-order process that involves both the rf and Raman fields, explaining its smallness. We have explored the Raman-rf system for a range of coupling strengths as shown in the spectra in Figs. 4(a) and 4(b). With a careful choice of the Raman-rf coupling strengths, spinful flat bands can be realized (see Supplemental Material, Fig. S3 [15]), where interactions should play a dominant role [21].

To illustrate how the energy bands along with the corresponding eigenstates can be extracted, we reconstruct the energy bands along with the spin texture for $\hbar\Omega_R = 0.93(7)E_R$ and $\hbar\Omega_{\mathrm{RF}} = 0.28(2)E_R$, as shown in Fig. 4(c). The energies of the bands are obtained from the resonant frequencies in the spin-injection spectra, while the spin composition $S_{y,z}$ is extracted from the relative weights of the signal in the two spin channels (see Supplemental Material [15]). In Figs. 4(d)–4(f), we show the extracted value of $S_y(k_x)$ and $|S_z(k_x)|$ for the bottommost band when $\hbar\Omega_R = 0.93(7)E_R$ and $\hbar\Omega_{\mathrm{RF}} = 0.28(2)E_R$. For more general spin-orbit Hamiltonians involving σ_x, one can extract the phase between all three components of $\vec{S}(k_x)$ with additional rf pulses and fully characterize the eigenstate for the corresponding quasimomentum q. The topology of the band, encoded in the evolution of its eigenstates across the Brillouin zone, can thus be measured.

In summary, we have created and directly probed a spin-orbit gap in a Fermi gas of ultracold atoms and realized a fully gapped band structure allowing for spinful flat bands. We introduced spin-injection spectroscopy to characterize the spin-textured energy-momentum dispersion. We further show that spin-injection spectroscopy allows reconstruction of eigenstates in a spinful lattice system. Extensions of this method can reveal the nontrivial topology of bands in more general spin-orbit coupled systems [22], opening a path to probing topological insulators with ultracold atoms. Similar spectroscopic techniques should

allow the demonstration of effective p-wave interactions in a single component spin-orbit coupled Fermi gas, either near an s-wave Feshbach resonance or for flat bands as realized here. In these systems, interactions may lead to BCS pairing in a p-wave channel and, in a two-dimensional Fermi gas with pure Rashba coupling, to $p_x + ip_y$ pairing and chiral superfluidity [23,24].

This work was supported by the NSF, a grant from the Army Research Office with funding from the DARPA OLE program, ARO-MURI on Atomtronics, AFOSR-MURI, ONR YIP, DARPA YFA, an AFOSR PECASE, and the David and Lucile Packard Foundation. Z. H. acknowledges funding from EPSRC under Grant No. EP/I010580/1.

[1] M. Z. Hasan and C. L. Kane, Rev. Mod. Phys. **82**, 3045 (2010).
[2] X.-L. Qi and S.-C. Zhang, Rev. Mod. Phys. **83**, 1057 (2011).
[3] R. Winkler, *Spin-Orbit Coupling Effects in Two-Dimensional Electron and Hole Systems*, Springer Tracts Mod. Phys. Vol. 191 (Springer, Berlin, 2003).
[4] Y. A. Bychkov and E. I. Rashba, J. Phys. C **17**, 6039 (1984).
[5] G. Dresselhaus, Phys. Rev. **100**, 580 (1955).
[6] C. H. L. Quay, T. L. Hughes, J. A. Sulpizio, L. N. Pfeiffer, K. W. Baldwin, K. W. West, D. Goldhaber-Gordon, and R. de Picciotto, Nature Phys. **6**, 336 (2010).
[7] S. Nadj-Perge, V. S. Pribiag, J. W. G. van den Berg, K. Zuo, S. R. Plissard, E. P. A. M. Bakkers, S. M. Frolov, and L. P. Kouwenhoven, Phys. Rev. Lett. **108**, 166801 (2012).
[8] X.-J. Liu, M. F. Borunda, X. Liu, and J. Sinova, Phys. Rev. Lett. **102**, 046402 (2009).
[9] J. Dalibard, F. Gerbier, G. Juzeliūnas, and P. Öhberg, Rev. Mod. Phys. **83**, 1523 (2011).
[10] Y.-J. Lin, Jiménez-García, and I. B. Spielman, Nature (London) **471**, 83 (2011).
[11] Y.-J. Lin, R. L. Compton, Jiménez-García, J. V. Porto, and I. B. Spielman, Nature (London) **462**, 628 (2009).
[12] M. Aidelsburger, M. Atala, S. Nascimbéne, S. Trotzky, Y.-A. Chen, and I. Bloch, Phys. Rev. Lett. **107**, 255301 (2011).
[13] P. Wang, Z.-Q. Yu, Z. Fu, J. Miao, L. Huang, S. Chai, H. Zhai, and J. Zhang, preceding Letter, Phys. Rev. Lett. **109**, 095301 (2012).
[14] E. Zhao, N. Bray-Ali, C. J. Williams, I. B. Spielman, and I. I. Satija, Phys. Rev. A **84**, 063629 (2011).
[15] See Supplemental Material at http://link.aps.org/supplemental/10.1103/PhysRevLett.109.095302 for details of the experimental setup and data analysis.
[16] Z. Hadzibabic, S. Gupta, C. A. Stan, C. H. Schunck, M. W. Zwierlein, K. Dieckmann, and W. Ketterle, Phys. Rev. Lett. **91**, 160401 (2003).
[17] M. Hoesch, T. Greber, V. N. Petrov, M. Muntwiler, M. Hengsberger, W. Auwrter, and J. Osterwalder, J. Electron Spectrosc. Relat. Phenom. **124**, 263 (2002).
[18] D. Hsieh, Y. Xia, L. Wray, D. Qian, A. Pal, J. H. Dil, J. Osterwalder, F. Meier, G. Bihlmayer, C. L. Kane, Y. S. Hor, R. J. Cava, and M. Z. Hasan, Science **323**, 919 (2009).
[19] J. T. Stewart, J. P. Gaebler, and D. S. Jin, Nature (London) **454**, 744 (2008).
[20] K. Jiménez-García, L. J. LeBlanc, R. A. Williams, M. C. Beeler, A. R. Perry, and I. B. Spielman, Phys. Rev. Lett. **108**, 225303 (2012).
[21] K. Sun, Z. Gu, H. Katsura, and S. Das Sarma, Phys. Rev. Lett. **106**, 236803 (2011).
[22] J. D. Sau, R. Sensarma, S. Powell, I. B. Spielman, and S. Das Sarma, Phys. Rev. B **83**, 140510 (2011).
[23] R. A. Williams, L. J. LeBlanc, K. Jiménez-García, M. C. Beeler, A. R. Perry, W. D. Phillips, and I. B. Spielman, Science **335**, 314 (2011).
[24] C. Zhang, S. Tewari, R. M. Lutchyn, and S. Das Sarma, Phys. Rev. Lett. **101**, 160401 (2008).

Bibliography

[1] A.A. Abrikosov, L.P. Gor'kov, and I.E. Dzyaloshinski. *Methods of Quantum Field Theory in Statistical Physics.* Dover Publications, New York, 1975.

[2] A. Altmeyer, S. Riedl, C. Kohstall, M. J. Wright, R. Geursen, M. Bartenstein, C. Chin, J. Hecker-Denschlag, and R. Grimm. Precision measurements of collective oscillations in the BEC-BCS crossover. *Physical Review Letters*, 98(4):040401, 2007.

[3] B. P. Anderson, P. C. Haljan, C. A. Regal, D. L. Feder, L. A. Collins, C. W. Clark, and E. A. Cornell. Watching dark solitons decay into vortex rings in a Bose-Einstein condensate. *Physical Review Letters*, 86:2926–2929, 2001.

[4] M.H. Anderson, J.R. Ensher, M.R. Matthews, C.E. Wieman, and E.A. Cornell. Observation of Bose-Einstein condensation in a dilute atomic vapor. *Science*, 269:198–201, 1995.

[5] M. R. Andrews, C. G. Townsend, H. J. Miesner, D. S. Durfee, D. M. Kurn, and W. Ketterle. Observation of interference between two Bose-Einstein condensates. *Science*, 275(5300):637–641, 1997.

[6] Mauro Antezza, Franco Dalfovo, Lev P. Pitaevskii, and Sandro Stringari. Dark solitons in a superfluid fermi gas. *Physical Review A*, 76(4):043610, 2007.

[7] Peter Arnold, E. Drut, Joaquin, and Dam Thanh Son. Next-to-next-to-leading-order epsilon expansion for a Fermi gas at infinite scattering length. *Physical Review A*, 75(4):043605, 2007.

[8] G. E. Astrakharchik, J. Boronat, J. Casulleras, and S. Giorgini. Equation of state of a Fermi gas in the BEC-BCS crossover: A Quantum Monte-Carlo study. *Physical Review Letters*, 93:200404, 2004.

[9] M. Bartenstein, A. Altmeyer, S. Riedl, R. Geursen, S. Jochim, C. Chin, J. Hecker-Denschlag, R. Grimm, A. Simoni, E. Tiesinga, C. J. Williams, and P. S. Julienne. Precise determination of ^{6}Li cold collision parameters by radio-frequency spectroscopy on weakly bound molecules. *Physical Review Letters*, 94:103201, 2005.

[10] M. Bartenstein, A. Altmeyer, S. Riedl, S. Jochim, C. Chin, J. Hecker-Denschlag, and R. Grimm. Collective excitations of a degenerate gas at the BEC-BCS crossover. *Physical Review Letters*, 92(20):203201, 2004.

[11] Christoph Becker, Simon Stellmer, Parvis Soltan-Panahi, Sren Drscher, Mathis Baumert, Eva-Maria Richter, Jochen Kronjger, Kai Bongs, and Klaus Sengstock. Oscillations and interactions of dark and darkbright solitons in boseeinstein condensates. *Nature Physics*, 4(6):496–501, 2008.

[12] Immanuel Bloch, Jean Dalibard, and Wilhelm Zwerger. Many-body physics with ultracold gases. *Reviews of Modern Physics*, 80(3):885–80, 2008.

[13] T. Bourdel, L. Khaykovich, J. Cubizolles, J. Zhang, F. Chevy, M. Teichmann, L. Tarruell, S.J.J.M.F. Kokkelmans, and C. Salomon. Experimental study of the BEC-BCS crossover region in lithium-6. *Physical Review Letters*, 93:050401, 2004.

[14] C.C. Bradley, C.A. Sackett, J.J. Tollet, and R.G. Hulet. Evidence of Bose-Einstein condensation in an atomic gas with attractive interactions. *Physical Review Letters*, 75:1687–1690, 1995.

[15] G. Bruun and C. Pethick. Spin diffusion in trapped clouds of cold atoms with resonant interactions. *Physical Review Letters*, 107(25):255302, 2011.

[16] G. M. Bruun. Spin diffusion in Fermi gases. *New Journal of Physics*, 13(3):035005, 2011.

[17] G. M. Bruun, A. Recati, C. J. Pethick, H. Smith, and S. Stringari. Collisional properties of a polarized Fermi gas with resonant interactions. *Physical Review Letters*, 100(24):240406, 2008.

[18] G. M. Bruun and H. Smith. Shear viscosity and damping for a fermi gas in the unitarity limit. *Physical Review A*, 75(4):043612, 2007. Copyright (C) 2010 The American Physical Society Please report any problems to prola@aps.org PRA.

[19] S. Burger, K. Bongs, S. Dettmer, W. Ertmer, and K. Sengstock. Dark solitons in Bose-Einstein condensates. *Physical Review Letters*, 83:5198–5201, 1999.

[20] Th. Busch and J. R. Anglin. Dark-bright solitons in inhomogeneous Bose-Einstein condensates. *Physical Review Letters*, 87:010401, 2001.

[21] Thomas Busch, Berthold-Georg Englert, Kazimierz Rzążewski, and Martin Wilkens. Two cold atoms in a harmonic trap. *Foundations of Physics*, 28(4):549–559, 1998.

[22] C. Cao, E. Elliott, J. Joseph, H. Wu, J. Petricka, T. Schafer, and J. E. Thomas. Universal quantum viscosity in a unitary Fermi gas. *Science*, 331(6013):58–61, 2011.

[23] P. M. Chaikin and T. C. Lubensky. *Principles of Condensed Matter Physics.* Cambridge, 2000.

[24] B.S. Chandrasekhar. A note on the maximum critical field of high-field superconductors. *Applied Physics Letters*, 1:7, 1962.

[25] Lawrence Cheuk, Ariel Sommer, Zoran Hadzibabic, Tarik Yefsah, Waseem Bakr, and Martin Zwierlein. Spin-injection spectroscopy of a spin-orbit coupled fermi gas. *Physical Review Letters*, 109(9):095302, 2012.

[26] F. Chevy. Universal phase diagram of a strongly interacting Fermi gas with unbalanced spin populations. *Physical Review A*, 74(6):063628, 2006.

[27] Cheng Chin, Rudolf Grimm, Paul Julienne, and Eite Tiesinga. Feshbach resonances in ultracold gases. *Reviews of Modern Physics*, 82(2):1225, 2010. Copyright (C) 2011 The American Physical Society Please report any problems to prola@aps.org RMP.

[28] Cheng Chin and Paul S. Julienne. Radio-frequency transitions on weakly bound ultracold molecules. *Physical Review A*, 71(1):012713, 2005.

[29] A.M. Clogston. Upper limit for the critical field in hard superconductors. *Physical Review Letters*, 9(6):266, 1962.

[30] R. Combescot and S. Giraud. Normal state of highly polarized Fermi gases: Full many-body treatment. *Physical Review Letters*, 101(5):050404, 2008.

[31] R. Combescot, A. Recati, C. Lobo, and F. Chevy. Normal state of highly polarized Fermi gases: Simple many-body approaches. *Physical Review Letters*, 98(18):180402, 2007.

[32] J. Cubizolles, T. Bourdel, S.J.J.M.F. Kokkelmans, G.V. Shlyapnikov, and C. Salomon. Production of long-lived ultracold Li_2 molecules from a Fermi gas. *Physical Review Letters*, 91:240401, 2003.

[33] Irene D'Amico and Giovanni Vignale. Theory of spin Coulomb drag in spin-polarized transport. *Physical Review B*, 62(8):4853–4857, 2000.

[34] K. B. Davis, M.-O. Mewes, M. R. Andrews, N. J. van Druten, D. S. Durfee, D. M. Kurn, and W. Ketterle. Bose-Einstein condensation in a gas of sodium atoms. *Physical Review Letters*, 75(22):3969–3973, 1995.

[35] Theja De Silva and Erich Mueller. Surface tension in unitary Fermi gases with population imbalance. *Physical Review Letters*, 97(7):070402, 2006.

[36] B. DeMarco and D. S. Jin. Spin excitations in a fermi gas of atoms. *Physical Review Letters*, 88(4):040405, 2002.

[37] B. DeMarco and D.S. Jin. Onset of Fermi degeneracy in a trapped atomic gas. *Science*, 285:1703–1706, 1999.

[38] J. Denschlag, J. E. Simsarian, D. L. Feder, Charles W. Clark, L. A. Collins, J. Cubizolles, L. Deng, E. W. Hagley, K. Helmerson, W. P. Reinhardt, S. L. Rolston, B. I. Schneider, and W. D. Phillips. Generating solitons by phase engineering of a Bose-Einstein condensate. *Science*, 287:97–101, 2000.

[39] Jeroen Devreese, Sergei Klimin, and Jacques Tempere. Resonant enhancement of the Fulde-Ferell-Larkin-Ovchinnikov state in three dimensions by a one-dimensional optical potential. *Physical Review A*, 83(1):013606, 2011.

[40] Jeroen P. Devreese, Michiel Wouters, and Jacques Tempere. Controlling the pair momentum of the Fulde-Ferrell-Larkin-Ovchinnikov state in a three-dimensional fermi gas through a one-dimensional periodic potential. *Physical Review A*, 84(4):043623, 2011.

[41] K. Dieckmann, C. A. Stan, S. Gupta, Z. Hadzibabic, C. Schunck, and W. Ketterle. Decay of an ultracold fermionic lithium gas near a Feshbach resonance. *Physical Review Letters*, 89:203201, 2002.

[42] John F. Dobson. Harmonic-potential theorem: Implications for approximate many-body theories. *Physical Review Letters*, 73(16):2244, 1994.

[43] A. J. Drew, J. Hoppler, L. Schulz, F. L. Pratt, P. Desai, P. Shakya, T. Kreouzis, W. P. Gillin, A. Suter, N. A. Morley, V. K. Malik, A. Dubroka, K. W. Kim, H. Bouyanfif, F. Bourqui, C. Bernhard, R. Scheuermann, G. J. Nieuwenhuys, T. Prokscha, and E. Morenzoni. Direct measurement of the electronic spin diffusion length in a fully functional organic spin valve by low-energy muon spin rotation. *Nat Mater*, 8(2):109–114, 2009.

[44] X. Du, L. Luo, B. Clancy, and J. E. Thomas. Observation of anomalous spin segregation in a trapped Fermi Gas. *Physical Review Letters*, 101(15):150401, 2008.

[45] P. Dyke, E. D. Kuhnle, S. Whitlock, H. Hu, M. Mark, S. Hoinka, M. Lingham, P. Hannaford, and C. J. Vale. Crossover from 2D to 3D in a weakly interacting Fermi gas. *Physical Review Letters*, 106(10):105304, 2011.

[46] J. Dziarmaga and K. Sacha. Gap soliton in superfluid fermi gas at zero and finite temperature. *Laser Physics*, 15(4):674–678, 2005.

[47] Jacek Dziarmaga and Krzysztof Sacha. Depletion of the dark soliton: The anomalous mode of the Bogoliubov theory. *Physical Review A*, 66(4):043620, 2002.

[48] Jacek Dziarmaga and Krzysztof Sacha. Bogoliubov theory of a Bose-Einstein condensate in the particle representation. *Physical Review A*, 67(3):033608, 2003.

[49] D. M. Eagles. Possible pairing without superconductivity at low carrier concentrations in bulk and thin-film superconducting semiconductors. *Physical Review*, 186:456, 1969.

[50] Tilman Enss and Rudolf Haussmann. Quantum mechanical limitations to spin diffusion in the unitary Fermi gas. *Physical Review Letters*, 109(19):195303, 2012.

[51] Tilman Enss, Rudolf Haussmann, and Wilhelm Zwerger. Viscosity and scale invariance in the unitary Fermi gas. *Annals of Physics*, 326(3):770–796, 2011.

[52] P. O. Fedichev, A. E. Muryshev, and G. V. Shlyapnikov. Dissipative dynamics of a kink state in a Bose-condensed gas. *Physical Review A*, 60(4):3220–3224, 1999.

[53] Albert Fert. Nobel lecture: Origin, development, and future of spintronics. *Reviews of Modern Physics*, 80(4):1517–1530, 2008.

[54] Karsten Flensberg, Thomas Stibius Jensen, and Niels Asger Mortensen. Diffusion equation and spin drag in spin-polarized transport. *Physical Review B*, 64(24):245308, 2001. PRB.

[55] Michael McNeil Forbes, Stefano Gandolfi, and Alexandros Gezerlis. Resonantly interacting fermions in a box. *Physical Review Letters*, 106(23):235303, 2011. Copyright (C) 2011 The American Physical Society Please report any problems to prola@aps.org PRL.

[56] Bernd Fröhlich, Michael Feld, Enrico Vogt, Marco Koschorreck, Wilhelm Zwerger, and Michael Köhl. Radio-frequency spectroscopy of a strongly interacting two-dimensional Fermi gas. *Physical Review Letters*, 106(10):105301, 2011.

[57] P. Fulde and R.A. Ferrell. Superconductivity in a strong spin-exchange field. *Physical Review*, 135:A550, 1964.

[58] Stefano Giorgini, Lev P. Pitaevskii, and Sandro Stringari. Theory of ultracold atomic fermi gases. *Reviews of Modern Physics*, 80(4):1215–60, 2008.

[59] O. Goulko, F. Chevy, and C. Lobo. Collision of two spin-polarized fermionic clouds. *Physical Review A*, 84(5):051605(R), 2011.

[60] O. Goulko, F. Chevy, and C. Lobo. Boltzmann equation simulation for a trapped fermi gas of atoms. *New Journal of Physics*, 14(7):073036, 2012.

[61] Olga Goulko. *Thermodynamic and hydrodynamic behaviour of interacting Fermi gases.* PhD thesis, University of Cambridge, 2011.

[62] S. R. Granade, M. E. Gehm, K. M. O'Hara, and J. E. Thomas. All-optical production of a degenerate Fermi gas. *Physical Review Letters*, 88:120405, 2002.

[63] Markus Greiner, Cindy A. Regal, and Deborah S. Jin. Emergence of a molecular Bose-Einstein condensate from a Fermi gas. *Nature*, 426:537, 2003.

[64] Rudolf Grimm, Matthias Weidemller, and Yurii B. Ovchinnikov. Optical dipole traps for neutral atoms. *Advances in Atomic and Molecular Physics*, 42:95–170, 2000.

[65] David Gury-Odelin, Francesca Zambelli, Jean Dalibard, and Sandro Stringari. Collective oscillations of a classical gas confined in harmonic traps. *Physical Review A*, 60:4851, 1999.

[66] Z. Hadzibabic, S. Gupta, C.A. Stan, C.H. Schunck, M.W. Zwierlein, K. Dieckmann, and W. Ketterle. Fifty-fold improvement in the number of quantum degenerate fermionic atoms. *Physical Review Letters*, 91:160401, 2003.

[67] Z. Hadzibabic, C. A. Stan, K. Dieckmann, S. Gupta, M.W. Zwierlein, A. Goerlitz, and W. Ketterle. Two species mixture of quantum degenerate Bose and Fermi gases. *Physical Review Letters*, 88:160401, 2002.

[68] Zoran Hadzibabic, Peter Kruger, Marc Cheneau, Baptiste Battelier, and Jean Dalibard. Berezinskii-Kosterlitz-Thouless crossover in a trapped atomic gas. *Nature*, 441(7097):1118–1121, 2006.

[69] R. Haussmann, W. Rantner, S. Cerrito, and W. Zwerger. Thermodynamics of the BCS-BEC crossover. *Physical Review A*, 75(2):023610, 2007.

[70] R. Haussmann and W. Zwerger. Thermodynamics of a trapped unitary Fermi gas. *Physical Review A*, 78(6):063602, 2008.

[71] Tin-Lun Ho and Erich J. Mueller. High temperature expansion applied to fermions near feshbach resonance. *Physical Review Letters*, 92(16):160404, 2004.

[72] M. Houbiers, H. T. C. Stoof, W. I. McAlexander, and R. G. Hulet. Elastic and inelastic collisions of ^{6}Li atoms in magnetic and optical traps. *Physical Review A*, 57:R1497, 1998.

[73] H. Hu, X.-J. Liu, and P.D. Drummond. Equation of state of a superfluid Fermi gas in the BCS-BEC crossover. *Europhysics Letters*, 74(4):574–580, 2006.

[74] S. Jochim, M. Bartenstein, A. Altmeyer, G. Hendl, S. Riedl, C. Chin, J. Hecker-Denschlag, and R. Grimm. Bose-Einstein condensation of molecules. *Science*, 302:2101, 2003.

[75] M.A. Joffe. *Trapping and cooling atoms at high densities.* Ph.d., Massachusetts Institute of Technology, 1993.

[76] L.V. Keldysh and A.N. Kozlov. Collective properties of excitons in semiconductors. *Zh. Eksp. Teor. Fiz.*, 54:978, 1968.

[77] W. Ketterle, D.S. Durfee, and D.M. Stamper-Kurn. Making, probing and understanding Bose-Einstein condensates. In M. Inguscio, S. Stringari, and C.E. Wieman, editors, *Bose-Einstein condensation in atomic gases, Proceedings of the International School of Physics Enrico Fermi, Course CXL, Varenna, 7-17 July 1998*, pages 67–176. IOS Press, 1999.

[78] Hyungwon Kim and David Huse. Heat and spin transport in a cold atomic Fermi gas. *Physical Review A*, 86(5):053607, 2012.

[79] J. Kinast, A. Turlapov, and J. E. Thomas. Breakdown of hydrodynamics in the radial breathing mode of a strongly-interacting Fermi gas. *Physical Review A*, 70:051401, 2004.

[80] J. Kinast, A. Turlapov, J. E. Thomas, Q. Chen, J. Stajic, and K. Levin. Heat capacity of a strongly-interacting Fermi gas. *Science*, 307:1296–1299, 2005.

[81] Walter Kohn. Cyclotron resonance and de Haas-van Alphen oscillations of an interacting electron gas. *Physical Review*, 123(4):1242–1244, 1961.

[82] J. M. Kosterlitz and D. J. Thouless. Long range order and metastability in two dimensional solids and superfluids. *Journal of Physics C: Solid State Physics*, 5(11):L124, 1972.

[83] J M Kosterlitz and D J Thouless. Ordering, metastability and phase transitions in two-dimensional systems. *Journal of Physics C: Solid State Physics*, 6(7):1181, 1973.

[84] Mark Ku, Jens Braun, and Achim Schwenk. Finite-size and confinement effects in spin-polarized trapped Fermi gases. *Physical Review Letters*, 102(25):255301, 2009.

[85] Mark J. H. Ku, Ariel T. Sommer, Lawrence W. Cheuk, and Martin W. Zwierlein. Revealing the superfluid lambda transition in the universal thermodynamics of a unitary Fermi gas. *Science*, 335(6068):563–567, 2012.

[86] Ryogo Kubo. Statistical-mechanical theory of irreversible processes. I. *Journal of the Physical Society of Japan*, 12(6):570–586, 1957.

[87] L. D. Landau and E. M. Lifshitz. *Quantum Mechanics: Non-Relativistic Theory*, volume 3 of *Course of Theoretical Physics*. Butterworth-Heinmann, 1977.

[88] M. Lang. Quasi-twodimensional organic superconductors. *Supercond. Rev.*, 2:1, 1996.

[89] Christian Langmack, Marcus Barth, Wilhelm Zwerger, and Eric Braaten. Clock shift in a strongly interacting two-dimensional Fermi gas. *Physical Review Letters*, 108(6):060402, 2012.

[90] A.J. Larkin and Y.N. Ovchinnikov. Inhomogeneous state of superconductors. *Zh. Eksp. Teor. Fiz.*, 47:1136, 1964.

[91] C. Law. Dynamic quantum depletion in phase-imprinted generation of dark solitons. *Physical Review A*, 68(1):015602, 2003.

[92] A.J. Leggett. *Diatomic molecules and Cooper pairs*, pages 13–27. Springer-Verlag, Berlin, 1980.

[93] Renyuan Liao and Joachim Brand. Traveling dark solitons in superfluid fermi gases. *Physical Review A*, 83(4):041604(R), 2011.

[94] Y. Liao, M. Revelle, T. Paprotta, A. Rittner, Wenhui Li, G. Partridge, and R. Hulet. Metastability in spin-polarized Fermi gases. *Physical Review Letters*, 107(14):145305, 2011.

[95] Y. J. Lin, K. Jimenez-Garcia, and I. B. Spielman. Spin-orbit-coupled bose-einstein condensates. *Nature*, 471(7336):83–86, 2011.

[96] Xia-Ji Liu, Hui Hu, and Peter D. Drummond. Virial expansion for a strongly correlated Fermi gas. *Physical Review Letters*, 102(16):160401, 2009. Copyright (C) 2011 The American Physical Society Please report any problems to prola@aps.org PRL.

[97] C. Lobo, A. Recati, S. Giorgini, and S. Stringari. Normal state of a polarized Fermi gas at unitarity. *Physical Review Letters*, 97(20):200403–4, 2006. TY - JOUR N1 - lobo06 UR - http://link.aps.org/abstract/PRL/v97/e200403.

[98] L. Luo, B. Clancy, J. Joseph, J. Kinast, and J. E. Thomas. Measurement of the entropy and critical temperature of a strongly interacting Fermi gas. *Physical Review Letters*, 98(8):080402, 2007.

[99] K. W. Madison, F. Chevy, W. Wohlleben, and J. Dalibard. Vortices in a stirred Bose-Einstein condensate. *Journal of Modern Optics*, 47:2715, 2000.

[100] Kirill Martiyanov, Vasiliy Makhalov, and Andrey Turlapov. Observation of a two-dimensional Fermi gas of atoms. *Physical Review Letters*, 105(3):030404, 2010.

[101] M.R. Matthews, B.P. Anderson, P.C. Haljan, D.S. Hall, C.E. Wieman, and E.A. Cornell. Vortices in a Bose-Einstein condensate. *Physical Review Letters*, 83:2498–2501, 1999.

[102] M.-O. Mewes, M. R. Andrews, N. J. van Druten, D. M. Kurn, D. S. Durfee, C. G. Townsend, and W. Ketterle. Collective excitations of a Bose-Einstein condensate in a magnetic trap. *Physical Review Letters*, 77(6):988–991, 1996.

[103] Kazumasa Miyake. Fermi liquid theory of dilute submonolayer ^{3}he on thin ^{4}he ii film. *Progress of Theoretical Physics*, 69(6):1794–1797, 1983.

[104] S. Nascimbéne, N. Navon, K. J. Jiang, F. Chevy, and C. Salomon. Exploring the thermodynamics of a universal Fermi gas. *Nature*, 463(7284):1057–1060, 2010.

[105] S. Nascimbene, N. Navon, K. J. Jiang, L. Tarruell, M. Teichmann, J. McKeever, F. Chevy, and C. Salomon. Collective oscillations of an imbalanced Fermi gas: Axial compression modes and polaron effective mass. *Physical Review Letters*, 103(17):170402–4, 2009.

[106] Chetan Nayak, Steven H. Simon, Ady Stern, Michael Freedman, and Sankar Das Sarma. Non-abelian anyons and topological quantum computation. *Reviews of Modern Physics*, 80(3):1083–1159, 2008. RMP.

[107] P. Nozires and S. Schmitt-Rink. Bose condensation in an attractive fermion gas: from weak to strong coupling superconductivity. *Journal of Low Temperature Physics*, 59(3/4):195–211, 1985.

[108] K. M. O'Hara, S. L. Hemmer, M. E. Gehm, S. R. Granade, and J. E. Thomas. Observation of a strongly interacting degenerate Fermi gas of atoms. *Science*, 298:2179, 2002.

[109] G. Orso, L. P. Pitaevskii, S. Stringari, and M. Wouters. Formation of molecules near a Feshbach resonance in a 1D optical lattice. *Physical Review Letters*, 95(6):060402, 2005.

[110] Meera M. Parish and David A. Huse. Evaporative depolarization and spin transport in a unitary trapped Fermi gas. *Physical Review A*, 80(6):063605, 2009.

[111] Jee Woo Park, Cheng-Hsun Wu, Ibon Santiago, Tobias G. Tiecke, Sebastian Will, Peyman Ahmadi, and Martin W. Zwierlein. Quantum degenerate bose-fermi mixture of chemically different atomic species with widely tunable interactions. *Physical Review A*, 85:051602, 2012.

[112] G. B. Partridge, Wenhui Li, Y. Liao, R. G. Hulet, M. Haque, and H. T. C. Stoof. Deformation of a trapped Fermi gas with unequal spin populations. *Physical Review Letters*, 97(19):190407, 2006.

[113] Guthrie B. Partridge, Wenhui Li, Ramsey I. Kamar, Y. Liao, and Randall G. Hulet. Pairing and phase separation in a polarized Fermi gas. *Science*, 311:503, 2006.

[114] C.J. Pethick and H. Smith. *Bose-Einstein Condensation in Dilute Gases*. Cambridge, 2008.

[115] D. S. Petrov and G. V. Shlyapnikov. Interatomic collisions in a tightly confined Bose gas. *Physical Review A*, 64(1):012706, 2001.

[116] S. Pilati and S. Giorgini. Phase separation in a polarized Fermi gas at zero temperature. *Physical Review Letters*, 100(3):030401, 2008.

[117] Marco Polini and Giovanni Vignale. Spin drag and spin-charge separation in cold Fermi gases. *Physical Review Letters*, 98(26):266403, 2007.

[118] V.N. Popov. Theory of a Bose gas produced by bound states of Fermi particles. *Zh. Eksp. Teor. Fiz.*, 50:1550, 1966.

[119] N. V. Prokof'ev and B. V. Svistunov. Bold diagrammatic Monte Carlo: A generic sign-problem tolerant technique for polaron models and possibly interacting many-body problems. *Physical Review B*, 77(12):125101, 2008.

[120] Nikolay Prokof'ev and Boris Svistunov. Fermi-polaron problem: Diagrammatic Monte Carlo method for divergent sign-alternating series. *Physical Review B*, 77(2):020408, 2008.

[121] Xiao-Liang Qi and Shou-Cheng Zhang. Topological insulators and superconductors. *Reviews of Modern Physics*, 83(4):1057–1110, 2011.

[122] C. Raman, J.R. Abo-Shaeer, J. M. Vogels, K. Xu, and W. Ketterle. Vortex nucleation in a stirred Bose-Einstein condensate. *Physical Review Letters*, 87:210402, 2001.

[123] M. Randeria, J.-M. Duan, and L.Y. Shieh. Bound states, Cooper pairing, and Bose condensation in two dimensions. *Physical Review Lettres*, 62(9):981, 1989.

[124] A. Recati, C. Lobo, and S. Stringari. Role of interactions in spin-polarized atomic Fermi gases at unitarity. *Physical Review A*, 78(2):023633, 2008.

[125] C. A. Regal, M. Greiner, and D. S. Jin. Observation of resonance condensation of fermionic atom pairs. *Physical Review Letters*, 92(4):040403, 2004.

[126] C. A. Regal and D. S. Jin. Measurement of positive and negative scattering lengths in a Fermi gas of atoms. *Physical Review Letters*, 90:230404, 2003.

[127] S. Riedl, E. Snchez Guajardo, C. Kohstall, A. Altmeyer, M. Wright, J. Denschlag, R. Grimm, G. Bruun, and H. Smith. Collective oscillations of a Fermi gas in the unitarity limit: Temperature effects and the role of pair correlations. *Physical Review A*, 78(5):053609, 2008.

[128] G. Roati, F. Riboli, G. Modugno, and M. Inguscio. Fermi-Bose quantum degenerate ^{40}K - ^{87}Rb mixture with attractive interaction. *Physical Review Letters*, 89:150403, 2002.

[129] Christian Sanner, Edward Su, Aviv Keshet, Wujie Huang, Jonathon Gillen, Ralf Gommers, and Wolfgang Ketterle. Speckle imaging of spin fluctuations in a strongly interacting Fermi gas. *Physical Review Letters*, 106(1):010402, 2011.

[130] Andre Schirotzek. *Radio-Frequency Spectroscopy of Ultracold Atomic Fermi Gases.* PhD thesis, Massachusetts Institute of Technology, 2010. Cambridge, MA, USA.

[131] Andre Schirotzek, Yong Shin, Christian H. Schunck, and Wolfgang Ketterle. Determination of the superfluid gap in atomic Fermi gases by quasiparticle spectroscopy. *Physical Review Letters*, 101(14):140403, 2008.

[132] Andre Schirotzek, Cheng-Hsun Wu, Ariel Sommer, and Martin W. Zwierlein. Observation of fermi polarons in a tunable Fermi liquid of ultracold atoms. *Physical Review Letters*, 102(23):230402–4, 2009.

[133] S. Schmitt-Rink, C. M. Varma, and A. E. Ruckenstein. Pairing in two dimensions. *Physical Review Letters*, 63(4):445, 1989.

[134] F. Schreck, L. Khaykovich, K. L. Corwin, G. Ferrari, T. Bourdel, J. Cubizolles, and C. Salomon. Quasipure Bose-Einstein condensate immersed in a Fermi sea. *Physical Review Letters*, 87:080403, 2001.

[135] C.H. Schunck, Y.-I. Shin, A. Schirotzek, M.W. Zwierlein, and W. Ketterle. Pairing without superfluidity: The ground state of an imbalanced Fermi mixture. *Science*, 316:867, 2007.

[136] Christian H. Schunck. *Study of an ultracold cloud of fermionic ^{6}Li atoms near a Feshbach resonance.* PhD thesis, University of Heidelberg, 2002.

[137] Christian H. Schunck, Yong Shin, Andre Schirotzek, and Wolfgang Ketterle. Determination of the fermion pair size in a resonantly interacting superfluid. *Nature*, 454(7205):739–743, 2008.

[138] R. G. Scott, F. Dalfovo, L. P. Pitaevskii, and S. Stringari. Dynamics of dark solitons in a trapped superfluid fermi gas. *Physical Review Letters*, 106(18):185301, 2012.

[139] R. G. Scott, F. Dalfovo, L. P. Pitaevskii, S. Stringari, O. Fialko, R. Liao, and J. Brand. The decay and collisions of dark solitons in superfluid fermi gases. *New Journal of Physics*, 14(2):023044, 2012.

[140] Y. Shin, C. H. Schunck, A. Schirotzek, and W. Ketterle. Tomographic RF spectroscopy of a trapped Fermi gas at unitarity. *Physical Review Letters*, 99(9):090403, 2007.

[141] Y. Shin, M.W. Zwierlein, C.H. Schunck, A. Schirotzek, and W. Ketterle. Observation of phase separation in a strongly interacting imbalanced Fermi gas. *Physical Review Letters*, 97:030401, 2006.

[142] Yong-Il Shin. Determination of the equation of state of a polarized Fermi gas at unitarity. *Physical Review A*, 77(4):041603–4, 2008.

[143] Yong-il Shin, Christian H. Schunck, Andre Schirotzek, and Wolfgang Ketterle. Phase diagram of a two-component Fermi gas with resonant interactions. *Nature*, 451(7179):689–693, 2008.

[144] John Singleton and Charles Mielke. Quasi-two-dimensional organic superconductors: A review. *Contemporary Physics*, 43(2):63–96, 2002.

[145] Ariel Sommer, Mark Ku, Giacomo Roati, and Martin W. Zwierlein. Universal spin transport in a strongly interacting Fermi gas. *Nature*, 472(7342):201–204, 2011.

[146] Ariel Sommer, Mark Ku, and Martin W. Zwierlein. Spin transport in polaronic and superfluid Fermi gases. *New J. Phys.*, 13:055009, 2011.

[147] Ariel T. Sommer, Lawrence W. Cheuk, Mark J. H. Ku, Waseem S. Bakr, and Martin W. Zwierlein. Evolution of fermion pairing from three to two dimensions. *Physical Review Letters*, 108(4):045302, 2012.

[148] D. M. Stamper-Kurn, H. J. Miesner, S. Inouye, M. R. Andrews, and W. Ketterle. Collisionless and hydrodynamic excitations of a Bose-Einstein condensate. *Physical Review Letters*, 81(3):500–503, 1998.

[149] D.M. Stamper-Kurn. *Peeking and poking at a new quantum fluid: Studies of gaseous Bose-Einstein condensates in magnetic and optical traps.* Ph.d., Massachusetts Institute of Technology, 1999.

[150] C. A. Stan. *Experiments with Interacting Bose and Fermi Gases.* Phd, Massachusetts Institute of Technology, 2005.

[151] J. T. Stewart, J. P. Gaebler, C. A. Regal, and D. S. Jin. Potential energy of a ^{40}K Fermi gas in the BCS-BEC crossover. *Physical Review Letters*, 97(22):220406, 2006.

[152] S. Stringari. Collective excitations of a trapped Bose-condensed gas. *Physical Review Letters*, 77:2360–2363, 1996.

[153] S. Stringari. Collective oscillations of a trapped superfluid Fermi gas near a Feshbach resonance. *Europhysics Letters*, 65:749–752, 2004.

[154] Meng Khoon Tey, Leonid A. Sidorenkov, Edmundo R. Sanchez Guajardo, Rudolf Grimm, Mark J. H. Ku, Martin W. Zwierlein, Yan-Hua Hou, Lev Pitaevskii, and Sandro Stringari. Collective modes in a unitary Fermi gas across the superfluid phase transition. *Preprint*, 2012. arXiv:1211.2659 [cond-mat.quant-gas].

[155] M. Tinkham. *Introduction to Superconductivity.* Dover, Mineola, New York, second edition edition, 2004.

[156] Andrew G. Truscott, Kevin E. Strecker, William I. McAlexander, Guthrie B. Partridge, and Randall G. Hulet. Observation of Fermi pressure in a gas of trapped atoms. *Science*, 291:2570–2572, 2001.

[157] Igor uti, Jaroslav Fabian, and S. Das Sarma. Spintronics: Fundamentals and applications. *Reviews of Modern Physics*, 76(2):323–410, 2004.

[158] K. Van Houcke, F. Werner, E. Kozik, N. Prokof/'ev, B. Svistunov, M. J. H. Ku, A. T. Sommer, L. W. Cheuk, A. Schirotzek, and M. W. Zwierlein. Feynman diagrams versus fermi-gas feynman emulator. *Nat Phys*, 8(5):366–370, 2012. 10.1038/nphys2273.

[159] Bert Van Schaeybroeck and Achilleas Lazarides. Normal-superfluid interface scattering for polarized fermion gases. *Physical Review Letters*, 98(17):170402, 2007.

[160] L. Vichi and S. Stringari. Collective oscillations of an interacting trapped fermi gas. *Physical Review A*, 60(6):4734, 1999.

[161] Xiao-Gang Wen. *Quantum Field Theory of Many-Body Systems.* Oxford Graduate Texts. Oxford, Oxford, 2007.

[162] Flix Werner and Yvan Castin. Unitary quantum three-body problem in a harmonic trap. *Physical Review Letters*, 97(15):150401, 2006.

[163] S. A. Wolf, D. D. Awschalom, R. A. Buhrman, J. M. Daughton, S. von Molnar, M. L. Roukes, A. Y. Chtchelkanova, and D. M. Treger. Spintronics: a spin-based electronics vision for the future. *Science*, 294(5546):1488–95, 2001.

[164] M. J. Wright, S. Riedl, A. Altmeyer, C. Kohstall, E. R. Sanchez Guajardo, J. Hecker-Denschlag, and R. Grimm. Finite-temperature collective dynamics of a Fermi gas in the BEC-BCS crossover. *Physical Review Letters*, 99(15):150403, 2007.

[165] Cheng-Hsun Wu, Jee Woo Park, Peyman Ahmadi, Sebastian Will, and Martin W. Zwierlein. Ultracold fermionic feshbach molecules of ^{23}na^{40}k. *Physical Review Letters*, 109(8):085301, 2012.

[166] Cheng-Hsun Wu, Ibon Santiago, Jee Woo Park, Peyman Ahmadi, and Martin W. Zwierlein. Strongly interacting isotopic bose-fermi mixture immersed in a fermi sea. *Physical Review A*, 84(1):011601, 2011.

[167] Tarik Yefsah, Rmi Desbuquois, Lauriane Chomaz, Kenneth Gnter, and Jean Dalibard. Exploring the thermodynamics of a two-dimensional Bose gas. *Physical Review Letters*, 107(13):130401, 2011.

[168] V. E. Zakharov and A. B. Shabat. Interaction between solitons in a stable medium. *Sov. Phys. JETP*, 37:823–828, 1973.

[169] G. Zürn, T. Lompe, A. N.Wenz, S. Jochim, P. S. Julienne, and J. M. Hutson. Precise characterization of ^{6}Li Feshbach resonances using trap-sideband resolved RF spectroscopy of weakly bound molecules. *Preprint*, 2012. arXiv:1211.1512 [cond-mat.quant-gas].

[170] M. W. Zwierlein, J. R. Abo-Shaeer, A. Schirotzek, C. H. Schunck, and W. Ketterle. Vortices and superfluidity in a strongly interacting Fermi gas. *Nature*, 435:1047–1051, 2005.

[171] Martin W. Zwierlein. *High-Temperature Superfluidity in an Ultracold Fermi Gas.* PhD thesis, Massachusetts Institute of Technology, 2006.

[172] Martin W. Zwierlein, Andr Schirotzek, Christian H. Schunck, and Wolfgang Ketterle. Fermionic superfluidity with imbalanced spin populations. *Science*, 311:492–496, 2006.

[173] Martin W. Zwierlein, Christian H. Schunck, Andr Schirotzek, and Wolfgang Ketterle. Direct observation of the superfluid phase transition in ultracold Fermi gases. *Nature*, 442:54–58, 2006.

[174] M.W. Zwierlein, C.A. Stan, C.H. Schunck, S.M.F. Raupach, S. Gupta, Z. Hadzibabic, and W. Ketterle. Observation of Bose-Einstein condensation of molecules. *Physical Review Letters*, 91:250401, 2003.

[175] M.W. Zwierlein, C.A. Stan, C.H. Schunck, S.M.F. Raupach, A.J. Kerman, and W. Ketterle. Condensation of pairs of fermionic atoms near a Feshbach resonance. *Physical Review Letters*, 92:120403, 2004.